Development, Implementation, Calibration and Use of Practical Constitutive Models in Finite Element Analysis of Offshore Foundations

Scott Andrew Whyte

St. Catherine's College

University of Oxford

A thesis submitted for the degree of Doctor of Engineering (DEng)

St Catherine's College
Hilary Term 2020

Declaration

I declare that, except where specific reference is made to the works of others, the contents of this thesis are original and have never been submitted, in part or as a whole, to any other university for any degree, diploma or other qualifications.

Scott Andrew Whyte

March 2020

Acknowledgements

Firstly, I would like to express my sincere gratitude to my supervisors at the University of Oxford, Professor Harvey Burd and Professor Chris Martin, for their continued guidance and valuable advice throughout my studies. Both of them have a remarkable ability to focus on the most important aspects of complex problems making them more manageable to solve. I have very much enjoyed all of our discussions and meetings and look forward to continued collaboration in the future. I would also like to thank my industrial supervisor, Dr. Mike Rattley, from Fugro who has helped guide my research. It has been a pleasure to work with Mike, as he has an incredible enthusiasm for geotechnics and was always available for a stimulating discussion on soil mechanics.

This project would not have been possible without the financial support of Fugro. I have very much enjoyed my time at Oxford, and I am very grateful for the opportunity Fugro have given me.

Undertaking this DEng project, I have been lucky enough to have met and had support from many people within the offshore geotechnical engineering community and it would not be possible to thank them all. However, I would like to particularly thank Carl Erbrich who has been a great support throughout and Professor Mark Randolph for his guidance and supervision during my secondment to the University of Western Australia.

Abstract

The finite element method is routinely used for the design of offshore wind turbine foundations, with complex time-consuming three-dimensional (3D) finite element analysis (FEA) typically performed to calibrate site-specific simplified macro element or one-dimensional (1D) finite models for rapid foundation sizing design calculations. The soil constitutive model used in a FEA calculation significantly influences the predicted foundation response. Therefore, given the uptake by industry of FEA for offshore wind turbine foundation design, it is important that practical advanced constitutive models are available which can be demonstrated to work robustly and accurately as design tools.

There have been significant advances in constitutive modelling of soils over the last few decades, with many advanced models presented in the literature. However, the uptake of such advanced models in industry, for foundation design FEA, is still relatively low with more basic robust models typically preferred. The principal reasons for this are considered to be: difficulties in calibrating model parameters to standard laboratory test data; robust implementation of advanced constitutive models in FEA software is time consuming and complex; excessive analysis run times and convergence issues makes the use of some advanced models on design projects unfeasible; and there are few examples that demonstrate the robustness and predictive capabilities of many advanced models for complex 3D soil-structure interaction problems.

It is therefore important that practical constitutive models are also developed which can be demonstrated to work robustly and accurately as useful tools for design FEA. This project therefore considers the development and use of practical constitutive models for design, and includes a review of some existing models, with a focus on the predictive capability and parameter calibration process for foundation design FEA.

A practical robust sand model formulation and implementation is presented for use in design analysis with extensive calibration of the model to laboratory tests data, at a number of different sites, followed by FEA of monopile and suction bucket foundations. In addition, the formulation

and implementation of a multi-surface soil plasticity model, termed the PIMS model, which is suitable for short-term storm type loading conditions, is presented. Calibration of the PIMS model to North Sea overconsolidated clay laboratory test data is performed, followed by FEA of monopiles foundations under monotonic and cyclic loading. The suitability of a bounding surface plasticity model for sand to predict the uplift response of a suction bucket foundation under different loading rates is also investigated, with comparison of FEA predictions to previously-published centrifuge test results. Finally, numerical analysis of monopile foundations performed as part of geotechnical design progression for a large offshore wind farm development, in the North Sea is presented using a number of different constitutive models.

In all cases extensive calibration to laboratory element tests (primarily from North Sea soil units) is presented, followed by the comparison of FEA predictions to foundation load tests, where possible, to demonstrate that the models are suitable for design FEA of offshore wind turbine foundations.

Table of Contents

Section 1

INTRODUCTION AND OVERVIEW

Contents

1. INTRODUCTION AND OVERVIEW

1.1 Motivation

A number of substructure options can be used to support offshore wind turbines, including bottom-fixed structures (e.g. monopiles and jackets) and, in deeper water, floating structures (e.g. tension-leg-spars and semi-submersibles).

To support offshore bottom-fixed wind turbines, monopile, gravity base, mono-bucket, multi-bucket and multi-piled foundation concepts can be used (Figure 1.1). A suction bucket (also termed a suction installed caisson) consists of a large cylinder that is open at the base and closed at the top with embedded length to diameter (L/D) ratios typically between 0.5 and 1.0. Monopiles are single large diameter steel tubes, typically driven into the soil, with diameters generally between 8 m to 10 m for recent offshore wind farms (Byrne et al., 2017). Although monopiles have proved to be the most popular foundation concept to date, being utilised for 87% of the installed offshore wind turbines in Europe (Wind Europe, 2018), the multi-bucket foundation system has also proved to be popular in recent years for offshore wind farm developments. For example, the Aberdeen Offshore Wind Farm and Borkum Riffgrund 1 and 2 are recent offshore wind farms which have adopted multi-bucket foundation systems (Sturm, 2017; Shonberg et al., 2017).

This study focuses on performing design finite element analysis (FEA) of the suction bucket and monopile foundation concepts. The finite element method is routinely used for the design of offshore wind turbine foundations, with complex time-consuming three-dimensional (3D) FEA typically performed to calibrate simplified macro element or one-dimensional (1D) finite models for rapid foundation design calculations across large wind farms (e.g. Erbrich et al., 2010; Byrne et al., 2017; Suryasentana et al., 2017; Skau et al., 2018).

Although these relatively sophisticated site-specific design methods are a significant advance on the more traditional empirical rule-based approaches, it means the predictive capability of the FEA

models are of critical importance for the overall design of the foundations. Whereas, in the past 3D FEA was typically only used as a specialist tool to review a few complex design cases or as a validation tool to confirm conservatism in the design, it is now employed as the primary design tool. With computing power continually increasing, this trend of increased advanced 3D FEA being performed by industry for foundation design will likely continue. Figure 1.2 shows a flow chart of the design procedures employed for offshore wind turbine foundations, where it can be seen that the FEA performed is of pivotal importance.

Many components of a FEA design model will control the overall predicted foundation response (e.g. element type; boundary conditions; global solution strategy; constitutive model). The constitutive model is a fundamental aspect (Figure 1.3) and for geotechnical analysis it is typically regarded as the most important component with respect to obtaining realistic predictions of the foundation response. The constitutive model is a set of mathematical relations which controls the stress-strain response of the continuum material within a FEA calculation (Figure 1.3).

With the increased use of FEA for the design of offshore wind turbine foundations, clearly the use of suitable constitutive models becomes increasingly important to ensure accurate design analysis predictions are achieved (e.g. Taborda et al., 2019; Zdravković et al., 2019). There have been significant advances in constitutive modelling of soils over the last few decades, with many thousands of advanced models presented in the literature, some of which are discussed in Section 2. However, the uptake of such models in industry, for foundation design FEA, is relatively low with more basic robust models typically preferred (Grammatikopoulou et al., 2017). There are many reasons for this, such as:

i. Difficulties in calibrating model parameters using standard laboratory test data typically available from geotechnical site investigations;
ii. Little focus given in the literature to the parameter calibration procedure for specific models;
iii. Mathematical complexity resulting in models being black box tools;
iv. Robust implementation of models in FEA software is time consuming and complex;
v. Excessive analysis run times and convergence issues often makes the use of advanced models on design projects unfeasible;

vi. Many advanced constitutive models are only presented for single element calculations (i.e. not demonstrated to work robustly in complex 2D or 3D boundary value problems);

vii. There are few examples that validate the predictive capabilities of advanced models for complex 3D soil-structure interaction problems (e.g. comparison to foundation load tests and/or centrifuge experiments).

It is therefore important that practical constitutive models are available which can be demonstrated to work robustly and accurately as useful tools for design FEA.

Several authors have attempted to categorise constitutive models based on their predictive capability and general complexity. For example, Wood (1991) proposed a hierarchy of: Children models, Students' models, Engineers' models and Philosophers' models, similarly Kolymbas (2000) proposed to group models as either Elastic, Primitive, Ad hoc or Advanced. Within this study the following hierarchy, based partly on recommendations by Wood (1991), is proposed to categorise elastoplastic constitutive models:

A. Basic Models:

- Simplistic but very robust models;
- Examples are linear elastic perfectly-plastic Tresca or Mohr-Coulomb models;
- Generally, provide a poor prediction of the overall soil stress-strain response;
- Models suitable for only limited set of specific design cases (e.g. ultimate limit state).

B. Engineer Design Models:

- Models have improved predictive capability compared to Basic models;
- Additional modelling features incorporated within the constitutive model, which engineers, using their judgement, consider to be needed for the design application;
- Models have been validated by simulating foundation boundary value problems accurately (i.e. prediction compared to foundation load tests) and are suitably robust to be used for design FEA.

C. Philosopher Models:

- Mathematically complex models which aim to capture the soil response very accurately;
- Implementation of models is an extensive task due to model mathematical complexity;

- Models typically not fully validated, with most publications focusing on the single element response, and little evidence in the literature of the model's predictive performance in (for example) analysis of foundations.

As discussed by Wood (1991), there is a requirement for practical constitutive models which capture the most salient features of the soil behaviour affecting the specific foundation problem in question. Therefore, different practical constitutive models (i.e. a library of Engineer Design models) of varying complexity should be developed and utilised for specific loading conditions (e.g. monotonic, small number of load cycles); specific soil conditions (e.g. dense sand or overconsolidated clay) and even potentially specific design conditions (e.g. fatigue limit state or serviceability limit state), as opposed to a single all-encompassing constitutive model (i.e. Philosopher model). It is therefore proposed that a designer using FEA should have a library of constitutive models for a range of different problems and stages of design. For example, if FEA is to be performed at an early stage of design, e.g. Front-End Engineering Design (FEED), and few laboratory data are available then an advanced constitutive model that requires extensive calibration data, regardless of its potential predictive capability, is of little value. Equally, if extensive laboratory data exists and the design time schedule permits, a complex advanced constitutive model may be more appropriate, if available and robust in FEA. This is demonstrated visually in Figure 1.4 which shows that the complexity of constitutive model used should match the available site-specific measured test data when used in a design project. The level of accuracy required from FEA performed as part of an offshore foundation design project, and in turn the complexity of the constitutive model and laboratory test data required, should be decided by the lead foundation design engineer and is dependent on many factors (e.g. the design stage of the project; the purpose of FEA; design schedules). It should be noted, when the level of accuracy is considered to be lower, increased levels of conservativisms must be assumed when calibrating the model parameters.

Within this DEng project a library of practical robust Engineer Design constitutive models is developed to facilitate the design FEA of offshore wind turbine foundations. The models have

been developed for specific offshore foundation problems where few existing constitutive models are suitable for design FEA. An extensive overview of calibration to real soil data is provided for the developed models. Figure 1.5 outlines the proposed full constitutive model development process which is required. It is considered to be important that the full process is performed for the developed Engineer Design models by presenting calibration to real soil data, while also assessing the predictive performance and numerical robustness in the context of complex 3D soil-structure interaction problems simulated using FEA.

The Venn diagram presented in Figure 1.6 shows the three main components of work (Zones A, B and C) that should be performed in the development of a new constitutive model. Many previous authors have focused on intersection zones *I* and *III* within the Venn diagram (Figure 1.6); however, few have considered interaction zone *II* which looks at not only the development of a constitutive model but also its calibration to soil sample testing data followed by a detailed assessment of its performance in 3D FEA.

This DEng project considers the full development process of a number of new practical constitutive models and therefore occupies interaction zone II of the Venn diagram (Figure 1.6). This project considers extensive laboratory testing of soil (primarily from North Sea soil units); constitutive model implementation and development for a number of different specific design applications; model parameter calibration; and FEA of offshore foundations with validation against foundation load tests where possible. The practical constitutive models were developed specifically for use in design FEA of industry projects.

1.2 Outline of Portfolio

This project focused on the development, implementation and calibration of different constitutive models for the design FEA of offshore foundations. This project has been performed as a DEng portfolio of work in which the author has worked on a number of different industry focused

research projects at Fugro and the University of Oxford, as part of the Renewable Energy Marine Structures (REMS) Centre for Doctoral Training Centre (CDT).

The DEng portfolio presented in the following sections is structured such that each section is a stand-alone piece of work. Figure 1.7 presents the general outline of this DEng project in which three constitutive models are developed and implemented for a number of different specific design applications, with extensive model parameter calibration to laboratory test data along with FEA of offshore foundations. Although each section presented in this project is a stand-alone piece of work, they all have the common theme of developing constitutive models for foundation design FEA. Each model was developed for a particular foundation design problem (e.g. suitable for different foundation type, loading type or design stage) and as such address gaps in the available models in a practical design context . The range of different elastoplastic modelling approaches typically employed in the literature for modelling soils were considered within this study by developing single surface, bounding surface and multi-surface plasticity models. A summary of each section is given below:

Section 2: Overview of Soil Constitutive Modelling

Section 2 presents a constitutive modelling literature review. An overview of constitutive modelling concepts is presented followed by a review of specific constitutive models presented in the literature.

Section 3: Constitutive Model Implementation Overview

Section 3 details main preliminaries required to formulate an elastoplastic constitutive model together with the implementation approach used within this study.

Section 4: Development of Simple Dilational Sand Model

Section 4 presents a developed practical single surface model, named the Simple Dilational Sand (SDS) model, suitable for FEA of soil-structure interaction problems involving partially drained to undrained dense to very dense sand. This section includes a paper (Paper 1) titled, *A practical constitutive model for offshore foundation problems involving dense sands in*

partially drained to undrained conditions. The paper was published in the peer-reviewed 8th International Offshore Site Investigation and Geotechnics (OSIG) Conference 2017.

Section 5: Development, Implementation and use of the PIMS Model for Clay

Section 5 presents a developed model, named the Parallel Iwan Multi-Surface (PIMS) model, suitable for FEA of soil-structure interaction problems involving clay undergoing undrained monotonic and cyclic storm-type loading. The section includes a paper (Paper 2) titled, *Formulation and implementation of a practical multi-surface soil plasticity model*. The paper has been accepted for publication in the journal *Computers and Geotechnics*.

Section 6: Development and use of a Bounding Surface model for Sand

Section 6 describes the application of a bounding surface plasticity model to the analysis of suction bucket pull-out tests in sand. In this study a bounding surface model, based on the Manzari-Dafalias model architecture, is calibrated to laboratory element test data and subsequently used to predict the response of suction buckets under tension loading and compared to a number of different centrifuge model test results. The constitutive model formulation presented in this section includes several modifications to previously published versions of the model. A detailed description of the work performed is given in a paper (Paper 3) titled, *Comparison of numerical simulations using a bounding surface model to centrifuge tests of axial loaded suction buckets in dense sand*.

Section 7: Offshore Wind Farm Monopile Finite Element Analysis

Section 7 presents extensive numerical analysis of monopile foundations performed as part of the geotechnical design progression for a large offshore wind farm development, in the North Sea. This work formed part of a design project undertaken by Fugro. The work involved calibration of constitutive models and numerical analysis (3D FEA) of monopile lateral load response. Comparison to pile load test data is also presented along with a soil profile layering sensitivity study.

1.3 Figures

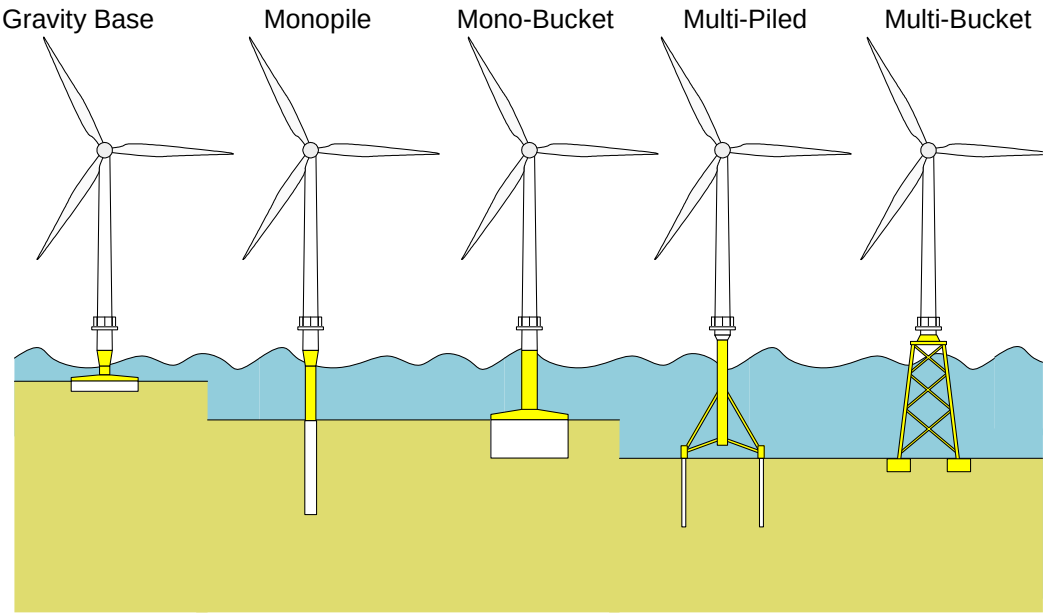

Figure 1.1: Offshore wind turbine bottom-fixed foundations concepts (Byrne, 2011)

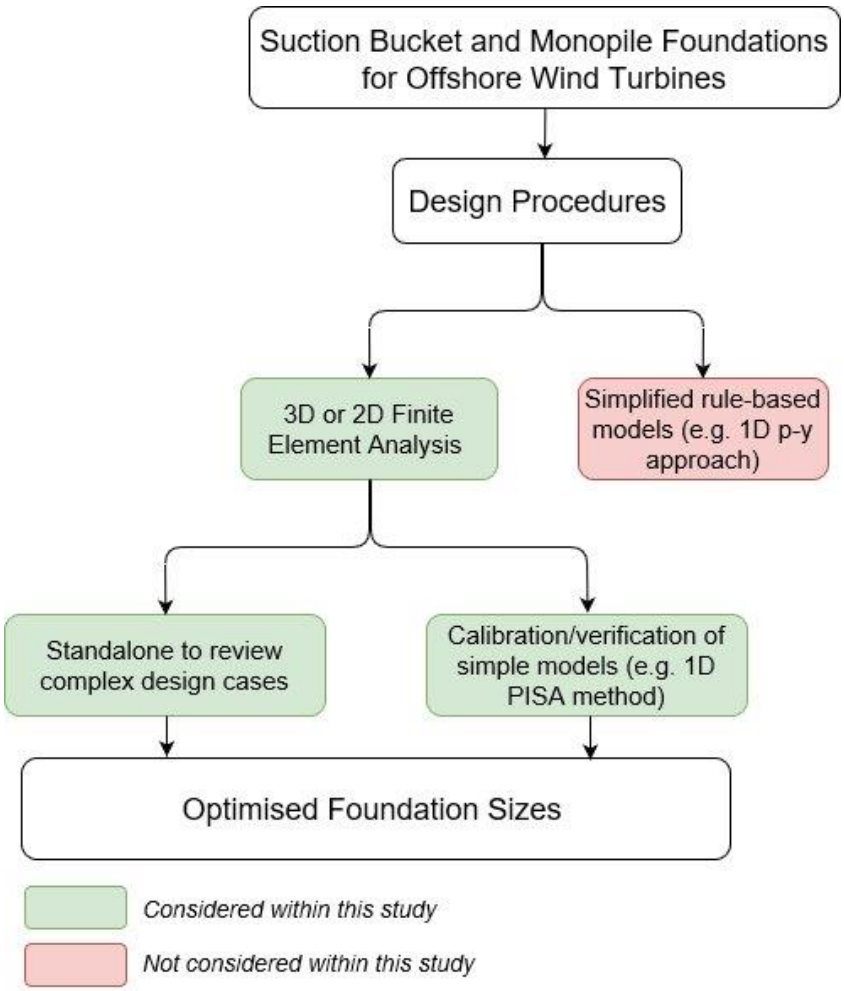

Figure 1.2: Offshore wind turbine foundation design procedures incorporating 2D and 3D finite element analysis

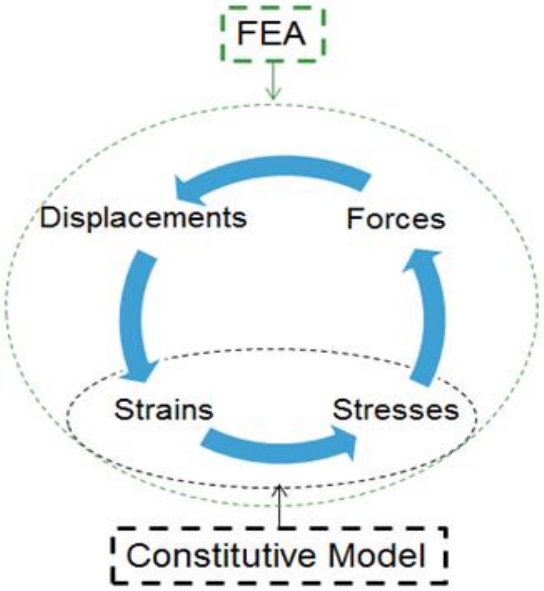

Figure 1.3: Finite element analysis calculation process

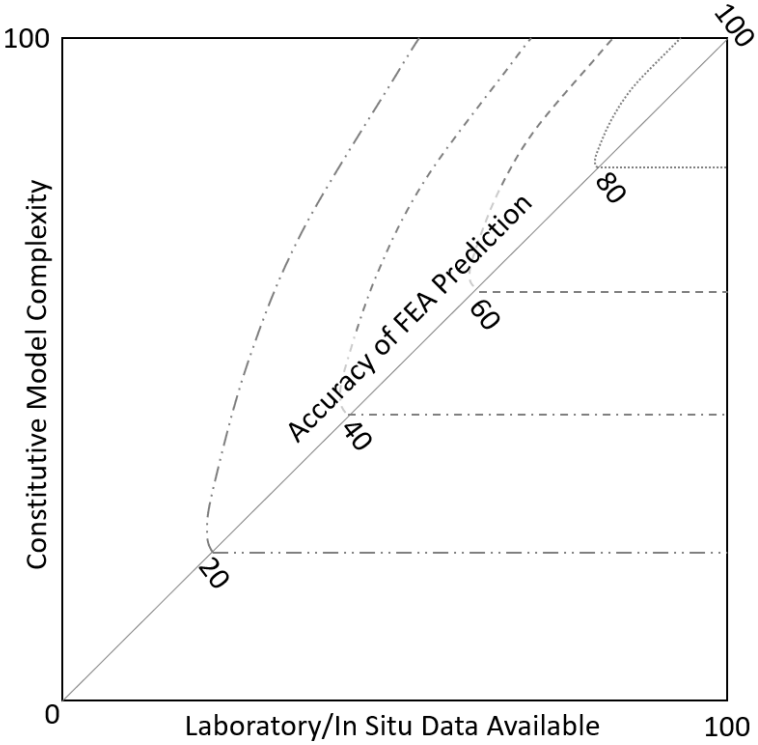

Figure 1.4: Accuracy of finite element analysis prediction

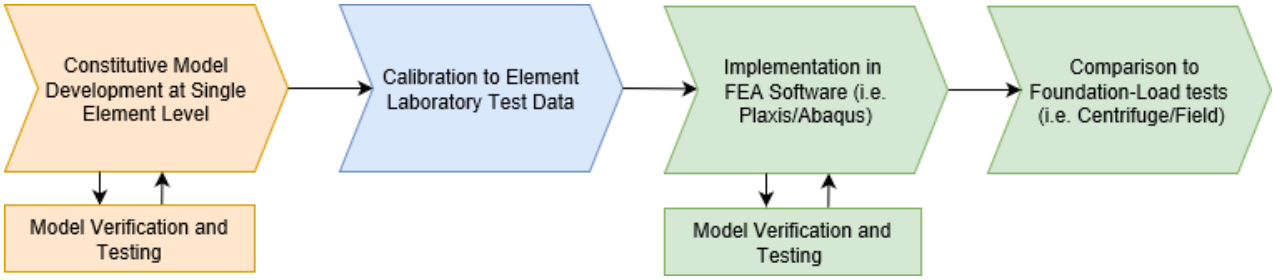

Figure 1.5: Constitutive model development process

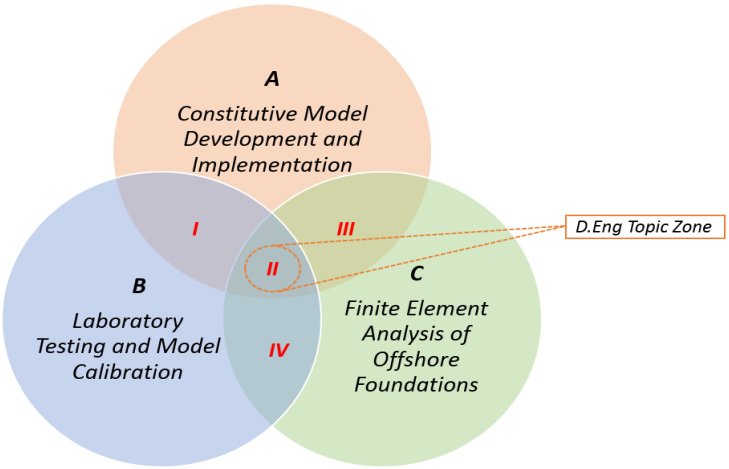

Figure 1.6: Constitutive model development Venn diagram

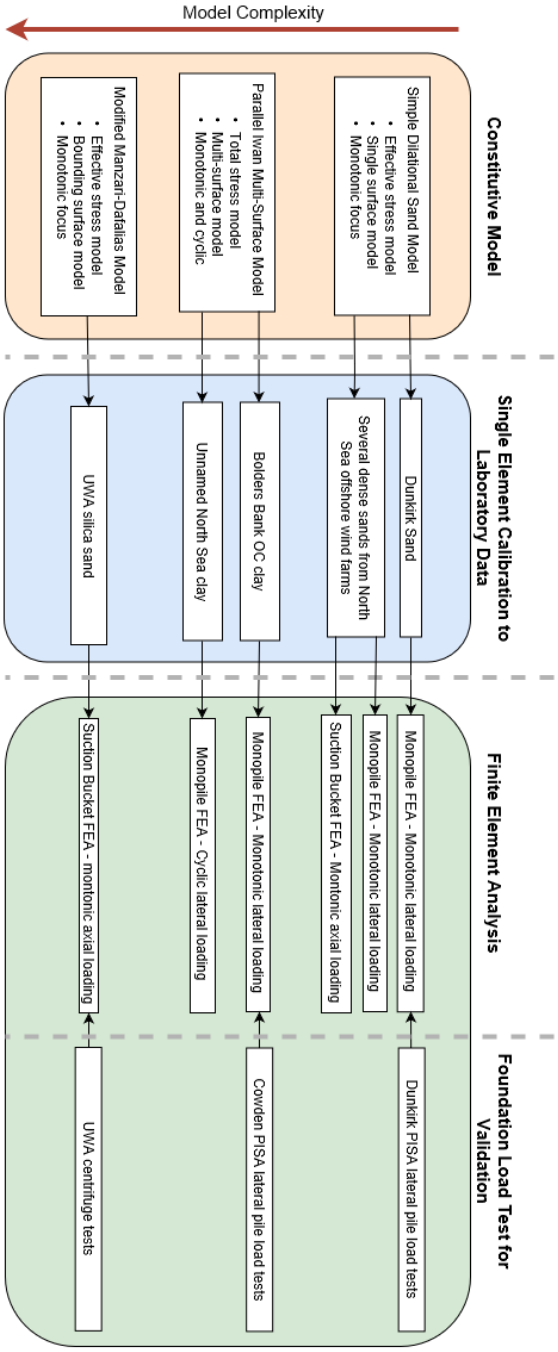

Figure 1.7: DEng project portfolio overview

Section 2

OVERVIEW OF SOIL CONSTITUTIVE MODELLING

Contents

2. OVERVIEW OF SOIL CONSTITUTIVE MODELLING

2.1 Basic Formulation of Elastoplastic Constitutive models

The basic formulation and implementation principles of an elastoplastic constitutive model are described by several authors (e.g. Britto and Gunn, 1987; Potts and Zdravković, 1999; Dunne and Petrinic, 2005). The following summary gives an overview of the main components required to formulate an elastoplastic constitutive model.

A conventional single surface elastoplastic constitutive model is made up four fundamental components: a yield surface, hardening/softening rule(s), a plastic potential function and an elastic model.

The yield surface separates the elastic behaviour from elastoplastic behaviour. Typically, the yield surface is formed in stress space ($\boldsymbol{\sigma}$); however, it is also possible to form it in strain space ($\boldsymbol{\varepsilon}$), where $\boldsymbol{\sigma} = \left[\sigma_{xx}, \sigma_{yy}, \sigma_{zz}, \tau_{xy}, \tau_{yz}, \tau_{zx}\right]^T$ is the stress tensor given in Voigt/vector form and $\boldsymbol{\varepsilon} = \left[\varepsilon_{xx}, \varepsilon_{yy}, \varepsilon_{zz}, 2\varepsilon_{xy}, 2\varepsilon_{yz}, 2\varepsilon_{zx}\right]^T$ is the strain tensor given in Voigt/vector form (further details of notation given in Section 3). The yield surface function (f) is typically dependent on the stress state and hardening/softening parameter (h) in conjunction with several calibrated input parameters.

If $f(\boldsymbol{\sigma}, h) < 0$ then the stress state is within the yield surface, i.e. no plastic straining occurs, and the response is fully elastic. If $f(\boldsymbol{\sigma}, h) = 0$, the stress state lies on the yield surface and elastoplastic behaviour is predicted. Acceptable stress states can never lie outside the yield surface i.e. it is always the case that $f(\boldsymbol{\sigma}, h) \leq 0$.

The hardening/softening rule(s) controls the variation of h with plastic strain, and this is then used to define an updated size and/or position of the yield surface in stress space. For elastic-perfectly-plastic models, no hardening/softening occurs, and the yield surface is fixed in stress space. However, for strain hardening/softening elastoplastic models h varies with plastic strain and the yield surface expands or contacts for isotropic hardening/softening and translates in stress space for kinematic hardening.

The plastic potential function (g) is used to define the direction of plastic straining for stress states on the yield surface. The outward normal to the plastic potential function at the current stress state, on the yield surface, provides the relative size of the components of the plastic strain increment. Hence, only the derivatives of the plastic potential function are used for formulation of an elastoplastic model. The infinitesimal increment of the plastic strain components ($\delta\boldsymbol{\varepsilon}^p$) is defined by the flow rule, which is given by,

$$\delta\boldsymbol{\varepsilon}^p = \Lambda\frac{\partial g}{\partial\boldsymbol{\sigma}} \tag{2.1}$$

where Λ is a scalar plastic multiplier which defines the magnitude and $\partial g/\partial\boldsymbol{\sigma}$ defines the direction of the incremental plastic strains. The main ingredients of the elastoplastic constitutive model are then put together to give a relationship between the incremental stresses and the incremental strains, for elastoplastic loading (i.e. $f(\boldsymbol{\sigma}, h) = 0$). The increment of strains can be decomposed additively into plastic strains and elastic strains and consequently the infinitesimal incremental stresses and strains can be linked by,

$$\delta\boldsymbol{\sigma} = \boldsymbol{D}_e(\delta\boldsymbol{\varepsilon} - \delta\boldsymbol{\varepsilon}^p) \tag{2.2}$$

where $\boldsymbol{D}_e$ is the elastic stiffness matrix. An isotropic linear $\boldsymbol{D}_e$ is given by,

$$\boldsymbol{D}_e = \begin{bmatrix} K+4G/3 & K-2G/3 & K-2G/3 & 0 & 0 & 0 \\ K-2G/3 & K+4G/3 & K-2G/3 & 0 & 0 & 0 \\ K-2G/3 & K-2G/3 & K+4G/3 & 0 & 0 & 0 \\ 0 & 0 & 0 & G & 0 & 0 \\ 0 & 0 & 0 & 0 & G & 0 \\ 0 & 0 & 0 & 0 & 0 & G \end{bmatrix} \tag{2.3}$$

where, G is the shear modulus and K is the bulk modulus. By substituting Equation 2.1 into 2.2 we can obtain,

$$\delta\boldsymbol{\sigma} = \boldsymbol{D}_e\delta\boldsymbol{\varepsilon} - \Lambda\,\boldsymbol{D}_e\frac{\partial g}{\partial\boldsymbol{\sigma}} \tag{2.4}$$

A fundamental principle of an elastoplastic model, as discussed above, is that the stresses must lie on the yield surface during plastic straining. This introduces the consistency condition, which is given by,

$$\delta f = \frac{\partial f}{\partial\boldsymbol{\sigma}}\,\delta\boldsymbol{\sigma} + \frac{\partial f}{\partial h}\,\delta h = 0 \tag{2.5}$$

By rearranging and combining Equations 2.4 and 2.5 we can obtain the following equation to determine the plastic multiplier,

$$\Lambda = \frac{\frac{\partial f}{\partial \boldsymbol{\sigma}}^T \boldsymbol{D}_e \delta \boldsymbol{\varepsilon}}{\frac{\partial f}{\partial \boldsymbol{\sigma}}^T \boldsymbol{D}_e \frac{\partial g}{\partial \boldsymbol{\sigma}} + H} \quad 2.6$$

where H is the hardening modulus which is given by,

$$H = -\frac{1}{\Lambda} \frac{\partial f}{\partial h}^T \delta h \quad 2.7$$

It is convenient to link the increment of stresses to an increment of strains by a single stiffness matrix termed the elastoplastic constitutive matrix ($\boldsymbol{D}_{ep}$) which is given by,

$$\delta \boldsymbol{\sigma} = \boldsymbol{D}_{ep} \delta \boldsymbol{\varepsilon} \quad 2.8$$

By combining Equations 2.4 and 2.6 we can then obtain the $\boldsymbol{D}_{ep}$ as,

$$\boldsymbol{D}_{ep} = \boldsymbol{D}_e - \frac{\boldsymbol{D}_e \frac{\partial g}{\partial \boldsymbol{\sigma}} \frac{\partial f}{\partial \boldsymbol{\sigma}}^T \boldsymbol{D}_e}{\frac{\partial f}{\partial \boldsymbol{\sigma}}^T \boldsymbol{D}_e \frac{\partial g}{\partial \boldsymbol{\sigma}} + H} \quad 2.9$$

As can be seen from Equation 2.9, the gradients of the yield surface and the plastic potential are required to form the elastoplastic constitutive matrix.

2.2 Overview of General Elastoplastic Modelling Approaches

2.2.1 Elasticity

2.2.1.1 Stress- and Strain-Dependent Elasticity

Extensive experimental studies, presented in the literature for different soil types, have shown that for monotonic loading, the variation of the tangent and secant shear stiffness ($G_{\tan}$ and $G_{\sec}$) with the logarithm of shear strain (γ) typically follows an S-shaped curve (e.g. Clayton, 2011; Vardanega and Bolton, 2013; Oztoprak and Bolton, 2013) with the very small strain shear modulus (G_0) representing a plateau at very small shear strains (e.g. $\gamma < 10^{-6}$). Figure 2.1 presents a typical shear stiffness-strain curve observed from laboratory testing of soil.

As discussed by Houlsby and Wroth (1991) the term elastic is rather ambiguous when considering the stress-strain response of soil since the truly recoverable elastic zone of soil is very small, i.e. for strains less than approximately 0.001% (Jardine, 1992); however, often within single yield surface constitutive models an elastic response is assumed within the yield surface for strain levels in which some irrecoverable plastic strains will occur in reality (e.g. Schroeder et al., 2015; Woo et al., 2017; Zdravković et al., 2019).

Experimental results presented in the literature have shown that G_0 is typically found to be a function of the mean effective stress (p') and void ratio (e) for sands, with the overconsolidation ratio (OCR) also considered for clays (e.g. Hardin and Black, 1969; Hardin and Drnevich, 1972; Clayton, 2011; Oztoprak and Bolton, 2013; Vardanega and Bolton, 2013). The following relationship proposed by Hardin and Richart (1963) and Hardin and Black (1969) is often adopted to define the elastic shear modulus within elastoplastic constitutive models (e.g. Dafalias and Manzari, 2004; Loukidis and Salgado, 2009; Woo et al., 2017).

$$G_0 = G_{ref}\, f(e)\, p_{ref} \left(\frac{p'}{p_{ref}}\right)^n \tag{2.10}$$

Where $f(e)$ is a function that controls the effect of void ratio and is typically given by,

$$f(e) = \frac{(fe_1 - e)^2}{1 + e} \tag{2.11}$$

The dimensionless input parameters G_{ref}, n and fe_1 are calibrated to laboratory (e.g. bender element or resonant column tests) and in situ test (e.g. seismic cone penetration tests) data and p_{ref} is a reference stress. Wichtmann and Triantafyllidis (2009) recommended values of fe_1 based on the particle size distribution curve of the soil.

To complete $\boldsymbol{D}_e$ (Equation 2.3) the elastic bulk modulus can either be specified independently, using a similar function to Equation 2.10, or it can be determined from the shear modulus by,

$$K = \frac{2\,G(1 + v)}{3\,(1 - 2\,v)} \tag{2.12}$$

where v is the Poisson's ratio. Clearly using a stress-dependent isotropic $\boldsymbol{D}_e$, based on G_0, within a single yield surface model will not accurately capture the nonlinear stress-strain behaviour at small to medium strains (Figure 2.1).

Given that the strain levels within the soil around foundations, under operational conditions, typically fall within the range of 0.01 to 0.1 % (Clayton, 2011) an accurate prediction of the soil response in this small to medium strain range (see Figure 2.1) is often of significant importance. In addition, when considering different design states for offshore wind turbine foundations it is important that the stiffness response of the soil is predicted accurately, by the constitutive model used in FEA, at a range of strain levels to avoid the need for a number of different calibrated parameter sets being used for each design state. For example, when considering typical operational load levels for fatigue limit state (FLS) design the very small to small strain response will be of importance, whereas when considering serviceability limit state (SLS) and ultimate limit state (ULS) conditions the medium to large strain response will be of increased importance (Kallehave et al., 2015; Arany et al., 2017; OWA, 2019).

Therefore, a number of empirical functions have been developed in the literature to represent the shear stiffness reduction curve with some measure of deviatoric strain (E_q) or γ (e.g. Jardine et al., 1986; Bolton et al., 1994; Darendeli, 2001; Taborda and Zdravković, 2012; Vardanega and Bolton, 2013). These models have been shown to provide a good fit with data at very small to medium strain levels; however, the predicted response at medium to large strain levels is typically poor. As a result, strain-dependent elastic functions are often incorporated within single surface elastoplastic constitutive models (e.g. Benz, 2007; Schroeder et al., 2015; Zdravković et al., 2019) to control the stiffness-strain response from very small to large strains (Figure 2.2). For incorporation within a constitutive model the tangent shear stiffness (G_{tan}) is required, therefore strain-dependent models formulated using G_{sec}, such as Darendeli (2001) and Vardanega and Bolton (2013) must first be converted to G_{tan}. To complete the strain-dependent $\boldsymbol{D}_e$ for use in constitutive models, the elastic tangent bulk stiffness (K_{tan}) can either be determined using

Poisson's ratio and Equation 2.12 (e.g. Benz, 2007; Schroeder et al., 2015), hence assuming the deviatoric strain and volumetric strain are intrinsically linked, or by defining a separate strain-dependent rule to define the K_{tan} degradation using accumulated volumetric strain as opposed to deviatoric strain (e.g. Taborda et al., 2016).

Although this approach of incorporating strain-dependent elasticity within the yield surface, to represent behaviour that in reality is likely to be elastoplastic, is an idealisation of the true soil response it has proved to be robust and accurate when used to perform FEA considering the monotonic loading of geotechnical structures. For example, Bolton et al. (1994) incorporated a strain-dependent elastic stiffness matrix, in which the shear stiffness was set as a power function of E_q, p' and OCR, within a Modified Cam Clay (MCC) model and used it to predict reasonably well the response of centrifuge tests of tunnels in clay performed by Mair (1979). Benz (2007) incorporated a modified form of the Hardin and Drnevich (1972) strain-dependent hyperbolic function to define the elastic stiffness matrix within an isotropic hardening Mohr-Coulomb model, which has been used by a number of authors to predict foundation response in FEA (e.g. Sheil and McCabe, 2016; Murphy et al., 2018; Shakeel and Ng, 2018). In addition, Schroeder et al. (2015) included the Jardine (1986) strain-dependent elastic model within a perfectly-plastic Mohr-Coulomb yield surface to perform FEA of offshore monopile foundations in sand for the Gode wind farm, and Zdravković et al. (2019) included the Taborda and Zdravković (2012) strain-dependent elastic stiffness model within an extended MCC model to simulate the response of monopiles in clay, obtaining results which compared very well to pile load test results.

The extensive use of such models presented in the literature for performing geotechnical FEA highlights a clear example of Engineer Design models (see Section 1) being developed which do not perfectly capture the known response from laboratory tests; however, are demonstrated to offer an acceptable idealisation to capture the response of foundations for practical design cases. Although this idealised approach has been shown to predict a reasonable response for a number of foundation analyses, it is important to note that the stress-dilatancy response will generally be poorly predicted within the yield surface and as such care should be taken if a single surface yield

surface model is to be used for a highly kinematically constrained problem (e.g. axially loaded pile or a deeply buried anchor).

Additionally, when considering unloading/reloading further rules must be incorporated within the elastic strain-dependent models to ensure a reasonable response is predicted (e.g. Benz, 2007; Taborda and Zdravković, 2012). For such cases the elastic models are typically formulated to predict a Masing type (Masing, 1926) hysteric response, i.e. assuming i) the tangent shear stiffness upon unloading is equal to the initial modulus and ii) the unload-reload stress-strain response is equal to the initial loading response but magnified two-fold.

2.2.1.2 Hyperelasticity

The elastic formulations discussed in Section 2.2.1.1 are in general examples of hypoelastic formulations. Many authors have included such hypoelastic formulations within elastoplastic constitutive models (e.g. Manzari and Dafalias, 1997; Benz, 2007; Taborda et al., 2014). However, it can be shown that these models are non-conservative from a thermodynamics perspective as discussed by Zytinski et al. (1978), Borja et al. (1997) and Houlsby et al. (2005). This is considered to be less of an issue for monotonic loading problems in comparison to problems considering cyclic loading (Potts and Zdravković, 1999). Therefore, a hyperelastic formulation, derived from a free energy potential, is ideally preferred since it results in a conservative elastic response which is guaranteed to be thermodynamically acceptable. A number of hyperelastic formulations have been proposed within the literature (e.g. Einav and Purzin, 2004; Houlsby et al., 2005).

Houlsby et al. (2005) presented a hyperelastic formulation, that is capable of capturing the stress dependency of the elastic stiffness and improved upon previous models. The elastic compliance matrix, in triaxial space, is given by:

$$\begin{bmatrix} \delta\varepsilon_{vol} \\ \delta\varepsilon_{q} \end{bmatrix} = \begin{bmatrix} \frac{1}{K_{ref}(1-n)p_{ref}^{1-n}p_0^n}\left[1-\frac{np^2}{p_0^2}\right] & \frac{npq}{3G_{ref}p_{ref}^{1-n}p_0^{n+2}} \\ \frac{npq}{3G_{ref}p_{ref}^{1-n}p_0^{n+2}} & \frac{1}{3G_{ref}p_{ref}^{1-n}p_0^n}\left[1-\frac{nk(1-n)q^2}{3G_{ref}p_0^2}\right] \end{bmatrix} \begin{bmatrix} \delta p' \\ \delta q \end{bmatrix} \qquad 2.13$$

where, K_{ref}, G_{ref}, n are experimentally derived constants and p_{ref} is a reference stress. The terms $\delta\varepsilon_{vol}$ and $\delta\varepsilon_q$ are the incremental volumetric and triaxial deviatoric strains respectively and $\delta p'$ and δq are the incremental mean effective stress and triaxial deviatoric stress respectively. A similar isotropic hypoelastic stress-dependent model, typically used in elastoplastic models (e.g. Manzari and Dafalias, 1997), is given by,

$$\begin{bmatrix} \delta\varepsilon_{vol} \\ \delta\varepsilon_q \end{bmatrix} = \begin{bmatrix} \dfrac{1}{K_{ref}\, F(e) p_{ref} \left(\dfrac{p'}{p_{ref}}\right)^n} & 0 \\ 0 & \dfrac{1}{3G_{ref}\, F(e) p_{ref} \left(\dfrac{p'}{p_{ref}}\right)^n} \end{bmatrix} \begin{bmatrix} \delta p' \\ \delta q \end{bmatrix} \qquad 2.14$$

Interestingly as can be seen from Equations 2.13 and 2.14, the hyperelastic formulation proposed by Houlsby et al. (2005) intrinsically predicts stress-induced anisotropic elastic behaviour. A drawback of the Houlsby et al. (2005) formulation, that was noted by Humrickhouse et al. (2010) and Golchin and Lashkari (2014), was that both compressive and tensile stresses were permitted; however, this drawback can be overcome by inclusion of the model within an elastoplastic constitutive model (e.g. within a Mohr-Coulomb yield surface). It was also noted by Golchin and Lashkari (2014) that the hyperelastic models proposed by Einav and Purzin (2004) and Houlsby et al. (2005) did not correctly predict the measured anisotropic elastic stiffness response when compared to measured triaxial test data for sand. Figure 2.3 shows the simulations versus the measured triaxial data presented by Golchin and Lashkari (2014) where it can be seen that the Einav and Purzin (2004) and Houlsby et al. (2005) models indeed do not precisely match the measured data; however, they do predict the correct trend and are a significant improvement compared to an isotropic stress-dependent hypoelastic model. An anisotropic hypoelastic model is shown to provide a better fit to the data (Figure 2.3); however, it should be noted that the Einav and Purzin (2004) and Houlsby et al. (2005) hyperelastic models do not incorporate inherent anisotropy, only stress induced anisotropy. Einav and Purzin (2004) presented FEA to investigate settlement at ground level due to installation of a tunnel using a hyperplastic MCC model and a

hypoelastic-plastic MCC model. Figure 2.4 presents the results, from which it can be seen that Einav and Purzin (2004) observed a difference between the two model formulations.

2.2.2 Yield Surfaces

2.2.2.1 Total Stress versus Effective Stress Formulation

Elastoplastic constitutive models are formulated either in total stress space ($\boldsymbol{\sigma}$) or effective stress space ($\boldsymbol{\sigma}'$). For total stress models, developed for undrained loading conditions, the yield and plastic potential functions are set to be independent of the mean stress. This form of the plastic potential ensures zero plastic volumetric strain. Linear elasticity assuming a Poisson's ratio of ~ 0.5 is then typically adopted for the elastic component of total stress models to ensure zero volumetric elastic strains develop. The von Mises (Figure 2.5a) and Tresca (Figure 2.5b) yield surfaces are examples of simple total stress formulations. The Drucker-Prager (Figure 2.5c) and Mohr-Coulomb (Figure 2.5d) yield surfaces are examples of simple effective stress formulations.

2.2.2.2 Yield Surface Shape in the Deviatoric Plane

The Mohr-Coulomb or Tresca yield surface shape is often used to formulate constitutive models in the deviatoric plane in stress space. The discontinuities at the corners of these surfaces can cause numerical issues and as such the corners are usually rounded off for implementation within FEA software (e.g. Abbo et al., 2011). A curved continuous surface which circumscribes the Mohr-Coulomb hexagon in the deviatoric plane can also be used to mitigate the corner issue. In addition, it has been shown that other surface shapes in the deviatoric plane, such as those presented in the seminal work by Matsuoka and Nakai (1974) and Lade and Duncan (1975), better represents measured data from true triaxial tests on sand and clay (e.g. Lade and Mustante, 1978; Prashant and Penumadu, 2004; Ye et al., 2014). Continuous yield surface functions which allow the shape in the deviatoric plane to be altered (e.g. Van Eekelen, 1980; Sheng et al., 2000) have been incorporated in a number of constitutive models (e.g. Khong, 2004; Karstunen et al., 2005; Sivasithamparam, 2012). Figure 2.6 presents example yield surface shapes in the deviatoric plane.

2.2.2.3 Yield Surface Strain Hardening

Models in which the yield surface is centred about the same position while hardening (i.e. expanding) are termed isotropic hardening models. For isotropic hardening, the hardening parameter h, controls the size of the yield surface, and is typically set as a function of $\boldsymbol{\varepsilon}^p$ i.e. $h(\boldsymbol{\varepsilon}^p)$. Additionally, it is also possible to incorporate a kinematic hardening rule in which the yield surface does not change in size but instead translates in stress space i.e. the centre, or the so-called yield surface back-stress, changes as a function of $\boldsymbol{\varepsilon}^p$. Figure 2.7 shows a schematic of the two hardening approaches typically employed, with the yield surface evolution and corresponding stress-strain response shown for a load-unload stress path. Although isotropic hardening is generally suitable for monotonic loading, as can be seen from Figure 2.7, this approach is less suitable for unloading-reloading (or cyclic loading) since an elastic response is assumed for all stress states within the expanded yield surface (i.e. the elastic zone is significantly larger). Whereas kinematic hardening models assume the elastic zone size (i.e. yield surface size) is constant and therefore predict a more realistic elastoplastic response upon unloading (Figure 2.7). In addition, isotropic and kinematic hardening are often combined within constitutive models to capture the observed response of soil (e.g. Manzari and Dafalias, 1997; Anastasopoulos et al., 2011).

2.2.2.4 Yield Surface Strain Softening

Post-peak softening is also observed for many soil types (e.g. overconsolidated clays, sensitive clays, dense sands and carbonate sands). Since strain softening is relatively simple to implement within a constitutive model (implemented in the same way as strain hardening) its incorporation in constitutive models for soils is common. For example, a simple linear strain softening Mohr-Coulomb model was presented by Potts et al. (1990) and used to analyse the progressive collapse of the Carsington Dam, and the MCC model (Roscoe and Burland, 1968) which incorporates strain softening on the dry side of critical state has been used extensively for numerical analysis in the literature. A significant number of more advanced constitutive models have also incorporated strain softening to capture soil response in recent years (e.g. Dafalias and Manzari, 2004; Taiebat

and Dafalias, 2008; Boulanger and Ziotopoulou, 2013). Although including strain softening within a constitutive model is relatively trivial, use of such models in FEA can be troublesome due to numerical convergence issues and increased mesh dependency (Potts et al., 1990; Brinkgreve, 1994; Summersgill et al., 2017c).

Figure 2.8 shows results from Summersgill et al. (2017c) in which a simple biaxial test simulation is performed with different levels of mesh refinement using a strain softening Mohr-Coulomb model. It can be seen from Figure 2.8 that the shear band thickness is significantly affected by the mesh element size. As a result, different rates of softening are predicted by the model despite the same softening parameters being used. Therefore, a practical approach typically used is to adjust the softening rate, within the constitutive model, to the element mesh size adopted to ensure a reasonable prediction is obtained for the particular mesh configuration employed (e.g. Sultaniya et al., 2017). Although this approach of scaling the softening parameters to the element size is suitable for mesh configurations in which all the elements are the same size, it is not suitable for a mesh in which variable element sizes are used across the problem domain. For such cases, in which variable element sizes are used, and extensive strain softening occurs, then so-called non-local regularisation techniques are often employed (e.g. Brinkgreve, 1994; Summersgill et al., 2017a; Summersgill et al., 2017b). Within these regularisation techniques a distribution weighting function is used to spread the strains at a point over a defined surrounding volume/area within the mesh and hence reduce the effects of local element size on the thickness of the shear band by using the calculated non-local strains within the constitutive model calculations.

2.2.3 Plastic Potential Functions

Within an elastoplastic model, the plastic potential controls the relative magnitude of the components of the plastic strain increment as the soil yields. The plastic potentials form a family of surfaces within stress space. If the plastic potential surfaces and the yield surfaces are the same, the material assumes normality and an associated flow rule is followed. Many developed models assume normality; however, experimental data has shown that soils can often deviate from

normality (Wood, 1990) and hence the yield function and the plastic potential function are different (i.e. non-associated flow). A suitable plastic potential within a constitutive model is pivotal for the accurate prediction of soil behaviour given its importance in forming the $\boldsymbol{D}_{ep}$ matrix.

The assumption of a simple plastic potential function, for example based on a fixed dilation angle or the associated flow rule assumed within the MCC model often does not agree with experimental test data and therefore several authors have proposed more versatile plastic potential functions which can be calibrated to experimental stress-dilatancy data independently of the yield surface (e.g. Erbrich, 1994; Lagioia et al., 1996; Dafalias and Manzari, 2004). The plastic dilatancy, D $\left(= d\varepsilon_v^p / d\varepsilon_q^p\right)$ can be determined, considering a triaxial state of stress, by taking the partial derivatives of the plastic potential function with respect to p' and q. Therefore D can be given by,

$$D = \frac{d\varepsilon_v^p}{d\varepsilon_q^p} = \frac{\Lambda \frac{\partial g}{\partial p'}}{\Lambda \frac{\partial g}{\partial q}} = \frac{\frac{\partial g}{\partial p'}}{\frac{\partial g}{\partial q}} \qquad 2.15$$

Rowe's dilatancy theory (Rowe, 1962) assumes that D is proportional to the difference between the current stress ratio $\eta = q/p'$ and a dilatancy stress ratio M_d. Many authors have proposed the use of state- and stress-dependent plastic potential functions based on Rowe's dilatancy theory to capture the response from laboratory testing (e.g. Dafalias and Manzari, 2004; Woo et al., 2017) by setting the M_d value as a function of the current soil state. A common measure of current soil state, used to control the stress-dilatancy response within a constitutive model, is the state parameter (ψ) proposed by Been and Jefferies (1985), which is based on the difference between the current void ratio (e) and the critical state void ratio (e_{cs}) at the same p' on the critical state line (CSL) in p': e space, i.e. $\psi = e - e_{cs}$. Other measures of the current soil state such as the state index (Ishihara et al., 1975) or the state pressure index (Wang et al., 2002) have also been used.

Laboratory element testing data presented in the literature has shown that the angle (χ) of the major principal effective stress (σ'_1) with respect to the sample axis and the value of the

intermediate principal stress ratio, $\zeta = \frac{\sigma_2' - \sigma_3'}{\sigma_1' - \sigma_3'}$, can have a significant effect on the overall stress-dilatancy response (Dafalias et al., 2004). During shearing under triaxial extension conditions ($\chi = 90°, \zeta = 1$), a more contractive and less dilative response is observed compared to triaxial compression conditions ($\chi = 0°, \zeta = 0$). This phenomenon, termed fabric anisotropy, was incorporated within the plastic potential function by Dafalias et al. (2004).

In reality the stress-dilatancy response of the soil and the peak friction angle are intrinsically coupled (Bolton, 1986) and as such it is not possible to review the effects of dilation in isolation when performing experiments. However, when considering a constitutive model, it is possible to have a state- and stress-dependent dilation angle with a fixed friction angle and in turn the effects of dilation and peak strength can be investigated independently. A review of the effect of the dilation on different geotechnical problems presented by Houlsby (1991) showed that the more kinematically constrained the problem, the more significant the effect of dilation on the predicted response. For example, the problem of slope stability was shown to be significantly less affected by the assumed dilation angle than an axially loaded pile (Houlsby, 1991). Similarly, the stress-dilatancy response of the constitutive model (i.e. the plastic potential function) is of significant importance when considering partially drained to undrained conditions. Therefore, it is considered important that the problem being modelled is considered carefully when deciding on the required complexity of the plastic potential function to incorporate within the constitutive model.

2.2.4 Multi-Surface Modelling Concepts

Constitutive models which only include a single isotropic hardening yield surface (e.g. Benz, 2007; Grimstad et al., 2012) are generally not suitable, without applying complex nonlinear elastic rules within the yield surface, for capturing the hysteretic unload-reload response of soils. Elastoplastic models incorporating multiple yield surfaces are therefore often developed to overcome this drawback. Multi-surface models are typically implemented using several nested kinematic hardening yield surfaces (e.g. Prevost, 1977; Houlsby, 1999; Elgamal et al., 2003). The individual yield surfaces translate in stress space when they are activated, such that all active yield surfaces are at the same stress condition. To control and track the translation of the yield surfaces,

a back-stress tensor is introduced for each yield surface. Prevost (1977) presented a multi-surface total stress von Mises model in which the yield surfaces are given by,

$$\mathrm{f} = \sqrt{\frac{3}{2}\,(\boldsymbol{s}-\boldsymbol{\alpha}_i) : (\boldsymbol{s}-\boldsymbol{\alpha}_i\,)} - k_i \qquad 2.16$$

where **s** is the deviatoric stress tensor given by,

$$\boldsymbol{s} = \boldsymbol{\sigma} - p\,\boldsymbol{I} \qquad 2.17$$

in which $\boldsymbol{\sigma}$ is the stress tensor, $\boldsymbol{I}$ is the second-order identity tensor and p is the mean total stress ($=\frac{1}{3}tr\,\boldsymbol{\sigma}$). For all surfaces, the $\boldsymbol{\alpha}_i$ defines the co-ordinates in stress space of the centre of the yield surface (i.e. back-stress tensor) and k_i defines each surface yield strength, where the subscript i defines the surface number. Such models can be termed 'series Mroz-Iwan' models after the seminal work of Mroz (1967) and Iwan (1967). Despite offering an elegant modelling approach for simulating a nonlinear hysteretic response, tensorial series Mroz-Iwan models can become complex and implementation can be difficult.

Chiang and Beck (1994), Einav and Collins (2008) and Grimstad et al. (2014) have demonstrated that the use of multi-surface models based on a 'parallel Iwan' approach, as first proposed by Iwan (1966), offers a simpler approach, while still providing a predictive capability similar to that of the series Mroz-Iwan approach. Iwan (1966) proposed a 1D model in which a number of spring-slider elements, with different yield strengths and different elastic stiffnesses, are arranged in parallel. The model assumes strain equivalence across all of the spring-slider elements. Following an increment of strain, the resulting stress from the model is determined from a weighted sum of the individual stresses in the spring-slider elements.

When the parallel Iwan approach is adopted as the basis of a continuum plasticity model, a set of individual constitutive models, termed micro models, are specified in parallel. All of the micro models are then subjected to the same strain history, with the macro stress tensor ($\boldsymbol{\sigma}$) calculated as the weighted sum of the individual micro model stress tensors ($\boldsymbol{\sigma}_{micro}$) by,

$$\boldsymbol{\sigma} = \sum_{i=1}^{n} w_i \, \boldsymbol{\sigma}_{micro} \qquad 2.18$$

where n is the number of micro models and w_i is the weight of each micro model's stress tensor with the sum of the weights constrained to be unity (i.e. $\sum w_i = 1$). This relatively simple modelling approach predicts a Masing-type nonlinear hysteretic response without the need for translating yield surfaces. As discussed by Grimstad et al. (2014) a major advantage of using a parallel Iwan approach is that each micro model is implemented in the same manner as any other single surface plasticity model.

Einav and Collins (2008) performed a number of finite difference calculations using an elastic-perfectly-plastic model assuming a probabilistic Weibull distribution of von Mises strengths across a 2500 element mesh, to represent the spatial variation of strength across a soil sample. Example contours of the von Mises strength distributions are presented in Figure 2.9. The virtual experiments presented by Einav and Collins (2008) compared well with a parallel Iwan von Mises model using the same statistical distribution of strengths. This endeavoured to show that the parallel Iwan approach has a clear micromechanical physical meaning, and that the micro model weights and strengths can be directly related to the statistical distribution of yield strengths in a representative volume of soil.

Figure 2.10 shows both a series and parallel configuration of a simple spring/slider element model. In addition, Figure 2.11 presents a schematic of a triaxial compression stress path and stress-strain response of a 3-surface von Mises model assuming a series Mroz-Iwan and a parallel arrangement.

2.2.5 Bounding Surface Models

Another modelling approach commonly adopted is the bounding surface formulation (Dafalias and Popov, 1975). In bounding surface plasticity, the current stress point on the yield surface is related to an image stress point on the bounding surface by a mapping rule. Several different mapping rules are presented within the literature. For example a mapping rule assuming the image stress point is determined as the intersection of a straight line with the bounding surface which

passes through the current stress point on the yield surface and the origin in stress space is often employed (e.g. Yu et al., 2007) or alternatively a radial mapping rule in the deviatoric plane is also often adopted (e.g. Dafalias and Manzari, 2004; Loukidis and Salgado, 2009). A rule is then specified to relate the hardening modulus at the current stress point to the image stress point on the bounding surface based on the distance between the points.

A significant proportion of constitutive models for sand are built upon the bounding surface model architecture presented by Manzari and Dafalias (1997). Extensive examples of Manzari-Dafalias type models have been presented, with comparisons of single element simulations to laboratory test data showing this modelling approach to be effective in capturing the response of sand (e.g. Papadimitiou and Bouckovalas, 2002; Dafalias and Manzari 2004; Dafalias et al., 2004; Taiebat and Dafalias, 2008; Loukidis and Salgado, 2009; Lashkari, 2010; Boulanger and Ziotopoulou, 2013; Golchin and Lashkari, 2014; Taborda et al., 2014; Petalas et al., 2019).

Similarly, the 'bubble model' proposed by Al-Tabbaa and Wood (1989), which considers a kinematic hardening yield surface within a Cam-Clay type bounding surface, has been utilised to develop a number of bounding surface constitutive models for clay (e.g. Stallebrass and Taylor, 1997; Rouainia and Wood, 2000; Sivasithamparam, 2012).

2.3 Other Modelling Approaches

2.3.1 Hypoplasticity

The hypoplasticity modelling approach has been adopted by several authors in the literature (e.g. Von Wolffersdorff, 1996; Mašín, 2012; Mašín, 2014) as an alternative to elastoplasticity. As discussed by Wu and Kolymbas (2000) the stress increment is determined using a hypoplastic constitutive model as,

$$\delta\boldsymbol{\sigma} = \boldsymbol{H}(\boldsymbol{\sigma}, \delta\boldsymbol{\varepsilon}) \tag{2.19}$$

where $\boldsymbol{H}$ is a nonlinear tensorial function linked to the current stress state ($\boldsymbol{\sigma}$) and the strain increment ($\delta\boldsymbol{\varepsilon}$). In contrast to elastoplasticity, hypoplasticity formulations do not decompose the strain into elastic and plastic increments. It should be noted, hypoplasticity has sometimes been

used to describe bounding surface models in the literature (Wang et al., 1990); however, this is contrary to the definition proposed by Wu and Kolymbas (2000) in which no yield surface and decomposition of strains is introduced. Hypoplastic models (e.g. Von Wolffersdorff, 1996; Herle and Kolymbas, 2004) have been used effectively to capture the response of foundations in FEA (e.g. Mašín and Herle, 2005; Thieken et al., 2014).

2.3.2 Hyperplasticity

Typically, when developing elastoplastic constitutive models for soils, the elastic model, yield function and plastic potential function are all derived independently to match observed laboratory data. Although this approach has been shown to provide impressive predictions of laboratory element and foundation-load tests when used in finite element calculations (e.g. Karstunen et al., 2005; Murphy et al., 2018; Taborda et al., 2019), it must be acknowledged that when developing the model formulation there is typically no consideration of the laws of thermodynamics.

Hyperplasticity defines a class of constitutive models which inherently satisfy the laws of thermodynamics and are derived from two scalar potential functions: an energy function and a dissipation function (Houlsby and Purzin, 2006).

A major advantage of hyperplasticity is that there are clearly defined rules imposed for the development of models, avoiding the application of arbitrary functions to fit laboratory data which may not obey the laws of thermodynamics. It should be noted that an elastoplastic constitutive model, developed without any thermodynamic considerations, may still be consistent with hyperplasticity; however, work would have to be done to investigate if the yield function and flow rule can be derived from free energy and dissipation functions. Therefore, as shown schematically in Figure 2.12, hyperplasticity represents a subset of elastoplastic models; however, to the author's knowledge no hypoplastic models have been shown to be consistent with hyperplasticity. Collins and Kelly (2002) presented examples of the derivation of well-known elastoplastic models as hyperplastic formulations. Figure 2.13 presents a flow chart from Collins and Kelly (2002) of the steps required to develop incremental elastoplastic constitutive models, which fulfil the criteria of a hyperplastic formulation.

2.4 Models Developed for Clay

A significant number of advanced elastoplastic constitutive models have been proposed in the literature to capture the behaviour of clay for monotonic and cyclic loading, utilising the modelling concepts discussed above. For example the, MIT-E3 (Whittle and Kavvadas, 1994), 3SKH (Stallebrass and Taylor, 1997), SANICLAY (Dafalias et al., 2006), SCLAY1S (Karstunen et al., 2005), B-SCLAY1S (Sivasithamparam, 2012) and Imperial College Extended MCC (Zdravković et al., 2019) models are examples of sophisticated effective stress constitutive models that can replicate many of the key trends observed in the stress-strain response of clay. Most of these models are developed using a MCC type base model architecture with modifications and extensions made to match observed laboratory trends. For example, the Imperial College Extended MCC model used by Zdravković et al. (2019) included a MCC model with an adapted yield surface and plastic potential shape on the dry side of critical state based on recommendations from Tsiampousi et al. (2013). Other authors have also included a similar modification to the MCC model to better capture the response of overconsolidated clay for use in FEA (e.g. Mita et al., 2004).

The original MCC model was developed based on testing of reconstituted samples; however, most natural clays contain some initial structure and bonding (Skempton and Northey, 1952; Gens and Nova, 1993; Liu and Carter, 2000). The effect of destructuration caused by the gradual damage to bonding, due to plastic straining, has been implemented within constitutive models. The framework was proposed by Gens and Nova (1993) in which the distance between the so-called ‘intrinsic yield surface’ and the ‘natural yield surface’ defines the level of bonding. As plastic straining occurs the distance between the surfaces consequently reduces in accordance with a destructuration law. This approach to modelling bonding and destructuration, which is considered very important for clays with high sensitivity values, has been implemented successfully within constitutive models and used for FEA calculations (e.g. Karstunen et al., 2005).

Additionally, the MCC model was formulated based on the results of laboratory tests on isotopically consolidated clay samples. However, element test results from clays which have been

anisotropically consolidated along the K_0 line have shown that the yield surface is not centred on the p' axis but rather centred approximately along the K_0 line (Parry and Nadarajah, 1973). As a result, several constitutive models in which the yield surface is inclined in stress space have been proposed (e.g. Sekiguchi and Ohta, 1977; Wheeler et al., 2003).

Figure 2.14 presents the SCLAY1S model in stress space, showing the inclined intrinsic and natural yield surfaces which are included to capture the effects of anisotropy and destructuration.

From a design perspective, a deficiency of effective stress models for clay is that the undrained shear strength (s_u) is not a direct input for such models; it depends on various other parameters and model features, such as: the assumed coefficient of earth pressure at rest (K_0), the overconsolidation ratio (OCR), the stress-dilatancy response, the initial void ratio, the critical state friction angle and, where relevant, approaches employed to model anisotropy and destructuration. This is a significant disadvantage for design analyses involving short-term loading of clays, for which prescribed undrained shear strength profiles and normalised stress-strain backbone curves are typically preferred inputs.

Therefore, in design situations involving short-term loading of a foundation embedded in a clay soil, total stress constitutive models can be an attractive option for use in FEA, as an alternative to effective stress approaches. Total stress models provide a means of specifying s_u as a model input parameter.

The stress-strain backbone curve, as well as the shear strength, has been shown to be stress path dependent for clay, with a significantly softer and weaker response observed in triaxial extension ($\chi = 90°, \zeta = 1$) than triaxial compression ($\chi = 0°, \zeta = 0$) conditions (Grimstad et al., 2012). As a result, anisotropic total stress models such as NGI-ADP (Grimstad et al., 2012) and AUS (Kouretzis et al., 2017) offer practical alternatives to an effective stress clay model. The NGI-ADP and AUS models incorporate inherent anisotropy by using a modified deviatoric stress tensor to define the yield and plastic potential functions. Shifted and unshifted yield surfaces (i.e. with and

without anisotropy) of the AUS model, using the modified deviatoric stress tensor, are shown in Figure 2.15.

2.5 Models Developed for Sand

The Extended Mohr-Coulomb model, shown in Figure 2.16, proposed by Doherty and Wood (2013) and the Hardening Soil with a small strain overlay (HSsmall) model proposed by Benz (2007) are examples of relatively simple isotropic hardening Mohr-Coulomb models which are often used in the literature to predict the response of geotechnical structures (e.g. Yiu et al., 2017; Murphy et al., 2018). Although both models fail to capture some potentially important features of sand response such as a realistic dilational response, post-peak softening and anisotropy, they are considered to be useful models for design FEA if carefully calibrated.

A significant number of more complicated sand models have been proposed in the literature. Examples include the NorSand model proposed by Jefferies (1993), the Manzari-Dafalias type models originally proposed by Manzari and Dafalias (1997) and the Severn-Trent model proposed by Gajo and Wood (1999), all of which have formed the basis of many of the recently developed models for sand.

The Manzari-Dafalias type models are formulated in a normalised deviatoric plane (Figure 2.17) using a deviatoric stress ratio tensor given by $\boldsymbol{r} = \boldsymbol{s}/p'$. The model includes a critical state surface, dilatancy surface and bounding surface in stress space (Figure 2.17), all of which control the evolution of the yield surface and plastic potential function during a strain increment. The bounding surface and dilatancy surface are controlled by the state parameter (ψ) and therefore both approach the critical state surface as ψ tends to zero.

Many extensions have been proposed to the original Manzari and Dafalias (1997) model to improve its predictive capability (e.g. Papadimitiou and Bouckovalas, 2002; Dafalias and Manzari 2004; Dafalias et al., 2004; Taiebat and Dafalias, 2008; Loukidis and Salgado, 2009; Lashkari, 2010; Boulanger and Ziotopoulou, 2013; Golchin and Lashkari, 2014; Taborda et al., 2014). The

most significant differences between the proposed Manzari-Dafalias type models are with respect to the hardening modulus. This is true for any bounding surface model in which many different functions can be adopted to fit laboratory test data. Typically, the hardening modulus is set to be a function of the distance between the current stress point and the bounding surface, the current mean effective stress, the current void ratio, and an elastic shear modulus constant (e.g. Dafalias and Manzari, 2004; Papadimitriou and Bouckovalas, 2002; Taborda et al., 2014). Dafalias et al. (2004) also incorporated fabric anisotropy into the hardening modulus by using a second-order fabric tensor in combination with a loading tensor to derive a scalar measure of anisotropy. This was then used by Dafalias et al. (2004) to control the position of the CSL which in turn made the size of the bounding and dilatancy surfaces dependent on the inherent anisotropy relative to the loading direction. Although, there is some doubt in the literature about the validity of a non-unique CSL (Jefferies and Been, 2015) this was incorporated by Dafalias et al. (2004) purely to capture the observed stress-strain response within the bounding surface modelling framework.

Dafalias and Manzari (2004) also incorporated a fabric-induced dilatancy function to better predict the observed stress-dilatancy laboratory trends under cyclic loading. Similarly, Corti et al. (2016) incorporated an additional surface in stress space termed the ‘memory surface’ within the Gajo and Wood (1999) bounding surface model. This memory-enhanced bounding surface plasticity approach has since been adopted by Liu et al. (2018) within a Manzari-Dafalias type model.

2.6 Use of Models for Design Finite Element Analysis

It is typically acknowledged that highly advanced constitutive models, i.e. so-called Philosopher models, are not suitable for practical design FEA due to difficulty in implementation, lack of model validation, high computational times and lengthy parameter calibration procedures which require non-routine laboratory testing (e.g. Kolymbas, 2000; Grammatikopoulou et al., 2017). Therefore, simpler constitutive models (i.e. Engineer Design models), which only capture the most salient features of the soil behaviour and have been shown to predict a realistic foundation response, are adopted by practising engineers. This was summarised by Wood (1991) who stated:

"The art of soil modelling thus lies in being able to identify important characteristics while leaving the model as simple as possible…. There is a law of diminishing returns as attempts are made to use progressively more sophisticated – and hence potentially more realistic (?) – models for design and analysis."

Although it might be assumed simpler models are more commonly used for practical design FEA, it is difficult to verify this premise. In an attempt to demonstrate this, a high-level review of all constitutive models presented in the proceedings of the 3rd International Symposium on Frontiers in Offshore Geotechnics (ISFOG) has been performed. ISFOG is a highly regarded offshore geotechnical conference held every five years and was selected because it includes significant contributions from both industry and academia. In total 197 papers peer-reviewed were published at ISFOG 2015 and 58 of these involved FEA. Figure 2.18 presents a review of the constitutive models used in these studies. It can be seen from Figure 2.18 that the majority of these models are relatively simple formulations. Only 5 papers included relatively advanced user-defined constitutive models (e.g. bounding surface effective stress model).

An additional consideration for any constitutive model used for foundation design FEA is the calibration process of the model parameters. Unfortunately, in the author's opinion, from review of the literature this is typically an area that is overlooked in most publications which present FEA of foundations, with assumed soil parameters often used and very little information given on calibration to laboratory data. Of course, this is not true in all cases, for example Taborda et al. (2019) and Zdravković et al. (2019) are recent examples of FEA of monopiles in which there was a detailed discussion of model calibration to laboratory and in situ test data.

The importance of parameter calibration is demonstrated by the shallow foundation load-displacement prediction event reported by Doherty et al. (2018), in which extensive laboratory and in situ test data were made available to entrants. The test site, situated in Ballina, Northern New South Wales, consisted of soft estuarine clay to a depth of approximately 14 m underlain by silty sand to a depth of 20 m. A total of 50 predictions were made within this study and the average predicted foundation response was not in good agreement with the measured foundation load test data, as shown in Figure 2.19. A range of methods were used from simple empirical methods to

FEA; however, there was no clear trend with respect to the complexity of the analysis method and the accuracy of the prediction. Doherty et al. (2018) presented FEA using a simple linear elastic Tresca model and showed that if carefully calibrated to the extensive laboratory and in situ test data, a very good match with the measured data could be achieved. This highlights that the calibration approach and engineering judgments made are as (if not more) important than the complexity of the model employed.

2.7 Figures

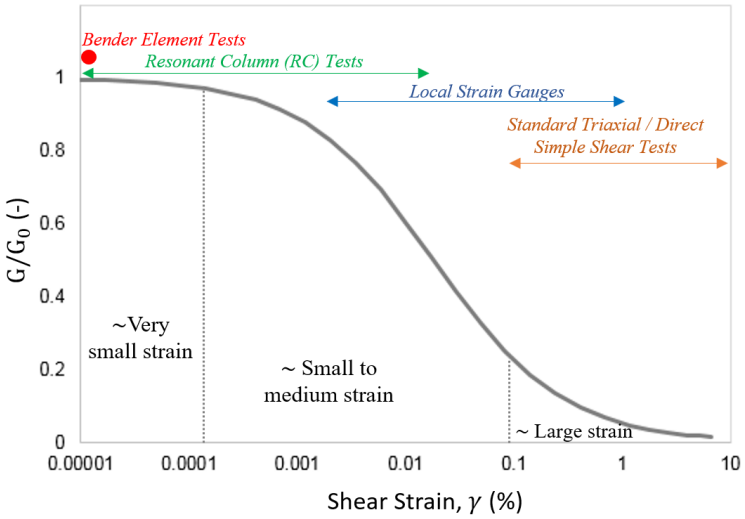

Figure 2.1: Example normalised shear stiffness versus shear strain curve with laboratory testing range labelled (after. Mair, 1993)

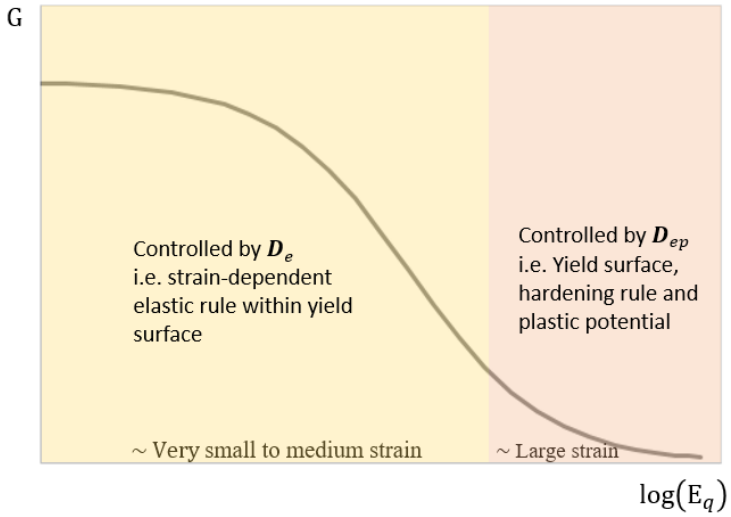

Figure 2.2: Variation of shear stiffness with deviatoric strain in single yield surface model incorporating strain-dependent elastic rule

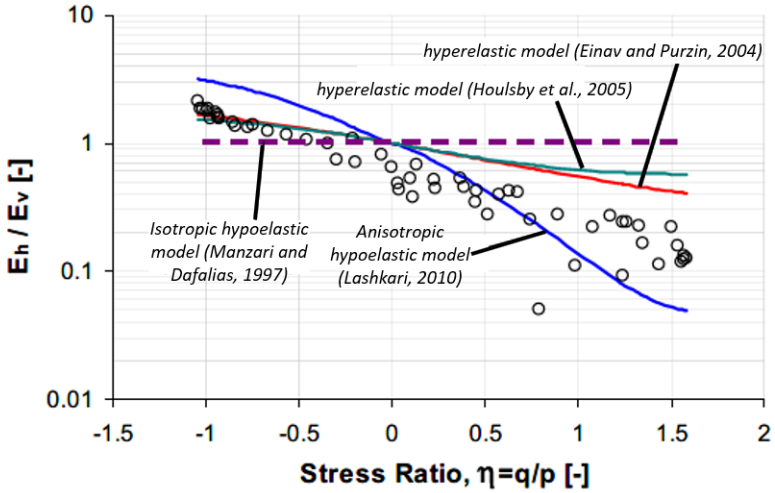

Figure 2.3: Horizontal to vertical elastic Young's modulus ratio (E_h/E_v) predicted by simulations using different elastic models compared to measured data from small unload-reload triaxial tests (after. Golchin and Lashkari, 2014)

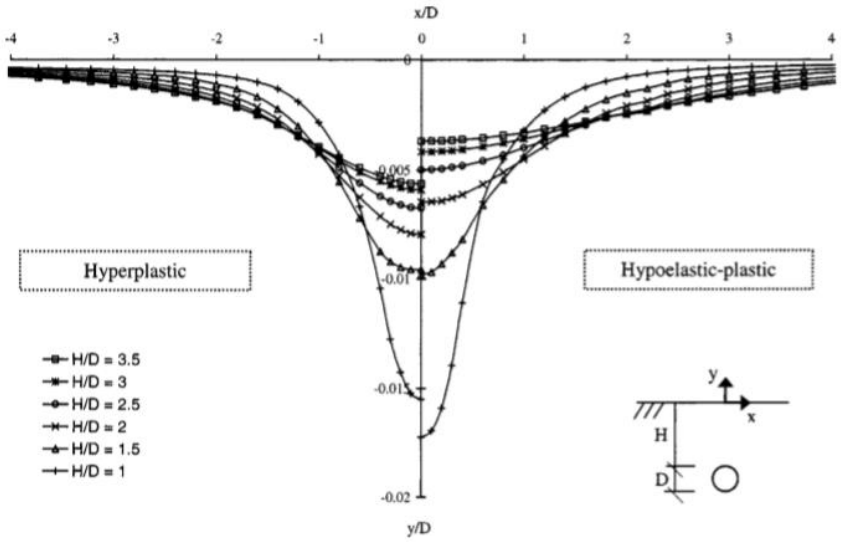

Figure 2.4: Normalised settlement at ground level for a range of different normalised tunnel burial depths (H/D) considering a hyperplastic and a hypoelastic-plastic model (Einav and Purzin, 2004)

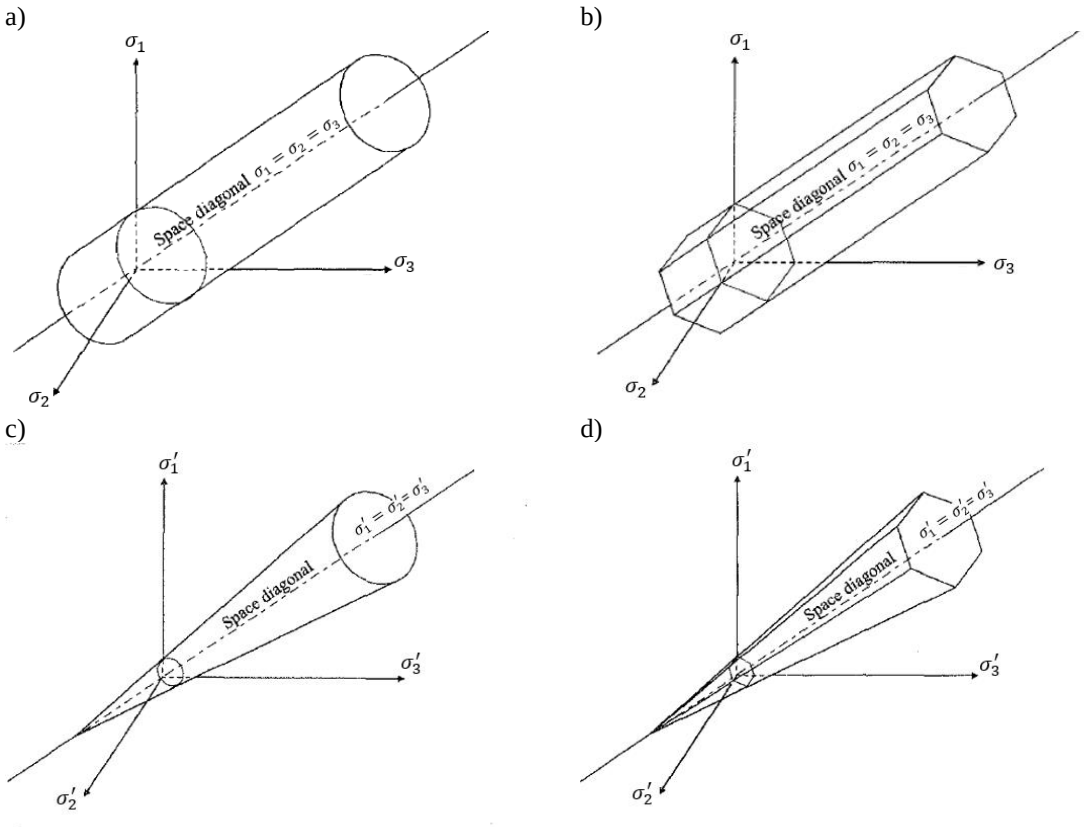

Figure 2.5: Total stress yield surfaces a) von Mises and b) Tresca and effective stress yield surfaces c) Drucker-Prager d) Mohr-Coulomb (after. Potts and Zdravković, 1999)

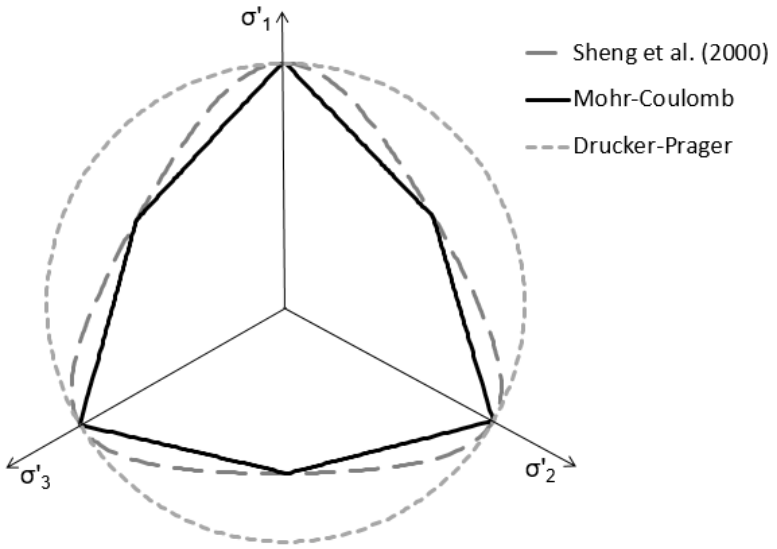

Figure 2.6: Failure surface in deviatoric plane

a) Isotropic hardening

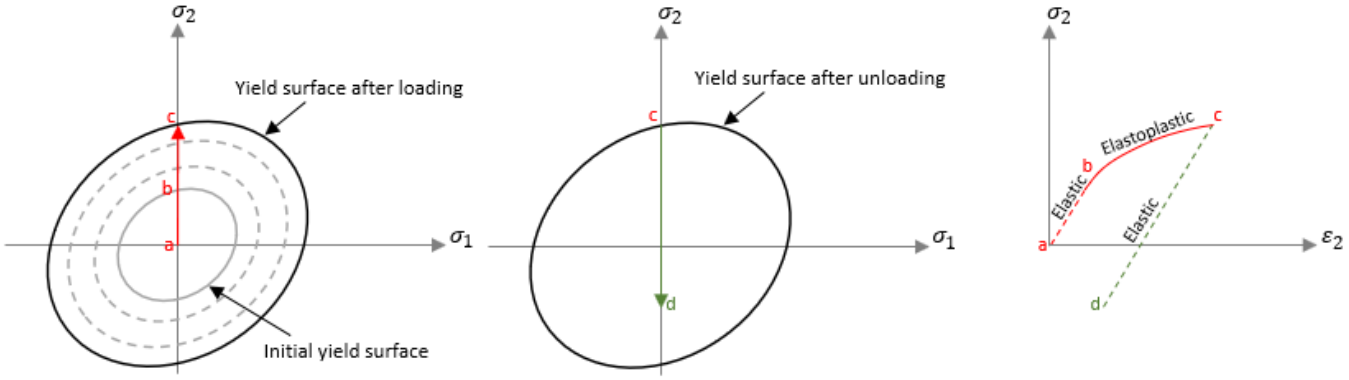

b) Kinematic hardening

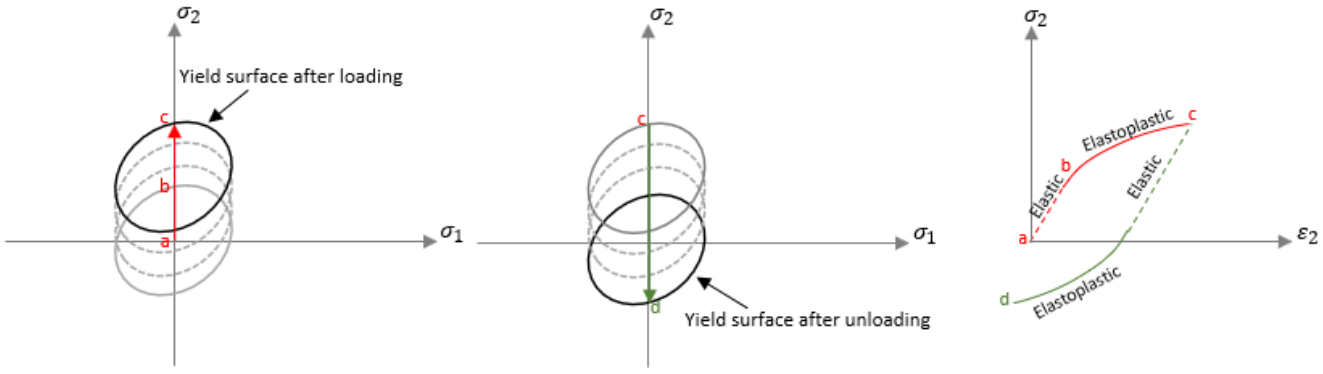

Figure 2.7: yield surface expansion/translation and stress-strain response for load-unload stress path for a) isotropic hardening model b) kinematic hardening model

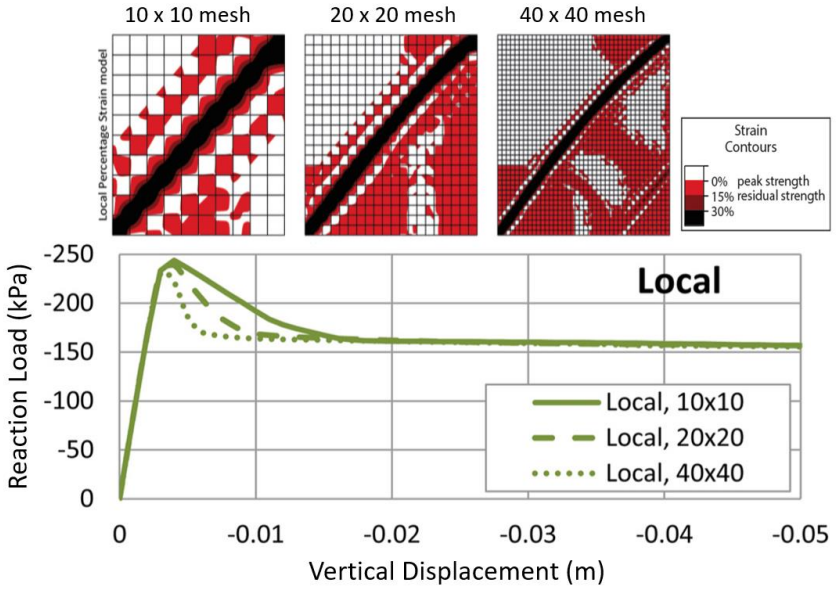

Figure 2.8: Biaxial simulation results using softening Mohr-Coulomb model with different mesh refinements (Summersgill et al., 2017c)

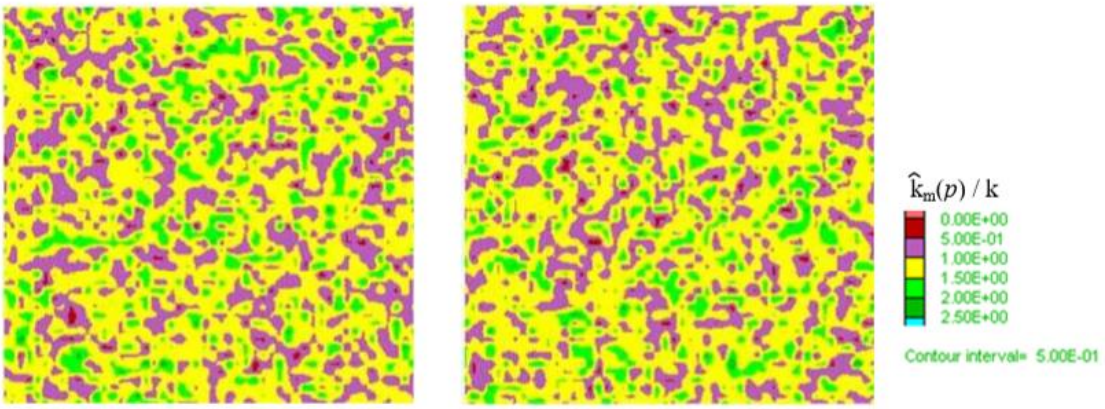

Figure 2.9: Contours of normalised von Mises strength Weibull distributions in 2500 element mesh (Einav and Collins, 2008)

a) Spring/slider model (series form)

b) Spring/slider model (Parallel form)

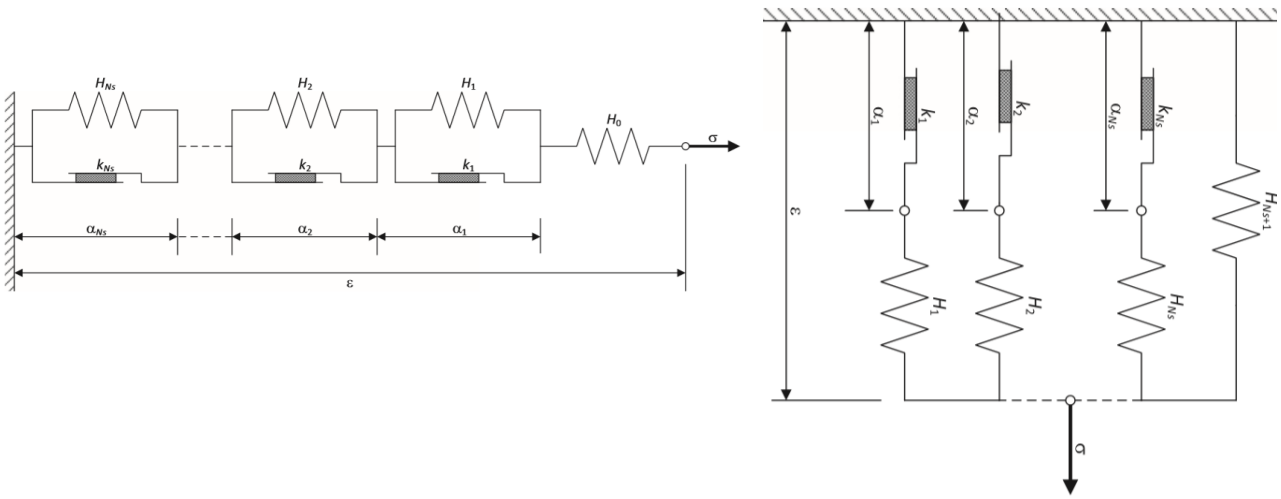

Figure 2.10: Spring/slider elements in a)series form and b) parallel form (Houlsby et al., 2017)

a) Series Mroz-Iwan von Mises model

b) Parallel Iwan von Mises model

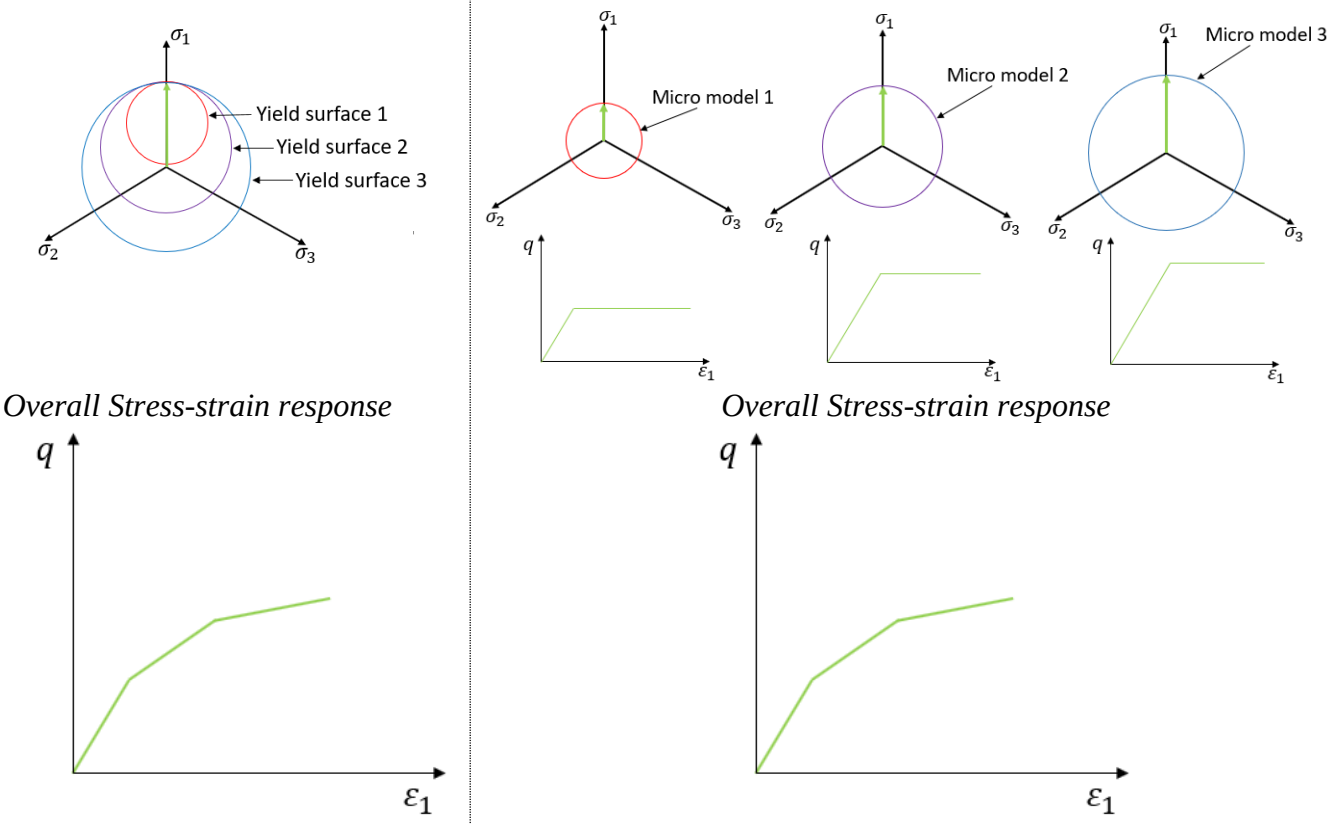

Figure 2.11: Triaxial compression stress path considering a) a series Mroz-Iwan von Mises model with 3 yield surfaces and b) a parallel Iwan model with 3 von Mises micro models

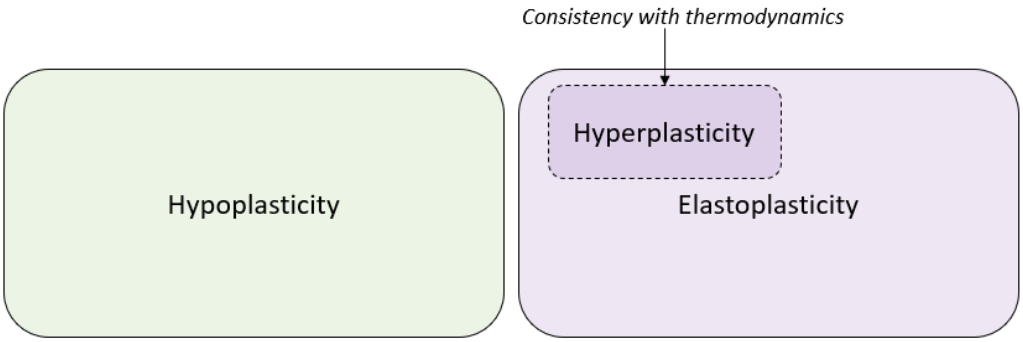

Figure 2.12: Theories of plasticity (after. Einav, 2012)

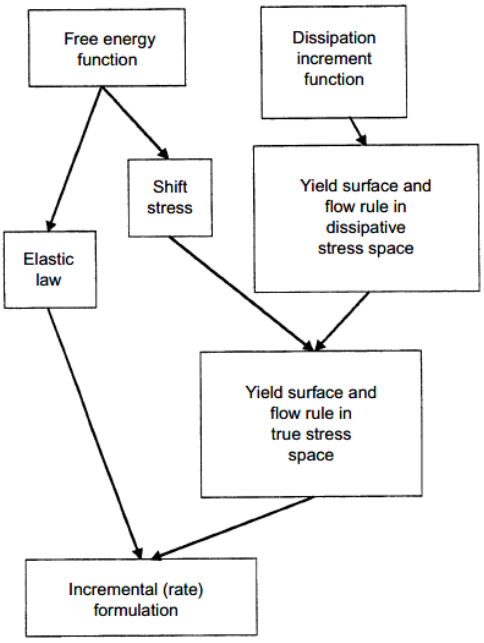

Figure 2.13: Flow chart outlining steps to develop elastoplastic constitutive laws from the free energy and dissipation functions (Collins and Kelly, 2002)

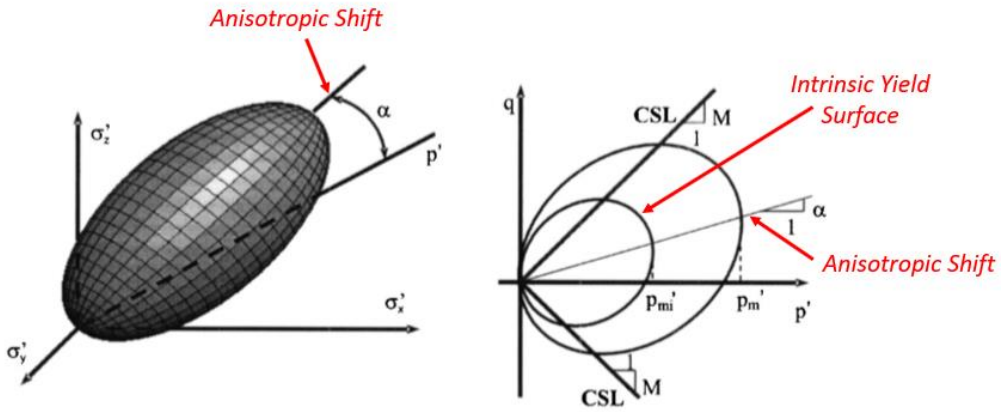

Figure 2.14: SCLAY1S yield surfaces in a) three-dimensional stress space and b) triaxial stress space with intrinsic yield surface and anisotropic shift annotated (after. Karstunen et al., 2005)

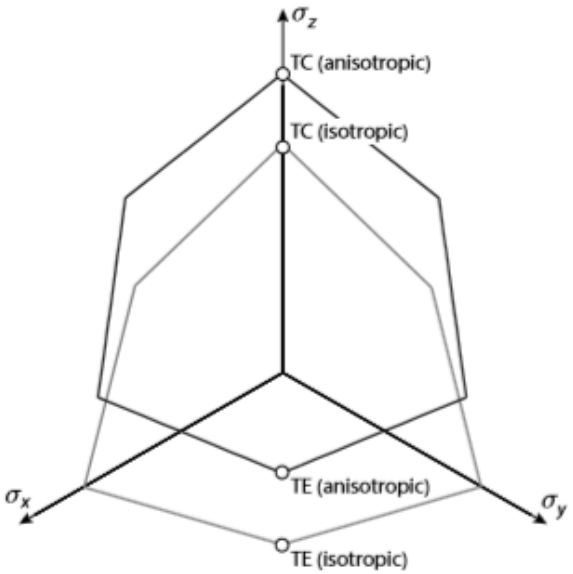

Figure 2.15: AUS model isotropic and anisotropic generalized Tresca surfaces (Kouretzis et al., 2017)

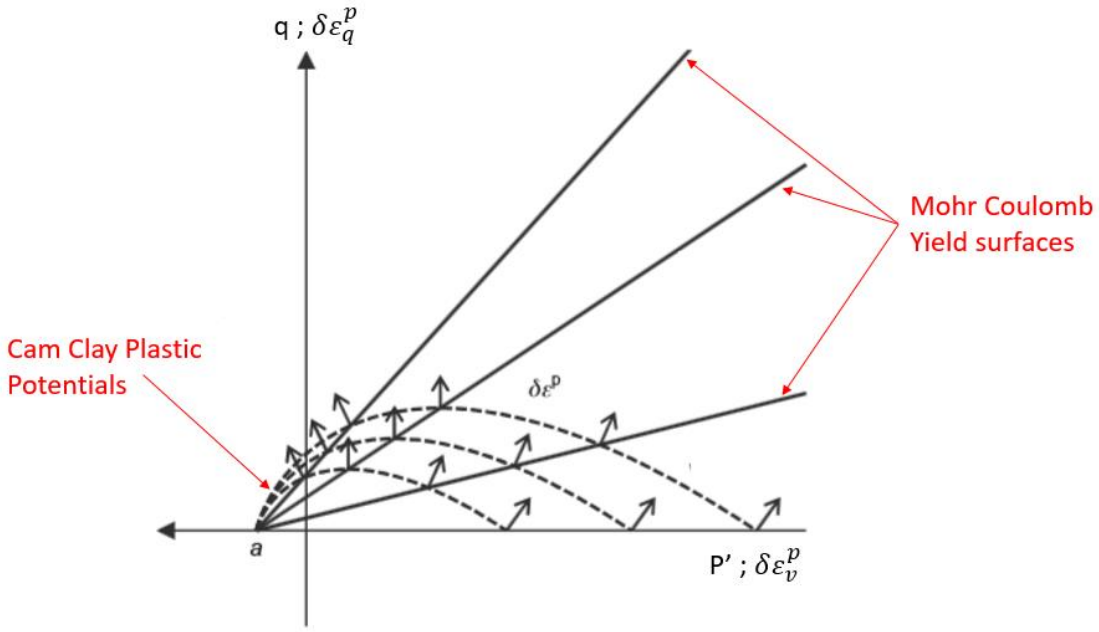

Figure 2.16: Extended Mohr-Coulomb model (after. Doherty and Wood, 2013) with direction of plastic strain increments shown normal to plastic potential (dashed line) and example hardening yield surfaces (solid lines)

a)

b)

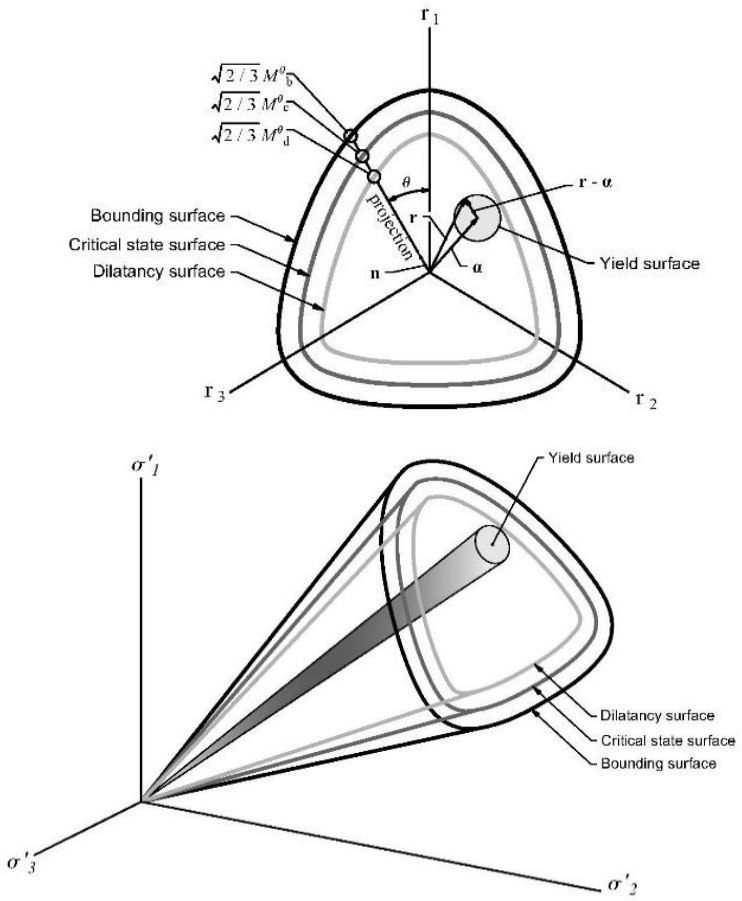

Figure 2.17: Illustration of the Manzari-Dafalias model yield, bounding, dilatancy and critical state surfaces in a) the normalised deviatoric plane and b) principal stress space

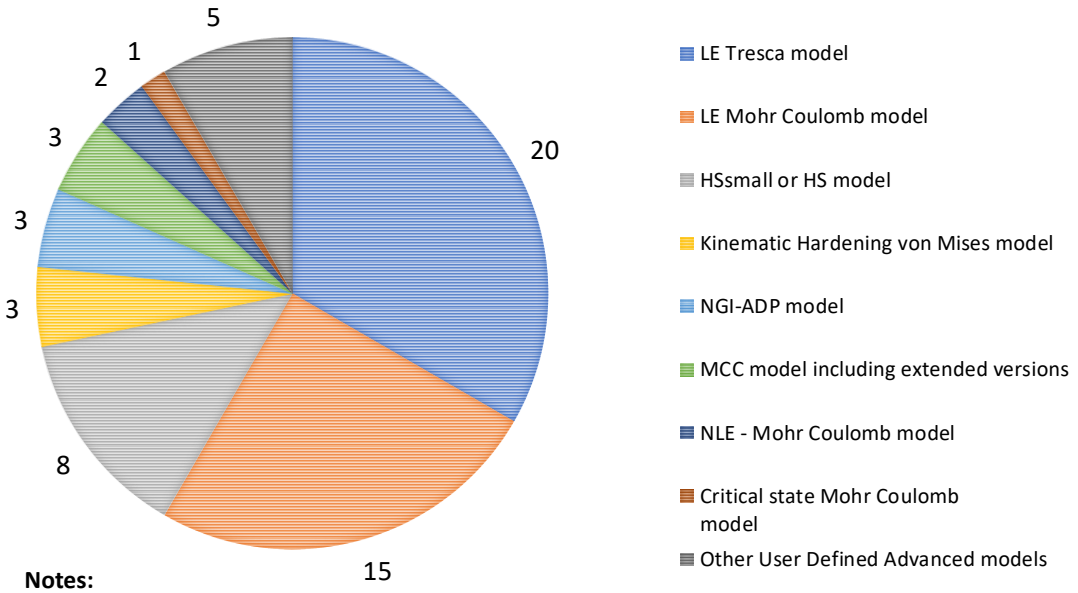

Notes:
LE = Linear elastic
HSsmall = Hardening Soil model with small strain stiffness overlay (Benz,2007)
NLE = Non-linear elastic
NGI-ADP = Modified Anisotropic Hardening Tresca (Grimstad et al., 2012)
MCC = Modified Cam Clay
Other User Defined Advanced models = A number of advanced user defined models including e.g. a sand bounding surface model (Taborda et al., 2014) and a hypoplasticity model with cyclic extension (Niemunis et al., 2005)

Figure 2.18: Review of constitutive models used for finite element analysis papers presented at the 3rd International Symposium on Frontiers in Offshore Geotechnics (ISFOG)

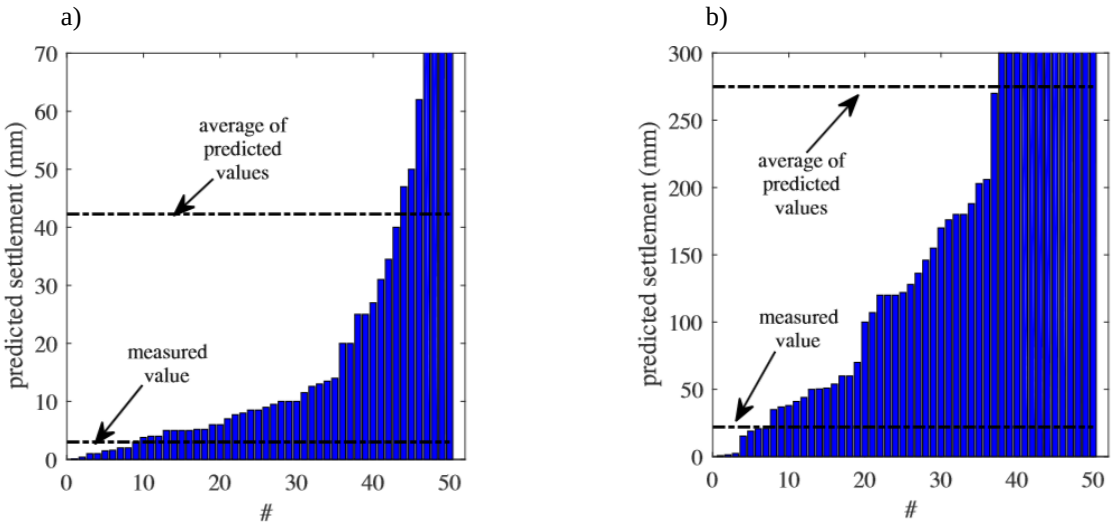

Figure 2.19: Comparison of predictions and measured foundation response for a) 25% of failure load and b) 100 % of failure load (Doherty et al., 2018)

Section 3

CONSTITUTIVE MODEL IMPLEMENTATION OVERVIEW

Contents

3. CONSTITUTIVE MODEL IMPLEMENTATION OVERVIEW

The constitutive model calculations (i.e. determination of updated stresses from a strain increment), termed the local problem, are calculated at all integration points in each finite element across the mesh of the global problem during a FEA calculation. The most common constitutive model type, used for soil, is an elastoplastic constitutive model. The development, implementation and use of practical elastoplastic constitutive models for foundation design is the focus of this study and hence the following subsections give an overview of the preliminaries required for the implementation of an elastoplastic constitutive model. It should be noted since the purpose of this chapter is to outline the adopted methodology and prerequisites for model implementation based on a review of the literature, it does not include original work. Sections 4 to 7 then present the implementation and use of particular elastoplastic constitutive models in FEA for modelling offshore foundations.

3.1 Model Generalisation

When developing a model in multiaxial stress space, typically stress invariants are used to form the yield surface and plastic potential function. The following subsections give an overview of the stress invariants, with Potts and Zdravković (1999) and Martin and Burd (2018) the primary references used for the equations presented. The adopted sign convention assumed in this study for the definition of the stress invariants for constitutive model implementation assumes compression positive. It should be noted although compression positive is used for model implementation in all sections, for the presentation of output results a different convention is used and specified in each section where relevant.

3.1.1 Stress Invariants

The 3D stress state of a material in a Cartesian axes (x,y,z) is represented by the stress tensor:

$$\widehat{\boldsymbol{\sigma}} = \begin{bmatrix} \sigma_{xx} & \tau_{xy} & \tau_{xz} \\ \tau_{yx} & \sigma_{yy} & \tau_{yz} \\ \tau_{zx} & \tau_{zy} & \sigma_{zz} \end{bmatrix} \tag{3.1}$$

Although tensorial notation, where $\widehat{\ }$ above the symbol denotes a tensor, is useful for theoretical descriptions, when implementing models, it can be more convenient to work with vectors. The stress tensor can also be given in Voigt/vector form by $\boldsymbol{\sigma} = \left[\sigma_{xx}, \sigma_{yy}, \sigma_{zz}, \tau_{xy}, \tau_{yz}, \tau_{zx}\right]^T$, with the effective

stress notation given as $\boldsymbol{\sigma'} = [\sigma'_{xx}, \sigma'_{yy}, \sigma'_{zz}, \tau_{xy}, \tau_{yz}, \tau_{zx}]^T$, where $\boldsymbol{\sigma} = \boldsymbol{\sigma'} + u_w[1,1,1,0,0,0]^T$ and u_w is the pore water pressure. It is useful to formulate an isotropic constitutive model in terms of stress invariants, particularly when defining an isotropic yield surface and plastic potential function. The stress invariants have a constant magnitude no matter the direction of the co-ordinate axes (i.e. they are invariant to the axes). For brevity $\boldsymbol{\sigma}$ is used, as opposed to $\boldsymbol{\sigma'}$, in the equations below.

The stress tensor can be additively split into a hydrostatic mean stress (p) and a deviatoric stress tensor ($\boldsymbol{s}$). The mean stress is:

$$p = \frac{1}{3}(\sigma_{xx} + \sigma_{yy} + \sigma_{zz}) = \frac{I_1}{3} \tag{3.2}$$

where, I_1 is the first invariant of the stress tensor (i.e. trace($\widehat{\boldsymbol{\sigma}}$)). The deviatoric stress tensor, $\hat{\boldsymbol{s}}$ is:

$$\hat{\boldsymbol{s}} = \begin{bmatrix} s_{xx} & s_{yy} & s_{xz} \\ s_{yx} & s_{yy} & \sigma_{yz} \\ s_{zx} & s_{zy} & s_{zz} \end{bmatrix} = \begin{bmatrix} \sigma_{xx} - p & \tau_{xy} & \tau_{xz} \\ \tau_{yx} & \sigma_{yy} - p & \tau_{yz} \\ \tau_{zx} & \tau_{zy} & \sigma_{zz} - p \end{bmatrix} \tag{3.3}$$

The first invariant of the deviatoric stress tensor (J_1) is zero, and its second invariant (J_2) is then given by:

$$J_2 = \frac{1}{2}\boldsymbol{s} : \boldsymbol{s} \tag{3.4}$$

where the contraction symbol : denotes the trace of the product of two tensors (i.e. **x**:**y**=trace(**xy**)). With some algebra J_2 can be shown to be equivalent to the useful expression in terms of stress components,

$$J_2 = \frac{1}{6}\left[(\sigma_{xx} - \sigma_{yy})^2 + (\sigma_{yy} - \sigma_{zz})^2 + (\sigma_{zz} - \sigma_{xx})^2\right] + \tau_{xy}{}^2 + \tau_{yz}{}^2 + \tau_{zx}{}^2 \tag{3.5}$$

The third deviatoric stress invariant (J_3) is,

$$J_3 = det(\hat{\boldsymbol{s}}) \tag{3.6}$$

where *det* is the determinant of the second-order tensor.

The J_2 value is often scaled for use in developing constitutive models. The scaled value $\sqrt{2J_2}$ is often used, since it represents the perpendicular distance of the stress point from the space diagonal

(Figure 3.1) in principal stress space. Finally, within soil mechanics it is often preferred to define a scaled version of J_2 as,

$$q = \sqrt{3\,J_2} = \sqrt{\frac{3}{2}\,\hat{\boldsymbol{s}} : \hat{\boldsymbol{s}}} \tag{3.7}$$

which is termed the 'deviatoric stress' in soil mechanics or more traditionally in metal plasticity the 'von Mises equivalent stress'.

The Lode angle (θ) which is an angular measure of the position of the stress point within the deviatoric plane in principal stress space, is given by,

$$\theta = \frac{1}{3}\sin^{-1}\left(-\frac{3\sqrt{3}}{2}\,\frac{J_3}{(J_2)^{3/2}}\right) \tag{3.8}$$

In this form the θ takes a value of $-30°$ for triaxial compression and +30° for triaxial extension conditions. This is based on the assumption that compression is positive and hence for studies in which compression is taken as negative these would reverse. In addition, it should be noted, an alternative form of the Lode angle is also sometimes presented in the literature (e.g. Manzari and Dafalias, 1997) in which triaxial compression is 60° and triaxial extension is 0°. Within this study, for all constitutive model implementation, Equation 3.8 is used to define θ (i.e. $-30°$ for triaxial compression).

The invariants p, q and θ are typically used for the development of soil constitutive models given their significance in soil mechanics. However, it should be noted that different forms of stress invariants could be used to define a constitutive model, for example the invariants of the stress tensor (i.e. I_1, I_2 and I_3) or the principal stresses (i.e. $\sigma_1, \sigma_2, \sigma_3$) could be used. The principal stresses ($\sigma_1, \sigma_2, \sigma_3$), which are the eigenvalues of the stress tensor, are defined in numerical order as $\sigma_1 \geq \sigma_2 \geq \sigma_3$ and can also be used to define a particular stress state. However, it is generally more convenient to use some form of scaled stress invariants as discussed above (e.g. p, q and θ). The principal stresses can easily be found directly from the stress invariants discussed by:

$$\sigma_1 = \frac{1}{3}I_1 + \frac{2}{\sqrt{3}}\sqrt{J_2}\sin\left(\theta + \frac{2\pi}{3}\right) \tag{3.9}$$

$$\sigma_2 = \frac{1}{3} I_1 + \frac{2}{\sqrt{3}} \sqrt{J_2} \sin(\theta)$$
$$\sigma_3 = \frac{1}{3} I_1 + \frac{2}{\sqrt{3}} \sqrt{J_2} \sin\left(\theta - \frac{2\pi}{3}\right)$$

The geometric interpretation of the invariants (I_1, J_2 and θ) in principal stress space is presented in Figure 3.1.

3.1.2 Stress Invariant Derivatives

The required partial derivatives to form the $\boldsymbol{D}_{ep}$ matrix can be simply determined using stress invariants by applying the chain rule,

$$\frac{\partial f}{\partial \boldsymbol{\sigma}} = \frac{\partial f}{\partial p}\frac{\partial p}{\partial \boldsymbol{\sigma}} + \frac{\partial f}{\partial q}\frac{\partial q}{\partial \boldsymbol{\sigma}} + \frac{\partial f}{\partial \theta}\frac{\partial \theta}{\partial \boldsymbol{\sigma}} \quad 3.10$$

$$\frac{\partial g}{\partial \boldsymbol{\sigma}} = \frac{\partial g}{\partial p}\frac{\partial p}{\partial \boldsymbol{\sigma}} + \frac{\partial g}{\partial q}\frac{\partial q}{\partial \boldsymbol{\sigma}} + \frac{\partial g}{\partial \theta}\frac{\partial \theta}{\partial \boldsymbol{\sigma}} \quad 3.11$$

where the stress invariants (p, q, θ) are typically used to define the yield and plastic potential functions. The partial derivatives of the stress invariants, required to determine $\partial f/\partial \boldsymbol{\sigma}$ and $\partial g/\partial \boldsymbol{\sigma}$, are then given by,

$$\frac{\partial p}{\partial \boldsymbol{\sigma}} = \frac{1}{3}\,[1, 1, 1, 0, 0, 0]^T \quad 3.12$$

$$\frac{\partial q}{\partial \boldsymbol{\sigma}} = \frac{\sqrt{3}}{2q}\left[s_{xx},\ s_{yy},\ s_{zz}, 2\tau_{xy}, 2\tau_{yz}, 2\tau_{zx}\right]^T \quad 3.13$$

$$\frac{\partial \theta}{\partial \boldsymbol{\sigma}} = \frac{\sqrt{3}}{2J_2^{3/2} cos3\theta}\left(\frac{3}{2}\frac{J_3}{J_2}\frac{\partial J_2}{\partial \boldsymbol{\sigma}} - \frac{\partial J_3}{\partial \boldsymbol{\sigma}}\right) \quad 3.14$$

$$\frac{\partial J_2}{\partial \boldsymbol{\sigma}} = \left[s_{xx},\ s_{yy},\ s_{zz}, 2\tau_{xy}, 2\tau_{yz}, 2\tau_{zx}\right]^T \quad 3.15$$

$$\frac{\partial J_3}{\partial \boldsymbol{\sigma}} = \begin{bmatrix} \frac{1}{3}\left(\sigma_{xx}s_{xx} + \sigma_{yy}s_{zz} + \sigma_{zz}s_{yy} + {\tau_{xy}}^2 + {\tau_{yz}}^2 + {\tau_{zx}}^2\right) \\ \frac{1}{3}\left(\sigma_{yy}s_{yy} + \sigma_{zz}s_{xx} + \sigma_{xx}s_{zz} + {\tau_{yz}}^2 - 2{\tau_{zx}}^2 + {\tau_{xy}}^2\right) \\ \frac{1}{3}\left(\sigma_{zz}s_{zz} + \sigma_{xx}s_{yy} + \sigma_{yy}s_{xx} + {\tau_{zx}}^2 - 2{\tau_{xy}}^2 + {\tau_{yz}}^2\right) \\ -2\tau_{xy}s_{zz} + 2\tau_{yz}\tau_{zx} \\ -2\tau_{yz}s_{xx} + 2\tau_{zx}\tau_{xy} \\ -2\tau_{zx}s_{yy} + 2\tau_{xy}\tau_{yz} \end{bmatrix} \quad 3.16$$

3.1.3 Strain Invariants

It is also occasionally useful when developing some components of constitutive models (e.g. strain dependent elastic rules within the yield surface) to use some form of strain invariants (e.g. deviatoric and volumetric strains). The strain tensor in a Cartesian axes (*x*,*y*,*z*) is,

$$\hat{\boldsymbol{\varepsilon}} = \begin{bmatrix} \varepsilon_{xx} & \varepsilon_{xy} & \varepsilon_{xz} \\ \varepsilon_{yx} & \varepsilon_{yy} & \varepsilon_{yz} \\ \varepsilon_{zx} & \varepsilon_{zy} & \varepsilon_{zz} \end{bmatrix} \quad 3.17$$

or in Voigt/vector form, given by $\boldsymbol{\varepsilon} = \left[\varepsilon_{xx}, \varepsilon_{yy}, \varepsilon_{zz}, 2\varepsilon_{xy}, 2\varepsilon_{yz}, 2\varepsilon_{zx}\right]^T$. The first invariant of $\hat{\boldsymbol{\varepsilon}}$, which is equal to the volumetric strain, is given by,

$$I_{1,\varepsilon} = \varepsilon_{xx} + \varepsilon_{yy} + \varepsilon_{zz} = \varepsilon_{vol} \quad 3.18$$

The deviatoric strain tensor (**e**) is,

$$\boldsymbol{e} = \begin{bmatrix} e_{xx} & e_{xy} & e_{xz} \\ e_{yx} & e_{yy} & e_{yz} \\ e_{zx} & e_{zy} & e_{zz} \end{bmatrix} = \begin{bmatrix} \varepsilon_{xx} - \dfrac{\varepsilon_{vol}}{3} & \varepsilon_{xy} & \varepsilon_{xz} \\ \varepsilon_{yx} & \varepsilon_{yy} - \dfrac{\varepsilon_{vol}}{3} & \varepsilon_{yz} \\ \varepsilon_{zx} & \varepsilon_{zy} & \varepsilon_{zz} - \dfrac{\varepsilon_{vol}}{3} \end{bmatrix} \quad 3.19$$

The second invariant of the deviatoric strain tensor ($J_{2,e}$) in terms of strain components is given by,

$$J_{2,e} = \frac{1}{6}\left[\left(\varepsilon_{xx} - \varepsilon_{yy}\right)^2 + \left(\varepsilon_{yy} - \varepsilon_{zz}\right)^2 + \left(\varepsilon_{zz} - \varepsilon_{xx}\right)^2\right] + \frac{1}{4}\left({\gamma_{xy}}^2 + {\gamma_{yz}}^2 + {\gamma_{zx}}^2\right) \quad 3.20$$

where engineering strains are used and given by, $\gamma_{xy} = 2\varepsilon_{xy}$, $\gamma_{yz} = 2\varepsilon_{yz}$, $\gamma_{zx} = 2\varepsilon_{zx}$. A scalar measure of deviatoric strain may be required to formulate a constitutive model (e.g. strain-dependent elastic rules within the yield surface), and in such cases it is convenient to use a scaled value of $J_{2,e}$. The von Mises equivalent or deviatoric strain (E_q) is:

$$E_q = \left(\frac{2}{9}\left[\left(\varepsilon_{xx} - \varepsilon_y\right)^2 + \left(\varepsilon_{yy} - \varepsilon_{zz}\right)^2 + \left(\varepsilon_{zz} - \varepsilon_{xx}\right)^2\right] + \frac{1}{3}\left[\gamma_{xy}^2 + \gamma_{yz}^2 + \gamma_{zx}^2\right]\right)^{1/2} \quad 3.21$$

which is equal to $\frac{2}{\sqrt{3}}\sqrt{J_{2,e}}$. Other scaled forms of the second invariant of the deviatoric strain tensor are used for constitutive model implementation (e.g. Zdravković et al., 2019); however, the form in Equation 3.21 is particularly useful because under triaxial conditions, where only axial (ε_a) and radial strains (ε_r) are applied (i.e. $\varepsilon_a = \varepsilon_{zz};\ \varepsilon_r = \varepsilon_{xx} = \varepsilon_{yy};\ \gamma_{xy} = \gamma_{yz} = \gamma_{zx} = 0$), E_q is identical to the triaxial deviatoric strain, ε_q (=$2/3(\varepsilon_a - \varepsilon_r)$, which is commonly used in soil mechanics.

3.2 Implementation

3.2.1 Stress Point Algorithm

A fundamental part of any FEA calculation involves integrating the constitutive relations across a finite strain increment ($\Delta\boldsymbol{\varepsilon}$) to determine the updated stress state ($\boldsymbol{\sigma}$). The integration procedure used to determine the updated $\boldsymbol{\sigma}$ is of critical importance when implementing a constitutive model. The approach used to determine the updated $\boldsymbol{\sigma}$ is termed the stress point algorithm. Explicit substepping algorithms have been proposed by many authors and used successfully for implementation of constitutive models (e.g. Sloan, 1987; Sloan et al., 2001; Potts and Ganendra, 1994; Zhao et al., 2005). Separately, implicit return algorithms are also presented in the literature for implementing a variety of constitutive models (e.g. Borja and Lee, 1990; Manzari and Nour, 1997; Rouainia and Wood, 2001), in which an elastic predictor is first calculated with an iterative algorithm used to transfer the stress state back to the yield surface.

With respect to simple explicit substepping algorithms with no automatic error control, the main perceived drawback is typically their accuracy; however, development of automatic substepping schemes with error control (e.g. Sloan, 1987; Sloan et al., 2001) have overcome this drawback. Implementation of implicit methods can be complex and time consuming, with second-order derivatives of the plastic potential function required. As discussed by Zhao et al. (2005) this can become particularly laborious for complex constitutive models. Another drawback of implicit schemes is the likelihood of local non-convergence when using highly nonlinear yield or plastic potential functions (Ding et al., 2015). Potts and Ganendra (1994) presented a comparison of the two stress point algorithms for element triaxial tests and a boundary value problem of a pile using the Modified Cam Clay model. Their findings showed the automatic substepping approach with error control to be more accurate than an implicit scheme.

Therefore, based on the above observations an explicit substepping scheme with automatic error control was used within this study for all constitutive model implementation (Sections 4 to 7). The

stress point algorithm implemented is based on the recommendations and procedures outlined in Sloan et al. (2001).

3.2.2 Automatic Substepping Scheme with Error Control

A detailed description of the algorithm used in this study, for model implementation, is presented by Sloan et al. (2001) and a basic overview is given below.

The following two main tasks must be performed by any explicit algorithm: i) determine if the strain increment is elastic, elastoplastic or mixed (i.e. partly elastic and partly elastoplastic) and if the stress state crosses the yield surface during the strain increment, then determine the intersection point and ii) perform integration of the nonlinear stress-strain relations.

3.2.2.1 Elastic Increment Prediction and Yield Surface Intersection

First an elastic trial stress ($\boldsymbol{\sigma}_e$) is predicted from the increment of total strain ($\Delta\boldsymbol{\varepsilon}$) by,

$$\boldsymbol{\sigma}_e = \boldsymbol{\sigma}_0 + \boldsymbol{D}_e \Delta\boldsymbol{\varepsilon} \tag{3.22}$$

where $\boldsymbol{\sigma}_0$ is the stress at the beginning of the increment. It should be noted, that Equation 3.22 assumes linear elasticity within the yield surface and therefore no integration scheme is required to determine $\boldsymbol{\sigma}_e$ in this case. If $f(\boldsymbol{\sigma}_e, h) \leq FTOL$, where $FTOL$ is a small user-defined tolerance, then the updated stress lies within the yield surface, the behaviour is fully elastic and $\boldsymbol{\sigma}_e$ is accepted as the updated stress ($\boldsymbol{\sigma} = \boldsymbol{\sigma}_e$). A value of *FTOL*, which is assumed to be 10^{-6} in this study, is used as approximation for zero to account for finite precision arithmetic effects. However, if $f(\boldsymbol{\sigma}_e, h) > FTOL$ and $\boldsymbol{\sigma}_0$ was within the yield surface, then plastic yielding occurs over $\Delta\boldsymbol{\varepsilon}$ and the yield surface intersection point must be identified to determine the elastic portion of the $\Delta\boldsymbol{\varepsilon}$. Therefore, the scalar value α which satisfies the following equation must be found,

$$|f(\boldsymbol{\sigma}_0 + \boldsymbol{D}_e \alpha \Delta\boldsymbol{\varepsilon}, h)| \leq FTOL \tag{3.23}$$

where, $0 < \alpha < 1$. To solve the above equation a number of different methods can be used (e.g. Bisection, Pegasus or Modified Regula-Falsi). In this study a Modified Regula-Falsi method is used. Once α and the intersection stress state ($\boldsymbol{\sigma}_{int} = \boldsymbol{\sigma}_0 + \boldsymbol{D}_e \alpha \Delta\boldsymbol{\varepsilon}$) are determined (Figure 3.2) the portion

of strain that is associated with elastoplastic loading is given as $\Delta\boldsymbol{\varepsilon}_s = \Delta\boldsymbol{\varepsilon}(1-\alpha)$. The $\boldsymbol{\sigma}_{int}$ and $\Delta\boldsymbol{\varepsilon}_s$ are then used to determine the elastoplastic increment for which an integration scheme is needed (Section 3.2.2.2).

When the initial stress state lies on the yield surface (i.e. $|f(\boldsymbol{\sigma}_0, h)| \leq FTOL$) additional rules are applied based on recommendations by Sloan et al. (2001) since two scenarios are possible from this position, when $f(\boldsymbol{\sigma}_e, h) > FTOL$, based on the elastic trial stress prediction: 1) fully elastoplastic loading from the yield surface or 2) elastic unloading inside the yield surface followed by elastoplastic loading. Therefore, it must be determined if unloading occurs from an initial stress state on the yield surface (i.e. the stress path enters the yield surface) before elastoplastic loading. This is done by checking if the angle (ς) between the yield surface gradient ($\partial f/\partial\boldsymbol{\sigma}_0$) and the elastic stress increment ($\Delta\boldsymbol{\sigma}_e$) is larger than 90° (i.e. if $\varsigma > 90°$ unloading occurs). This unloading case from the yield surface is presented schematically in Figure 3.3. The ς angle is determined by,

$$\cos(\varsigma) = \frac{\frac{\partial f}{\partial \boldsymbol{\sigma}_0}\Delta\boldsymbol{\sigma}_e}{\left\|\frac{\partial f}{\partial \boldsymbol{\sigma}_0}\right\| \|\Delta\boldsymbol{\sigma}_e\|} \tag{3.24}$$

If $\cos(\varsigma) < -LTOL$, where $LTOL$ is a small user defined tolerance, then unloading is deemed to have occurred. A value of $LTOL = 10^{-6}$ was used as a suitable tolerance based on recommendations by Sloan et al. (2001). If unloading from the yield surface, followed by elastoplastic loading is deemed to occur, then the $\Delta\boldsymbol{\varepsilon}$ is split into ten smaller subincrements to find the yield surface intersection. Further details of the specific algorithm used are given in Sloan et al (2001).

3.2.2.2 Integration Scheme

The increment of strain supplied to the elastoplastic constitutive equations is integrated using an explicit Runga-Kutta-Dormand-Prince integration scheme with automatic error control to determine the updated stress state based on recommendations in Sloan et al. (2001). The error control is achieved by subtracting higher order and lower order solutions then checking against a set error tolerance to determine whether the step should be accepted. If the step is not accepted a reduced subincrement size is attempted. The following main steps are performed by the integration scheme.

Step 1: Determine subincrement of strain

The subincrement $\Delta\boldsymbol{\varepsilon}_s$ is the increment of strain in which plastic loading occurs (i.e. based on yield surface intersection). Substepping is performed by subdividing this increment of strain into smaller subincrements ($\Delta\boldsymbol{\varepsilon}_n$), determined by:

$$\Delta\boldsymbol{\varepsilon}_n = \Delta T_n \Delta\boldsymbol{\varepsilon}_s \tag{3.25}$$

where ΔT_n is the pseudo time subincrement which is a measure of the assumed substep size with the total pseudo time increment (T) then given by:

$$T = T + \Delta T_n \tag{3.26}$$

where $T = 0$ at the start of the increment and $T = 1$ at the end of the increment. The pseudo time subincrement is initially assumed to be equal to 1 for the trial increment size and subsequently reduced in size if required.

Step 2: Calculate the higher and lower order accurate solutions

Within the subincrement, the stresses and hardening parameter(s) are evaluated at a number of improved estimations of the stress and hardening state ($\boldsymbol{\sigma}_i, h_i$) following a Runga-Kutta-Dormand-Prince scheme by the following,

$$\boldsymbol{\sigma}_1 = \boldsymbol{\sigma}_{n-1} \qquad h_1 = h_{n-1} \tag{3.27}$$

$$\boldsymbol{\sigma}_2 = \boldsymbol{\sigma}_{n-1} + \frac{1}{5}\Delta\boldsymbol{\sigma}_1 \qquad h_2 = \mathrm{h}_{n-1} + \frac{1}{5}\Delta h_1 \tag{3.28}$$

$$\boldsymbol{\sigma}_3 = \boldsymbol{\sigma}_{n-1} + \frac{3}{40}\Delta\boldsymbol{\sigma}_1 + \frac{9}{40}\Delta\boldsymbol{\sigma}_2 \qquad h_3 = \mathrm{h}_{n-1} + \frac{3}{40}\Delta\mathrm{h}_1 + \frac{9}{40}\Delta\mathrm{h}_2 \tag{3.29}$$

$$\boldsymbol{\sigma}_4 = \boldsymbol{\sigma}_{n-1} + \frac{3}{10}\Delta\boldsymbol{\sigma}_1 - \frac{9}{10}\Delta\boldsymbol{\sigma}_2 + \frac{6}{5}\Delta\boldsymbol{\sigma}_3 \qquad h_4 = h_{n-1} + \frac{3}{10}\Delta h_1 - \frac{9}{10}\Delta h_2 + \frac{6}{5}\Delta h_3 \tag{3.30}$$

$$\boldsymbol{\sigma}_5 = \boldsymbol{\sigma}_{n-1} + \frac{226}{729}\Delta\boldsymbol{\sigma}_1 - \frac{25}{27}\Delta\boldsymbol{\sigma}_2 + \frac{880}{729}\Delta\boldsymbol{\sigma}_3 + \frac{55}{729}\Delta\boldsymbol{\sigma}_4 \qquad h_5 = h_{n-1} + \frac{226}{729}\Delta h_1 - \frac{25}{27}\Delta h_2 + \frac{880}{729}\Delta h_3 + \frac{55}{729}\Delta h_4 \tag{3.31}$$

$$\boldsymbol{\sigma}_6 = \boldsymbol{\sigma}_{n-1} - \frac{181}{270}\Delta\boldsymbol{\sigma}_1 + \frac{5}{2}\Delta\boldsymbol{\sigma}_2 - \frac{226}{297}\Delta\boldsymbol{\sigma}_3 - \frac{91}{27}\Delta\boldsymbol{\sigma}_4 + \frac{189}{55}\Delta\boldsymbol{\sigma}_5$$
$$h_6 = h_{n-1} - \frac{181}{270}\Delta h_1 + \frac{5}{2}\Delta h_2 - \frac{226}{297}\Delta h_3 - \frac{91}{27}\Delta h_4 + \frac{189}{55}\Delta h_5 \qquad 3.32$$

where,

$$\Delta\boldsymbol{\sigma}_i = \boldsymbol{D}_{ep}(\boldsymbol{\sigma}_i, \mathrm{h}_i)\Delta\varepsilon_n$$
$$\Delta\boldsymbol{\varepsilon}_i^p = \Lambda(\boldsymbol{\sigma}_i, h_i, \Delta\boldsymbol{\varepsilon}_n)\frac{\partial g}{\partial \boldsymbol{\sigma}_i} \qquad 3.33$$
$$\Delta h_i = \Delta h(\Delta\boldsymbol{\varepsilon}_i^p)$$

Subsequently, the fourth order solutions for the stress state and the hardening parameter(s) are given by,

$$\boldsymbol{\sigma}_{4th,n} = \boldsymbol{\sigma}_{n-1} + \frac{31}{540}\Delta\boldsymbol{\sigma}_1 + \frac{190}{297}\Delta\boldsymbol{\sigma}_3 - \frac{145}{108}\Delta\boldsymbol{\sigma}_4 + \frac{351}{220}\Delta\boldsymbol{\sigma}_5 + \frac{1}{20}\Delta\boldsymbol{\sigma}_6$$
$$h_{4th,n} = h_{n-1} + \frac{31}{540}\Delta h_1 + \frac{190}{297}\Delta h_3 - \frac{145}{108}\Delta h_4 + \frac{351}{220}\Delta h_5 + \frac{1}{20}\Delta h_6 \qquad 3.34$$

and the fifth order solutions are then given by,

$$\boldsymbol{\sigma}_{5th,n} = \boldsymbol{\sigma}_{n-1} + \frac{19}{216}\Delta\boldsymbol{\sigma}_1 + \frac{1000}{2079}\Delta\boldsymbol{\sigma}_3 - \frac{125}{216}\Delta\boldsymbol{\sigma}_4 + \frac{81}{88}\Delta\boldsymbol{\sigma}_5 + \frac{5}{56}\Delta\boldsymbol{\sigma}_6$$
$$h_{5th,n} = h_{n-1} + \frac{19}{216}\Delta h_1 + \frac{1000}{2079}\Delta h_3 - \frac{125}{216}\Delta h_4 + \frac{81}{88}\Delta h_5 + \frac{5}{56}\Delta h_6 \qquad 3.35$$

The local error measure for the subincrement of strain ($\Delta\varepsilon_n$) is found by taking the difference between the higher (fifth) order and the lower (fourth) order solutions. The local errors for the stress update (E_σ) and hardening parameter(s) update (E_h) are then given by,

$$E_\sigma = \boldsymbol{\sigma}_{5th,n} - \boldsymbol{\sigma}_{4th,n} = \frac{11}{360}\Delta\boldsymbol{\sigma}_1 - \frac{10}{63}\Delta\boldsymbol{\sigma}_3 + \frac{55}{72}\Delta\boldsymbol{\sigma}_4 - \frac{27}{40}\Delta\boldsymbol{\sigma}_5 + \frac{11}{280}\Delta\boldsymbol{\sigma}_6$$
$$E_h = h_{5th,n} - h_{4th,n} = \frac{11}{360}\Delta h_1 - \frac{10}{63}\Delta h_3 + \frac{55}{72}\Delta h_4 - \frac{27}{40}\Delta h_5 + \frac{11}{280}\Delta h_6 \qquad 3.36$$

Finally, the updated stresses and hardening parameter(s) are given by,

$$\boldsymbol{\sigma}_{T+\Delta T} = \boldsymbol{\sigma}_{5th,n} = \boldsymbol{\sigma}_T + \frac{19}{216}\Delta\boldsymbol{\sigma}_1 + \frac{1000}{2079}\Delta\boldsymbol{\sigma}_3 - \frac{125}{216}\Delta\boldsymbol{\sigma}_4 + \frac{81}{88}\Delta\boldsymbol{\sigma}_5 + \frac{5}{56}\Delta\boldsymbol{\sigma}_6$$
$$h_{T+\Delta T} = h_{5th,n} = h_T + \frac{19}{216}\Delta h_1 + \frac{1000}{2079}\Delta h_3 - \frac{125}{216}\Delta h_4 + \frac{81}{88}\Delta h_5 + \frac{5}{56}\Delta h_6 \qquad 3.37$$

It should be noted that different integration schemes (i.e. lower order) can also be used in place of the fifth order scheme presented above (e.g. Modified Euler method). However, it was found, although slower, the higher order scheme presented above was more robust in FEA calculations.

Step 3: Error Check

The relative error (R) for the current subincrement of strain ($\Delta\boldsymbol{\varepsilon}_n$) is then found by,

$$R = max\left\{\frac{\|E_\sigma\|}{\|\boldsymbol{\sigma}_{T+\Delta T}\|}, \frac{|E_h|}{h_{T+\Delta T}}\right\} \tag{3.38}$$

The relative error is then checked against the specified tolerated error (*STOL*). If *R>STOL* the substep is rejected, the stresses are not updated, and the subincrement size is reduced for another attempt at the stress update calculation. The *STOL* for the integration scheme was set as 10^{-5} for all model implementation presented (Sections 4 to 7). For rejected substeps the new subincrement size is determined by,

$$\Delta T_n = \Delta T_n \, Q \tag{3.39}$$

where Q is given by,

$$Q = 0.8\left[\frac{STOL}{R}\right]^{1/5} \tag{3.40}$$

Note, 0.8 is applied as a factor to reduce the number of failed substeps. The new value of ΔT_n is then used to determine the new strain subincrement and the above steps are repeated without the stress being updated.

If $R \leq STOL$ the substep is accepted, and the stress and hardening parameters are updated according to Equation 3.37 with steps 1 to 3 repeated using the updated stresses. This procedure continues until $\sum \Delta T_n = T = 1$.

At the end of each strain subincrement the calculated stresses may diverge from the yield surface (i.e. $f(\boldsymbol{\sigma}, h) > FTOL$). Therefore, if required, the stresses are corrected to the yield surface at the end of each strain subincrement. However, given the tight error control and the high order integration scheme used within this study, this correction rarely has to be applied. Sloan et al. (2001) outlines the stress correction algorithm, termed the consistent correction method, which has been employed in the current study. The correction process, outlined in Sloan et al. (2001), involves correcting the stresses and the hardening parameter(s) until $|f(\boldsymbol{\sigma}, h)| \leq FTOL$ with the $\Delta\boldsymbol{\varepsilon}_n$ remaining unchanged.

3.2.2.3 Special Case of Nonlinear Elasticity

If a linear elastic stiffness matrix is used within the yield surface, then no integration scheme is required to determine the updated stress state for an increment of elastic strain i.e. Equation 3.22 can be used to determine the updated stress state. However, if a non-linear stress- and/or strain-dependent elastic stiffness matrix is utilised it is also necessary to incorporate a numerical yintegration scheme for the elastic strain increments within the yield surface. In a Similar way to the integration of the elastoplastic increments, the Sloan et al. (2001) Runga-Kutta-Dormand-Prince integration scheme with automatic error control is used to integrate nonlinear elastic constitutive relations in this study.

A fundamental component of the stress update procedure is to compute the yield surface intersection stress state as the stresses pass from elastic to plastic. When using a nonlinear elastic model within the yield surface, this criterion is checked at every accepted substep within the Runga-Kutta-Dormand-Prince integration scheme. If a substep is found to cross the yield surface, then a Modified Regula-Falsi intersection scheme is used to determine the yield surface intersection stress state within the associated strain subincrement.

3.2.3 Element Stiffness Matrices

When performing FEA calculations the constitutive model must also supply a material stiffness matrix as an input to form the element stiffness matrices ($\boldsymbol{K}_E$) which are assembled into the global stiffness matrix ($\boldsymbol{K}_G$) to define governing global set of equations given by,

$$\boldsymbol{K}_G \delta \boldsymbol{d}_G = \delta \boldsymbol{R}_G \tag{3.41}$$

where $\delta \boldsymbol{d}_G$ is a vector containing nodal displacement increment and $\delta \boldsymbol{R}_G$ is the global load vector increment. The global set of equations is then typically solved iteratively using a Modified or Full Newton-Raphson algorithm (the global problem). When using an explicit substepping approach (as discussed above) either the $\boldsymbol{D}_{ep}$ matrix or $\boldsymbol{D}_e$ matrix could be used to form $\boldsymbol{K}_E$. Although, within the literature there is extensive information on the implementation of explicit stress point algorithms (e.g. Sloan, 1987; Potts and Zdravković, 1999; Sloan et al., 2001) there is little information on the

most appropriate stiffness matrix to use for FEA calculations. A detailed review of the best approach is not presented in this study; however, from the author's experience of implementing several different constitutive models (Sections 4 to 7) it was found that the use of $\boldsymbol{D}_e$, although slower, was less susceptible to divergence of the FEA equilibrium iterations. These observations are consistent with those of Brinkgreve (1994) who found the use of $\boldsymbol{D}_e$ to be the more robust method for complex non-associated plasticity models. All models presented in subsequent sections therefore use the $\boldsymbol{D}_e$ matrix to form the element stiffness matrices, which is consistent with Brinkgreve (1994) and Plaxis (2017).

3.2.4 User-Defined Constitutive Models in Plaxis or Abaqus

All constitutive models presented in subsequent sections were programmed in Fortran as user defined soil models (UDSM) for use in Plaxis (Plaxis, 2017) and as UMAT subroutines for use in Abaqus (Dassault Systèmes, 2014). The overall implementation approach is the same for both cases and only slight differences are required with respect to variable names and interaction with the main FEA software. For a UDSM the Fortran code is precompiled as a dynamic link library (.dll) file for use in Plaxis, whereas the Fortran programmed UMAT subroutines are compiled using an Intel Fortran Compiler linked with Abaqus. The Intel Fortran Composer XE 2011 Update 6 (compiler 12.1) was used within this study. Details of the variable passing mechanisms required for implementation are presented in Plaxis (2017) and Dassault Systèmes (2014).

3.3 Figures

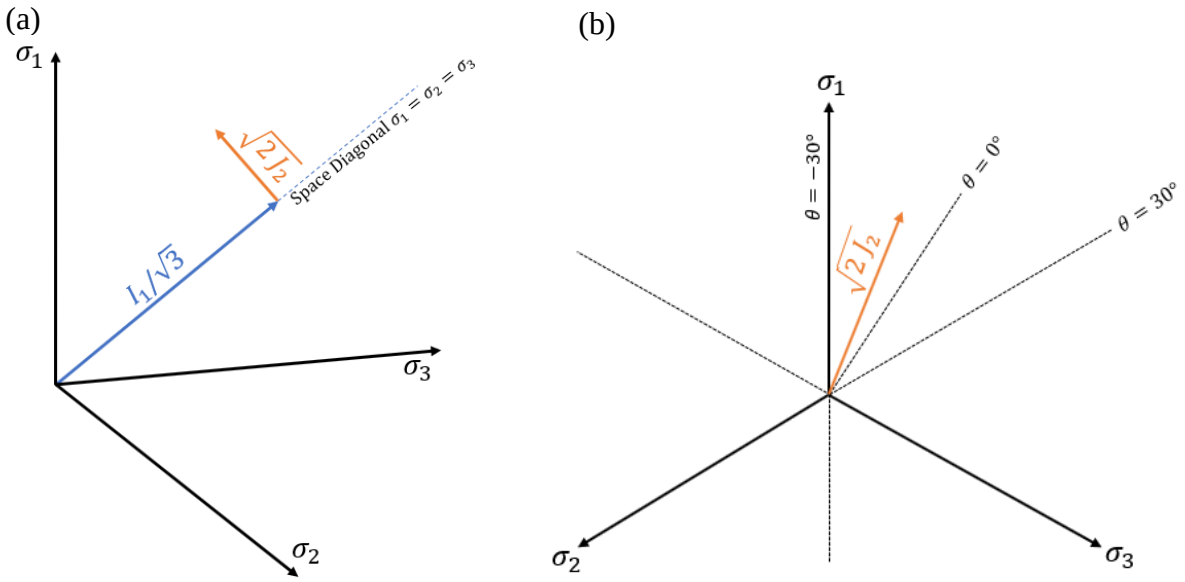

Figure 3.1: View of stress invariants in a) principal stress space with b) presenting view in deviatoric plane

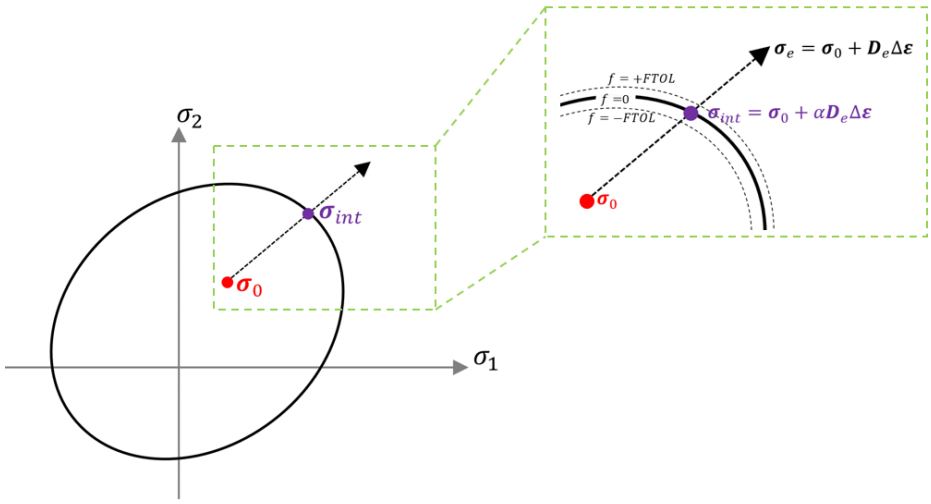

Figure 3.2: Yield surface intersection schematic

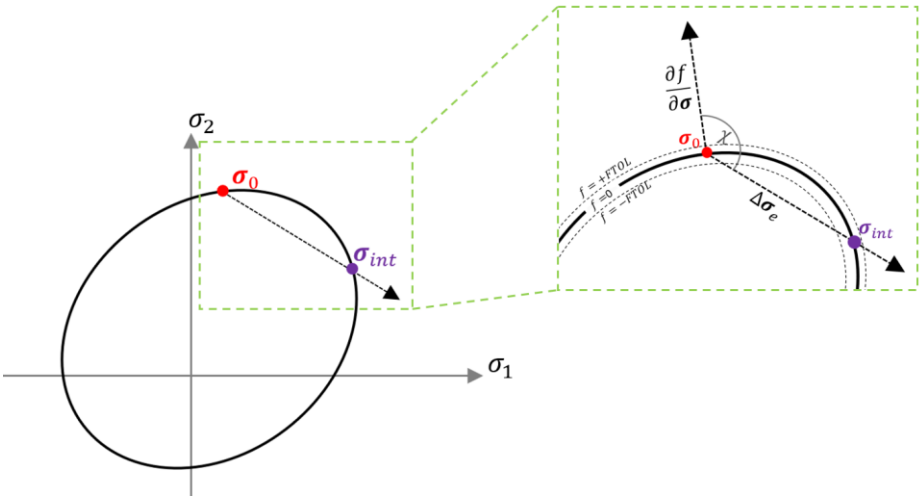

Figure 3.3: Yield surface intersection schematic with unloading from yield surface

Section 4

DEVELOPMENT OF SIMPLE DILATIONAL SAND MODEL

Contents

4. DEVELOPMENT OF SIMPLE DILATIONAL SAND MODEL

This section presents an overview of a developed model, named the Simple Dilational Sand (SDS) model, for FEA of soil-structure interaction problems involving partially drained to undrained dense sand. The SDS model is developed by combining several different elastoplastic model components previously published in the literature, with the state- and stress-dependent plastic potential function based on Erbrich (1994), the stress-dependent elastic stiffness matrix based on Houlsby et al. (2005), and the yield surface shape based on Sheng et al. (2000). In addition, a version of the model which incorporates a strain-dependent elastic model in the yield surface, termed the Fugro Dilational Model (FDM), is also presented. The models were implemented in both Plaxis as a user defined soil model (UDSM) and within Abaqus as a user material model (UMAT) subroutine using the procedures outlined in Section 3. This Section outlines the model development and implementation. The models were developed specifically as practical models for simulating suction bucket foundations in dense sand under partially drained conditions in FEA. A previous elementary version of the model proposed by Erbrich (1994), which was an adapted version of the Abaqus Modified Capped Drucker-Prager (MCDP) model (Dassault Systèmes, 2014), was used successfully by Bye et al. (1995) for the suction bucket design FEA of the Europipe 16/11E Riser jacket and Sleipner T jacket suction bucket foundations.

4.1 Introduction

The response of undrained to partially drained dense sand at low initial mean effective stresses (p') is primarily controlled by the dilational response, which manifests as negative excess pore pressures. This is illustrated in Figure 4.1, which presents a schematic of the typical reponse observed when shearing dense (Figure 4.1a) and loose (Figure 4.1b) sands in an undrained triaxial test. The salient feature of dense sand response under undrained conditions is the dilatational behaviour which manifests as the development of negative excess pore pressures. As can be seen from Figure 4.1a, for dense sand only a small amount of contractive behaviour (i.e. development of positive excess pore pressure in undrained conditions) typically occurs (for low initial p') and a

dilational response begins at low deviatoric strain values. Therefore, when considering suction buckets, in which the in situ p' is low due to shallow embedment depths, it is expected that in dense sand the dilational response of the constitutive model will control the foundation response under partially drained to undrained conditions.

There is a lack of practical constitutive models, available as built-in soil models within commercially available FEA software, that are suitable for predicating the response of dense sands at low initial p' values when considering undrained to partially drained conditions. Most constitutive models that are available in commercial FEA packages are not suitable without careful calibration of the parameters. For example, the in-built Plaxis hardening soil (HS) model (Schanz et al., 1999; Plaxis, 2017), which is a popular model for simulating sand in boundary value problems, is not suited for modelling dense to very dense sand under partially drained to undrained conditions. The HS model and HS with a small strain stiffness overlay (HSsmall) model (Benz, 2007) can be considered reasonable for predicting the response of contractive sands (i.e. loose to medium dense sands) in undrained conditions; however, because they incorporate a fixed dilation angle (when yield surface is equal to the peak friction angle), an infinite undrained shear strength is predicted, if a non-zero dilation angle is specified. Since the mobilised dilation angles can be very large for dense sands at low p' values, if not carefully calibrated, a very unconservative prediction of the undrained stress-strain response, could be achieved using the HS or HSsmall models.

Within the commercially available FEA software package Abaqus, the in-built MCDP model (Dassault Systèmes, 2014) is often used by practising engineers due to its numerical stability in complex boundary value problems (C Erbrich, personal communication, 10 November, 2015). Although this model does not incorporate a constant dilation angle, and therefore could be considered more realistic than the HS model, the stress-dilatancy response is not well predicted for dense sand. Figure 4.2 shows the maximum plastic dilatancy (D) versus p' predicted by the Abaqus MCDP model, where $D = d\varepsilon_v^p / d\varepsilon_q^p$ and ε_v^p and ε_q^p are the plastic triaxial volumetric and

deviatoric strains. A poor prediction of D, at low mean effective stresses, is observed from a comparison of the MCDP to observed published laboratory trends from Bolton (1986) for sand with an initial relative density (D_r) of 100%, where $D_r = (e_{max} - e_0)/(e_{max} - e_{min})$ and e_0, e_{min}, e_{max} are the initial, minimum and maximum void ratios respectively. The plastic potential function within the MCDP model, which controls the stress-dilatancy response, cannot be adapted with any specific input parameters and as such cannot be calibrated to measured stress-dilatancy data.

Post-peak softening also occurs within a dense sand. Although this is important for drained loading conditions at high strain levels, it is not considered significant for undrained to partially drained conditions. A number of constitutive models developed have included state- and stress-dependent plastic potential functions which represent the dilational response of sand reasonably well; however, most also include a strain-softening yield surface (e.g. Dafalias and Manzari, 2004). Although the inclusion of a post-peak softening yield surface within a constitutive model is relatively simple to implement at element level, it can lead to complications when used within boundary value problems. Significant post-peak softening is difficult to deal with in standard FEA and can lead to convergence issues and increasingly mesh-dependent results. In addition, as discussed in Section 2 and by Grammatikopoulou et al. (2017) such models are in some instances not practical for design FEA across large wind farm sites due to lengthy parameter calibration procedures and computational constraints (i.e. extensive analysis times and convergence issues).

Therefore, based on the above discussion, the Simple Dilational Sand (SDS) model was developed and implemented within Abaqus and Plaxis as a practical robust constitutive model for capturing the response of dense sand in undrained to partially drained conditions. The SDS model was developed specifically for the Front End Engineering Design (FEED) of suction bucket foundations at the Hornsea One offshore wind farm, looking at the response of the foundations in dense sand under different loading rates.

4.2 Paper 1

An overview of the SDS model is presented in Paper 1 titled, *A practical constitutive model for offshore foundation problems involving dense sands in partially drained to undrained conditions*. The paper was published in the peer-reviewed 8th International Offshore Site Investigation and Geotechnics (OSIG) Conference 2017.

Although not included in the paper or in the current study, the implemented SDS model was successfully used as part of the Hornsea One offshore wind farm suction bucket FEED feasibility study in which a series of fully coupled flow-deformation FEA simulations in Abaqus were performed. The 3D FEA considered several different realistic storm load histories, with an average tension load, to review the potential for drainage-induced upward 'ratcheting' of the bucket foundations. Although the results are not presented in this study, it is promising to note that the model proved to be very numerically robust (i.e. no significant convergence issues) for the suction bucket design analysis run in Abaqus, even more so than the built-in simple Mohr-Coulomb (MC) model, making it particularly suitable for industry use at early design stages. It should be noted that the cyclic loading analysis performed using the SDS model was early stage engineering analysis (as opposed to detailed design analysis) intended to provide indicative results to review the risk associated with upward ratcheting of the buckets caused primarily by the dissipation of negative excess pore pressure. It is therefore important to note that the model in its current form is not suitable for predicting the fully undrained or fully drained stress-strain cyclic response of sand.

4.2.1 Authorship

The contribution of the DEng candidate to this paper was approximately 80%. He implemented the constitutive model, performed all the FEA and prepared the paper. The other authors guided the work and reviewed the paper.

A PRACTICAL CONSTITUTIVE MODEL FOR OFFSHORE FOUNDATION PROBLEMS INVOLVING DENSE SANDS IN PARTIALLY DRAINED TO UNDRAINED CONDITIONS

S Whyte
University of Oxford, Oxford, UK and Fugro GB Marine Limited, Wallingford, UK
M Rattley
Fugro GB Marine Limited, Wallingford, UK
CE Erbrich
Fugro Advanced Geomechanics, Perth, Australia
HJ Burd and CM Martin
University of Oxford, Oxford, UK

Abstract
Despite significant advances in constitutive modelling within academia over the last few decades, the resulting advanced models are seldom used by practising engineers, particularly at the initial stages of design, due to their mathematical complexity, potential numerical instabilities, slow runtimes, and the often large number of model parameters required. From a practical perspective, it is therefore important that constitutive models focus on the features of soil behaviour which are most likely to drive the overall behaviour of the specific foundation problem in question, with the aim of keeping the model as simple as possible. In this paper, a simple constitutive model is presented which aims to capture the salient features of the behaviour of dense sand for the analysis of a suction bucket foundation under tension loading. The model was developed for early stage design of a suction bucket in dense sand under rapid loading in which drainage conditions are intermediate between partially drained and undrained. Description of the model calibration procedure is outlined and an example axisymmetric finite element analysis of a suction bucket under tension loading is presented.

1. Introduction

The predictive accuracy of any finite element analysis (FEA) of a geotechnical problem is strongly dependent on the constitutive model(s) used. Despite the high usage of FEA by practising geotechnical engineers within industry projects, the constitutive models commonly used may be non-representative of some fundamental characteristics of soil response, particularly for overconsolidated soils such as those found in parts of the North Sea.

There have been significant advances in constitutive modelling over the last few decades, with a vast number of advanced models proposed from various research groups. However, industry uptake of such models is rare. This may be related to: numerical instabilities, slow runtimes, difficulties in calibration of (often) numerous model parameters, and lack of availability in commercial FEA software packages. Even the transfer of many of these models between academic research groups is rarely feasible given the significant effort required for robust numerical implementation in FEA programs (Kolymbas, 2000). Therefore, there is an industry requirement for relatively simple constitutive models which capture only the most important features of the soil behaviour affecting the specific foundation problem in question. It is often the case that the effort required to capture a large range of soil behaviour will give diminishing returns on the accuracy of model predictions beyond a small number of key parameters.

Accepting that FEA is a necessary component of the geotechnical design process for foundation-critical projects, a hierarchical approach to FEA is recommended for industry analysis. In this approach, a relatively simple FEA model is considered at the start of a design and additional complexity is added as the project develops. This will generally coincide with the availability of more advanced soil laboratory testing. Indeed, the approach allows the input data requirements of the FEA to inform the laboratory test programme. It should be considered that advances in computing power and improvements in automatic scripting capabilities in commercially available FEA packages make constructing models and post-processing the results a faster process; as a result the use of

FEA has become a viable proposition at the early stages of design.

This paper presents a simple and robust constitutive model which was developed and implemented, within a project timescale, for the analysis of a suction bucket in dense sand under short-term tension loading. The proposed application of the constitutive model is toward the early stage of the design process (e.g. at the front end engineering design (FEED) stage), given its relative simplicity. The model provides a basis for consideration of more complex soil behaviour. The model discussed is primarily suited to foundation problems in dense sand in which the behaviour is expected to be intermediate between partially drained and undrained.

2. Axially Loaded Suction Bucket Overview

Suction buckets are an attractive foundation concept for many offshore windfarm developers, since they have the potential to provide significant cost savings and avoid the (often) excessive noise associated with installation of driven piles. The most common option is a monopod foundation system; however, as wind turbines become larger and windfarms move to deeper waters, multi-pod foundation systems are increasingly being considered. The large overturning moment, generated from the thrust at the turbine hub and from the wave action on the tower, causes opposing, "push-pull" tension and compression loads on the foundations of a multi-pod structure. Although multi-pod suction bucket structures can be designed to avoid tension loading under most conditions (Houlsby et al., 2005a) it is typically uneconomical to avoid short periods of tension loading during extreme loading conditions. Additionally, many designers are keen to explore the potential for increased cost savings by designing the suction buckets to resist significant tension loads during short-term loading.

Design codes do not give explicit guidance on the design of suction buckets in tension loading, meaning that code-based calculation methods for slender piles in sand are often used in current practice. Alternatively, design methods proposed specifically for suction buckets (e.g. Houlsby et al., 2005b) can be applied. However, most design approaches for tension loading of suction buckets in sand conservatively assume that the soil will behave in a drained manner and therefore that the maximum tension load cannot exceed the skirt friction of the bucket. This can lead to significant overdesign since, under typical storm loading rates, the behaviour is likely to be intermediate between partially drained and undrained. This state will result in an increased capacity under tension loading due to an increase in the mobilised strength from dilational effects, manifesting as negative excess pore pressure.

Since significant negative excess pore pressures are generated during rapid tension loading of suction buckets in dense sand, the water cavitation pressure is often the limiting factor for the tension capacity in shallow waters (Kelly et al., 2006). However, as windfarms move to deeper waters, the cavitation pressure may cease to govern.

The behaviour of a suction bucket is dependent on numerous factors. These include soil permeability, soil stress-dilatancy response, loading rate and direction, average load during cyclic loading, water depth, and the bucket dimensions. As a result, even for simplified early-stage design, fully coupled consolidation-deformation FEA with a constitutive model that can capture the dilational response of the soil is required.

3. Constitutive Behaviour and Calibration

The soil constitutive model presented, termed the simple dilational sand model, is developed within an elasto-plastic framework in which the yield and plastic potential functions are derived to fit experimentally observed data. The main aim of this work was to develop and implement a versatile constitutive model that was relatively simple and numerically robust, for implementation within complex FEA. The model was to be suitable for early stage design analysis, but have a reasonable predictive capability for the case of a suction bucket under rapid loading, where the behaviour is expected to be partially drained to undrained. An initial version of the model was originally presented by Bye et al. (1995) with a comparison of its prediction in FEA to model testing data for a suction bucket in sand.

The model offers a hierarchical improvement to a standard Mohr-Coulomb (MC) type model for dense sand problems. It is important to note, however, that the model in its current form is not capable of predicting post-peak softening behaviour, as arising in drained conditions due to softening of the yield surface. This feature

could be added to the model; however, in the current work it was not included as the design loading rates to be modelled were expected to cause partially drained to undrained behaviour. Under these conditions, for dense sand at shallow depth, yield surface softening behaviour is not considered to have a significant impact on foundation response. If the soil response was found to be fully drained, or close to fully drained, then careful selection of the most appropriate strength value would be required depending on the region of interest (e.g. strain range of interest).

3.1 Review of Suitability of Familiar Models

It is important that any constitutive model used for the fully coupled consolidation-deformation FEA of a suction bucket under tension loading, even at the initial stage of design, is capable of reasonable predictions of the dilational response of the soil. Most built-in models in commercial FEA software (e.g. Plaxis and Abaqus) are not considered suitable for this purpose.

Typically the MC models implemented in commercial FEA programs, or similar simple models with a pressure dependent yield function, incorporate a plastic potential which has a fixed gradient that is defined by the dilatancy angle (ψ). However, as a result of having a plastic potential with a fixed gradient, the model predicts that the soil will dilate indefinitely at a constant dilation rate, such that a critical state condition will never be reached. This is a particular concern for problems where there is a restriction on volume change. Therefore a model with a fixed dilation angle typically cannot be used for undrained or partially drained foundation analysis. For the hardening soil model (Schanz et al., 1999) the dilatancy response is stress dependent; however, under undrained conditions, for behaviour on the shear surface, the soil will dilate indefinitely which will manifest as negative excess pore pressure. This will result in an infinite undrained shear strength. Similarly, the extended MC model (Doherty & Wood, 2013) is not suitable for such analysis, for the same reason. A dilatancy cutoff can typically be added to these models; however, since this cutoff is specified in terms of void ratio it will not activate during undrained loading.

Commercially available models such as the Modified Capped Drucker Prager model (built-in Abaqus model) and the Modified Cam Clay model (built-in model within Plaxis and Abaqus) are able to predict a critical state condition in undrained conditions. However, these models do not produce an adequate representation of the dilational response of dense sands, and a more versatile stress-dilatancy rule is needed to match observed experimental data.

There are numerous other more sophisticated models, not available as built-in models within commercial FEA software, which could be used to better represent the behaviour of dense sand. However, as discussed in Section 1, these models are typically not considered practical for efficient engineering design. More advanced models could potentially be used during detailed design, assuming they have been implemented robustly in FEA software, to investigate critical areas of foundation response, where appropriate laboratory test data are available to calibrate the model.

3.2 Constitutive Model Overview

The main function of the constitutive model is to link a given strain increment to a stress increment within an FEA calculation. It is convenient to link the increment of stresses to an increment of total strains by a single stiffness matrix termed the elasto-plastic constitutive matrix.

The model yield function presented does not consider hardening or softening, and hence there is no hardening modulus within the elasto-plastic stiffness matrix. Therefore, the main components of the elasto-plastic stiffness matrix are the yield function, the elastic law and the plastic potential function.

3.2.1 Yield function

The yield function is a wedge type pressure dependent surface which is perfectly plastic (i.e. there is no isotropic or kinematic hardening or softening). This avoids some associated issues, such as instability and increased mesh dependency from softening, while still providing a reasonable representation of behaviour under partially drained to undrained conditions. The yield function (F) is:

$$F = q - M_c g(\theta)(p' + d/M_c) \quad (1)$$

where, q, p' and θ are stress invariants (defined in Appendix 1), d is the apparent cohesion in the p'-q space, M_c is the failure stress ratio (q/p') measured from triaxial compression tests and $g(\theta)$ is the function which controls the shape of the yield function in the deviatoric

plane. The $g(\theta)$ function used in this study was originally proposed by Sheng et al. (2000) and is given below:

$$g(\theta) = \left(\frac{2\alpha^4}{1+\alpha^4-(1-\alpha^4)\sin 3\theta}\right)^{\frac{1}{4}} \quad (2)$$

where $\alpha = M_e/M_c$ and M_e is the failure stress ratio (q/p') in triaxial extension. This allows for a high level of versatility in the shape of the yield function, in the deviatoric plane, to fit with experimental data. In the absence of suitable laboratory test data, the value of α can also be defined from a friction angle (ϕ') to approximate the MC failure surface shape by the following equation:

$$\alpha = \frac{3-\sin\phi'}{3+\sin\phi'} \quad (3)$$

The yield function remains convex, and hence valid, only when $\alpha \geq 0.6$ which relates to a friction angle $\phi' \leq 48.59°$.

3.2.2 Elastic Behaviour

The model incorporates a simple hyperelastic formulation as proposed by Houlsby et al. (2005c) which results in a nonlinear elastic stiffness as a power function of the current stresses.

Many elasto-plastic soil models incorporate empirically derived nonlinear elastic functions. However, a hyperelastic formulation, derived from a free energy potential, is preferred since it results in a conservative elastic response which is thermodynamically acceptable. The hyperelastic formulation proposed by Houlsby et al. (2005c) is no more complicated than other stress dependent non-conservative elastic models and, interestingly, as a consequence of the hyperelastic formulation, the model intrinsically predicts stress-induced anisotropic elastic behaviour. The elastic stiffness matrix is given by:

$$D_{ijkl} = p_a\left(\frac{p_0}{p_a}\right)^n\left[\left(nk\frac{\sigma'_{ij}\sigma'_{kl}}{{p_0}^2}\right) + k(1-n)\delta_{ij}\delta_{kl} + 2g(\delta_{ik}\delta_{jl} - \frac{1}{3}\delta_{kl}\delta_{ij})\right] \quad (4)$$

where δ_{ij} is the Kronecker delta and:

$${p_0}^2 = p'^2 + \frac{k(1-n)q^2}{3g} \quad (5)$$

where, k, g and n are experimentally derived constants and p_a is a reference stress, which is set to atmospheric pressure.

3.2.3 Plastic Potential

The plastic potential function (G) used in the model is:

$$G = \sqrt{\frac{1}{A\,{p'}_{cv}}\left({p'}_{cv} - p'\right)^x + q^y} \quad (6)$$

where A, x, y are additional parameters which define the dilational soil response and are calibrated for a particular site-specific soil unit. The parameter ${p'}_{cv}$ is the mean effective stress at which no further dilation occurs, i.e. analogous to the critical state within critical state soil mechanics. The initial value of ${p'}_{cv}$, defined by the user, is dependent on the *in situ* relative density of the soil (i.e. it is dependent on the stress history). Therefore, for a particular soil unit only the value of ${p'}_{cv}$ is changed to reflect a change in relative density, with all other additional plastic potential parameters held constant. A cap surface could be added originating at the p'_{cv} point; however, it was not included here for simplicity.

The versatility of the plastic potential means that the dilational response of the site-specific soil can be matched to experimental data. Therefore, the plastic potential within the model can be calibrated to fit the dilation response as measured in triaxial compression, triaxial extension, or more complex stress controlled tests depending on the expected dominant stress path in the foundation problem being modelled. Selection of the test type for calibration is important, as the stress-dilatancy behaviour of sand can be very different in compression and extension loading. Clearly, in practice it is difficult to determine a dominant stress path as in any non-trivial foundation problem there will be a range of stress paths. A possible adaptation to the model would be to allow the shape of the plastic potential in the deviatoric plane to be altered; however, this would require extensive further experimental investigation, which is likely to be beyond the scope of future industry application.

Within the model the ${p'}_{cv}$ evolution rule is set within $\varepsilon_v^p - p'$ space as a user defined curve with no embedded law. A user defined ${p'}_{cv}$ evolution curve allows for more flexibility in fitting experimental data. This flexibility is ex-

pected to be particularly important for sand, where a very versatile compression law is often required to match experimental data (Sheng et al., 2008). During the initialisation of the state variables within an FEA calculation, the initial plastic volumetric strain (ε_v^p) is determined from the specified input initial p'_{cv} value, reflecting the stress history of the soil, by numerical interpolation between the data points of the user defined curve. The starting value of ε_v^p will be a relatively large positive (i.e. compressive) value and subsequently, during plastic shearing on the yield surface when $p' < p'_{cv}$, there is a progressive development of negative (i.e. dilational) ε_v^p and as this occurs p'_{cv} softens and is updated according to the user defined curve. As p'_{cv} softens the family of plastic potential surfaces changes shape according to equation 6. The zero dilation condition is approached gradually as p' approaches p'_{cv}.

3.3 Numerical Implementation

A key component of nonlinear FEA is the integration of the constitutive relations over a finite strain increment. The stress update procedure implemented within this study follows a substepping explicit approach with automated error control based on the recommendations presented by Sloan et al. (2001). The model was implemented in Abaqus as a UMAT subroutine and in Plaxis as a UDSM.

4. Application of Model

Extensive 3D FEA, using both Abaqus and Plaxis, has been performed by the authors using the simple dilational sand model to assess suction bucket foundation performance under different loading conditions. The subsections below present an example calibration of the model for a typical North Sea site. Some results from axisymmetric FEA, using Plaxis 2D, of a suction bucket under axial loading are also presented.

4.1 Site Conditions and Calibration Overview

A site was selected, which represents typical North Sea soil conditions, for the model calibration and example FEA. The site consists, within the depth of influence for this study, primarily of dense to very dense silty fine to medium sand. The laboratory testing results available represent a typical dataset from a North Sea site investigation in which the testing programme was not specifically tailored to the calibration of a constitutive model. Although not ideal, it is common that FEA is performed for sites where the site investigation and laboratory testing programmes were completed prior to the requirement for FEA being identified. In such cases it may be necessary for the selected constitutive model parameters to be calibrated using the available laboratory data together with previous experience of similar soil behaviour.

The dilational parameters were derived by fitting the plastic potential function to the maximum measured dilation rate from a selection of isotropically consolidated drained (CID) triaxial tests at different initial stress conditions. For this calibration approach it is important that all samples are at a similar initial void ratio and are from the same geological unit with the same min/max void ratios (i.e. same initial relative density). As discussed above, once the dilational parameters are calibrated, the value of p'_{cv} is the only input parameter which is altered for different *in situ* relative densities. Therefore the void ratio is not an input to the model and if the initial *in situ* relative density changes with depth, within the same soil unit, the initial input p'_{cv} should be varied with depth to reflect this.

Consistent with the approach it is recommended that a number of sand samples collected from a large site investigation (e.g. for a proposed windfarm) are batched by geological unit as this provides a more consistent set of data for model calibration, while still representing the average response of the soil unit being considered.

Figure 1 illustrates the calibration of the dilational parameters with measured CID triaxial data for a relative density of approximately 90% (very dense). The stress-dilatancy response from the model is derived from the plastic potential function by taking derivatives with respect to p' and q. For an ideal case, constant p' stress probing triaxial tests at a range of confining pressures would allow the lower stress range to be explored in more detail. Additionally, very small elastic unload-reload loops performed during triaxial shearing would allow better quantification of plastic strain development. However, such testing is not routinely performed and was not available for the site considered as part of this study. In the absence of an optimum site-specific testing dataset, the dilation rate versus mean effective stress trend proposed by Bolton (1986) and refined for low confining stresses by Chakraborty and Salgado (2010) can be used in conjunction with availa-

ble test data from similar sites to assist with calibration of the dilational parameters.

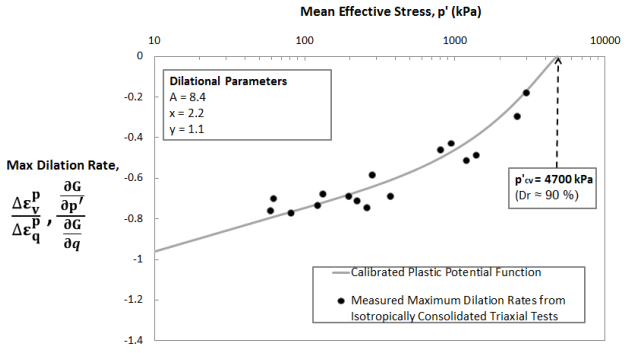

Figure 1: Dilational Response Calibration

The p'_{cv} evolution trend was determined from reviewing the void ratio at critical state curve, as measured from the available site-specific CID triaxial data, and using it to specify a user defined curve in $\varepsilon_v^p - p'$ space consistent with observations from a database of similar dense North Sea sand. If limited data are available, a general assumption on the shape of the p'_{cv} evolution trend could be developed based on a simple rule, as is done in most critical state models. The calibrated model parameters are presented in Table 1.

Following calibration of the model, the predictive performance was reviewed in comparison to a selection of individual tests. The volumetric response predictions of the model compared reasonably well to a selection of CID triaxial tests performed at the same initial relative density (90%) with different initial confining pressures (Figure 2). For this case the input p'_{cv} value was set as 4700 kPa with an initial ε_v^p value of 0.066, which was automatically initialised from the user defined p'_{cv} evolution curve (Table 1). As discussed, if soil from the same geological unit (with the same min/max densities) was tested at a different initial void ratio, only the initial p'_{cv} value would have to be altered.

Table 1: Calibrated Soil Parameters for North Sea Site

	Parameter	Value
Hyperelastic Parameters	g	125
	k	160
	n	0.3
Yield Function Parameters	M_c	1.5
	M_e	1.2
	d	1 kPa
Plastic Potential - Dilational Parameters	A	8.4
	x	2.2
	y	1.1

	p'_{cv}	4700 kPa
	p'_{cv} (kPa)	ε_v^p
p'_{cv} Evolution Curve	1	0
	10	0.008
	100	0.017
	200	0.019
	400	0.022
	1000	0.025
	2000	0.028
	3000	0.030
	4000	0.039
	4500	0.056
Initial Conditions	**4700**	**0.066**
	5000	0.080
	6000	0.122

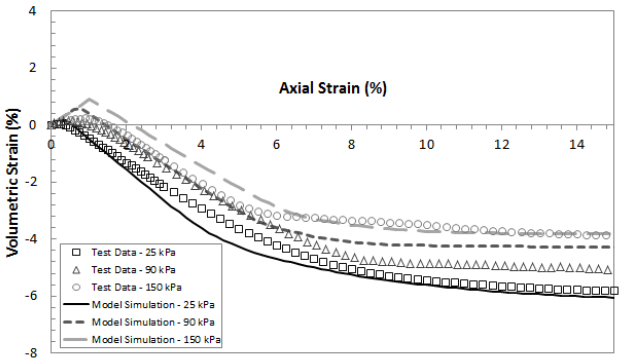

Figure 2: Drained Triaxial Test Simulations and Test Data

It was important to review the performance of the model under both undrained and drained conditions since it was used for fully coupled consolidation-deformation FEA in which the drainage condition of the soil varied during loading. In Figure 3 the undrained shear strength (s_u) profile predicted by the model, as calibrated to triaxial test data at different confining stresses, is compared to site-specific undrained laboratory test data. Unfortunately, as is common, few undrained tests were available for the sand at the site and therefore the s_u profile estimated from the measured cone resistance (q_c) is also presented in Figure 3 for comparison. The relationship used to determine s_u from q_c (Equation 7) is based on undrained testing from the Fugro database for similar North Sea sands and some site-specific data:

$$\frac{s_u}{\sigma'_v} = a\left(\frac{q_c}{\sigma'_v}\right)^b \quad (7)$$

where a and b are the database empirical constants.

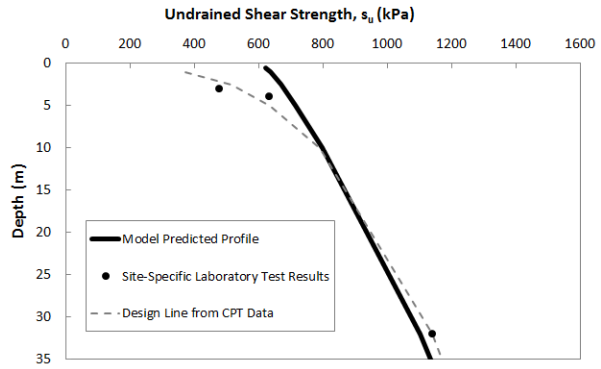

Figure 3: Undrained Shear Strength Profile

4.2 Example Suction Bucket FEA

Example axisymmetric consolidation-deformation FEA of a single suction bucket foundation from a multi-pod substructure for a wind turbine are presented in Figure 4. The analyses have been performed using the simple dilational sand model discussed above and the calibrated parameters for a typical North Sea site (Section 4.1). Table 2 presents additional properties used in the FEA.

Table 2: Additional FEA Model Properties

Description	Value	Units
Bucket radius	5.0	m
Bucket height	5.0	m
FEA model lateral extent	100	m
FEA model vertical extent	50	m
Permeability	$5x10^{-4}$	m/s
Soil-steel friction angle	26	°
Lateral earth pressure coefficient	1.0	-
Water depth	55.0	m

In the FEA model, the soil was assumed to be fully bonded to the base of the suction bucket. A number of authors have proposed the use of a thin layer (e.g. 10 mm) of water elements between the soil and the base of the suction bucket (e.g. Mana et al., 2014; Achmus and Thieken, 2014). This was not included in this analysis; however, it should be noted that the mean effective stress predicted is very low in the small area near the base of the suction bucket, hence the stiffness predicted is likely to be very low in this zone. Additionally, zero-thickness interface elements are used on the inside and outside of the skirt wall together with a Mohr-Coulomb model for the interface strength prescribing a friction angle of 26°, dilation angle of 0° and cohesion of 0 kPa.

Monotonic pull-out displacement controlled analyses were performed with several different velocities. Peak load cycle analysis was also performed. Two load cycles with a period of 8 seconds, a crest of +21 MN, a trough of –19 MN and an average tension load of +1.0 MN, were applied. This represents a peak vertical load cycle within a typical storm history for an offshore wind turbine supported by a multi-pod substructure.

Figure 4 presents the load-displacement response of the example suction bucket under different loading conditions. Most of the pull-out results presented in Figure 4 have not reached the ultimate bearing capacity; however, as expected, and as presented by several other authors (e.g. Achmus and Thieken, 2014) the load-bearing behaviour observed is significantly affected by the pull-out velocity.

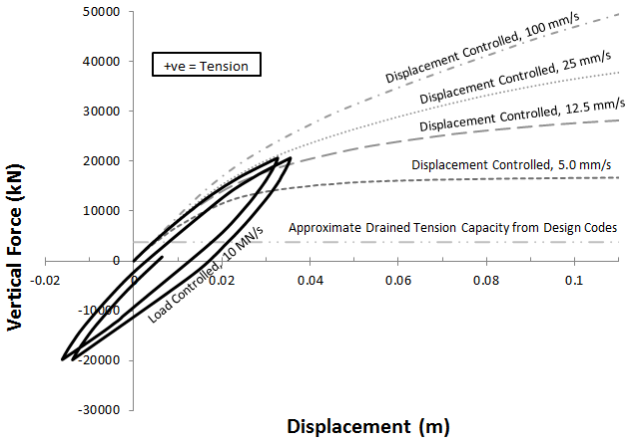

Figure 4: Suction Bucket FEA Results

At pull-out velocities greater than 100 mm/s, only minor differences in the load-displacement response were observed, indicating the 100 mm/s pull-out rate is behaving close to fully undrained. As the pull-out rate is reduced, partial drainage of the soil occurs during loading, resulting in a concurrent reduction in capacity. The response would be similarly affected by altering the permeability of the soil, while keeping the pull-out velocity constant.

The example peak load cycles show a variable partially drained to fully undrained behaviour. The foundation can clearly resist the load from a peak storm load cycle, under the loading rate prescribed, as it is well below the maximum bearing capacity. However, it can be seen that there is a net permanent upward displacement following the two cycles. Ultimately such behaviour may lead to the gradual, drainage-induced, upward ratcheting of the foundation out of the ground over the course of a full storm history. A lower stiffness response is observed for tension loading in comparison to compression loading during the loading cycles. Addi-

tionally, it was observed that during compressive loading a high mean effective stress developed on the inside of the skirt, whereas during tension loading a high mean effective stress developed on the outside of the skirt, with a typical stress bulb shape developing below the skirt tip in both cases (Figure 5).

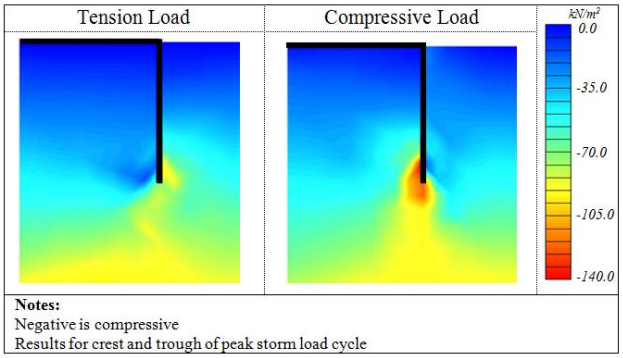

Figure 5: Mean Effective Stress for Peak Storm Cycle

Similar analyses in 3D were performed for a single suction bucket footing of a multi-pod structure considering a full storm history and two-component horizontal loads. At the levels investigated, these analyses showed that the horizontal loads had only a minor influence on the axial ratcheting displacement of the bucket under partially drained conditions. Therefore, an axisymmetric model considering only the vertical loading from a storm history may be considered sufficient to capture the partially drained ratcheting behaviour. The ratcheting response predicted is due to the change in dilational response and excess pore pressures predicted during cyclic loading. The simple dilational sand model is not capable of predicting any drained plastic strain accumulation from cyclic loading and hence it is not suitable for simulating long term cyclic ratcheting effects. However, drainage-induced upward ratcheting of the buckets during a storm is considered to be a key consideration in design.

5. Conclusions

Many designers are keen to explore the potential to design suction buckets in dense sand to resist significant tension loads. However, given the complexity of this problem, relatively complex FEA is required. To ensure that such analysis can be performed efficiently for industry projects, suitable (practical) constitutive models are required.

This paper has presented a simple and robust constitutive model which was developed and implemented to assess the behaviour of a suction bucket foundation under short-term loading. The constitutive model addresses a gap in the range of models provided as standard in commercially available FEA software packages. The model aims to capture only the salient features of dense sand behaviour which are expected to control the predicted foundation behaviour. Since during typical short-term loading of a suction bucket in dense sand, the behaviour is likely to be intermediate between partially drained and undrained, the dilational behaviour of the sand is expected to be a significant response driver.

From some example FEA of a suction bucket in dense sand it has been highlighted that a peak load cycle within a storm loading distribution is likely to cause partially drained to fully undrained soil response, and result in a small amount of permanent upward displacement. This could ultimately lead to the gradual drainage-induced upward ratcheting of the foundation out of the ground during a full storm history. It is recommended that further FEA should be performed considering a full storm history to review the potential for this phenomenon to occur. Additionally, the difference in stiffness response observed in tension and compression should be explored in more detail as part of further work.

6. Acknowledgement

This work was supported by grant EP/L016303/1 for Cranfield University and the University of Oxford, Centre for Doctoral Training in Renewable Energy Marine Structures - REMS (http://www.rems-cdt.ac.uk/) from the UK Engineering and Physical Sciences Research Council (EPSRC).

References

Achmus, M. & Thieken, K., 2014. Numerical simulation of the tensile resistance of suction buckets in sand. Twenty-fourth International Ocean and Polar Engineering Conference, 3(4), 475–483.

Bolton, M.D., 1986. The strength and dilatancy of sands. Géotechnique, 36(1), 65–78.

Bye, A., Erbrich, C., Rognlien, B. & Tjelta, T.I., 1995. Geotechnical Design of Bucket Foundations. Offshore Technology Conference 1995 – Houston, Texas, 1-4 May 2006, Paper OTC 7793.

Chakraborty, T. & Salgado, R., 2010. Dilatancy and shear strength of sand at low confining pressures. Journal of Geotechnical and Geoenvironmental Engineering, 136(3), 527–553.

Doherty, J.P. & Wood, D.M., 2013. An extended Mohr–Coulomb (EMC) model for predicting the settlement of shallow foundations on sand. Géotechnique, 63(8), 661–673.

Houlsby, G.T., Ibsen, L. & Byrne, B.W., 2005a. Suction caissons for wind turbines. Frontiers in Offshore Geotechnics: ISFOG 2005, 75–94.

Houlsby, G.T., Kelly, R.B. & Byrne, B.W., 2005b. The tensile capacity of suction caissons in sand under rapid loading. Frontiers in Offshore Geotechnics: ISFOG 2005, 405–410.

Houlsby, G.T., Amorosi, A. & Rojas, E., 2005c. Elastic moduli of soils dependent on pressure: a hyperelastic formulation. Géotechnique, 55(5), 383–392.

Kelly, R.B., Byrne, B.W. & Houlsby, G.T., 2006. Transient vertical loading of model suction caissons in a pressure chamber. Géotechnique, 56(10), 665–675.

Kolymbas, D., 2000. Constitutive modelling of granular materials, 1st ed. Berlin: Springer.

Mana, D.S.K., Gourvenec, S. & Randolph, M.F., 2014. Numerical modelling of seepage beneath skirted foundations subjected to vertical uplift. Computers and Geotechnics, 55, 150–157.

Plaxis, 2016. Material Models Manual. R. B. J. Brinkgreve, S. Kumarswamy, & W. M. Swolfs, eds., Delft, Netherlands: Plaxis bv.

Schanz, T., Vermeer, P.A. & Bonnier, P.G., 2000. The Hardening Soil model – formulation and verification. Beyond 2000 in Computational Geotechnics – 10 Years of Plaxis. Amsterdam: Balkema, 281–296.

Sheng, D., Sloan, S.W. & Yu, H.S., 2000. Aspects of finite element implementation of critical state models. Computational Mechanics, 26(2), 185–196.

Sheng, D., Yao, Y. & Carter, J.P., 2008. A volume–stress model for sands under isotropic and critical stress states. Canadian Geotechnical Journal, 45(11), 1639–1645.

Sloan, S.W., Abbo, A.J. & Sheng, D., 2001. Refined explicit integration of elastoplastic models with automatic error control. Engineering Computations, 18(1/2), 121–194.

Appendix 1 - Stress Invariants:

The stress invariants are given by:

$$p' = \frac{(\sigma'_{11} + \sigma'_{22} + \sigma'_{33})}{3}$$

$$q = \sqrt{3 J_2}$$

$$\theta = \frac{1}{3}\sin^{-1}\left(-\frac{3\sqrt{3}}{2}\frac{J_3}{J_2^{3/2}}\right)$$

where:

$$J_2 = \frac{1}{2} s_{ij} s_{ji}$$

$$J_3 = \det(s_{ij})$$

$$s_{ij} = \sigma'_{ij} - p'\delta_{ij}$$

4.3 Supplementary Information to Paper 1

The following sub-sections outline additional information not included within Paper 1, which presented an overview of the formulation, implementation and use of the SDS model. The SDS model presented in Paper 1 included a stress-dependent hyperelasticity model but did not include strain-dependent elasticity within the yield surface. Therefore, an additional version of the model, termed the Fugro Dilational Model (FDM) is presented which includes stress- and strain-dependent hypoelasticity within the yield surface.

4.3.1 Incorporation of Strain-Dependent Elasticity

It is well established that the stress-strain response of soil is highly nonlinear at small strains. For monotonic loading, the variation of tangent and secant shear modulus (G_{tan} and G_{sec}) with the logarithm of triaxial deviatoric strain (ε_q) typically follows an S-shaped curve with the small-strain shear modulus (G_0) representing a plateau at very small shear strains. Therefore, for cases where the stiffness-strain response within the yield surface is of significant importance for the boundary value problem being modelled, it is considered necessary to also include a strain-dependent elastic G_{tan}. This is considered to be of particular importance for certain design states when considering offshore wind turbine foundations in which the stiffness response at small strain levels can be important when considering typical operational load levels for fatigue and serviceability limit states (Kallehave et al., 2015; Arany et al., 2017; OWA, 2019). The inclusion of a strain-dependent elastic rule within single yield surface constitutive models has been proposed by many authors as a practical approach when performing FEA of offshore wind turbine foundations (e.g. Schroeder et al., 2015; Zdravković et al., 2019).

An additional version of the SDS model that included strain-dependent elastic stiffness within the yield surface, termed the FDM, was therefore developed and implemented for use in Plaxis and Abaqus.

The FDM incorporates an isotropic elastic stiffness matrix ($\boldsymbol{D}_e$) which replaces the hyperelastic formulation presented in the SDS model (i.e. Equation 4 in Paper 1). The G_{tan} used to form $\boldsymbol{D}_e$ in the FDM, is given by the following hyperbolic expression, described by Measham et al. (2014) and Zdravković et al. (2019):

$$G_{tan} = \frac{(fe_1 - e_0)^2}{1 + e_0} \, G_{ref} \; p'^{n1} \left[R_{Gmin} + \frac{1 - R_{Gmin}}{1 + \left(\frac{E_q}{a}\right)^b} \right] \tag{4.1}$$

where fe_1, G_{ref} and $n1$ are input parameters which are calibrated to match the measured G_0 test data (e.g. from bender element tests and in situ measurements), a and b are input parameters which control the rate of G_{tan} degradation with von Mises equivalent strain (E_q), finally R_{Gmin} then defines the minimum value of G_{tan}/G_0 that can be achieved (i.e. a stiffness degradation cap). Note, E_q is equal to ε_q under triaxial conditions (see Section 3). To complete $\boldsymbol{D}_e$ the tangent bulk modulus, K_{tan}, is given by,

$$K_{tan} = G_{tan} \, \frac{2(1 + \nu)}{3(1 - 2\nu)} \tag{4.2}$$

where ν is the Poisson's ratio. Within Equation 4.1 the accumulated E_q ($= \sum \Delta E_q$) is used as opposed to the current value of E_q. As discussed by Potts and Zdravković (1999) the use of the current E_q value is only suitable for simple strain paths typically observed in laboratory tests (i.e. straight strain paths in the deviatoric plane) and therefore the accumulated E_q should be used if complex strain paths are expected. Measham et al. (2014) also showed this by presenting numerical simulations of a deep excavation in which strain-dependent elastic models were used, which incorporated the current strain and the accumulated strain methods of stiffness degradation. The numerical analysis results presented by Measham et al. (2014) highlighted that use of the current strain to control the stiffness degradation can result in an unconservative prediction. It should be noted that the model discussed above is only applicable for monotonic loading. If cyclic loading was to be considered, additional rules would have to be incorporated within the elastic stiffness degradation model (e.g. Taborda, 2011).

As shown in Section 3, the $\boldsymbol{D}_e$ is used to form the elastoplastic stiffness matrix ($\boldsymbol{D}_{ep}$). Although in many cases the $\boldsymbol{D}_e$ used to form the $\boldsymbol{D}_{ep}$ typically has minimal effect on the overall response under elastoplastic loading (i.e. loading on the yield surface), this is not true for all cases. For example, when considering undrained loading it can be shown that the K used to form $\boldsymbol{D}_e$ can have a significant effect on the stress-dilatancy response. The plastic dilatancy under drained triaxial conditions ($D_{drained}$) is calculated by,

$$D_{drained} = \frac{d\varepsilon_v^p}{d\varepsilon_q^p} \approx \frac{\delta\varepsilon_v - \delta\varepsilon_v^e}{\delta\varepsilon_q - \delta\varepsilon_q^e} \tag{4.3}$$

and the plastic dilatancy under undrained triaxial conditions ($D_{undrained}$) can then be calculated by,

$$D_{undrained} \approx \frac{-\frac{\delta p'}{K}}{\delta\varepsilon_q - \frac{\delta q}{3G}} \tag{4.4}$$

where G and K define the assumed elastic shear and bulk stiffness used to determine the increment in elastic deviatoric strain ($\delta\varepsilon_q^e$) and volumetric strain ($\delta\varepsilon_v^e$) respectively. One option is to use the undegraded $\boldsymbol{D}_e$ when forming the $\boldsymbol{D}_{ep}$ i.e. $\boldsymbol{D}_e$ based on the small-strain shear modulus (G_0) and bulk modulus (K_0).

Figure 4.3 shows a comparison of the stress-dilatancy response from undrained and drained triaxial tests performed on clean Ottawa sand specimens by Loukidis and Salgado (2009), within which the plastic dilatancy was calculated using G_0 and K_0 to determine the elastic strains. Figure 4.3 shows that there is a significant difference between the calculated stress-dilatancy response in undrained and drained triaxial shearing. In part to circumvent this issue Loukidis and Salgado (2009) proposed to calibrate the degradation rule for the elastic G and K to ensure the $D_{undrained} \approx D_{drained}$ within their bounding surface sand model.

Regardless of the approach adopted to determine the elastic G and K it is clearly not acceptable for design analysis to use G_0 and K_0 within the $\boldsymbol{D}_e$ to form the $\boldsymbol{D}_{ep}$ as it is likely to be unconservative for foundation design in a dense sand in which unrealistically high mobilisation rates of the negative excess pore pressure would be predicted, which in turn would result in a stiffer response. Therefore it is proposed to introduce the additional parameter E_{fact} to directly alter the elastic G and K used in the $\boldsymbol{D}_e$ when forming the $\boldsymbol{D}_{ep}$. This approach allows the $\boldsymbol{D}_e$ within yield surface to be controlled by Equations 4.1 and 4.2, and as such a realistic stress-strain response can be modelled; however, importantly an altered $\boldsymbol{D}_e$ is then used to form the $\boldsymbol{D}_{ep}$, during elastoplastic loading, to ensure the dilatancy response is consistent in both undrained and drained shearing. Therefore, when forming the $\boldsymbol{D}_{ep}$ the following equation is used, in combination with Equation 4.2, to define the shear modulus within the $\boldsymbol{D}_e$ matrix.

$$G = \frac{(f e_1 - e_0)^2}{1 + e_0} \, G_{ref} \; p'^{n1} E_{fact} \qquad 4.5$$

where E_{fact} is a user input parameter which defines the degraded elastic stiffness to use when forming $\boldsymbol{D}_{ep}$. It should be noted this approach is considered to be a conservative assumption for design FEA to avoid unconservative predictions in undrained conditions.

4.3.2 Additional Implementation Considerations

Since the elastic stiffness matrices incorporated within the SDS and FDM models are non-linear it is also necessary to utilise a numerical integration scheme for the elastic strain increments within the yield surface. Similarly to the integration of the elastoplastic increments, the Runga-Kutta-Dormand-Prince integration scheme with automatic error control was used within the yield surface for elastic strain increments, as discussed in Section 3. Figure 4.4 presents triaxial single element simulations of the FDM model with a different number of global strain increment steps ($\Delta\boldsymbol{\varepsilon}$) used for each test. The results, as expected, show the same response, regardless of the global step size used which confirms the implemented integration and yield surface intersection schemes are working effectively.

4.3.3 Analysis of Run Times

The MC model was used as a benchmark model to review the numerical performance of the SDS model, in terms of speed, within the FEA suction bucket example problem presented in Paper 1. The benchmark MC model parameters used are presented in Table 4.1.

Benchmark comparison analysis was performed for the 100 mm/s tension pull-out case presented in Paper 1 to assess the efficiency of the SDS model. Benchmark comparison analysis was performed for the 100 mm/s tension pull-out case in Plaxis. The analyses were all run using an Intel Core I7-4790 with a clock speed of 3.6 GHz. The axisymmetric model (Paper 1) had a mesh consisting of 1,586 15-noded triangular elements. The analysis run times are shown in Table 4.2.

As discussed in Section 3, $\boldsymbol{D}_e$ was used to form the element stiffness matrices for formulation of the overall global stiffness matrix. Run times could potentially be improved by using the $\boldsymbol{D}_{ep}$; however, it was observed, despite this being slightly faster, it led to global convergence issues at an early stage of the analysis. Alternatively, the error tolerances in the stress point algorithm could potentially be relaxed. However, overall the numerical robustness and speed of the implemented model is considered acceptable when compared to the very simplistic elastic-perfectly plastic built-in MC model. When performing FEA within a foundation design environment, the numerical robustness of the model is important, since there are typically short design schedules and as a result the risk of numerical convergence issues or lengthy simulation times causing a delay to the overall project would generally be considered an unacceptable risk.

4.3.4 Cavitation Cut-Off

High negative excess pore pressures can develop when considering a suction bucket under rapid tension loading in dense sand. However, in reality, the absolute pore pressures (u_w) that develop are limited by the cavitation pressure, which is given as $u_c = -100$kPa. The allowable negative excess pressure depends on the water depth (h_w) with the maximum allowable negative excess pore pressure development given by $u_e = u_c - (z + h_w)\,\gamma_w$, where γ_w is the unit weight of water and z is the depth below seafloor. A cavitation cut-off scheme was not considered for the analyses

presented in Paper 1. Applying a cavitation cut-off is not possible as standard in most commercial FEA packages and hence is not applied typically in FEA. However, it should be noted since significant negative excess pore pressures develop during rapid shear loading in dense sand, the water cavitation pressure is often the limiting factor for the capacity in shallow waters when considering large displacements (i.e. ULS design). The application of a cavitation cut-off scheme within FEA is explored in Section 7.

4.4 Conclusions

Many designers are keen to explore the potential to design suction buckets in dense sand to resist significant tension loads. However, given the complexity of this problem, relatively complex FEA is required. To ensure that such analysis can be performed efficiently for industry projects, suitable (practical) constitutive models are required.

This section describes a simple and robust constitutive model which was developed and implemented to assess the behaviour of a suction bucket foundation under short-term loading. The constitutive model, which can be implemented relatively easily, addresses a gap in the range of standard models in commercially available FEA software packages. The model aims to capture only the salient features of dense sand behaviour which are expected to control the predicted foundation behaviour. Since during typical short-term loading of a suction bucket in dense sand, the behaviour is likely to be intermediate between partially drained and undrained, the dilational behaviour of the sand is expected to be a significant foundation response driver.

4.5 Tables

Table 4.1: Mohr Coulomb model parameters used for speed benchmark analysis

Parameter	Value
Friction Angle, φ	37.0°
Dilation Angle, ψ	5.0°
Youngs Modulus, E	50 MPa
Poisson's Ratio, ν'	0.3

Table 4.2: Analysis time comparison for suction bucket under tension loading analysis

Task	CPU Time (seconds)	
	MC model	SDS model
Complete Calculation	182	600
Stress Increment Calculations*	32	280

Notes: MC = Mohr Coulomb; SDS = Simple Dilational Sand (Paper 1); * = Total time for stress update calculations
Analysis is for 100 mm/s pull-out rate presented in Paper 1

4.6 Figures

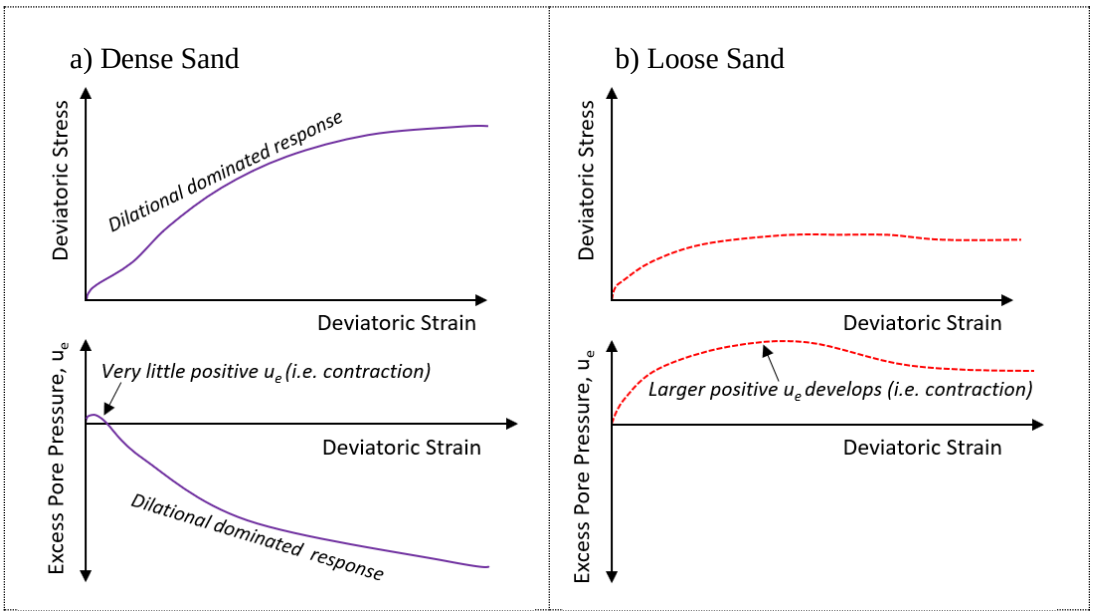

Figure 4.1: Example consolidated undrained triaxial tests on a) dense sand and b) loose sand

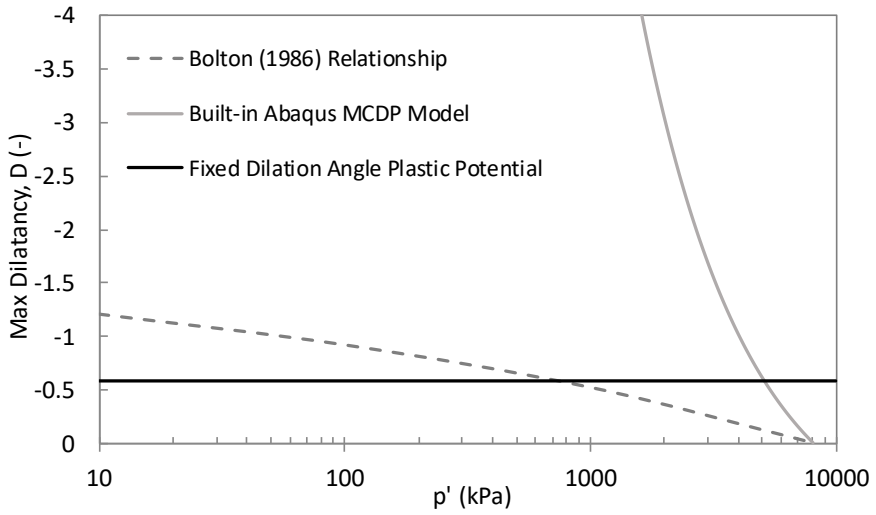

Figure 4.2: Example of stress-dilatancy response of Modified Capped Drucker-Prager and Hardening Soil models with representative dilation angle compared to Bolton (1986) trend for very dense sand

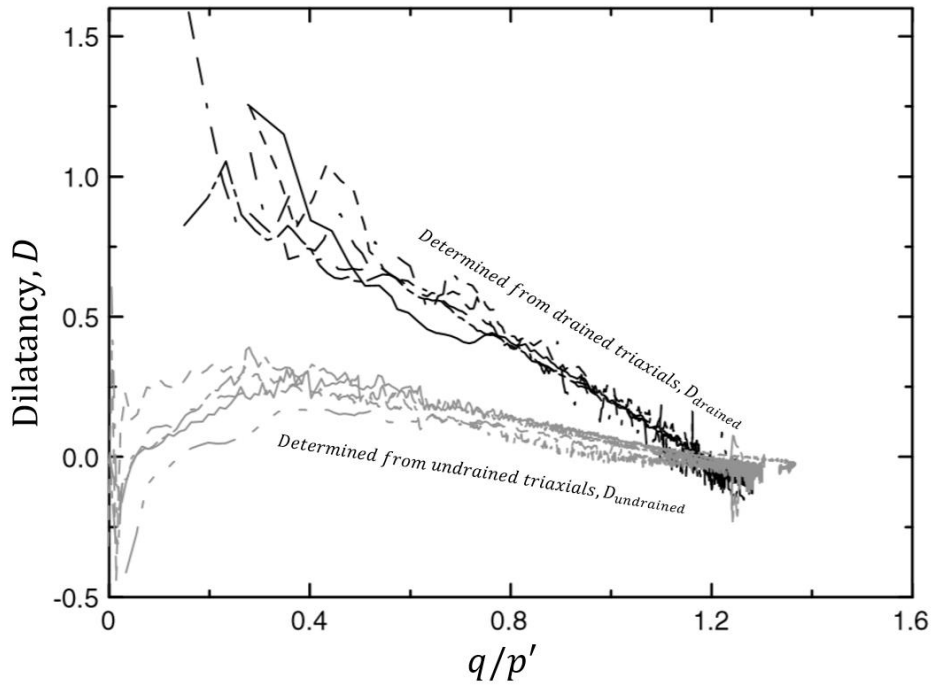

Figure 4.3: Stress–dilatancy curves from drained and undrained triaxial tests performed on clean Ottawa sand specimens (after Loukidis and Salgado, 2009)

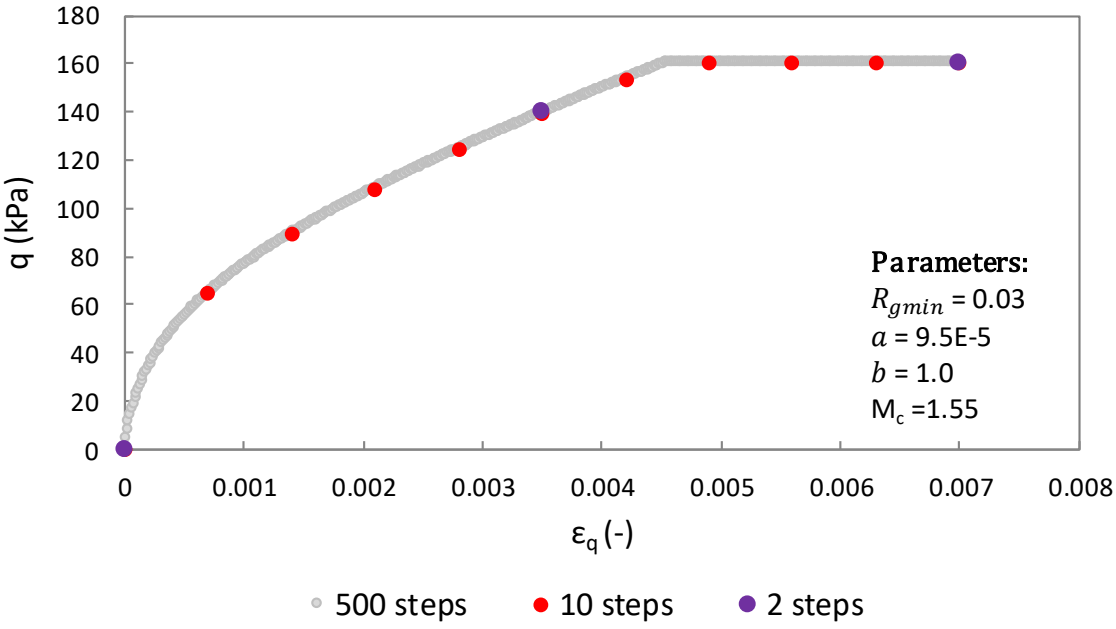

Figure 4.4: Isotropically consolidated drained triaxial test with initial mean effective stress of 50 kPa simulations using the Fugro Dilational Model with different global step sizes

Section 5

DEVELOPMENT, IMPLEMENTATION AND USE OF THE PIMS MODEL FOR CLAY

Contents

5. DEVELOPMENT, IMPLEMENTATION AND USE OF THE PIMS MODEL

5.1 Introduction

This section presents an overview of a developed model, named the Parallel Iwan Multi-Surface (PIMS) model, for the analysis of soil-structure interaction problems involving clay under undrained monotonic and cyclic storm-type loading. The model was implemented in both Plaxis as a user defined soil model (UDSM) and within Abaqus as a user material model (UMAT) subroutine. The model employs a parallel Iwan approach (Iwan, 1966), consisting of multiple elastic-perfectly-plastic micro models. Degradation of stiffness and strength during cyclic loading is incorporated using an empirical cyclic overlay method. This model, together with associated finite element implementation and calibration procedures, has been developed specifically to facilitate robust geotechnical calculations for practical applications relating to offshore foundations under short-term storm loading conditions.

5.2 Paper 2

A detailed description of the PIMS model, together with its application in FEA of a monopile, is given in Paper 2 titled, *Formulation and implementation of a practical multi-surface soil plasticity model*. The paper has been accepted for publication in the journal Computers and Geotechnics.

5.2.1 Authorship

The contribution of the DEng candidate to this paper was approximately 80%. He implemented the constitutive model, performed all the FEA and prepared the paper. The other authors guided the work and reviewed the paper.

Formulation and implementation of a practical multi-surface soil plasticity model

S Whyte[1*+], H J Burd[+] and C M Martin[+], M Rattley[*]

[+]Department of Engineering Science, University of Oxford, Parks Road, Oxford, OX1 3PJ, UK

[*]Fugro GB Marine Limited, Wallingford, Oxfordshire, OX10 9RB, UK

[1]Corresponding author: scott.whyte@eng.ox.ac.uk

ABSTRACT

This paper presents a new constitutive model for clay, for undrained monotonic and cyclic loading, that has been developed specifically for geotechnical design applications. The model employs a parallel Iwan approach, consisting of multiple elastic-perfectly-plastic micro models. Degradation of stiffness and strength during cyclic loading is incorporated using an empirical cyclic overlay method. The theoretical framework and calibration processes for the model are presented. An implementation of the model in a commercial finite element program is then described; this implementation is demonstrated via 3D finite element analyses of example offshore monopile foundations subjected to monotonic and cyclic lateral loading.

Keywords: Undrained clay, Monopile, Offshore foundation, Cyclic loading, Constitutive model, Parallel Iwan model

1. INTRODUCTION

Various advanced constitutive models have been proposed to capture the behaviour of clay for monotonic and cyclic loading. MIT-E3 (Whittle and Kavvadas, 1994), 3SKH (Stallebrass and Taylor, 1997), SANICLAY (Dafalias et al., 2006) and B-SCLAY1S (Sivasithamparam, 2012) are examples of sophisticated effective stress constitutive models that can replicate many of the key trends observed in the monotonic and cyclic response of clay. However, uptake of such models by practising geotechnical engineers has remained low. It is considered that this is due to the inherent complexity of effective stress models of this sort, and also because the model parameters are often difficult to calibrate using soil data acquired in typical geotechnical site investigations. For example, the undrained shear strength (s_u) is not a direct input for such models; it depends on various other parameters and model features, such as: the assumed coefficient of earth pressure at rest (K_0), the overconsolidation ratio (OCR), the stress-dilatancy response, the initial void ratio, the critical state friction angle and, where relevant, approaches employed to model anisotropy and destructuration. This is a significant disadvantage for analyses involving short-term loading of clays, for which prescribed undrained shear strength profiles are a preferred input.

The analysis of offshore monopile foundations under undrained cyclic lateral loading is a design application where three-dimensional (3D) finite element analysis (FEA) can be usefully applied in practice. Although examples of such cyclic analyses can be found in the research literature (e.g. Corciulo et al., 2017) these analyses are typically limited to a relatively small number of cycles. Possible reasons for this include the prevalence of numerical convergence issues and lengthy run times, particularly when effective stress models are used. For example, Haiderali et al. (2015) used a subloading-type effective stress constitutive model to perform fully coupled flow-deformation 3D FEA of a laterally loaded monopile in clay, but only 12 cycles of relatively low amplitude loading could be applied because of the high computational cost.

In design situations involving short-term loading of a foundation embedded in a clay soil, total stress constitutive models are an attractive option for use in FEA, as an alternative to effective stress approaches. Total stress models provide a means of specifying undrained shear strength as a model input parameter. Additionally, they tend to be simpler to implement, faster to compute and more stable than advanced effective stress models. However, there are few examples in the literature of total stress models that can realistically capture the salient features of the response of undrained clay under both monotonic and cyclic loading. For monotonic loading, a simple isotropic hardening Tresca or von Mises model, typically available as a standard built-in model in commercial FEA codes, is a popular choice for practising engineers. More advanced total stress models such as NGI-ADP (Grimstad et al., 2012) and AUS (Kouretzis et al., 2017) offer higher fidelity predictions of the monotonic stress-strain response, but they are not suitable for capturing the hysteretic unload-reload response, or any strength and stiffness changes that may develop during cyclic loading.

From a practical design perspective, there is therefore an ongoing need for total stress constitutive models that are suitable for simulating monotonic and cyclic loading of undrained clay. Such models should ideally (i) be straightforward to implement (ii) have parameters that can be calibrated using data from typical geotechnical site investigations (iii) facilitate efficient and stable computations of boundary value problems using 3D FEA. This paper presents a model, termed the 'Parallel Iwan Multi-Surface' (PIMS) model, that offers these characteristics. It is developed as a hierarchical model in which cyclic behaviour can be activated or deactivated depending on the analysis being performed.

The current model was primarily developed for implementation in a FEA program to predict the performance of offshore foundations in clay soils during, and immediately after, short-term storm-type cyclic loading events. The model is capable of capturing (i) nonlinear stiffness response from very small to large strains for different stress paths (ii) different undrained shear strengths for

different stress paths (iii) effects of recent stress history (iv) hysteretic unload-reload response (v) cyclic degradation of stiffness and strength. Rate effects typically also need to be considered when calibrating and using a constitutive model for clay for cyclic loading. In the current model, rate effects are included in a rudimentary way, by scaling the model parameters to develop a family of rate-corrected normalised stress-strain curves.

The paper begins with an overview of the important features of the behaviour of undrained clay under monotonic and cyclic loading, as observed in laboratory testing. The theoretical framework and implementation process for the proposed constitutive model are then provided, together with an overview of the parameter calibration procedure. The model is implemented in a commercial finite element program (PLAXIS) and this implementation is demonstrated via a case study based on recently published pile load tests in overconsolidated clay, for monotonic lateral loading. Finally, calibration of the model to cyclic laboratory test data is presented, together with an example 3D FEA of a large-diameter offshore monopile under cyclic lateral loading, for a representative storm loading history.

2. EXPERIMENTAL AND MODELLING BACKGROUND

2.1 Experimental observations

2.1.1 Monotonic behaviour

The pre-failure stress-strain response of soil is highly nonlinear. For monotonic loading of clay, the variation of tangent and secant shear stiffness ($G_{\tan}$ and $G_{\sec}$) with the logarithm of shear strain, γ, typically follows an S-shaped curve (Clayton, 2011; Vardanega and Bolton, 2013) with the small-strain shear modulus (G_0) representing a plateau at very small shear strains ($\gamma < 10^{-5}$). For practical design applications, it is advantageous if constitutive models can be calibrated directly to this stiffness variation curve (referred to as the 'stiffness backbone curve') or the parent stress-strain curve ('stress-strain backbone curve'). It has been shown that these (inter-related) curves are strain rate dependent (e.g. Sheehan et al., 1996; Torisu et al., 2012), and the most

appropriate backbone curve for use in a particular context depends on the loading rate in the problem being modelled. The backbone curve is also known to depend on factors such as structure (i.e. the combined effect of fabric and inter-particle forces), the recent stress history (i.e. stress history in which consolidation, creep and ageing effects are not considered), and the imposed stress path (e.g. Prevost, 1977; Ladd, 1991; Grimstad et al., 2012).

The dependency of the backbone curve on the stress path can be observed by comparing the results of undrained triaxial compression (CUc), undrained triaxial extension (CUe), and undrained direct simple shear (UDSS) laboratory tests on clay samples having the same initial state; the backbone curves for these tests are typically significantly different. Laboratory element test data presented in the literature show that the angle, α, of the major principal stress, σ_1, with respect to the sample axis and the value of the intermediate principal stress ratio, $\zeta = \frac{\sigma_2 - \sigma_3}{\sigma_1 - \sigma_3}$, has a significant effect on the overall mechanical response of clay (e.g. Grimstad et al., 2012). The stress-strain backbone curve, as well as the shear strength, has been shown to be stress path dependent for clay, with a significantly softer response in triaxial extension ($\alpha = 90°, \zeta = 1$) than triaxial compression conditions ($\alpha = 0°, \zeta = 0$).

A comparison of the measured undrained shear strength, s_u, in different types of laboratory test is often cited as a measure of the 'strength anisotropy' of the clay; however, this terminology is potentially misleading when used to describe a general stress path dependency. As noted by Kouretzis et al. (2017), an isotropic model may exhibit different s_u values for triaxial compression and extension tests due to the yield strength in the deviatoric plane being dependent on Lode angle (θ). For example, when the Mohr-Coulomb yield function, or similar, is used in an effective stress model, different strengths in triaxial compression and extension are predicted even though the model is isotropic. The Tresca yield function incorrectly predicts the same undrained strength for all shearing stress paths, but is routinely employed in isotropic total stress models for clay. Additionally, experimentalists have shown (e.g. Callisto and Calabresi, 1998; Nishimura et al.,

2007) that naturally deposited clays often exhibit anisotropic properties caused by their structural fabric arrangement (inherent anisotropy) and current stress conditions (induced anisotropy). Therefore, for a total stress constitutive model, it is desirable to be able to define an isotropic yield surface shape with Lode angle dependency, and to incorporate anisotropy separately, if necessary and if suitable calibration data are available.

2.1.2 Cyclic behaviour

Fig. 1 shows a schematic diagram of an idealised response observed in a symmetrical, strain controlled, 2-way cyclic triaxial test conducted on a sample of undrained clay. This figure employs the conventional triaxial parameters; deviatoric stress, $q = \sigma_a - \sigma_r$, and triaxial shear strain, $\varepsilon_q = \frac{2}{3}(\varepsilon_a - \varepsilon_r)$, where the subscripts a and r denote the axial and radial directions (compression positive) respectively. Initially (Point A), the sample is isotropically consolidated. The sample is then loaded to Point B and a single unload-reload cycle is applied (cycle 1 on Fig. 1). The first cycle secant shear stiffness $G_{sec,1}$ is defined as shown in the figure. Further strain cycles are then applied; Fig. 1 shows the N^{th} cycle. These strain cycles cause the secant shear stiffness to reduce to $G_{sec,N}$, with an associated reduction in strength (compare the 'backbone curve' with the 'cyclically degraded backbone curve' in Fig. 1). In previous studies (e.g. Vucetic and Dobry, 1988; Okur and Ansal, 2007; Andersen, 2015; Wichtmann and Triantafyllidis, 2017); these observed reductions in stiffness and strength during cyclic loading – collectively referred to in this paper as 'cyclic degradation' – were attributed to the combined effect of destructuration and pore pressure accumulation.

Various empirical cyclic models for undrained clay have been developed (e.g. Idriss et al., 1978). These typically link cycle number, N, to a 'degradation factor' that is applied to the loads/stresses to determine a cyclically degraded backbone curve (thus reducing both the stiffness and strength). Although these simple empirical cyclic degradation models have been used extensively by practising geotechnical engineers (e.g. Andersen, 2015), they fail to capture the detailed response

within individual cycles and are applicable only to the stress path for which they have been developed; they therefore may not be suitable for multiaxial cyclic loading. Vucetic and Dobry (1988) showed that using accumulated deviatoric strain, as opposed to cycle number, to control the rate of degradation in the model allows this approach to be applied more generally to different test configurations, and permits empirical cyclic extensions to be implemented within elasto-plastic constitutive models.

The rate of cyclic degradation has been shown to depend on various factors. For example, the degree to which the backbone curve has been mobilised prior to unloading, and the strain amplitude of each cycle, significantly affect the rate of cyclic degradation (e.g. Vucetic and Dobry, 1988; Lefebvre and Pfendler, 1996; Andersen, 2015). Vucetic and Dobry (1988) also showed that the rate of cyclic degradation is influenced by the initial overconsolidation ratio (OCR). The effect of OCR on the rate of cyclic degradation has been discussed by many authors (e.g. Hyde and Ward, 1986; Yasuhara et al., 2003; Thian and Lee, 2017). Additionally, Vucetic (1994) and Mortezaie and Vucetic (2016) showed that below a certain shear strain value, termed the 'cyclic threshold shear strain', cyclic degradation does not occur to any significant degree. The magnitude of the cyclic threshold strain value is typically considered to be unaffected by the previous cyclic loading history.

It has been shown extensively in the literature that the small-strain shear modulus, G_0, is dependent on the current mean effective stress (e.g. Hardin and Black, 1968); G_0 would therefore be expected to reduce during undrained cyclic loading when positive pore pressures accumulate. However, bender element tests performed in undrained cyclic triaxial tests, reported by Gu et al. (2014), on two remoulded clays from eastern China, showed that G_0 degrades significantly more rapidly during cyclic loading than would be expected solely on the basis of a reduction in the effective stresses.

In summary, according to previous experimental studies, the salient features of the undrained cyclic response of saturated clay are:

i. A reduction in secant stiffness and strength with number of cycles (cyclic degradation) occurs, unless the strain amplitude is below a certain threshold value.

ii. The small-strain shear modulus G_0 has also been shown to degrade with number of cycles.

iii. The rate of cyclic degradation depends on the cyclic strain amplitude and the degree to which the backbone curve has been previously mobilised.

iv. The rate of cyclic degradation depends on the OCR.

2.2 Modelling approaches

2.2.1 Multi-surface modelling overview

Total stress constitutive models which only include a single isotropic hardening yield surface (e.g. Grimstad et al., 2012) are not suitable, without applying complex nonlinear elastic rules within the yield surface, for capturing the hysteretic unload-reload response of clay. An elasto-plastic model with linear kinematic hardening can be used to simulate a Masing-type response, although a single kinematic hardening yield surface lacks the resolution required to predict realistic soil behaviour (Houlsby, 1999). A common approach for overcoming such issues is to use a ‘bounding surface’ model, though as discussed by Houlsby (1999), such models must include complex, somewhat arbitrary, mapping rules to control their behaviour and often lack the ability to capture recent stress history effects accurately. Therefore, an elasto-plastic model incorporating multiple yield surfaces is preferred. Multi-surface models are typically implemented using several nested kinematic hardening yield surfaces (e.g. Prevost, 1977; Houlsby, 1999; Elgamal et al., 2003). The individual yield surfaces translate in stress space when they are activated, such that all active yield surfaces are at the same stress condition. Such models can be termed ‘series Mroz-Iwan’ models after the seminal work of Mroz (1967) and Iwan (1967). Despite offering an elegant modelling

approach for simulating a nonlinear hysteretic response, tensorial series Mroz-Iwan models can become complex and implementation can be difficult.

Chiang and Beck (1994), Einav and Collins (2008) and Grimstad et al. (2014) have demonstrated that the use of multi-surface models based on a 'parallel Iwan' approach, as first proposed by Iwan (1966), offers a method that is simpler to develop and implement, while still providing a predictive capability similar to that of the series Mroz-Iwan approach. Iwan (1966) proposed a one-dimensional (1D) model in which a number of spring-slider elements, with different yield strengths and different elastic stiffnesses, are arranged in parallel. The model assumes strain equivalence across all of the spring-slider elements. Following an increment of strain, the resulting stress from the model (termed 'macro stress') is determined from a weighted sum of the individual stresses (termed 'micro stresses') in the spring-slider elements. Fig. 2 illustrates a 1D parallel Iwan model with three spring-slider elements. Virtual experiments performed by Einav and Collins (2008) showed that the parallel Iwan modelling approach has clear micromechanical physical meaning, and the model parameters can be directly related to the statistical distribution of strength in a representative volume of soil.

When the parallel Iwan approach is adopted as the basis of a continuum plasticity model, a set of individual constitutive models, here termed 'micro models', are specified in parallel. Typically, and in the model developed in this paper, each micro model is an elastic-perfectly-plastic model, i.e. with a single stationary yield surface. All of the micro models are subjected to the same strain history, with the macro stress tensor ($\boldsymbol{\sigma}$) calculated as,

$$\boldsymbol{\sigma} = \sum_{i=1}^{n} w_i \, \boldsymbol{\sigma}_{\text{micro}} \tag{1}$$

where n is the number of micro models and w_i is the weight of each micro models' stress tensor, $\boldsymbol{\sigma}_{\text{micro}}$, with the sum of the weights constrained to be unity (i.e. $\sum w_i = 1$). As discussed by Einav and Collins (2008), from a micromechanical perspective it is preferable for all micro models to have the same stiffness and to specify the desired backbone behaviour by employing different

yield strengths and weights for the micro models. In a practical implementation of the model, a choice needs to be made on the number of micro models, n, to be employed. If n is large, then the computer time and storage requirements may become excessive. Alternatively, if a relatively small number of micro models is chosen, then the modelled stress-strain response will not be smooth and therefore unrepresentative of reality. In the current paper, the yield strength of each micro model is specified to increase monotonically with micro model index i.

Fig. 3 illustrates the response of an example parallel Iwan model with four von Mises micro models, for a strain controlled cyclic triaxial test. It is apparent that the stress state of each micro model is different from that of the overall model (the macro stress); indeed the latter may lie outside some of the micro model yield surfaces. It is important to note, however, that the consistency condition is fulfilled for all micro models, i.e. the micro stresses are constrained to remain on their micro yield surfaces during plastic deformation. This example demonstrates how several simple micro models in a parallel Iwan arrangement can produce a Masing-type nonlinear hysteretic response without the need for translating yield surfaces.

A major advantage of using a parallel Iwan approach is that each micro model is implemented in the same manner as any other single surface perfect plasticity model. As a result, any single-surface constitutive model that has been implemented as a user-defined soil model can be extended to a multi-surface model by applying a relatively simple parallel Iwan 'wrapper' code. This is a significant advantage, as despite the benefits of multi-surface models, the complexity of implementation is often considered to be a barrier. The parallel Iwan approach is therefore adopted for the development of the PIMS model presented in this paper.

2.2.2 Cyclic degradation

Incorporating a cyclic degradation overlay within a constitutive model, in which the stiffness and strength are degraded as a function of accumulated deviatoric strain, offers a simple way of capturing cyclic loading behaviour that is consistent with the established cyclic degradation

approach described in Section 2.1.2. Huang and Liu (2015) presented such an approach in which a simple cyclic degradation rule, based on accumulated plastic deviatoric strain, was applied to a kinematic hardening von Mises model and used to perform FEA of cyclic axial loading of piles in clay. A similar approach (although employing the sum of the plastic and elastic deviatoric strains to control the degradation behaviour) is employed in the PIMS model.

Iwan and Cifuentes (1986) extended the parallel Iwan approach to develop a 1D model capable of simulating the degrading hysteretic response of structures subjected to earthquake motions, by including the effects of stiffness and strength degradation. This model incorporated additional deteriorating elastic-plastic elements in parallel with standard elastic-plastic elements. The additional deteriorating elements were similar to the standard (non-degrading) elements, but were set to 'break' when the strain exceeded a prescribed threshold for that element. Once broken, the relevant elements were removed from the model. A similar approach is adopted in the PIMS model. However, rather than the sudden breakage adopted by Iwan and Cifuentes (1986), there is gradual 'breakage' of the micro models, achieved by reducing their weights, based on the accumulation of a deviatoric strain measure during cyclic loading. This allows various detailed features of the soil response to be captured.

3. FORMULATION AND IMPLEMENTATION OF THE PIMS MODEL

This section first presents the formulation of the elastic-perfectly-plastic model that is used for each micro model in the parallel Iwan arrangement. The multi-surface formulation is then explained, followed by the cyclic degradation extension. The adopted sign convention is compression positive.

3.1 Micro model formulation

Since the model is developed for undrained conditions, the yield (f) and plastic potential (g) functions are independent of the mean stress. This form of the plastic potential ensures zero plastic volumetric strain. Linear elasticity based on the small-strain elastic shear modulus G_0, and a

Poisson's ratio of 0.495 is adopted for the elastic component of the model. The yield function for each micro model is,

$$f = \sqrt{\frac{3}{2}\,\mathbf{s} : \mathbf{s}} - m \tag{2}$$

where **s** is the deviatoric stress tensor given by,

$$\mathbf{s} = \boldsymbol{\sigma} - p\,\mathbf{I} \tag{3}$$

in which $\boldsymbol{\sigma}$ is the micro stress tensor, **I** is the second order identity tensor and $p = \frac{1}{3}\mathrm{tr}\,\boldsymbol{\sigma}$. The 'yield strength' m is,

$$m = q_{uc}\,R(\theta) \tag{4}$$

where q_{uc} is the deviator stress yield strength in triaxial compression for the micro model, and $R(\theta)$ is a function that controls the shape of the yield surface in the deviatoric plane. Here the $R(\theta)$ function proposed by Sheng et al. (2000) is used,

$$R(\theta) = \left(\frac{2\beta^4}{1 + \beta^4 + (1 - \beta^4)\sin 3\theta}\right)^{\frac{1}{4}} \tag{5}$$

where the Lode angle θ is,

$$\theta = \frac{1}{3}\sin^{-1}\left(-\frac{3\sqrt{3}}{2}\,\frac{\det \mathbf{s}}{\left(\frac{1}{2}\,\mathbf{s} : \mathbf{s}\right)^{3/2}}\right) \tag{6}$$

The maximum value of $R(\theta)$ is $R = 1$ when $\theta = -30°$ (triaxial compression), and the minimum value is $R = \beta$ when $\theta = +30°$ (triaxial extension). The parameter β is referred to in this paper as 'triaxial extension factor'. The yield function is convex only when $\beta \geq 0.6$. A circular shape in the deviatoric plane is adopted for the plastic potential (i.e. no Lode angle dependency). This is consistent with experimental findings (e.g. Callisto and Calabresi, 1998; Prashant and Penumadu, 2004). The plastic potential function is therefore defined as,

$$g = \sqrt{\mathbf{s} : \mathbf{s}} \tag{7}$$

Three parameters are therefore required to calibrate each micro model, with q_{uc} and β defining the plastic behaviour and G_0 defining the elastic response. The values of q_{uc} and β can be different for each micro model, but the same value of G_0 is applied to all of the micro models.

3.2 Multi-surface extension

For the complete model, a selected number of micro model instances are assembled in a parallel Iwan arrangement. All of the micro models are subjected to the same strain history, and the overall macro stress tensor, $\boldsymbol{\sigma}$, is calculated as a weighted average of the micro model stress tensors, $\boldsymbol{\sigma}_{\mathrm{micro}}$, (Equation (1)). For an infinitesimal increment of strain, $\delta\boldsymbol{\varepsilon}$, the resulting increment of the macro stress, $\delta\boldsymbol{\sigma}$, is,

$$\delta\boldsymbol{\sigma} = \sum_{\mathrm{i}=1}^{n} w_i \ \mathbf{D}^{\mathrm{ep}}\delta\boldsymbol{\varepsilon} \tag{8}$$

where,

$$\mathbf{D}^{\mathrm{ep}} = \mathbf{D}^{\mathrm{e}} - \frac{\mathbf{D}^{\mathrm{e}}\left(\frac{\partial g}{\partial \boldsymbol{\sigma}_{\mathrm{micro}}}\right)\left(\frac{\partial f}{\partial \boldsymbol{\sigma}_{\mathrm{micro}}}\right)^{\mathrm{T}}\mathbf{D}^{\mathrm{e}}}{\left(\frac{\partial f}{\partial \boldsymbol{\sigma}_{\mathrm{micro}}}\right)^{\mathrm{T}}\mathbf{D}^{\mathbf{e}}\left(\frac{\partial g}{\partial \boldsymbol{\sigma}_{\mathrm{micro}}}\right)} \tag{9}$$

and $\boldsymbol{\sigma}_{\mathrm{micro}}$ is the micro stress tensor. The elastic stiffness matrix ($\mathbf{D}^{\mathrm{e}}$) is based on the selected value of G_0 and the prescribed value of Poisson's ratio (0.495 in the current implementation of the model).

In the finite element implementation of the model (described later), the response of the model to a finite strain increment $\Delta\boldsymbol{\varepsilon}$ is determined by integrating Equation (8) using an explicit sub-stepping approach.

The PIMS model formulation described in the current paper is isotropic. The model does not include the influence of inherent anisotropy and it is recognised that this omission may be significant for some natural clays. However, the model can readily be extended to include the influence of inherent anisotropy by using a modified deviatoric stress tensor $\bar{\mathbf{s}}$ to define the yield

and plastic potential functions for all of the micro models, following a similar approach to Prevost (1977), Grimstad et al. (2012) and Kouretzis et al. (2017). In this case, all occurrences of **s** in the definition of the yield surface and plastic potential of each micro model (Section 3.1) are replaced by $\bar{\mathbf{s}}$.

3.3 Cyclic extension

Within the basic parallel Iwan framework described above, an extension to account for cyclic loading is achieved by gradually reducing the weight of each micro model from the onset of cyclic loading by a cyclic degradation factor, d ($d \leq 1$), so that the current weights are dw_i. This extension employs an 'overlay' approach, i.e. only the weights of the micro models are altered, with the underlying elastic-perfectly-plastic micro models functioning as previously described. It is important to note that this could lead to overall softening behaviour causing increased levels of mesh dependency.

The cyclic degradation overlay model is activated only if the current increment of loading is considered to be cyclic; therefore, an important component of the model is the method used to determine if cyclic loading is occurring. The current formulation makes this process relatively straightforward, with specific micro models being tracked to identify whether cyclic degradation should be applied for the current increment of strain. In the current model this is achieved by tracking the yield surfaces of three designated micro models, as described below.

i. One micro model is designated as the 'cyclic threshold surface' ($i = i_{\mathrm{thr}}$). Any cyclic loading that does not cause this model to yield does not cause degradation. The designation of the cyclic threshold surface index does not change during the calculation.
ii. The index of the 'largest currently active surface' ($i = i_{\mathrm{lca}}$) is stored and continually updated during the calculation. A micro model is deemed active if the micro stresses lie on the yield surface (i.e. plastic straining occurring).

iii. The index of a 'memory surface' ($i = i_{\mathrm{mem}}$) is stored and continually updated during the calculation. i_{mem} is the index of the largest micro model that has previously experienced plastic straining.

Cyclic degradation is activated for the current strain increment if $i_{\mathrm{thr}} \leq i_{\mathrm{lca}} < i_{\mathrm{mem}}$. To explain the approach, Fig. 4 shows a schematic of a strain-controlled load-unload-reload loop in a triaxial compression test, applied to a parallel Iwan model with four micro models employing von Mises yield surfaces. In this example, the cyclic threshold micro model is $i_{thr} = 1$. The initial loading stage (Fig. 4a,b) causes no cyclic degradation since the memory surface and the largest currently active surface are the same throughout loading (i.e. $i_{\mathrm{lca}} = i_{\mathrm{mem}}$). At the end of initial loading, $i_{\mathrm{lca}} = i_{\mathrm{mem}} = 3$. During unloading (Fig. 4c,d) and reloading (Fig. 4e,f), i_{mem} is unchanged but i_{lca} is updated, being set to zero as soon as unloading occurs. Therefore, for this example, cyclic degradation occurs during the unloading and reloading stages (except when the stresses lie inside the cyclic threshold surface).

Once the cyclic degradation model has been activated, degradation of stiffness and strength begins to occur; degradation is controlled by a set of cyclic degradation rules. The general approach adopted is consistent with empirical models derived from experimental studies, in which the rate of degradation has been found to depend on the cyclic strain amplitude, the OCR and the degree to which the backbone stress-strain curve has been mobilised prior to any load reversal (e.g. Vucetic and Dobry, 1988; Lefebvre and Pfendler, 1996; Andersen, 2015). Here the control parameter for cyclic degradation is the accumulated value of the von Mises equivalent strain, defined as,

$$E_q = \left(\frac{2}{9}\left[\left(\varepsilon_x - \varepsilon_y\right)^2 + \left(\varepsilon_y - \varepsilon_z\right)^2 + \left(\varepsilon_z - \varepsilon_x\right)^2\right] + \frac{1}{3}\left[\gamma_{xy}^2 + \gamma_{xz}^2 + \gamma_{yz}^2\right]\right)^{1/2} \quad \textbf{(10)}$$

When computing the updated stresses due to the k^{th} increment of von Mises equivalent strain ($\Delta E_{q,k}$), the cyclic degradation factor (d_k) for the current strain increment is determined as:

$$d_k = \left(A\,\Delta E_{q,k} + {E_q}^*\right)^{-a} \quad \textbf{(11)}$$

where A is a parameter and ${E_q}^*$ is:

$$ {E_q}^* = {d_{k-1}}^{-\frac{1}{a}} \quad \textbf{(12)} $$

where d_{k-1} is the cyclic degradation factor for the previous strain increment. At the start of the analysis, the cyclic degradation factor is initialised as $d_0 = 1.0$ (i.e. no degradation), so that ${E_q}^*$ also has an initial value of 1.0. This provides a straightforward practical approach, but it clearly ignores any von Mises equivalent strains that may have developed in in situ soil, due to prior geological processes, or in laboratory test samples, due to sample preparation procedures. The degradation rule employed in the PIMS model employs the accumulated total von Mises equivalent strain as the control parameter. An alternative approach would be to relate the degradation to the accumulated plastic strain. The current, empirical, approach is preferred, however, on the basis that it provides a more straightforward way of calibrating the model to laboratory test data.

The value of a in Equations (11) and (12) is determined by the micro stress conditions in the 'outer' micro model (i.e. for $i = n$) as,

$$ a = \frac{r}{\mathrm{OCR}^c}\left(\frac{q_{max,n}}{q_{uc,n}}\right)^b \quad \textbf{(13)} $$

where b, c, r are parameters, $q_{uc,n}$ is the outer micro model's yield surface size parameter, and $q_{max,n}$ is the maximum mobilised micro deviatoric stress value that has previously been experienced by the outer micro model of the quantity,

$$ q_n = \sqrt{\frac{3}{2}\,\mathbf{s_n} : \mathbf{s_n}} \quad \textbf{(13b)} $$

where $\mathbf{s_n}$ is the deviatoric stress tensor for the outer micro model. This modelling approach means that the rate of degradation depends on the amplitude of the cyclic strain and also on the degree to which the backbone curve has been mobilised prior to unloading.

The exponent c in Equation (13) allows the rate of cyclic degradation to depend on the initial overconsolidation ratio, OCR (e.g. Vucetic and Dobry, 1988; Yasuhara et al., 2003; Thian and Lee, 2017). In the examples presented later in this paper, however, this dependence on OCR is excluded by setting $c = 0$. This aspect of the model is therefore not considered in the examples presented later.

Fig. 5 provides an illustration of the adopted cyclic degradation modelling approach, for an arbitrary parameter set. Three packets of two-way cyclic strain-controlled loading are applied, for triaxial test conditions, as shown in Fig. 5a. Each cycle is applied in four strain increments. The dashed coloured lines (i.e. short broken segments) in Fig. 5a indicate cases when cyclic degradation does *not* occur in the model (since in these cases $i_{mem} = l_{lca}$); conversely, the solid lines indicate when cyclic degradation is active. The evolution of the degradation factor, d, with strain increment number, k, is shown in Fig. 5b. It can be seen that when the amplitude of cyclic loading changes (i.e. at increments 41 and 82) the degradation rate also changes due to the updated value of the exponent a in Equation (11). The use of $E_q{}^*$, (Equation (12), ensures that there is no sudden 'jump' in degradation factor when the cyclic strain amplitude changes.

The value of d_k calculated from Equation (11) is applied equally to the weights of the micro models,

$$w_{i,k} = d_k w_i \quad \textbf{(14)}$$

As the weight $w_{i,k}$ of each micro model is reduced due to cyclic degradation, the overall sum of the weights reduces such that $\sum w_{i,k} \neq 1$. Conceptually it is considered that the degraded portion of the weight, $w_d = 1.0 - d_k$, is moved to a notional micro model with zero stiffness and strength (analogous to element breakage in the 1D model of Iwan and Cifuentes (1986)).

The various components of the model (i.e. the dependence on cyclic amplitude, backbone mobilisation and OCR, and the inclusion of a cyclic threshold) allow established experimental trends to be captured.

The cyclic degradation component of the model, discussed above, will result in an accumulation of strain during a stress-controlled cyclic simulation; however, in its current form the model does not predict the accumulation of strain during cyclic loading without degradation (i.e. ratcheting type behaviour) at element level. Although this is a limitation of the model, it should be noted that purely ratcheting type behaviour with no stiffness degradation is not often observed in cyclic laboratory element tests in clay for a low number of cycles (e.g. Vucetic and Dobry, 1988; Okur and Ansal, 2007; Andersen, 2015; Wichtmann and Triantafyllidis, 2017) for which the model described in this paper has been developed.

3.4 Implementation

The PIMS model has been implemented as a user-defined soil model in the commercial finite element code Plaxis (Plaxis, 2017). The soil model was implemented as a dynamic link library (DLL), programmed in Fortran. The Fortran DLL routine receives information on the current micro stress states, $\boldsymbol{\sigma}_{\mathrm{micro},k-1}$, the current model indices $i_{mem,k-1}$ and $i_{lca,k-1}$ and the overall strain increment, $\Delta\boldsymbol{\varepsilon}_{k-1}$. The model then delivers updated values of the micro stresses, $\boldsymbol{\sigma}_{\mathrm{micro},k}$, and the corresponding macro stress, $\boldsymbol{\sigma}_k$ employing an explicit sub-stepping approach with automated error control, based on the recommendations presented by Sloan et al. (2001). Updated values of $i_{mem,k}$ and $i_{lca,k}$ are also returned.

The micro stresses need to be stored and tracked for each micro model, which results in a significant data storage requirement at each integration point in the analysis. For example, for a parallel Iwan model with $n = 10$ micro models and a mesh consisting of tetrahedral elements with four integration points, 264 individual stress values per element (including micro stresses and the overall model macro stress) need to be stored, together with the current values of i_{mem} and

i_{lca}. Although this implies a high memory demand, it is somewhat offset by the fact that the micro model constitutive calculations are extremely simple and hence fast to compute.

4. CALIBRATION OF THE PIMS MODEL

4.1 Monotonic calibration

To apply the model, the parameters for each micro model's yield surface ($q_{uc,i}, \beta_i$) and the weights (w_i) need to be calibrated, together with the overall small-strain elastic shear modulus (G_0). This calibration is conducted in terms of normalised, dimensionless, variables as described below. The calibration process is illustrated for an example case in Fig. 6.

It is convenient to calibrate the model using data from isotropically consolidated undrained triaxial compression and extension tests. This calibration process requires data on G_0 determined, for example, from triaxial testing using local strain gauges or via separate bender element tests. The model is calibrated in terms of the normalised variables $\bar{\varepsilon}_q$ and $\bar{q}$ where,

$$\bar{\varepsilon}_q = I_r^* \varepsilon_q; \qquad I_r^* = \frac{3G_0}{2s_{uc}}; \qquad \bar{q} = \frac{q}{q_{uc}} \tag{15}$$

where s_{uc} ($= q_{uc}/2$) is the undrained shear strength in triaxial compression (determined from the triaxial test data). The response of the model can be conveniently represented by the normalised tangent stiffness $\bar{G} = G_{\tan}/G_0$, where $G_{\tan}$ is the tangent shear stiffness. This normalisation approach has the desirable feature that the area beneath the $(\bar{\varepsilon}_q, \bar{G})$ curve is constrained to be equal to unity (i.e. $\int_0^\infty \bar{G}\, d\bar{\varepsilon}_q = 1$). On this basis, it is assumed that the normalised backbone curves $\bar{q}(\bar{\varepsilon}_q)$ and $\bar{G}(\bar{\varepsilon}_q)$ are a unique feature of any particular geotechnical unit identified in an overall ground model.

For implementation purposes, at a particular location in the geotechnical unit, calibrated values of β_i and w_i determined in this normalised space can be applied directly in the model. Appropriate values of the strength parameters $q_{uc,i}$ are determined by scaling the calibrated normalised values $\bar{q}_{uc,i}$ on the basis of the normalisation in Equation (15), employing the local (measured) value of s_{uc}. The elastic component of the model is specified directly using the local value of G_0. A comparable approach was adopted by Dong et al. (2015) to calibrate a multi-surface total stress model for Shanghai Clay.

The first step in the calibration process is to collect the available triaxial compression test data, for the particular geotechnical unit being modelled, on a single plot in $(\bar{\varepsilon}_q, \bar{q})$ space (Fig. 6a). Next, the number, n, of micro models to be employed is selected ($n = 9$ in the Fig. 6 example). It is then necessary to select desired values of 'normalised yield strain', $\bar{\varepsilon}_{qc,i}$, corresponding to the values of normalised triaxial shear strain $\bar{\varepsilon}_q$ at which yielding of each micro model first occurs. The 'inner' micro model, $i = 1,$ corresponds to the boundary of elastic behaviour; the value of $\bar{\varepsilon}_{qc,1}$ is therefore selected to define an appropriate strain limit on the small strain elastic behaviour implied by the model. The outer micro model ($i = n$) is specified to have a normalised yield strain $\bar{\varepsilon}_{qc,n}$ that is sufficiently large for the limiting state $\bar{q} = 1$ to have been reached in the test data. Values of the intermediate micro model normalised yield strains are then selected as required. (A logarithmic spacing along the $\bar{\varepsilon}_q$ axis is adopted in the Fig. 6 example). Additionally, if the cyclic overlay model is to be employed, a cyclic threshold surface $i = i_{thr}$ needs to be specified at an appropriate value of $\bar{\varepsilon}_{qc,thr}$ (see later). As a consequence of the adopted normalisation, the normalised micro model's triaxial compression shear strengths are determined straightforwardly by $\bar{q}_{uc,i} = \bar{\varepsilon}_{qc,i}$. Next, the triaxial compression data in $(\bar{\varepsilon}_q, \bar{q})$ space are fitted with a series of linear segments, joining points corresponding to the previously-defined $\bar{\varepsilon}_{qc,i}$ data (Fig. 6a). As a consequence of the adopted normalisation, the first line segment (Fig. 6a, inset) has a gradient of 1.0 . Thereafter, the ordinate of the line segment's endpoints are chosen (by eye or numerical optimisation) to provide a fit with the triaxial data, as shown in Fig. 6a. The resulting normalised

stiffness backbone curve implied by the model is illustrated in Fig. 6b. The weights w_i are determined from the steps in the backbone curve as,

$$w_i = \Delta\bar{G} = \bar{G}_i - \bar{G}_{i+1} \quad \textbf{(16)}$$

A typical normalised shear stiffness backbone curve for triaxial compression implied by the model is depicted in Fig. 7a. The corresponding normalised backbone curve in triaxial extension, shown in Fig. 7b, is determined by employing the weights w_i that were determined from the triaxial compression calibration, but with values of normalised yield strain given by $\bar{\varepsilon}_{\mathrm{qe,i}} = \beta_i \bar{\varepsilon}_{\mathrm{qc,i}}$ where β_i are the triaxial extension factors for each micro model. Although it is possible to specify each micro model to have different values of β_i, in the current implementation all micro models have the same value, $\beta_i = \beta$. In this case, the normalised stiffness backbone curve for triaxial extension, illustrated in Fig. 7b, is simply a scaled version of the triaxial compression backbone curve (scale factor β along the $\bar{\varepsilon}_{\mathrm{q}}$ axis). The area beneath the triaxial extension normalised shear stiffness backbone curve is $\int_0^\infty \bar{G}\, d\bar{\varepsilon}_{\mathrm{q}} = \beta$.

4.2 Cyclic calibration

An appropriate value of $\bar{\varepsilon}_{q,thr}$ (needed to specify the strength of the cyclic threshold micro model, $i = i_{thr}$) needs to be selected. This can be determined experimentally, by conducting low amplitude cyclic laboratory tests (e.g. Jardine, 1992).

The parameters A, r, b are conveniently calibrated using strain-controlled two-way cyclic tests, employing a similar approach to Vucetic and Dobry (1988). Values of degradation factor, d are determined from the test data as $d = G_{sec,N}/G_{sec,1}$ (see Fig. 1). By conducting tests at different strain amplitudes, the influence of the accumulated deviatoric strain ($\sum \Delta E_q$) on d can be examined and the parameters A, r, b determined.

Although, ideally, the model is calibrated using data from cyclic triaxial tests, (because in this case the stress conditions are fully defined), cyclic undrained direct simple shear (UDSScyc) tests are

typically preferred in geotechnical practice. This is because a smaller volume of soil is required, so the sample preparation process is more likely to provide a reasonably consistent set of undisturbed samples. In this case, stress-controlled tests (in which the cyclic strain amplitude evolves with each cycle) and strain-controlled tests should ideally both be performed, at varying cyclic stress amplitudes, to calibrate the model and verify its performance.

4.3 Model initialisation

Initialisation of isotropic in situ stress conditions (i.e. $K_0 = 1$) is performed by setting the initial micro stress tensor in each model directly equal to the in situ total stress state (i.e. $\boldsymbol{\sigma}_{\mathrm{micro},i} = \boldsymbol{\sigma}$). Therefore, when $K_0 = 1$ the initial stress state is at the centre of each micro model in the deviatoric plane (i.e. $q = 0$).

For non-isotropic initial in situ stress conditions (i.e. $K_0 \neq 1$) a mobilised deviatoric stress is applied within the model. To achieve this, first the required initial deviatoric stress is applied based on the in situ stress conditions. Subsequently, along the same strain path a load-unload increment, which is equal to the elastic threshold strain, is applied. The applied load-unload increment of strain, $\Delta\boldsymbol{\varepsilon}$, is set equal to the strain on the inner micro model (i.e. $\boldsymbol{\varepsilon}_1$). The rationale for applying the small load-unload strain increment is to ensure that the initial stress state within each micro model does not lie on the yield surface and the initial micro deviatoric stress of the inner micro model is equal to zero. This then ensures that the initial response predicted by the model is equal to the elastic stiffness until the deviatoric strain increment, ΔE_q, causes plastic straining to occur in the inner micro model.

5. APPLICATION OF THE PIMS MODEL

5.1 Overview of application examples

This section describes the calibration of the PIMS model to monotonic and cyclic laboratory test data for two overconsolidated clays, accompanied by 3D FEA of monopile foundations subjected to monotonic and cyclic lateral loading.

One of these calibrations is conducted on samples of Bolders Bank clay, from sites in the North Sea, based on previous triaxial test data obtained from routine offshore site investigations conducted by Fugro. Index properties are listed in Table 1. Due to limitations in the available data, this calibration consists of monotonic loading parameters only.

To demonstrate the cyclic loading capabilities of the PIMS model, a second calibration is presented, for an overconsolidated clay, based on samples acquired and tested by Fugro during a routine offshore site investigation in the Belgian Sector of the southern North Sea. The calibration samples were all extracted from the same geotechnical clay unit, termed Unit A. The index properties of this unit are also listed in Table 1.

These data sets include of both monotonic and cyclic DSS tests; it was therefore possible to use these data to calibrate the cyclic parameters, as well as the underlying elasto-plastic parameters, in the PIMS model.

5.2 Analysis of monopile embedded in Bolders Bank clay

5.2.1 Calibration of PIMS model for Bolders Bank clay

Triaxial compression tests were conducted on Bolders Bank samples that had been recovered during routine offshore geotechnical investigations (conducted by Fugro) at several sites in the southern North Sea. A range of different values of K_o were employed in the initial consolidation process employed in the triaxial tests. The OCR of the samples ranged from 2 to 7.

The Bolders Bank formation is also the main geotechnical unit at the Cowden test site, where laterally loaded pile tests were conducted during the PISA research project (Byrne et al., 2019). Triaxial test data from the Cowden site (Zdravković et al., 2019) were found to be broadly consistent with the Fugro data set employed to calibrate the PIMS model. On the basis of this observation, several of the PISA pile tests were analysed using the calibrated PIMS model and the computed results compared with the field data (Byrne et al., 2019).

Fig. 8 illustrates normalised data from ten triaxial compression tests on undisturbed samples from the Bolders Bank formation. These data were selected from the Fugro data set for cases where the consolidation process in the triaxial tests employed a K_0 value close to 1.0. For each sample, a bender element test was performed prior to shearing to determine G_0 (required for the normalisation). An average axial strain rate of approximately 0.5% per hour was applied during the shearing stage. The data in Fig. 8 were used to calibrate a 12-surface PIMS model using the procedure described in Section 4.1; the resulting backbone curve is shown in Fig. 8. Based on a limited number of triaxial extension tests, the triaxial extension factor was set to $\beta = 0.7$. The final calibration parameters are listed in Table 2.

5.2.2 Single element simulations

Simulations of several individual triaxial tests on Bolders Bank clay that were not included in the calibration process are shown in Fig. 9. Three of these cases (indicated 'Fugro data set') were consolidated using values of K_0 that departed from 1.0. In these cases, the simulations were conducted by applying appropriate axial and radial stresses to represent these initial K_0 conditions, using the approach discussed in Section 4.3, prior to modelling the shearing stage of the test. Also shown in Fig. 9 are separate data from a triaxial test conducted on a sample of clay till from the Cowden PISA test site (Zdravković et al., 2019) together with an equivalent simulation conducted using the current model calibration. The excellent agreement between the calibrated model and these test data provide an indication of the robustness of the calibration process. It is particularly noteworthy that the calibrated model is able to reproduce the triaxial test data obtained from the Cowden clay sample.

5.2.3 Monotonic lateral loading of a monopile

3D FEA of three monotonically-loaded pile tests at Cowden from the PISA research project (Byrne et al., 2019) have been conducted using the calibrated PIMS model. The pile load tests were carried out in a series of increments under displacement control at relatively slow constant

displacement rates, separated by periods of maintained load in which creep and consolidation were observed (further details are provided in Byrne et al., 2019). The pile configurations that have been considered are specified in Table 3. The strain rate used to calibrate the model was considered appropriate for the loading rate employed in the PISA tests.

In the finite element model the soil domain was discretised using approximately 30,000 10-noded tetrahedral elements, exploiting symmetry as shown in the mesh in Fig. 10. The pile was modelled using 6-noded plate elements, with 12-noded zero-thickness interface elements on the external pile wall. The steel pile was modelled as a linear elastic material with E = 210 GPa and ν = 0.3. The interface elements used an elasto-plastic Tresca model, with the elastic stiffness set to 10^5 kN/m^3 based on recommendations by Zdravković et al. (2019). Axial pile load testing performed by Lehane and Jardine (1994) at the Cowden test site found that the interface shear strength varied from 0.57 to 0.82 times the measured local undrained shear strength of the soil in triaxial compression; therefore, an interface shear strength of $0.7s_{uc}$ was adopted in the current work. A zero-tension cutoff was prescribed for the interface elements to allow gapping to occur at the pile-soil interface. The lateral boundaries were 25 m from the centre of the pile for all cases. Fig. 11 shows the profiles of s_{uc} and G_0 that were adopted for the analysis. The saturated bulk unit weight, γ_{sat}, was taken as 21.19 kN/m^3 for all analyses. These profiles are based on site-specific laboratory and in situ data reported by Zdravković et al. (2019).

Comparisons of the computed load-displacement responses with the measured pile load test data are shown in Fig. 12a (for the overall behaviour) and Fig. 12b (for the initial, small displacement, response). There is good agreement between the measured and computed responses; this provides an encouraging demonstration of the predictive capability of the PIMS model.

5.3 Monopile embedded in overconsolidated clay (Unit A)

5.3.1 Calibration of PIMS model for overconsolidated clay (Unit A)

A single undisturbed core sample from Unit A was sub-sampled for the UDSS test program. Symmetrical two-way cyclic loading with either a constant cyclic shear strain amplitude (γ_{cyc}) or a constant cyclic shear stress amplitude (τ_{cyc}) was applied to each specimen. The tests are specified in Tables 4 and 5.

The monotonic stress-strain backbone curve was first calibrated directly to UDSS1, using a 12-surface PIMS model. A triaxial extension factor of $\beta = 0.7$ was adopted. Calibration of the model was achieved by conducting simulations of UDSS1 and adjusting the weights, w_i, by eye to obtain a reasonable match between the data and the model. To simulate the test, the model was initialised for isotropic conditions (see Section 4.3). A shear stress was then applied, with zero lateral and vertical strain, to mimic the conditions in the UDSS test.

To calibrate for cyclic loading, it is necessary to consider the strain rate dependency of the soil. Viscous rate dependency of clays has been investigated experimentally by many authors, including Sheehan et al. (1996) and Torisu et al. (2012). The measured undrained shear strength is typically found to be adequately represented, for the range of strain rates considered in the current work, by a power function of the strain rate. To illustrate the cyclic performance of the model, a correction was applied to the undrained shear strength s_{uc} to simulate a viscous rate dependency. This was done by applying a rate correction factor, F_{rate}, to the shear strength values, where,

$$F_{\text{rate}} = \left(\frac{\dot{\varepsilon}_{\text{q}}}{\dot{\varepsilon}_{\text{q,ref}}} \right)^{h} \quad \textbf{(17)}$$

where $\dot{\varepsilon}_{\text{q,ref}}$ is the strain rate used to calibrate the reference backbone curve (i.e. 3% per hour). On the basis of the available data, a value of $h = 0.043$ was adopted. This power function of strain rate is shown to reproduce the laboratory results well across the strain rates considered (See Section 5.3.2). Within this study a single fixed strain rate is assumed across the whole region of

the FE mesh for calibration of the backbone curve i.e. the strain rate is assumed not to vary across the mesh. However, it should be noted if strain rate effects were to be incorporated explicitly in the model formulation, i.e. stress-strain backbone curve was set to vary across the FEA mesh depending on local strain rate, then this function should be used with caution as it will result zero strength in regions not being strained.

5.3.2 Single element simulations

The strain rate correction method described above assumed a constant strain rate. It is noted, however, that the cyclic tests employed a sinusoidal variation of the prescribed strains/stresses. This means that the strain rate varies during the cycling; a single representative strain rate, however, needs to be selected for the current modelling approach. A representative value of $\dot{\varepsilon}_q = 7000\%$ per hour was employed for the current analysis; this is based on the average strain rate applied during the first quarter cycle of a test, for tests UDSScyc2 and UDDScyc4 (i.e. corresponding to the highest and lowest strain rates applied in the testing). This strain rate correction approach is considered sufficient, as even relatively large variations in the strain rates applied in the cyclic tests cause only minor variations in the strain rate correction factor, when related to the reference strain rate of 3% per hour using the proposed power model. Fig. 13 compares the measured and simulated monotonic responses in various tests, with the strain rate correction applied in the simulations. The generally good agreement between the simulations and measured data, for different loading rates, highlights the suitability of the adopted rate correction method. The final calibration parameters for the cyclic rate corrected backbone curve are listed in Table 2.

The cyclic parameters were calibrated using a process, similar to the one outlined in Section 4.2, in which values of A, r, b are selected to provide a match between the model and the data. The final calibration values are listed in Table 6.

The performance of the model in simulating four separate UDSScyc tests is illustrated in Fig. 14. For 100 simulated cycles, the response of the calibrated model shows good agreement with the measured data in both strain-controlled tests (UDSScyc-1 and UDSScyc-2) and stress-controlled tests (UDSScyc-3 and UDSScyc-4). This is promising, since it indicates that the model is capable of capturing a reasonable response for conditions when the stress or strain amplitude varies over a number of cycles. The applied rate correction method also appears adequate as the first quarter cycle response in each cyclic test simulation shows reasonable agreement with the test data.

Although the cyclic single element simulation results presented are felt to be encouraging, further work is required to compare the performance of the model with laboratory data for a wider range of cyclic stress conditions (e.g. considering cases where the mean shear stresses are non-zero).

5.3.3 Cyclic lateral loading of a monopile

The calibrated cyclic model was used to perform 3D FEA of an example offshore monopile foundation subjected to a storm-type history of cyclic lateral loading. By employing the PIMS model in this application, it is possible to capture the stress history and the variable cyclic degradation across the soil domain. A uniform soil profile was used, taking $\gamma_{sat} = 20$ kN/m^3 and adopting the cyclic rate-corrected backbone curve (labelled 'UDSScyc Simulation' in Fig. 13), for which $G_0 = 116$ MPa and $s_{uc} = 252$ kPa.

The soil domain was discretised using 27,456 10-noded tetrahedral elements, with the lateral boundaries of the mesh situated 60 m from the centre of the pile. The pile and the pile-soil interface were modelled as specified in Section 5.1.3. Details of the pile geometry and loading conditions for this analysis are given in Table 7. One-way lateral cyclic loading was applied to the pile in two load-controlled packets to mimic storm loading conditions. Load packet 1 consisted of 70 cycles with a peak lateral load of 20 MN, followed by load packet 2 which consisted of 16 cycles with a peak load of 28 MN. In both cases the trough load was zero.

Fig. 15a shows the load-displacement response of the pile at seabed level. Within each cyclic loading packet there is a gradual accumulation of lateral displacement, though the rate of accumulation decreases with each cycle. Several centrifuge model testing studies investigating cyclic lateral loading of monopiles in clay (e.g. Zhang et al., 2010; Hong et al., 2017; Yu et al., 2018) have also shown a degradation in the cyclic lateral stiffness, together with a gradual accumulation of lateral displacement. It is interesting to note that the overall stiffness response of the pile does not degrade significantly within each cyclic load packet. For example, within load packet 2 (i.e. cycles 70 to 86) the FEA predicts a 3% reduction in the secant unload-reload stiffness (Fig. 15a) even though significantly higher levels of localised degradation occur in the soil over the same period (see next paragraph). Therefore, at a global level, ratcheting-type behaviour of pile is observed with little stiffness reduction. The computed accumulated displacements are shown more clearly in Fig. 15b, which presents a plot of the accumulated displacement versus number of cycles.

Fig. 16 shows the evolution of the cyclic degradation factor, d, in the soil around the pile. During each packet of cyclic loading there is progressive degradation (d reduces from its initial value of 1.0) and this gradually propagates to a larger volume of soil as the cyclic loading continues. It is clear that a complex spatial and temporal evolution of the cyclic degradation factor occurs. Fig. 16 shows that as the cyclic loading proceeds, the region of degradation also propagates down the pile, with the degradation at the pile toe becoming more significant as the rigid pile rotates; this is in contrast to a flexible pile, for which more localised cyclic degradation near the seabed would be expected. It is therefore likely that the propagation of cyclic degradation in the soil, and hence the overall cyclic response of the pile, will be significantly affected by the L/D ratio of the pile being considered.

6. CONCLUSIONS

A practical multi-surface total stress model – PIMS – is proposed to represent the monotonic and cyclic loading behaviour of clay, for cases where the soil is undrained. This model, together with associated finite element implementation and calibration procedures, has been developed specifically to facilitate robust geotechnical calculations for practical applications relating to offshore foundations.

The basic parallel Iwan framework that is adopted for the PIMS model is a well-established constitutive modelling approach, although there are few documented applications of this framework in geotechnical engineering. Although previous researchers have explored the application of *series* forms of the Iwan framework to represent soil behaviour, the current paper demonstrates that the *parallel* form is a particularly attractive option for practical geotechnical calculations. The parallel Iwan framework is relatively straightforward to explain (e.g. to clients, regulators and insurers) to implement (in finite element codes) and to calibrate (using routine site investigation procedures).

The basic Iwan framework employed in the PIMS model is capable of being extended, as required, to account for additional aspects of soil behaviour. An extension to the model, incorporating cyclic loading effects, is described in the current paper. A separate extension for inherent soil anisotropy has also been developed, although this extension is outside the current scope. Further extensions are considered feasible, for example to incorporate rate effects explicitly in the model, rather than employing the simple rate correction approach that is adopted in the current work. It would also be possible to incorporate different forms of cyclic response, for example employing separate models for the stiffness and strength degradation components of behaviour.

An important feature of the PIMS model, from a geotechnical practitioners' perspective, is that it can be calibrated using laboratory test procedures that are routinely employed in geotechnical site investigation practice. Calibration of the basic parallel Iwan framework is demonstrated in the

current paper using data from standard triaxial compression and extension tests (with bender elements) and direct simple shear tests. A calibration of the cyclic overlay model is also demonstrated, although the calibration procedure in this case is less systematic; it consists essentially of adjusting the model parameters until a satisfactory fit is obtained with data from cyclic triaxial and/or direct simple shear tests. This study has focused on calibration of the model using conventional laboratory tests only (triaxial test and direct simple shear test); further work should be performed to investigate the performance of the PIMS model when compared to laboratory test data performed under more complex stress paths (such as employing the hollow cylinder apparatus to impose rotation of the principal stresses during the test).

The Iwan framework has the considerable advantage that backbone curves of arbitrary shape can be represented, by appropriate choices of the number of micro models, the micro model parameters and the associated weights. However, the current modelling approach is unable to represent soil behaviour for cases where a peak, and post peak softening, occurs in the stress-strain backbone curve. In its current form, therefore, the model is unsuitable for heavily overconsolidated clay for which softening behaviour may be relevant.

The example 3D finite element analyses of laterally loaded monopiles presented in the paper demonstrate the practical application of the PIMS model. The analysis of three of the PISA test piles, although limited to monotonic behaviour, provides an indication of the predictive capabilities of the proposed modelling and calibration framework. This is particularly the case as the PIMS model was calibrated for this example using test data on Bolders Bank clay (considered to be the same geotechnical unit as the glacial clay till encountered at the Cowden site employed for the PISA tests) that relate to offshore locations at some distance from the PISA test site. The separate example presented in the paper, in which a monopile is subjected to cyclic lateral loading, is a hypothetical case and so field data on foundation performance are not available for comparison purposes. Nevertheless, this example analysis does demonstrate the robustness and

feasibility of the model implementation. Additionally, the computed results are broadly consistent with expected forms of behaviour.

ACKNOWLEDGEMENTS

This work was supported by grant EP/L016303/1 for Cranfield University and the University of Oxford, Centre for Doctoral Training in Renewable Energy Marine Structures - REMS (http://www.rems-cdt.ac.uk/) from the UK Engineering and Physical Sciences Research Council (EPSRC).

REFERENCES

Andersen KH. 2015. Cyclic soil parameters for offshore foundation design. In 3rd International Symposium on Frontiers in Offshore Geotechnics, Oslo, Norway, (1):p5-84.

Byrne BW, McAdam RA, Burd HJ, Beuckelaers WJA, Gavin K, Houlsby GT, Igoe D, Jardine RJ, Martin CM, Muir Wood A, Potts DM, Skov Gretlund J, Taborda DMG, Zdravković L. 2019. Monotonic lateral loaded pile testing in a stiff glacial clay till at Cowden. Géotechnique (in press).

Callisto L, Calabresi G. 1998. Mechanical behaviour of a natural soft clay. Géotechnique, 48(4):p495-513.

Chiang DY, Beck JL. 1994. A new class of distributed-element models for cyclic plasticity-I theory and application. International Journal of solids and structures, 31(4):p469-484.

Clayton CRI. 2011. Stiffness at small strain: research and practice. Géotechnique, 61(1):p5-37.

Corciulo S, Zanoli O, Pisano F. 2017. Supporting the Engineering Analysis of Offshore Wind Turbines Through Advanced Soil-Structure 3D Modelling. In ASME 2017 36th International Conference on Ocean, Offshore and Arctic Engineering (pp. V009T10A015-V009T10A015). American Society of Mechanical Engineers.

Dafalias YF, Manzari MT, Papadimitriou AG. 2006. SANICLAY: Simple anisotropic clay plasticity model. International Journal for Numerical and Analytical Methods in Geomechanics, 30(12):p1231-1257.

Dong YP, Burd HJ, Houlsby GT. 2015. Finite-element analysis of a deep excavation case history. Géotechnique, 66(1):p1–15.

Einav I, Collins IF. 2008. A thermomechanical framework of plasticity based on probabilistic micromechanics. Journal of Mechanics of Materials and Structures, 3(5):p867-892.

Elgamal A, Yang Z, Parra E, Ragheb A. 2003. Modelling of cyclic mobility in saturated cohesionless soils. International Journal of Plasticity, 19(6):p883-905.

Grimstad G, Andresen L, Jostad H. 2012. NGI-ADP: Anisotropic shear strength model for clay. International Journal for Numerical and Analytical Methods in Geomechanics, 36:p483-497.

Grimstad G, Rønningen J, Nøst H. 2014. Use of IWAN models for modelling anisotropic and cyclic behavior of clays. In 8th European Conference on Numerical Methods in Geotechnical Engineering, Delft, Netherlands, (1):p49-55.

Gu C, Wang J, Cai Y, Guo L. 2014. Influence of cyclic loading history on small strain shear modulus of saturated clays. Soil Dynamics and Earthquake Engineering, 66:p1-12.

Haiderali AE, Nakashima M, Madabhushi SPG. 2015. Cyclic lateral loading of monopiles for offshore wind turbines. In 3rd International Symposium on Frontiers in Offshore Geotechnics, Oslo, Norway, (1):p711-716

Hardin BO, Black WL. 1968. Vibration modulus of normally consolidated clay. J Soil Mech Found Div ASCE, 94(2):p353–369.

Hong Y, He B, Wang LZ, Wang Z, Ng, CWW, Mašín D. 2017. Cyclic lateral response and failure mechanisms of semi-rigid pile in soft clay: centrifuge tests and numerical modelling. Canadian Geotechnical Journal, 54(6):p806-824.

Houlsby, GT. 1999 A model for the variable stiffness of undrained clay. Proc. Int. Symp. on Pre-Failure Deformation Characteristics of Soils, Turin, (1):p443–450.

Huang M, Liu Y. 2015. Axial capacity degradation of single piles in soft clay under cyclic loading. Soils and Foundations, 55(2):p315-328.

Hyde AFL, Ward SJ. 1986. The effect of cyclic loading on the undrained shear strength of a silty clay. Marine Georesources and Geotechnology, 6(3):p299-314.

Idriss IM, Dobry R, Sing RD. 1978. Nonlinear behaviour of soft clays during cyclic loading. Journal of Geotechnical Engineering, 104(12):p1427-1447.

Iwan WD, Cifuentes AO. 1986. A model for system identification of degrading structures. Earthquake Engineering and Structural Dynamics, 14:p877-890.

Iwan WD. 1966. A distributed-element model for hysteresis and its steady-state dynamic response. Journal of Applied Mechanics, 33(4):p893-900.

Iwan WD. 1967. On a class of models for the yielding behavior of continuous and composite systems. Journal of Applied Mechanics, 34(3):p612-617.

Kouretzis G, Jubert P, Krabbenhøft K. 2017. Interpretation of vane shear tests for geotechnical stability calculations. Canadian Geotechnical Journal, 54(12):p1775-1780.
Ladd CC. 1991. Stability evaluation during staged construction. Journal of Geotechnical Engineering, 117(4):p540-615.
Lefebvre G, Pfendler P. 1996. Strain rate and preshear effects in cyclic resistance of soft clay. Journal of Geotechnical Engineering, 122(1):p21-26.
Lehane BM, and Jardine RJ. 1994. Displacement pile behaviour in glacial clay. Canadian Geotechnical Journal, 31(1):p79-90.
Mortezaie A, Vucetic M. 2016. Threshold shear strains for cyclic degradation and cyclic pore water pressure generation in two clays. Journal of Geotechnical and Geoenvironmental Engineering, 142(5):p1-14.
Mroz Z. 1967. On the description of anisotropic work hardening. Journal of the Mechanics and Physics of Solids, 15(3):p163-175.
Nishimura S, Minh NA, Jardine RJ. 2007. Shear strength anisotropy of natural London Clay. Géotechnique, 57(1):p49-62.
Okur DV, Ansal A. 2007. Stiffness degradation of natural fine grained soils during cyclic loading. Soil Dynamics and Earthquake Engineering, 27(9):p843-854.
Plaxis. 2017. Plaxis 3D, version 2017.1
Prashant A, Penumadu D. 2004. Effect of intermediate principal stress on overconsolidated kaolin clay. Journal of Geotechnical and Geoenvironmental Engineering, 130(3):p284-292.
Prévost JH. 1977. Mathematical modelling of monotonic and cyclic undrained clay behaviour. International Journal for Numerical and Analytical Methods in Geomechanics, 1(2):p195-216.
Sheahan TC, Ladd CC, Germaine JT. 1996. Rate-dependent undrained shear behaviour of saturated clay. Journal of Geotechnical Engineering, 122(2):p99-108.
Sheng D, Sloan SW, Yu HS. 2000. Aspects of finite element implementation of critical state models. Computational mechanics, 26(2):p185-196.
Sivasithamparam N. 2012. Development and implementation of advanced soft soil models in finite elements. PhD Thesis, University of Strathclyde. Glasgow, UK.
Skau KS. 2018. Modelling of skirted foundations for offshore wind turbines. PhD Thesis, Norwegian University of Science and Technology.
Sloan SW, Abbo AJ, Sheng D. 2001. Refined explicit integration of elastoplastic models with automatic error control. Engineering Computations,18(1/2):p121-194.
Stallebrass SE, Taylor RN, 1997. The development and evaluation of a constitutive model for the prediction of ground movements in overconsolidated clay. Géotechnique, 47(2):p235-253.
Thian SY, Lee CY. 2017. Cyclic stress-controlled tests on offshore clay. Journal of Rock Mechanics and Geotechnical Engineering, 9(2):p376-381.
Torisu SS, Pereira JM, De Gennaro V, Delage P, Puech A. 2012. Strain-rate effects in deep marine clays from the Gulf of Guinea. Géotechnique, 62(9):p767-775.
Vardanega PJ, Bolton MD. 2013. Stiffness of clays and silts: normalizing shear modulus and shear strain. Journal of Geotechnical and Geoenvironmental Engineering, 139(9):p1575-1589.
Vucetic M, Dobry R. 1988. Degradation of marine clays under cyclic loading. Journal of Geotechnical Engineering, 11(2):p133-149.
Vucetic M. 1994. Cyclic threshold shear strains in soils. Journal of Geotechnical Engineering, 120(12):p2208-2228.
Whittle AJ, Kavvadas MJ. 1994. Formulation of MIT-E3 constitutive model for overconsolidated clays. Journal of Geotechnical Engineering, 120(1):p173-198.
Wichtmann T, Triantafyllidis T. 2017. Monotonic and cyclic tests on kaolin: a database for the development, calibration and verification of constitutive models for cohesive soils with focus on cyclic loading. Acta Geotechnica, 13(5):p1103-1128.
Yasuhara K, Murakami S, Song BW, Yokokawa S, Hyde AF. 2003. Post-cyclic degradation of strength and stiffness for low plasticity silt. Journal of Geotechnical and Geoenvironmental Engineering, 129(8):p756-769.
Yu J, Leung CF, Huang M, Goh SC. 2018. Application of T-bar in numerical simulations of a monopile subjected to lateral cyclic load. Marine Georesources and Geotechnology, 36(6):p643-651.
Zdravković L, Taborda DMG, Potts DM, Abadias D, Burd HJ, Byrne BW, Gavin K, Houlsby GT, Jardine RJ, Martin CM, McAdam RA, Ushev E. 2019. Finite element modelling of laterally loaded piles in a stiff glacial clay till at Cowden. Géotechnique (in press).
Zhang C, White D, Randolph M. 2010. Centrifuge modelling of the cyclic lateral response of a rigid pile in soft clay. Journal of Geotechnical and Geoenvironmental Engineering, 137(7):p717-729.

PAPER 2 TABLES

Table 1: Index properties for Bolders Bank and Unit A clay

Index	Bolders Bank	Unit A
w	12 % – 25 %	25 % – 45 %
I_P	15 % – 25 %	15 % – 35 %
ρ_s	2.67 Mg/m^3 – 2.70 Mg/m^3	2.66 Mg/m^3 – 2.73 Mg/m^3
γ_{sat}	20.0 kN/m^3 – 22.5 kN/m^3	17.5 kN/m^3 – 20.0 kN/m^3

Notes: w = water content, I_P = plasticity index, ρ_s = density of solid particles, γ_{sat} = saturated unit weight

Table 2: PIMS calibration parameters for Bolders Bank and Unit A

Soil Unit		i=1	i=2	i=3	i=4	i=5	i=6	i=7	i=8	i=9	i=10	i=11	i=12
Bolders Bank	$\bar{\varepsilon}_{qc,i}$	0.0075	0.0225	0.0750	0.2250	4.0000	10.0000	16.8800	33.7500	56.2500	90.0000	135.0000	180.0000
	w	0.06333	0.18486	0.27928	0.43330	0.01923	0.00547	0.00624	0.00208	0.00267	0.00200	0.00089	0.00066
Unit A	$\bar{\varepsilon}_{qc,i}$	0.0066	0.0660	0.1980	0.6600	1.2000	3.3000	6.7500	15.0000	27.0000	34.5000	42.0000	52.5000
	w	0.43771	0.33502	0.07576	0.05892	0.04497	0.00414	0.01802	0.00962	0.00517	0.00533	0.00152	0.00382

Notes: $\bar{\varepsilon}_{qc}$= micro model normalised yield strain in triaxial compression, w = micro model weight, n = micro model number, β = 0.7 used for all micro models

Table 3: Analysed pile geometries from the PISA tests at Cowden (Byrne et al., 2019)

Pile Ref.	D (m)	L (m)	L/D	t (mm)	h (m)
CM2	0.762	2.24	2.94	10	10
CM9	0.762	4.98	5.22	11	10
CM3	0.762	7.59	9.96	25	10

Notes: D = pile diameter, L = pile embeded length, t = pile wall thickness, h = lever arm of horizontal load

Table 4: Cyclic undrained direct simple shear (UDSScyc) tests on Clay Unit A

Test Ref	Test Type	σ'_{v0} (kPa)	τ_{cyc} (kPa)	γ_{cyc} (%)
UDSScyc1	Strain-Controlled UDSScyc	188	N/A	$\pm$2.0
UDSScyc2	Strain-Controlled UDSScyc	188	N/A	$\pm$8.1
UDSScyc3	Stress-Controlled UDSScyc	188	$\pm$144	N/A
UDSScyc4	Stress-Controlled UDSScyc	188	$\pm$108	N/A

Notes: τ_{cyc}= cyclic shear stress amplitude, γ_{cyc}= cyclic shear stress amplitude, σ'_{v0} = initial vertical effective stress, N/A = not applicable, frequency of loading = 0.1 Hz

Table 5: Monotonic undrained direct simple shear (UDSS) tests on Clay Unit A

Test Ref	σ'_{v0} (kPa)	Loading Rate (%/hour)
UDSS1	188	3
UDSS2	188	300

Notes: σ'_{v0} = initial vertical effective stress

Table 6: Clay Unit A cyclic degradation overlay model parameters

Parameter	Value
A	2.82
b	0.43
r	0.6
c	0
$\bar{\varepsilon}_{qc,thr}$	0.066

Table 7: Analysed pile geometry for Clay Unit A

D (m)	L (m)	L/D	t (mm)	h (m)
7.5	25	3.33	75	25

Notes: D = pile diameter, L = pile embedded length, t = pile wall thickness, h = lever arm of horizontal load

PAPER 2 FIGURES

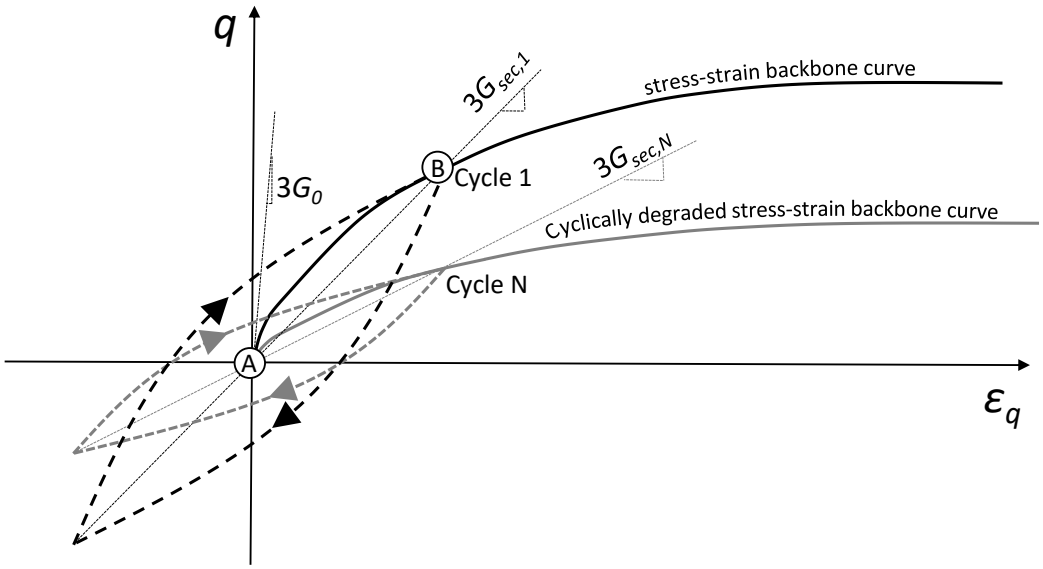

Figure 1: Schematic of stress-strain backbone curves before and after symmetrical two-way strain controlled cyclic loading, for triaxial conditions

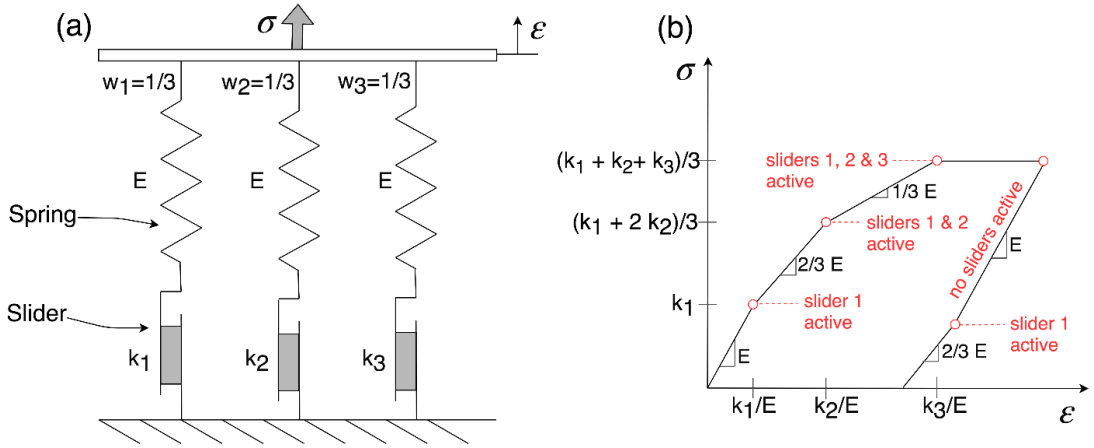

Figure 2: 1D parallel Iwan model consisting of three spring-slider elements with example stress-strain load-unload response

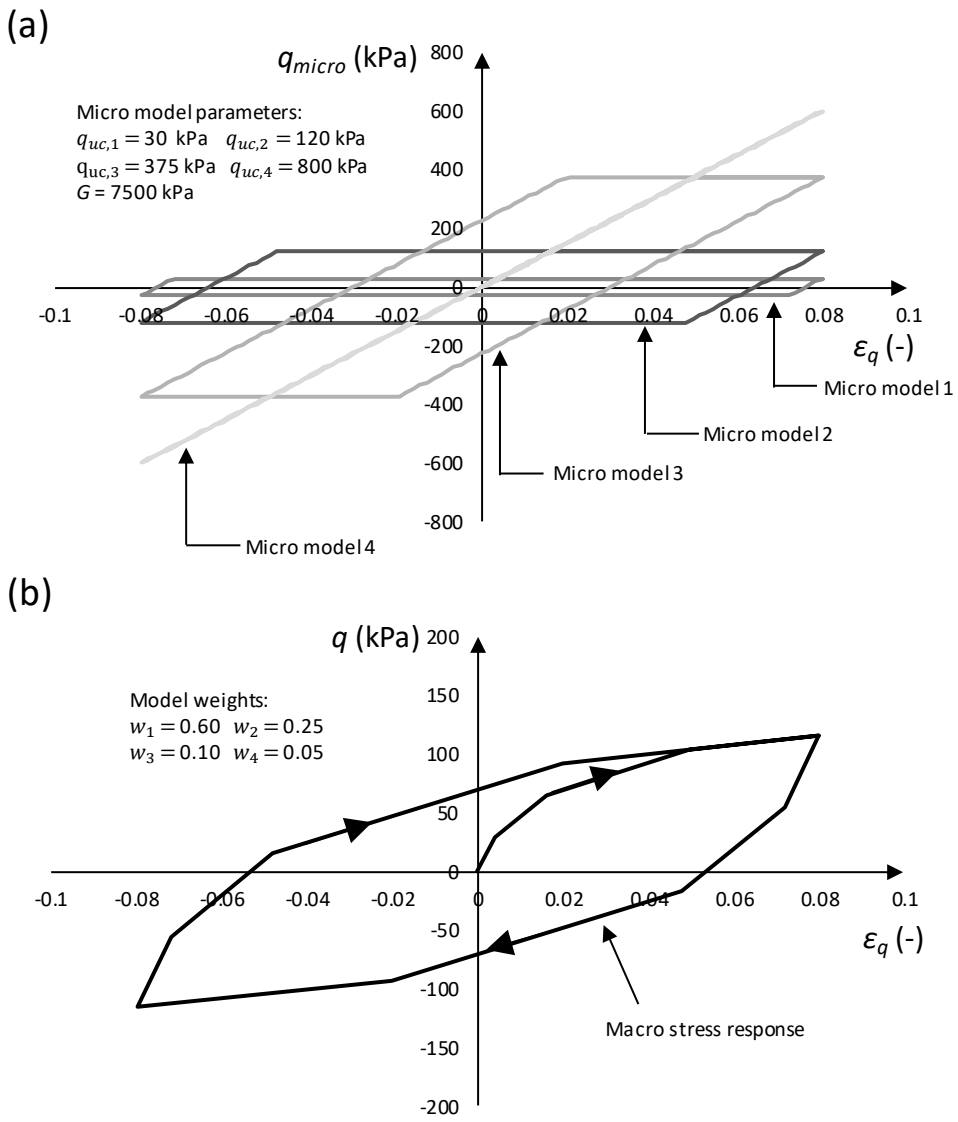

Figure 3: Example micro and macro stress-strain response for a parallel Iwan model consisting of four micro von Mises models in a symmetrical two-way strain-controlled cyclic triaxial test

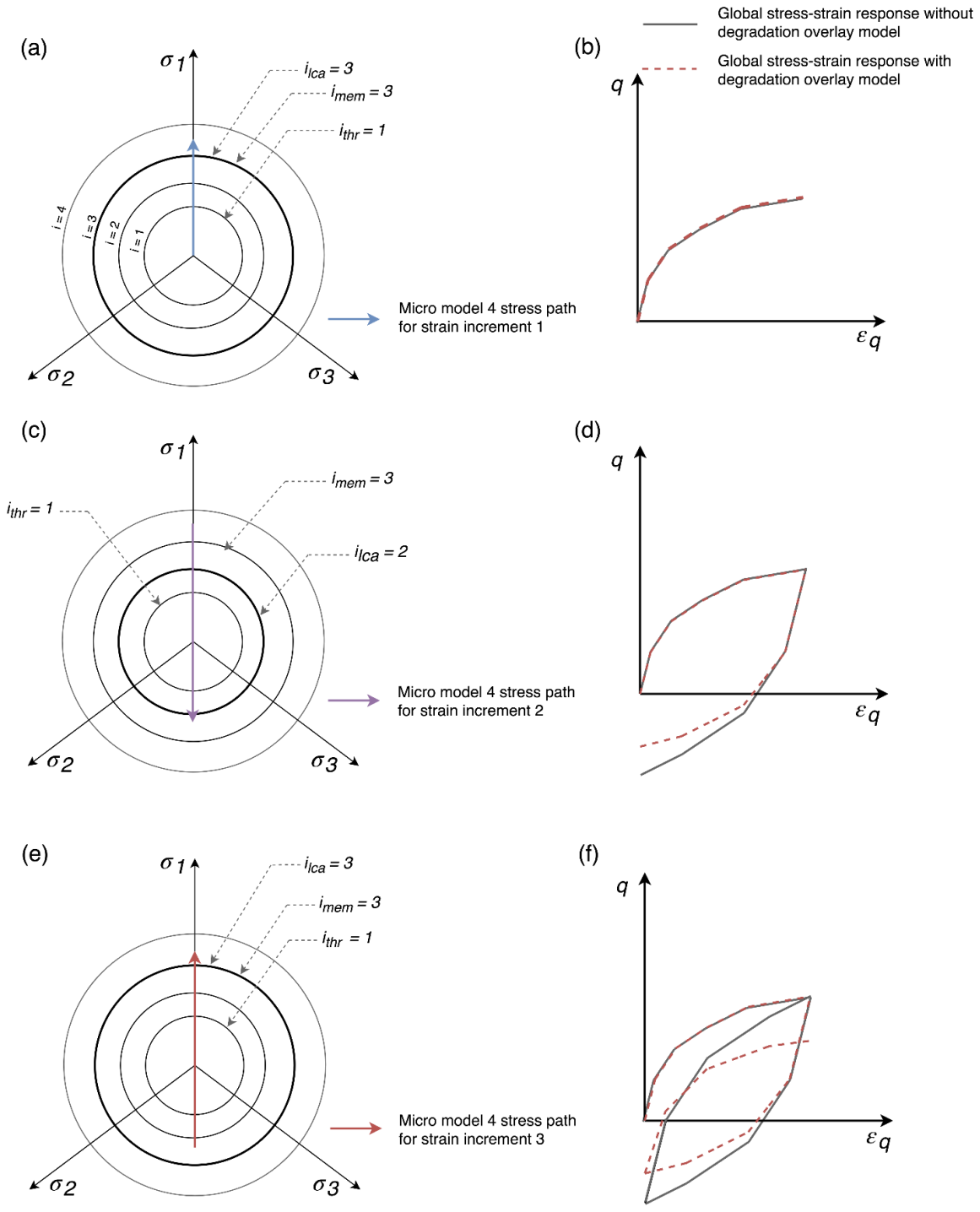

Figure 4: Schematic of the cyclic degradation overlay model with four von Mises micro models for a triaxial load-unload-reload test showing the stress path for micro model $i = 4$ and the overall macro stress-strain response with, and without, cyclic degradation applied

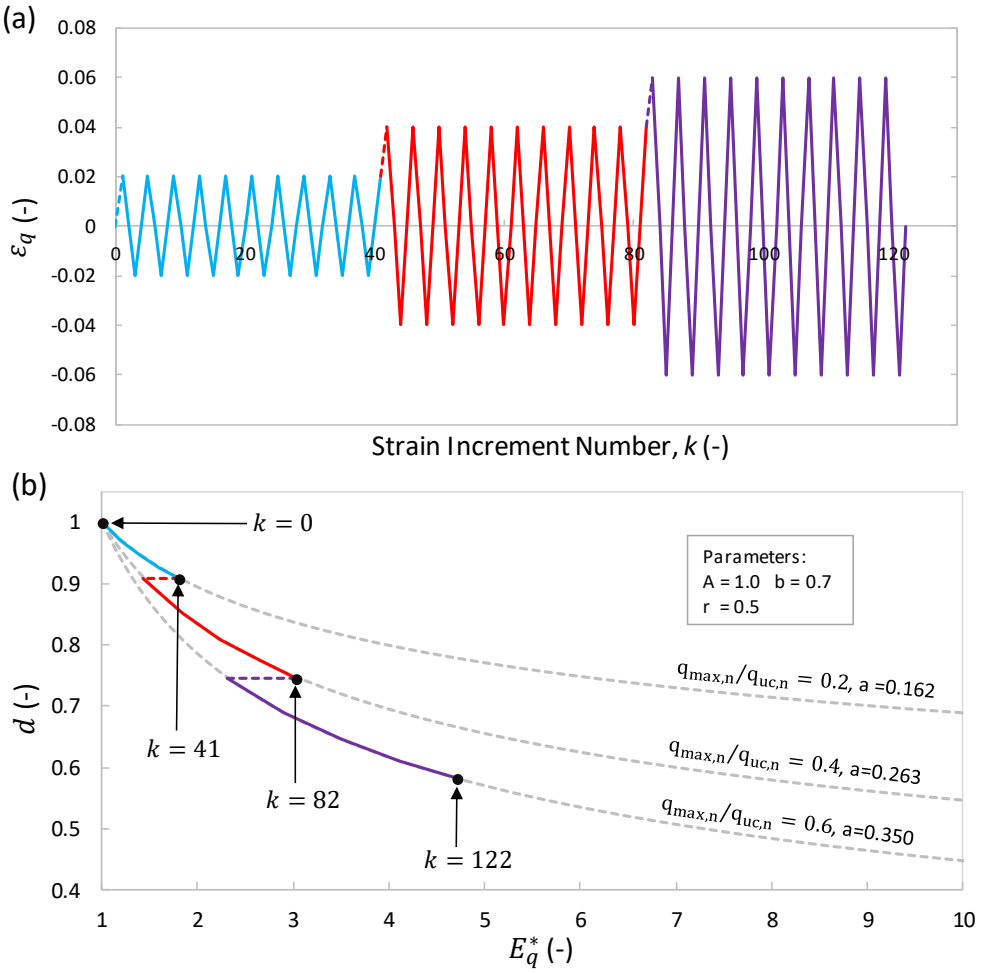

Figure 5: Example cyclic degradation factor calculation for a symmetrical two-way strain-controlled cyclic triaxial test with varying amplitudes using the PIMS model

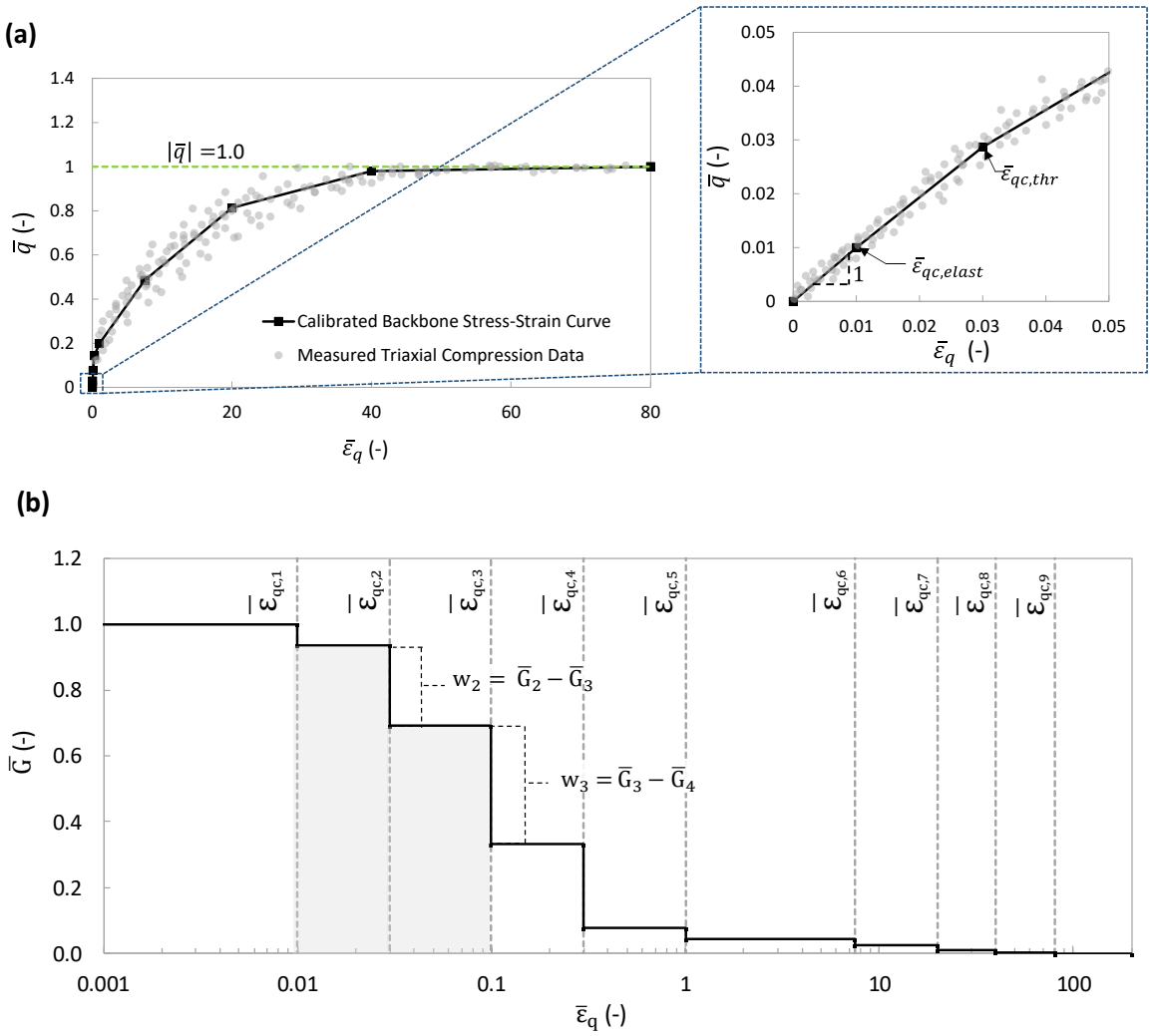

Figure 6: (a) Triaxial compression data and example best fit backbone curve stress-strain curve with small strain zoom view and with derivation of PIMS micro model parameters from (b) normalised stiffness degradation curve

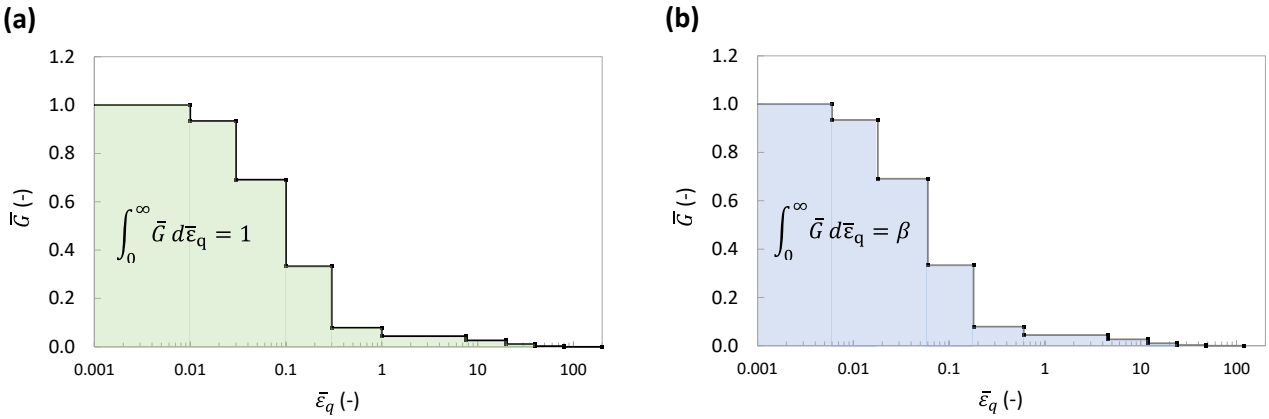

Figure 7: Example normalised tangent stiffness backbone curves in triaxial compression and extension with β = 0.6

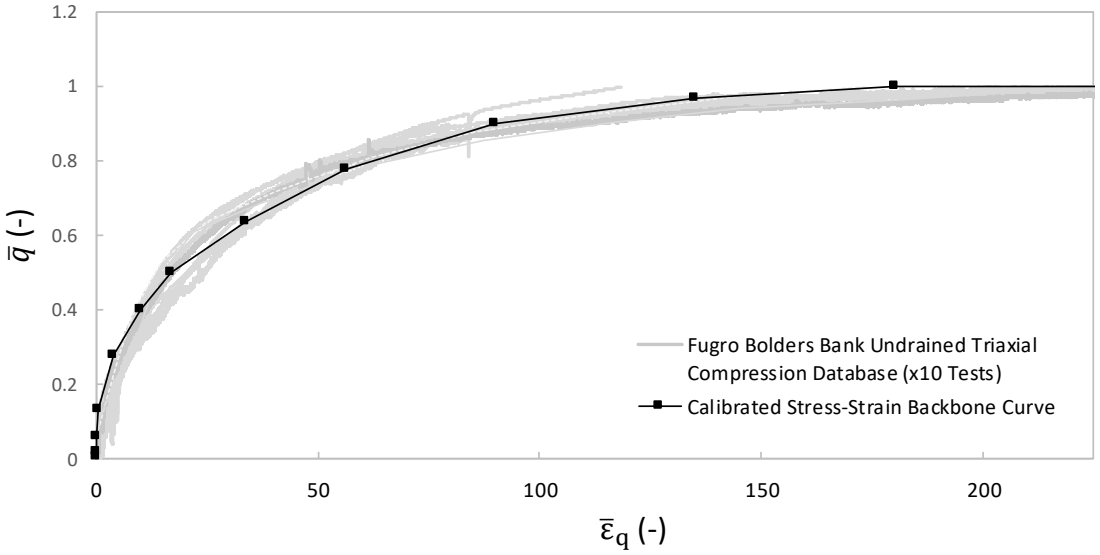

Figure 8: Bolders Bank clay undrained triaxial compression monotonic test data with double normalisation applied and the calibrated stress-strain backbone curve

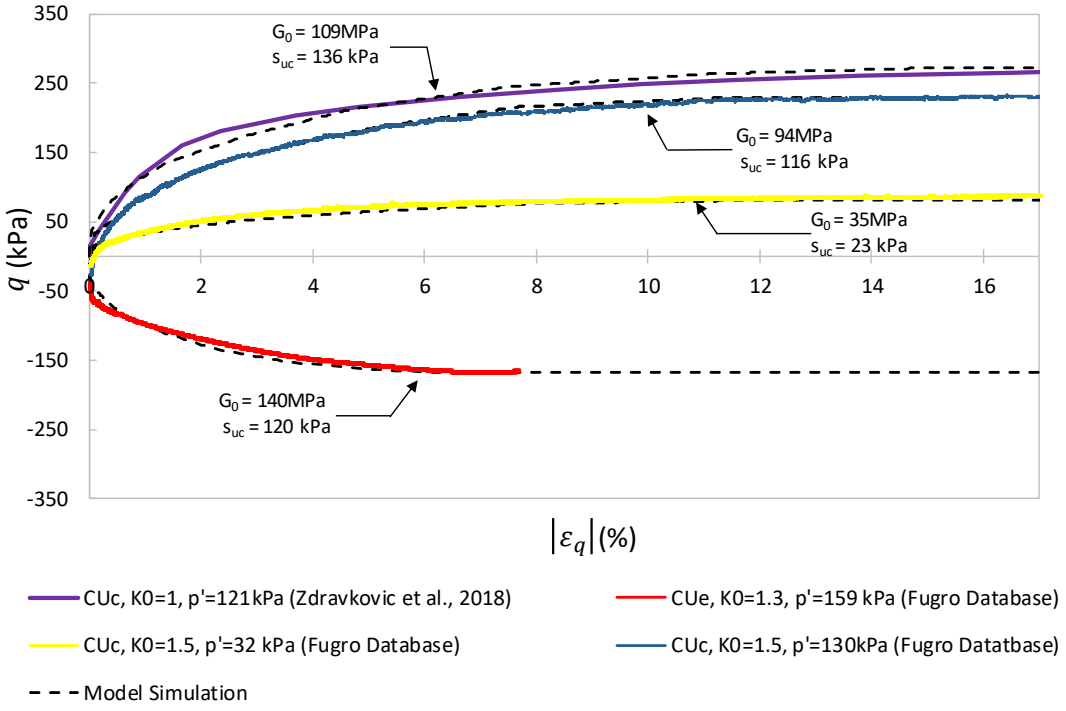

Figure 9: PIMS model simulations compared to triaxial laboratory test data from the Bolders Bank clay unit

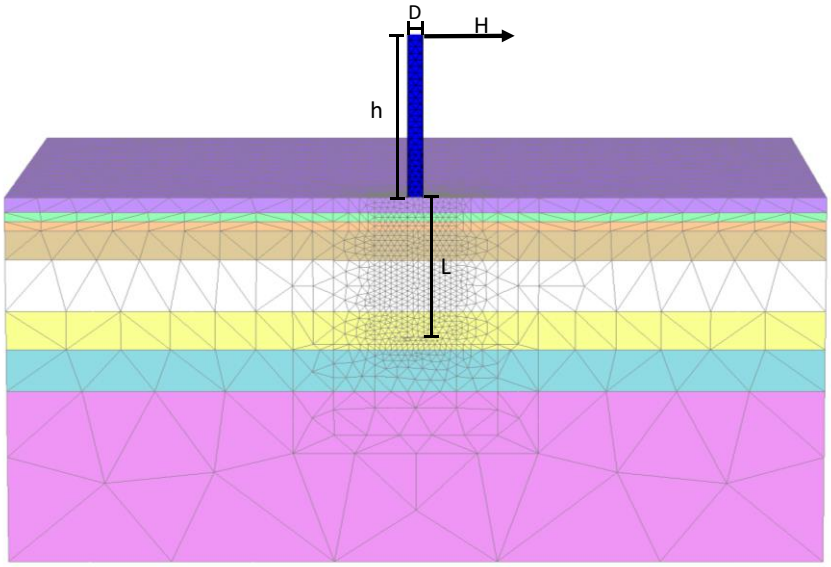

Figure 10: Example 3D mesh for pile with diameter of 0.762 m and an embedment length of 7.59 m (pile CM3 from PISA pile load tests)

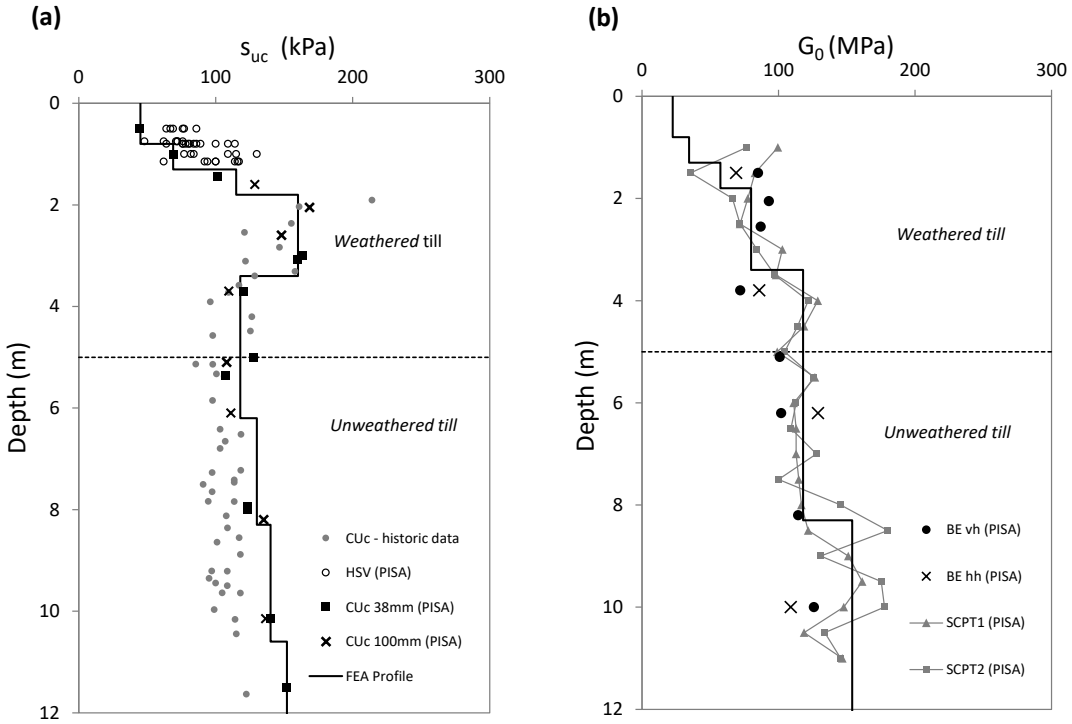

Figure 11: Undrained shear strength and small strain shear modulus data from the Cowden PISA pile tests site along with interpreted profiles used for finite element analyses; HSV = hand shear vane, BE = bender element, SCPT = seismic cone penetration test (test data from Zdravković et al., 2019)

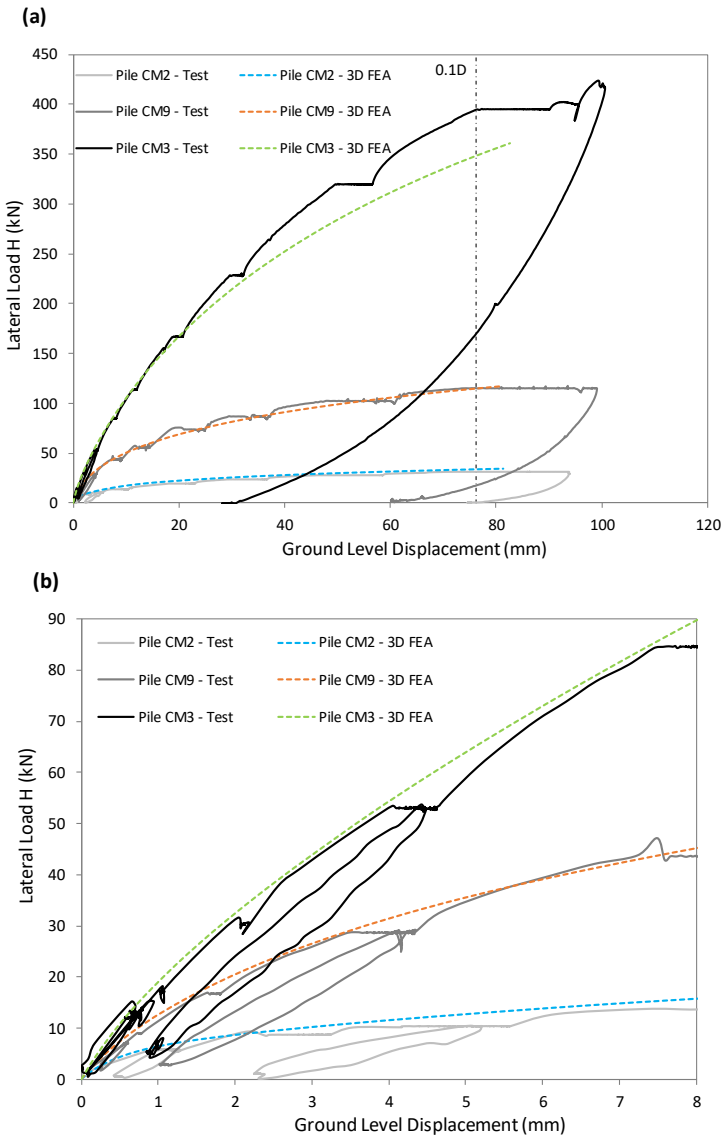

Figure 12: Pile load tests performed at the Cowden test site performed as part of the PISA research project (test data from Byrne et al., 2019) along with 3D FEA predictions using the calibrated PIMS model

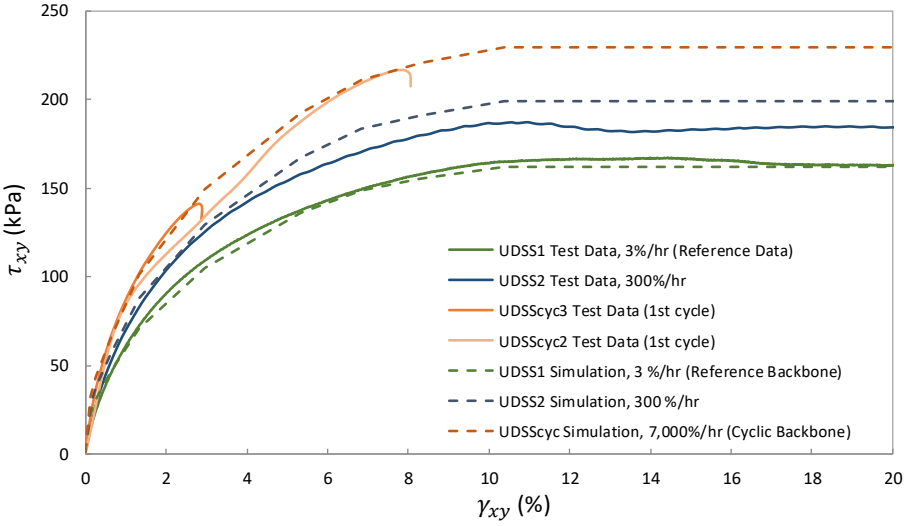

Figure 13: Measured monotonic undrained direct simple shear tests from Clay Unit A and PIMS model simulations for different loading rates

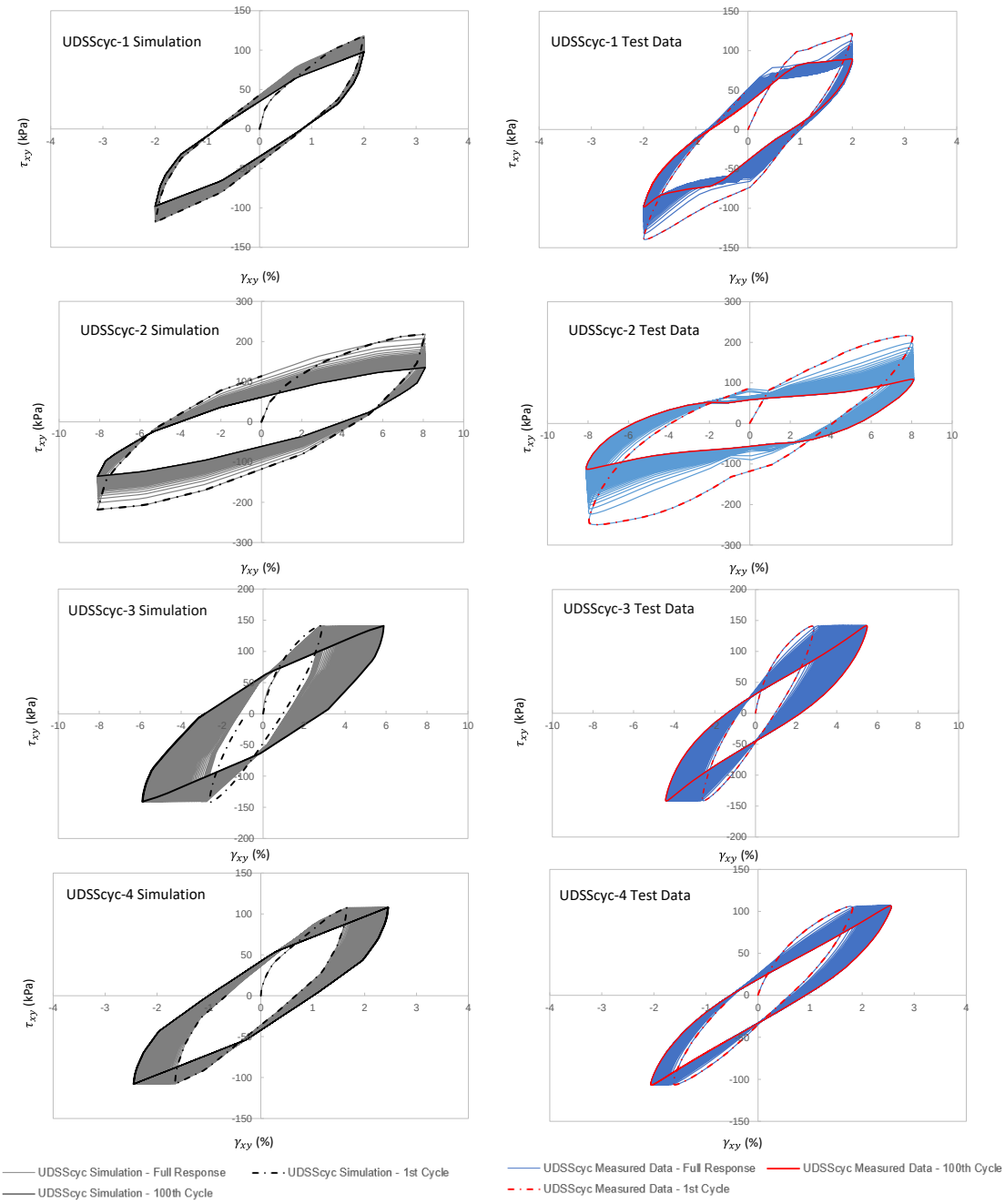

Figure 14: Measured cyclic undrained direct simple shear tests from Clay Unit A and PIMS model simulations

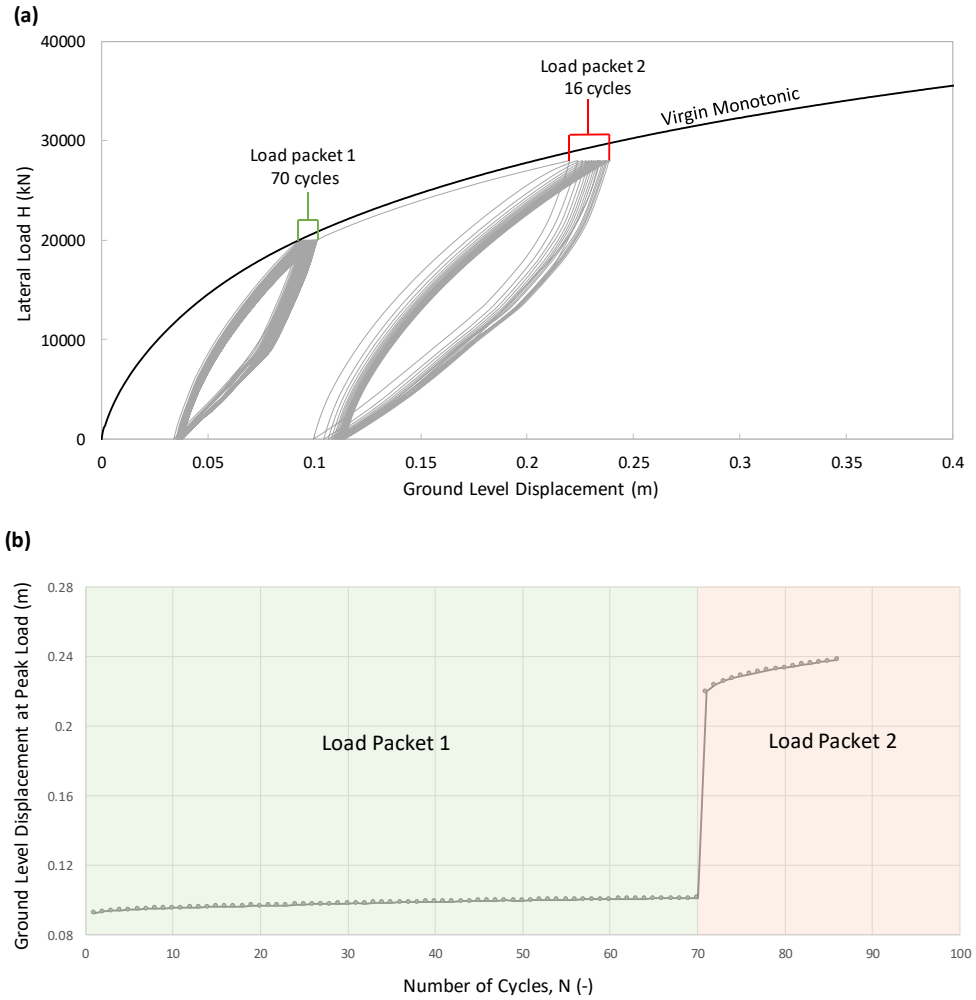

Figure 15: a) Cyclic load-displacement response at ground level and b) lateral displacement accumulation with number of cycles, of a pile with a diameter of 7.5 m and an embedment length of 25 m in a synthetic homogenous soil profile for Clay Unit A

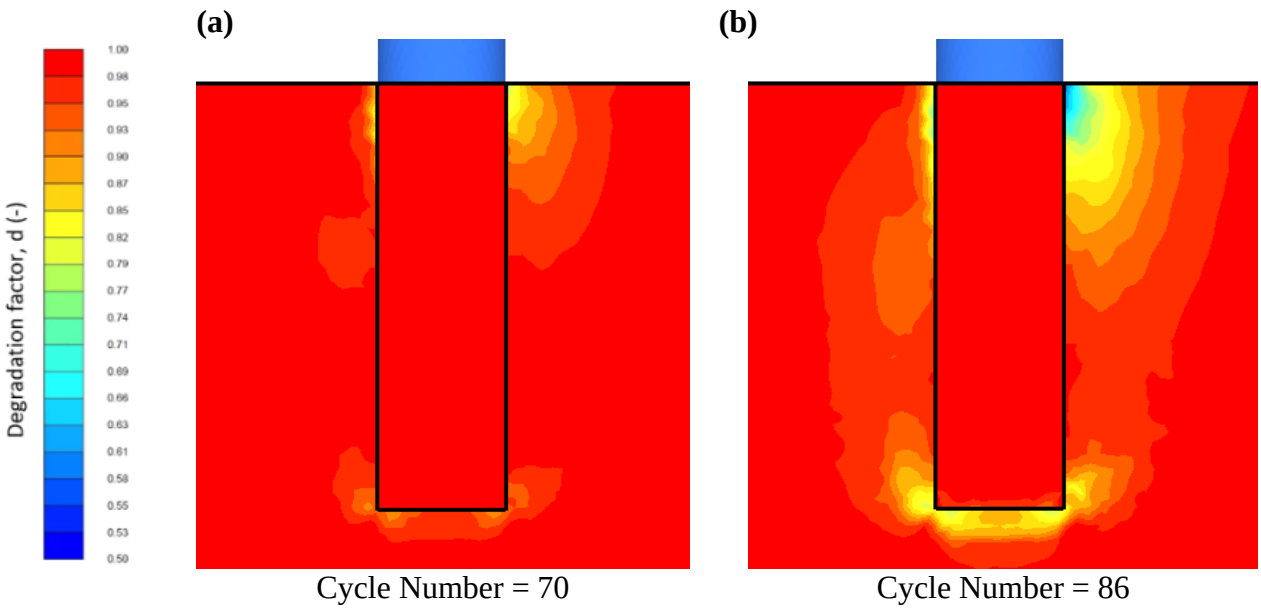

Figure 16: Predicted degradation factor around the pile at the end of load packet 1 and 2

5.3 Supplementary Information to Paper 2

5.3.1 Model Anisotropic Extension

The form of the PIMS model described in Paper 2 is isotropic with Lode angle dependency (termed PIMS-iso) and as a result the stress-strain response is not dependent on the angle of the major principal stress with respect to the sample axis (i.e. no inherent anisotropy is incorporated), which may not be representative of some natural clays. Therefore, if required, the model can be extended to include anisotropy (termed PIMS-aniso) by using a modified deviatoric stress tensor to define the yield and plastic potential functions for all of the micro models, following a similar approach to Prevost (1977), Grimstad et al. (2012) and Kouretzis et al. (2017). In this case, all occurrences of $\boldsymbol{s}$, when formulating each micro model (see Paper 2 for details), are replaced by a modified deviatoric stress tensor, $\bar{\boldsymbol{s}}$, defined by:

$$\bar{\boldsymbol{s}} = \boldsymbol{s} - \boldsymbol{\alpha}_{aniso} \tag{5.1}$$

where $\boldsymbol{\alpha}$ is the anisotropic shift tensor given by:

$$\boldsymbol{\alpha}_{aniso} = q_{ashift}\, \boldsymbol{r} \tag{5.2}$$

To model cross-anisotropy, which is the most prevalent type of anisotropy in soils due to the preferential fabric that develops during deposition, the traceless $\boldsymbol{r}$ tensor is given by:

$$\boldsymbol{r} = \begin{bmatrix} 1/3 & 0 & 0 \\ 0 & 1/3 & 0 \\ 0 & 0 & -2/3 \end{bmatrix} \tag{5.3}$$

where the vertical axis is in the *z*-direction. Figure 5.1 shows example shifted micro models in micro stress space, the input parameter q_{ashift} is introduced to control the level of anisotropic shift for each micro model (i.e. controls the permanent deviatoric back-stress of each micro model). It is important to note that the micro yield surfaces are still elastic-perfectly-plastic and hence the back-stress does not change with plastic strain. The yield strength m is now given by:

$$m = (q_{uc} - q_{ashift})\, R(\bar{\theta}) \tag{5.4}$$

Therefore, only one additional parameter ($q_{ashift,i}$) is needed to impose a degree of inherent anisotropy for each of the n micro models. This approach is considered to represent a rational framework to include anisotropy based on published laboratory studies, for example, interpretation of true triaxial tests on natural soft Pisa clay presented by Callisto and Calabresi (1998) showed the development of constant deviatoric strain contours with different shapes, shifted in the deviatoric plane. Example results from Callisto and Calabresi (1998) are presented in Figure 5.2, which could be matched directly by the model if an anisotropic shift tensor was included.

It is important to note that when including the anisotropic shift tensor within the model formulation, a modified Lode angle, $\bar{\theta}$, defined from $\bar{\boldsymbol{s}}$, must be used (i.e. $\boldsymbol{s}$ replaced by $\bar{\boldsymbol{s}}$ for model formulation). In addition, all model partial derivatives used to form the $\boldsymbol{D}_{ep}$ matrix must be calculated using the modified deviatoric stress tensor. This anisotropic extension is not explored here in any further detail; however, it is noted that it may be required to capture the response of certain natural clays under a range of different stress paths. Considering only the undrained shear strength (s_u), a comparison of the PIMS-iso and PIMS-aniso achievable s_u ratios under different typical laboratory tests is presented in Figure 5.3 and compared to measured test data. Within Figure 5.3, s_{ue} and s_{uc} are the undrained shear strengths from triaxial extension and compression tests respectively and s_{uss} refers to the undrained shear strength from an undrained direct simple shear test result. It can be seen from Figure 5.3 that there is a large scatter in the measured undrained shear strength ratios (i.e s_{ue}/s_{uc} and s_{uss}/s_{uc}) measured from different clays and therefore clearly a standard Tresca yield surface is unlikely to be suitable for a total stress model. The admissible zone of the PIMS-aniso model is shown to capture a significant amount of the measured laboratory data in terms of undrained shear strength. The PIMS-iso model is clearly less versatile; however, it is considered reasonable for some soil types. It should be noted, a reliable measurement of s_{ue} from triaxial extension tests is typically hard to achieve (Roscoe et al., 1964)

and hence a certain degree of error is likely with respect to the measured strength ratios presented in Figure 5.3.

5.3.2 Parallel Iwan Arrangement Wrapper Algorithm

The basic Parallel Iwan 'wrapper' algorithm used in Paper 2 is presented below. This algorithm could be applied to any existing implemented single surface constitutive model to extend it to a multi-surface Parallel Iwan model.

Parallel Iwan model arrangement wrapper algorithm:

1. *Enter soil model with the initial stress state ($\boldsymbol{\sigma}$), the total increment of strain ($\Delta\boldsymbol{\varepsilon}$), the model state variable array ($\boldsymbol{Statev}$), the user input parameter array ($\boldsymbol{Props}$) and set* $i = 0$
2. *Do steps 3 to 7, n times (where n is the number of micro models to be included) then leave with updated* $\boldsymbol{\sigma}$
3. $i = i + 1$
4. *Look-up and extract current micro model (i) parameters and weighting (w_i) from* $\boldsymbol{Props}$ *array saving them in micro model specific array ($\boldsymbol{Props}, \boldsymbol{i}$) and retrieve micro stresses for current micro model ($\boldsymbol{\sigma}_{micro,i}$) from* ***Statev*** *(micro stresses for each micro model are stored as state variables)*
5. *Call single surface user defined model subroutine (e.g. existing UMAT code), enter with* $\boldsymbol{\sigma}_{micro,i}$, $\boldsymbol{Props}, \boldsymbol{i}$, $\Delta\boldsymbol{\varepsilon}$ *and exit with* $\Delta\boldsymbol{\sigma}_{micro}$
6. *Update micro stresses* $\boldsymbol{\sigma}_{micro,i} = \boldsymbol{\sigma}_{micro,i} + \Delta\boldsymbol{\sigma}_{micro,i}$ *and overwrite previous values in* $\boldsymbol{Statev}$ *for current micro model stress state*
7. *Update model macro stresses* $\boldsymbol{\sigma} = \boldsymbol{\sigma} + w_i\, \Delta\boldsymbol{\sigma}_{micro}$

5.3.3 Normalisation of Backbone Curve

When using laboratory test data to develop stiffness or stress-strain backbone curves for calibrating the PIMS model, as discussed in Paper 2, it is convenient to introduce the following normalised variables:

$$\bar{\varepsilon}_q = I_r^* \varepsilon_q; \qquad I_r^* = \frac{3G_0}{2s_u}; \qquad \bar{q} = \frac{q}{2s_u}; \qquad \bar{G}_{sec} = \frac{G_{sec}}{G_0} \tag{5.5}$$

Vardanega and Bolton (2013) developed a stiffness reduction curve database for clay by collating data from a number of different previously published experimental results. The test data presented in Vardanega and Bolton (2013) was supplied to the author (P Vardanega, personal communication, 15 October, 2018) for use in this study. Figure 5.4 presents the Vardanega and

Bolton (2013) data along with some additional tests on North Sea OC clay from the Fugro testing database (specific site locations confidential).

As discussed in Paper 2, the normalisation approach should be applied to individual geotechnical soil units at a site for model calibration i.e. a different backbone curve calibration of each soil unit. Geotechnical soil units are identified as part of a large geotechnical site investigation based on the geological history, sample descriptions, index tests and general mechanical behaviour. Subsequently, the location-specific local G_0 and s_u values can be determined from seismic cone penetration tests (SCPTs) to develop local unnormalised stiffness backbone curves. On this basis, it is assumed that the normalised backbone curves $\overline{q}(\bar{\varepsilon}_q)$ and $\bar{G}_{sec}(\bar{\varepsilon}_q)$ are a unique feature of any particular geotechnical soil unit identified in an overall ground model. For a wind farm site investigation, it is common practice to perform in situ tests (e.g. SCPT) at each planned wind turbine location; however, typically few sampling boreholes on which laboratory testing can be undertaken, are performed.

The normalisation approach discussed above has been applied to the test data presented by Vardanega and Bolton (2013) for results in which s_u data were available. Figure 5.5 to Figure 5.8 show the normalised results for different geotechnical soil units. The tests were performed at different rates of loading; therefore, all data was corrected to a quasi-static 'slow' strain rate of 0.36 % per hour using the rate correction method presented in Paper 2 (Equation 17 in Paper 2) and assuming h = 0.05. It can be seen that there is a clear stiffness backbone curve trend for each geotechnical soil unit for which the PIMS model could be calibrated using the linear piecewise calibration approach discussed in Paper 2.

A number of empirical functions have been developed in the literature (e.g. Darendeli, 2001; Zhang et al., 2005; Kishida, 2008; Vardanega and Bolton, 2013) to represent the shear stiffness reduction curve. These models have been shown to provide a good fit with data at small to intermediate strain levels; however, the predicted response at intermediate to large strain levels is

typically poor. This can present a significant issue when such empirical stiffness reduction functions are used for geotechnical FEA in which it cannot be guaranteed that the strain levels will be below a certain strain threshold for the prescribed loading conditions. Although, it should be noted that this is less of an issue when nonlinear elasticity is used within an elastoplastic model, and a yield surface provides a strength/yield cut off.

Most proposed stiffness backbone functions use a $\gamma_{0.5}$ type parameter (i.e. the shear strain when $G/G_0 = 0.5$) which is typically related to plasticity index for clay (e.g. Darendeli, 2001; Zhang et al., 2005; Kishida, 2008; Vardanega and Bolton, 2013). Figure 5.9 presents a plot of $\gamma_{0.5}$ versus I_r^* derived from the Vardanega and Bolton (2013) database. It can be seen that $\gamma_{0.5}$ appears to be intrinsically dependent on the local I_r^* value of each test. This supports the validity of the proposed normalisation approach in which the shape of the backbone curve is a function I_r^*. Equation 5.6 below presents a proposed improved stiffness reduction function which uses the normalised variables and is considered suitably versatile to calibrate to laboratory data.

$$\bar{G}_{sec} = \left(\frac{1}{1 + \bar{\varepsilon}_q^{\,\bar{\varepsilon}_q\beta+\alpha}}\right)^{1/(\bar{\varepsilon}_q\beta+\alpha)} \qquad 5.6$$

The α value primarily controls the small strain to medium strain response and β mainly controls the medium to large strain response. Figure 5.10 presents example stiffness and stress-strain backbone curves from Equation 5.6 for different values of I_r^* (ranging from 250 to 2000) using $\alpha = 0.7$ and $\beta = 0.02$.

The response of the model can be conveniently represented by the normalised tangent stiffness $\bar{G}_{tan} = G_{\tan}/G_0$, where G_{tan} is the tangent shear stiffness which can be obtained by differentiating Equation 5.6 ($dG_{sec}/d\varepsilon_q$) and substituting into $G_{tan} = G_{sec} + \varepsilon_q \, dG_{sec}/d\varepsilon_q$. As discussed in Paper 2, it can then be shown that the normalisation approach adopted has the desirable feature that the area beneath the ($\bar{\varepsilon}_q, \bar{G}_{tan}$) curve is constrained to be equal to unity (i.e. $\int_0^\infty \bar{G}\, d\bar{\varepsilon}_q = 1$) and the maximum shear stress is equal to the prescribed undrained shear strength (i.e. $\tau_{max} = s_u$),

which is a significant advantage in comparison to other proposed stiffness reduction functions (e.g. Darendeli, 2001; Vardanega and Bolton, 2013).

5.4 Conclusions

A practical multi-surface total stress model – PIMS – is proposed to represent the monotonic and cyclic loading behaviour of clay, for cases where the soil is undrained. This model, together with associated finite element implementation and calibration procedures, has been developed specifically to facilitate robust geotechnical calculations for practical applications relating to offshore foundations.

The basic parallel Iwan framework that is adopted for the PIMS model is a well-established constitutive modelling approach, although there are few documented applications of this framework in geotechnical engineering. The parallel Iwan framework is relatively straightforward to explain (e.g. to clients, regulators and insurers) to implement (in finite element codes) and to calibrate (using routine site investigation procedures). As a result, it is considered particularly useful in a design context.

A detailed overview of a normalisation approach for clay is presented for parameter calibration, which makes use of the model for large offshore wind farm design feasible. It is also shown that this normalisation approach could be applied to improve existing stiffness reduction functions proposed in the literature.

The example 3D FEA presented demonstrates the practical application of the PIMS model. The analysis of three of the PISA test piles, although limited to monotonic behaviour, provides an indication of the predictive capabilities of the proposed modelling and calibration framework. A separate example of a monopile subjected to cyclic lateral loading demonstrates the robustness and feasibility of the model implementation, with the computed results consistent with expected forms of behaviour.

5.5 Figures

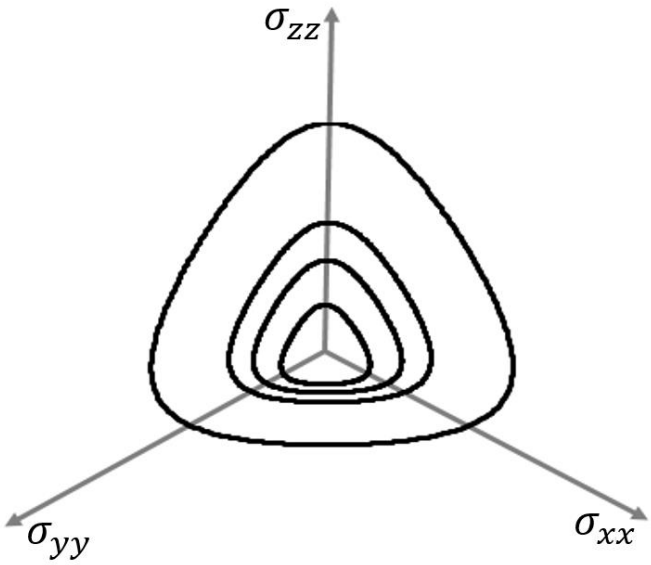

Figure 5.1:PIMS-aniso micro yield surfaces in micro stress space

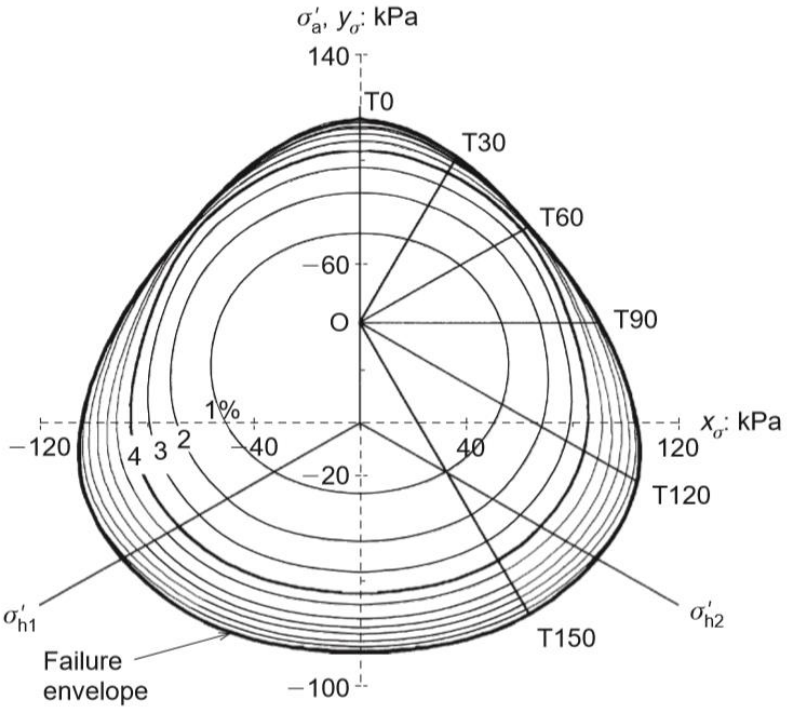

Figure 5.2: Shear strain contours from true triaxial tests on natural soft clay in the deviatoric plane for deviatoric strain values between 1% and 10 % (1 % strain increments presented), from Callisto and Calabresi (1998)

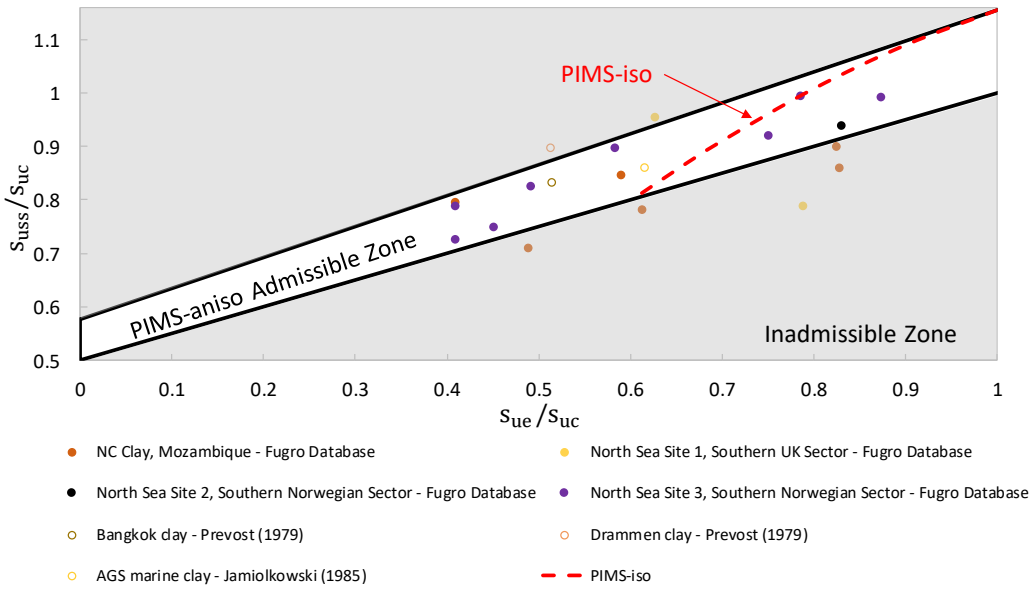

Figure 5.3: Admissible undrained shear strength from PIMS-iso and PIMS-aniso compared with laboratory data, published data from Wood (1990)

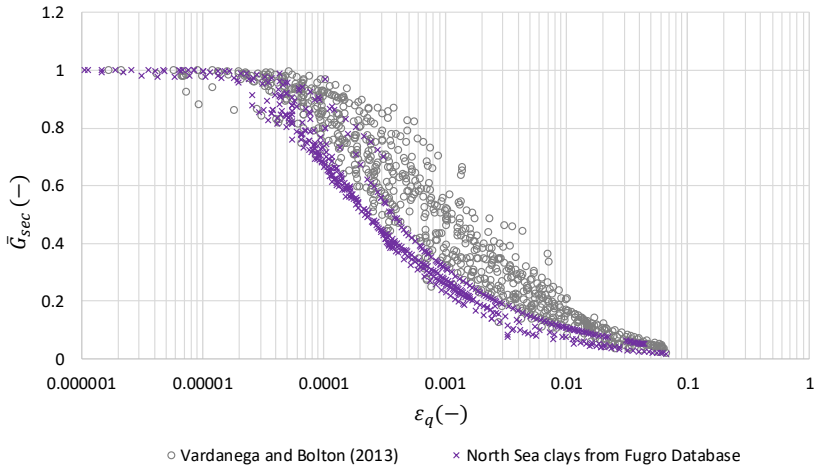

Figure 5.4: Experimental test data from Vardanega and Bolton (2013) and Fugro database with single normalisation applied to shear stiffness

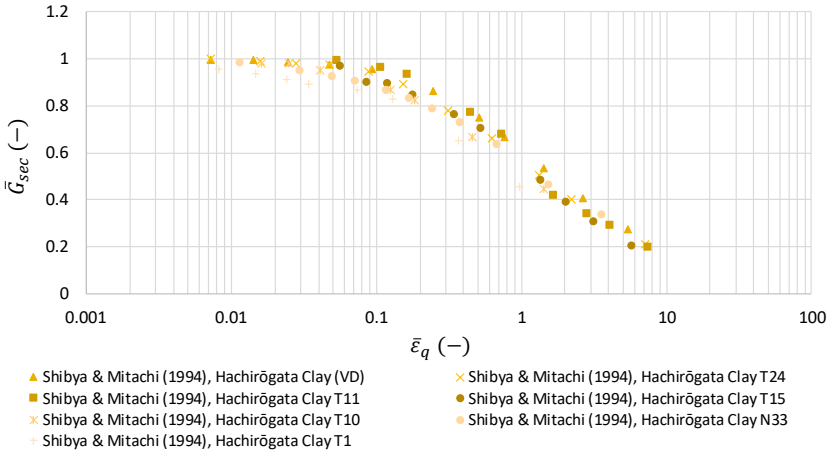

Figure 5.5: Hachirogata Clay from Shibya & Mitachi (1994) test data with double normalisation applied, summary of tests also available in Vardanega and Bolton (2013)

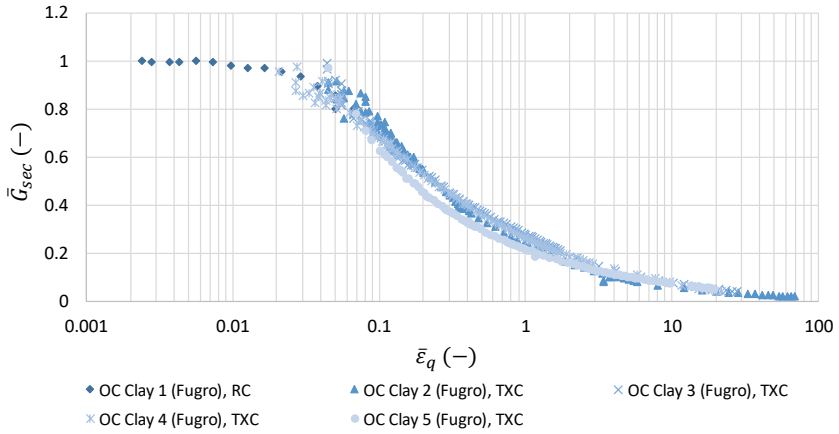

Figure 5.6: North Sea OC Clay unit test data from Fugro database with double normalisation applied

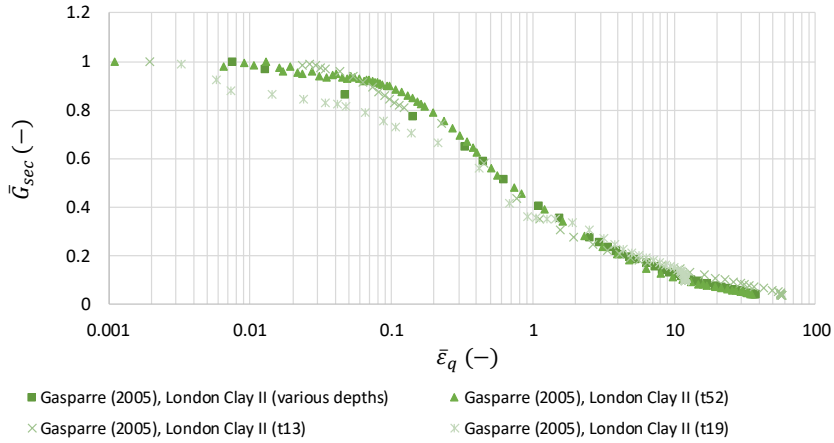

Figure 5.7: London Clay II test data from Gasparre (2005) with double normalisation applied, summary of tests also available in Vardanega and Bolton (2013)

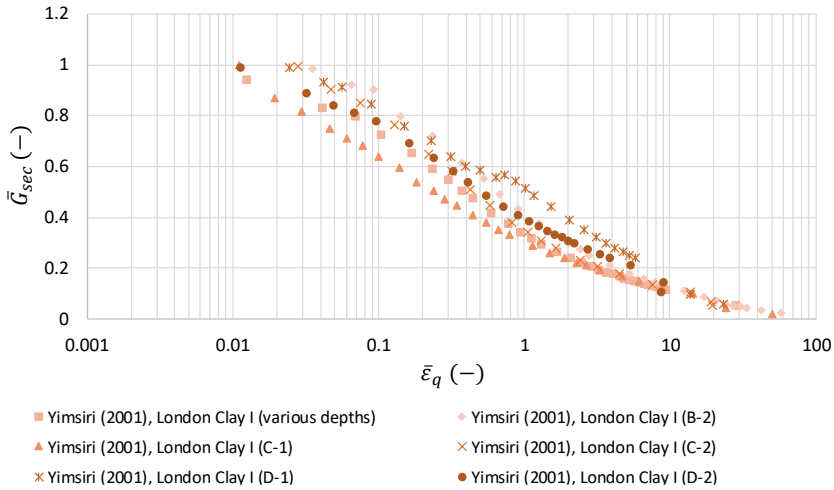

Figure 5.8: London Clay I test data from Yimsiri (2001) with double normalisation applied, summary of tests also available in Vardanega and Bolton (2013)

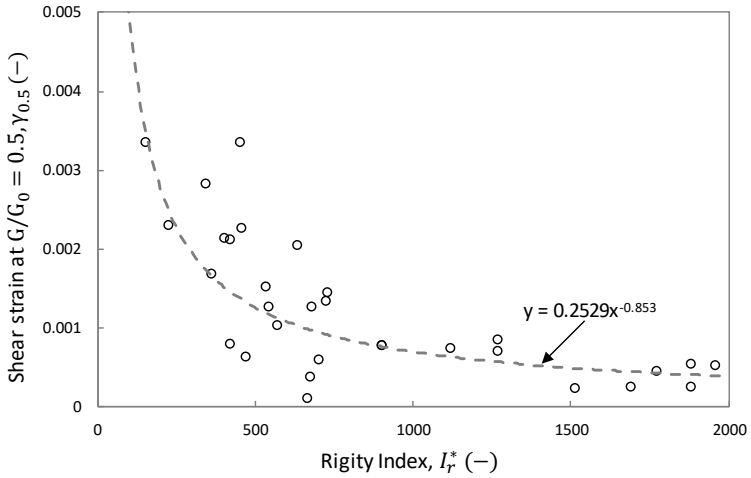

Figure 5.9 Shear strain at G/G_0 versus I_r^* with comparison to data from Vardanega and Bolton (2013) database with power curve trend line

(a)

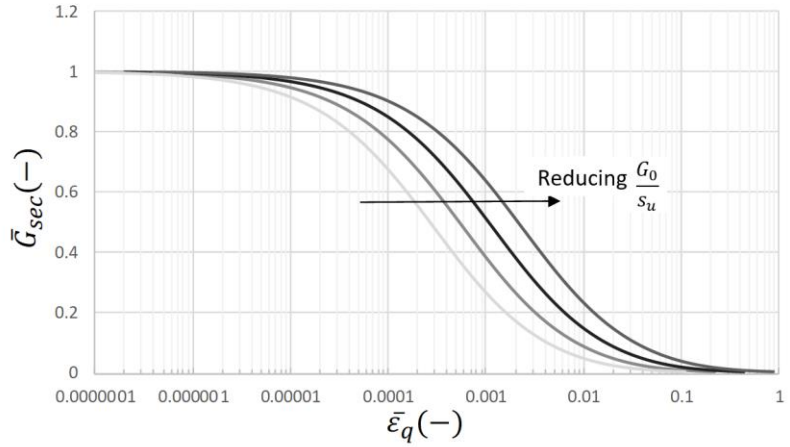

(b)

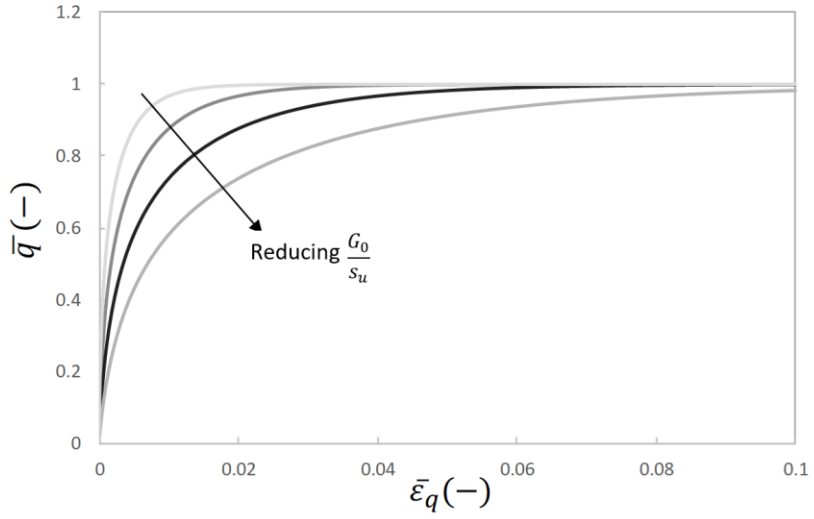

Figure 5.10: (a) Example stiffness backbone curves and (b) example stress-strain backbone curves using the proposed function with $\alpha = 0.7$ and $\beta = 0.02$

Section 6

DEVELOPMENT AND USE OF A BOUNDING SURFACE MODEL FOR SAND

Contents

6. DEVELOPMENT AND USE OF A BOUNDING SURFACE MODEL FOR SAND

6.1 Introduction

The motivation for the work presented in this section was two-fold: 1) to demonstrate the capability of a well-established advanced constitutive model to predict the response of laboratory element tests and foundation load tests and 2) to investigate the response of suction buckets under tension loading up to the point of cavitation.

As discussed in Sections 1 and 2, within the literature there are extensive examples of constitutive models being developed and used to perform single element simulations. However, there are few examples where detailed model calibration, to laboratory element test data, is followed by prediction of foundation load tests (field or centrifuge) with no back-calculation of the constitutive model parameters (i.e. design prediction). This is particularly the case for bounding surface type models for sand. As discussed in Section 2, single element simulations of laboratory tests (i.e. triaxial tests) using Manzari-Dafalias based models, have been shown to have an impressive predictive capability (e.g. Manzari and Dafalias, 1997; Dafalias and Manzari, 2004; Boulanger and Ziotopoulou, 2013; Taborda et al., 2014). Therefore, the bounding surface model proposed by Manzari and Dafalias (1997) and Dafalias and Manzari (2004), which is based on critical state soil mechanics principles, is the basis of the modelling procedure employed in this section. Several minor modifications were made to the original Manzari-Dafalias model to improve its predictive capability at element level for this study; however, the primary formulation was consistent with other Manzari-Dafalias type models presented in the literature.

The model presented in this section combines different aspects of other Manzari-Dafalias type models presented in the literature. However, the primary difference between the model outlined in this section and other Manzari-Dafalias type models presented in the literature (e.g. Manzari and Dafalias, 1997; Dafalias and Manzari, 2004; Taborda et al., 2014) is that it includes inherent anisotropy effects by the introduction of the so called ‘ anisotropic state parameter’. The inclusion of inherent anisotropy within the model is shown to be critical to ensure the accurate calibration of

laboratory element tests, under different stress paths, and to allow for reasonable prediction of a suction bucket under tension loading.

Tjelta (2015) presented the findings from three decades of field and model testing of suction bucket foundations in sand, within which it was shown that for typical storm loading rates the response of the sand is close to undrained. As a result, foundation designers are keen to take advantage of the increased mobilised resistance of suction buckets under fast tension loading rates in dense sand. For serviceability limit state design and ultimate limit state design, in which water cavitation is not a governing factor, FEA is routinely performed by designers to calibrate macro-element models (Sturm, 2017; OWA, 2019). The question is whether a reasonable load-displacement response is predicted by FEA when a constitutive model is calibrated to laboratory test data. To answer this question, FEA of suction buckets under tension loading was performed using a modified Manzari-Dafalias model for comparison with a number of different centrifuge model test results.

It should be noted that cyclic loading of suction buckets in dense sand is also important for design. Despite the response possibly being close to undrained for one cycle, when considering a full storm history, it is likely that drainage will occur. As a result, under certain cyclic loading conditions, drainage-induced upward ratcheting of the suction bucket can occur (Bienen et al., 2018). Although the potential for drainage-induced upward ratcheting is important for design, it is considered important to first demonstrate that the monotonic response under different loading rates can be predicted correctly by FEA before considering cyclic loading.

6.2 Paper 3

A detailed description of the work performed is given in Paper 3 titled, *Comparison of numerical simulations using a bounding surface model to centrifuge tests of axial loaded suction buckets in dense sand*.

6.2.1 Authorship

The contribution of the DEng candidate to this paper was approximately 80%. He produced all the FEA results and prepared the paper. The other authors guided the work, supplied the centrifuge data and reviewed the paper. The base UMAT implementation code for the original Manzari-Dafalias model (i.e. Dafalias and Manzari, 2004 formulation) was supplied by the University of Western Australia (UWA). Modifications to the model discussed in Paper 3 and conversion to a Plaxis UDSM were performed by the DEng candidate.

Comparison of numerical simulations using a bounding surface model to centrifuge tests of axial loaded suction buckets in dense sand

S Whyte[+*1], H J Burd[+], C M Martin[+], M F Randolph[~], B Bienen[~], M Rattley*, A Roy[~], M Stapelfeldt[-]

+ Department of Engineering Science, University of Oxford, Parks Road, Oxford, OX1 3PJ, UK
* Fugro GB Marine Limited, Wallingford, Oxfordshire, OX10 9RB, UK
~ Centre for Offshore Foundation Systems, The University of Western Australia, 35 Stirling Highway, Crawley WA 6009, Perth, Australia
- Institute of Geotechnical Engineering and Construction Management, Hamburg University of Technology, Harburger Schloßstraße 20, 21079 Hamburg

[1]Corresponding author: scott.whyte@eng.ox.ac.uk

Abstract:

This paper describes the application of a bounding surface plasticity model to the analysis of suction bucket pull-out tests in sand. Despite there being a significant number of examples in the literature of single-element calibration of advanced bounding surface constitutive models, there are few examples of model calibration followed by predictive foundation analysis of centrifuge or field test data. In this study a bounding surface model, based on the Manzari-Dafalias model architecture, is calibrated to laboratory element test data and subsequently used to predict the response of suction bucket foundations under tension loading for comparison with a number of different published centrifuge model test results. The constitutive model formulation presented in this paper includes several different model components from previously published Manzari-Dafalias models. It is demonstrated that careful formulation and calibration of the adopted constitutive model is essential to ensure an accurate prediction of suction bucket behaviour for different pull-out rates.

Keywords: Dense sand, Suction bucket foundations, Bounding surface plasticity, Centrifuge model tests

1 Introduction

Suction bucket foundations are an attractive option for the support of bottom-fixed offshore structures, since they have the potential to deliver significant cost savings and avoid the (often) excessive noise associated with installation of driven piles. A suction bucket foundation (also termed a suction-installed caisson) consists of a large cylinder that is open at the base and closed at the top with embedded length, L, to diameter, D, ratios typically between 0.5 and 1.0. Suction bucket foundations have historically been used to support oil and gas platforms (Bye et al., 1995; Tjelta, 2015); however, in recent years they have been used increasingly to support offshore wind turbines (Shonberg et al., 2017).

To support an offshore wind turbine, either a mono-bucket or a multi-bucket foundation system can be used. For bottom-fixed offshore wind turbines, the multi-bucket foundation system, consisting of a multi-legged jacket structure with a suction bucket supporting each leg, has proved to be a popular concept (Figure 1). Aberdeen Offshore Wind Farm and Borkum Riffgrund 1 and 2 are recent examples of offshore wind farms which have adopted multi-bucket foundation systems (Shonberg et al., 2017; Sturm, 2017).

Large overturning moments, generated from the thrust at the turbine hub and from wave action on the jacket, cause opposing ‘push-pull’ compression and tension axial loads on the foundations of a multi-bucket structure. Therefore, for design calculations, the critical loading of each bucket foundation is often simplified to consider only vertical loading (Thieken et al., 2014; Bienen et al., 2018a). For offshore wind turbines, the overturning moment in storm loading conditions is typically large relative to the restoring moment from the structure self-weight; therefore, short periods of net tension loading during extreme storm loading conditions may need to be considered in the design of multi-bucket structures. Additionally, many project stakeholders are keen to explore the potential for increased cost savings by designing the suction buckets to resist increased tension loads during short-term loading (Bye et al., 1995; Tjelta, 2015). As a result, the in-place performance of suction buckets under tension (rather than compression) loading conditions typically dominates the design. Despite this, there is still considerable uncertainty regarding the load-displacement response of

suction bucket foundations in sand under tension loading due to the lack of experimentally verified calculation methods. This is particularly the case as the suction bucket performance under tension loading depends on the loading rate. It should be noted that within this study the effect of different loading rates, on the foundation response, are considered in terms of the dissipation of excess pore pressures (i.e. by performing fully coupled flow-deformation FEA) rather than any fundamental rate dependency of the soil being included within the constitutive model formulation. This is considered acceptable as rate effects due to drainage are likely to govern within a sand when considering typical storm loading rates for offshore wind turbine foundations.

A large number of laboratory floor and centrifuge model tests have been carried out to investigate the behaviour of suction buckets in dense sand under axial loading (e.g. Iskander et al., 1993; Bye et al., 1995; Byrne, 2000; Feld, 2001; Kelly et al., 2004; Houlsby et al., 2005; Senders, 2008; Kakasoltani et al., 2011; Bienen et al., 2018a; Bienen et al., 2018b; Staplefeldt et al., 2019) with the majority of published examples in recent years being centrifuge model tests. These tests have shown that at fast pull-out rates a significantly higher mobilised capacity is achieved at a given displacement than for slow, drained pull-out; however, to mobilise the increased tension resistance, much higher displacements are required compared to compression loading. Additionally, some previous authors have presented fully coupled flow-deformation finite element analysis (FEA) using constitutive models which have been selected to capture the relevant soil behaviour (e.g. Bye et al., 1995; Thieken et al., 2014; Cerfontaine et al., 2015; Shen. et al., 2017, Whyte et al., 2017). Overall the experimental and numerical studies, taken together, have guided the offshore industry on best practice for the design of suction buckets in sand, particularly with respect to tension loading.

However, to optimise the design of suction buckets in sand, site-specific FEA is needed to predict the load-displacement response (serviceability assessment) for different loading and displacement rates. Such site-specific FEA is now performed routinely for suction buckets and is often used for calibration of macro-element foundation models used in structural analyses (Sturm, 2017; OWA, 2019). Results from site-specific FEA can be compared with those from centrifuge model tests in similar soil conditions to ensure that the predictions are reasonable (i.e. qualitative assessment).

However, there is a paucity of published direct comparisons between FEA predictions and centrifuge model test data where laboratory element testing has been performed on the centrifuge sand and used for model calibration. Given the large number of advanced constitutive models presented in the literature, and the limited verification of these models in realistic foundation boundary value problems, it may be difficult for designers and certification authorities to have confidence in FEA predictions. There is therefore a pressing need for more cases to be presented in the literature of the calibration of advanced models to laboratory data, together with comparison of FEA predictions to foundation load tests (i.e. completing the model verification/validation process). This is particularly important for suction buckets in sand under axial loading since considerable uncertainty typically exists in predicting the uplift behaviour.

The most well-established and widely used constitutive models for sand are based on bounding surface plasticity and incorporate the state parameter concept. A significant proportion of these models are built upon the model architecture presented by Manzari and Dafalias (1997). Extensive examples of Manzari-Dafalias type models have been presented in the literature (e.g. Papadimitiou and Bouckovalas, 2002; Dafalias and Manzari 2004; Dafalias et al., 2004; Taiebat and Dafalias, 2008; Loukidis and Salgado, 2009; Lashkari, 2010; Boulanger and Ziotopoulou, 2013; Golchin and Lashkari, 2014; Taborda et al., 2014; Petalas et al., 2019) with comparisons of single-element simulations to laboratory test data; these studies highlight the impressive predictive capability of the models at an element level for a range of initial stress and state conditions. However, despite this, there are very few examples of model calibration to laboratory test data followed by FEA of centrifuge or field foundation load test experiments, particularly with respect to suction buckets.

Thieken et al. (2014) performed FEA of suction buckets under axial tension loading using the hypoplastic model proposed by Von Wolffersdorff (1996) and compared the predictions with results from a laboratory floor model test performed by Iskander (1993) and a small-scale field test performed by Houlsby et al. (2006). The work presented an example of modelling suction buckets in dense sand using FEA; however, an arbitrary set of constitutive model parameters was used due to the lack of laboratory element tests available for calibration.

This paper describes the calibration of a bounding surface constitutive model of the Manzari-Dafalias type to laboratory element test data. The calibrated model is then applied to a relatively complex boundary value problem involving numerical simulation of centrifuge model tests on suction buckets under axial loading. A comparison of the responses observed in the centrifuge model tests and the numerical analyses predictions provides additional insight into the most important aspects of the constitutive model when performing FEA of suction buckets under tension loading. The influence of dilation behaviour, suction bucket pull-out rate, sand layering and anisotropy are investigated through sensitivity analyses.

2 Constitutive Model

2.1 Formulation

The bounding surface model proposed by Manzari and Dafalias (1997), which is based on critical state soil mechanics principles, is the basis of the numerical modelling employed in this study. The general framework for this constitutive model, termed the Manzari-Dafalias model architecture, is outlined in detail by several authors (e.g. Dafalias and Manzari, 2004; Loukidis and Salgado, 2009; Taborda et al., 2014); however, there are subtle differences in the formulations presented by the different authors. The formulation of the Manzari-Dafalias type model used here is specified in Table 1 (which includes Equations 1 to 21) and described below. For the model formulation, compression is taken to be positive.

2.1.1 Model surfaces

The model is formulated in a normalised deviatoric plane (Figure 2a) using a deviatoric stress ratio tensor, $\mathbf{r} = \mathbf{s}/\mathrm{p}'$, where the mean effective stress and deviatoric stress tensor are given by $\mathrm{p}' = \frac{1}{3}\mathrm{tr}\,\boldsymbol{\sigma}$ and $\mathbf{s} = \boldsymbol{\sigma} - \mathrm{p}'\,\mathbf{I}$, where $\boldsymbol{\sigma}$ is the effective stress tensor and $\mathbf{I}$ is the second-order identity tensor. The model includes a critical state surface (Equation 7, See Table 1), dilatancy surface (Equation 8, See Table 1) and bounding surface (Equation 10) in stress space (as shown in Figure 2a), all of which control the evolution of the yield surface, f, and plastic potential function, g, during a strain increment.

All of the surfaces are open-cones in stress space (Figure 2b). The yield surface, which defines the onset of plasticity, is a circle in the normalised deviatoric plane with the back-stress ratio tensor $\boldsymbol{\alpha}$ defining $\mathbf{r}$ at the centre (Figure 2a) and $\sqrt{2/3}\mathrm{m}$ defining the radius in the normalised deviatoric plane. In the model adopted for this study the yield surface only hardens kinematically and hence m is constant; this is consistent with most Manzari-Dafalias type models presented in the literature (e.g. Dafalias and Manzari, 2004; Loukidis and Salgado, 2009; Taborda et al., 2014). However, this modelling approach contrasts with the original Manzari and Dafalias (1997) formulation which included combined isotopic and kinematic hardening of the yield surface. The dilatancy, bounding and critical state surfaces are generally defined to be non-circular in the deviatoric plane (e.g. Dafalias and Manzari, 2004; Loukidis and Salgado, 2009; Taborda et al., 2014), with their shape defined as a function of the Lode angle which is given by,

$$\theta = \frac{1}{3}\sin^{-1}\left(-\frac{3\sqrt{3}}{2}\frac{\det \mathbf{s}}{\left(\frac{1}{2}\,\mathbf{s}:\mathbf{s}\right)^{\frac{3}{2}}}\right) \tag{22}$$

The maximum value of $R(\theta,\beta)$ given by Equation 6 is $R = 1$ when $\theta = -30°$ (triaxial compression) and the minimum value is $R = \beta$ when $\theta = +30°$ (triaxial extension). Therefore, the critical state, bounding and dilatancy surfaces are defined in stress space by M_{cs}, M_b, M_d and β where M_{cs}, M_b, M_d are the (fixed) values of q/p' in triaxial compression for each surface, and $q = \sqrt{\frac{3}{2}\,\mathbf{s}:\mathbf{s}}$; the Lode angle shape parameter, β, determined for the critical state surface is assumed to be the same for the dilatancy and bounding surfaces.

The critical state surface is fixed in stress space; however, the dilatancy and bounding surfaces evolve during shearing as the state parameter, ψ, changes. The value of ψ is determined from the critical state line in $e - p'$ space using Equations 4 and 5. The relationships between the state parameter and the maximum size (corresponding to triaxial compression) of the dilatancy and bounding surfaces (i.e. M_d and M_b) are given by Equations 9 and 11, respectively. The shapes of each surface in the deviatoric plane, for different Lode angles, are given by Equations 8 and 10. In

Equations 9 and 11 an 'anisotropic state parameter', ψ_A, is used in place of ψ in the current model; further details on the anisotropic state parameter are given in Section 2.1.4. It should also be noted that Equation 11 differs slightly from the original function proposed by Li and Dafalias (2000) to include Macaulay brackets (i.e. $\langle * \rangle = 0$ for $* < 0$ and $\langle * \rangle = *$ for $* > 0$) which ensures that the bounding surface is never inside the critical state surface. The state parameter dependency of the bounding and dilatancy surfaces means that the model can be used to simulate material response for different states (p' and e) with a single set of parameters.

2.1.2 Mapping rules for dilatancy and bounding surfaces

During plastic loading the distances between the current stress point and the dilatancy surface, d_d, and bounding surface, d_b, are used to control the plastic potential and the hardening modulus respectively. As discussed by Andrianopoulos et al. (2005), there are several possible mapping rules that could be used to determine the so-called 'image' stress ratio points on the dilatancy and bounding surfaces to determine d_d and d_b. The method used here to determine the image stress ratios and in turn the distances, is based on the mapping rule proposed by Manzari and Dafalias (1997) and presented schematically in Figure 2a. The distances between the current stress state and the image points are given by:

$$d_d = \left(\boldsymbol{\alpha}_d^{\theta} - \boldsymbol{\alpha}\right) : \mathbf{n} \tag{23}$$

$$d_b = \left(\boldsymbol{\alpha}_b^{\theta} - \boldsymbol{\alpha}\right) : \mathbf{n} \tag{24}$$

where the back-stress image points on the dilatancy and bounding surfaces, defined as $\boldsymbol{\alpha}_d^{\theta}$ and $\boldsymbol{\alpha}_b^{\theta}$ respectively, are determined by:

$$\boldsymbol{\alpha}_{\mathbf{d}}^{\theta} = \sqrt{\frac{2}{3}}\left(M_d^{\theta} - m\right)\mathbf{n} \tag{25}$$

$$\boldsymbol{\alpha}_b^{\theta} = \sqrt{\frac{2}{3}}\left(M_b^{\theta} - m\right)\mathbf{n} \tag{26}$$

and $\mathbf{n}$ is the loading tensor which is a traceless unit tensor that is normal to the yield surface and is obtained by:

$$\mathbf{n} = \frac{\mathbf{r} - \boldsymbol{\alpha}}{\sqrt{\frac{2}{3}}m} \tag{27}$$

As discussed by Dafalias and Manzari (2004) the rationale for using equivalent back stress ratios (i.e. $\boldsymbol{\alpha}_{\mathbf{d}}^{\theta}$ and $\boldsymbol{\alpha}_{\mathrm{b}}^{\theta}$) for the mapping rule, as opposed to stress ratios, is the resulting simplicity in formulation of the kinematic hardening rule.

2.1.3 Hardening modulus and stress-dilatancy

The stress-dilatancy response of the model is controlled by the gradient of the plastic potential at the current stress state, which is calculated by Equation 13. The volumetric component of the gradient of the plastic potential (i.e. $\frac{1}{3}A_0 d_d \mathbf{I}$) is based on the distance between the dilatancy surface and the current stress point (i.e. d_d) and an empirical stress-dilatancy constant, A_0. By comparing the gradients of the yield surface and the plastic potential function (Equations 12 and 13) it can be seen that the flow rule is non-associated since in general $\frac{\partial f}{\partial \boldsymbol{\sigma}} \neq \frac{\partial g}{\partial \boldsymbol{\sigma}}$. However, normality in the deviatoric plane is assumed in this study, which is consistent with Taborda et al. (2014), but in contrast to Dafalias and Manzari (2004) who incorporated Lode angle dependency in the deviatoric part of the plastic potential function.

There is a lack of consensus in the literature on the formulation of the hardening modulus within Manzari-Dafalias type models and as a result many different forms have been published to fit laboratory test data. However, typically the hardening modulus is set to be a function of the distance between the current stress point and the bounding surface (i.e. d_b), the current mean effective stress, the current void ratio, and an elastic shear modulus constant. The hardening modulus, H, is determined from Equation 14 using the current d_b with the variable h (Equation 15) included to improve the overall prediction of the model based on recommendations by Dafalias and Manzari (2004). The denominator of Equation 15 is included to account for stress reversals, where $\boldsymbol{\alpha}_{\mathrm{in}}$ is the value of $\boldsymbol{\alpha}$ at the initiation of a new loading process and is updated only when $(\boldsymbol{\alpha} - \boldsymbol{\alpha}_{\mathrm{in}}) : \mathbf{n} < 0$. The influence of the current void ratio on the hardening modulus is included using a linear function of void ratio (Equation 16), within which $e_h = e \leq e_{max}$ where e_{max} is the maximum void ratio. The effect of mean effective stress on the hardening modulus is included using a power function

(Equation 16) where the exponent, μ, is a parameter as proposed by Papadimitriou and Bouckovalas (2002).

2.1.4 Inherent anisotropy and state parameter

Laboratory element testing presented in the literature has shown that the angle, χ, of the major principal stress, σ'_1, with respect to the sample axis and the value of the intermediate principal stress ratio, $\zeta = \frac{\sigma'_2 - \sigma'_3}{\sigma'_1 - \sigma'_3}$, have a significant effect on the overall mechanical response of sand (Dafalias et al., 2004). During shearing under triaxial extension conditions ($\chi = 90°, \zeta = 1$), a significantly softer and less dilatant response is observed compared with triaxial compression conditions ($\chi = 0°, \zeta = 0$). This phenomenon, termed fabric anisotropy, was incorporated in a generalised constitutive model framework by Dafalias et al. (2004) by using a second-order fabric tensor, **F**, in combination with the loading tensor, **n**, to derive a scalar measure of anisotropy, A, as presented in Equation 18. The parameter a, which defines **F**, is a measure of the particle orientation, with the most common value being in the range $0 < a < \frac{1}{3}$, which corresponds to a preference towards a horizontal orientation (Papadimitriou et al., 2005). To capture the observed trends from laboratory test data for different loading directions, the position of the critical state line, CSL, in $p' - e$ space was set as a function of A by Dafalias et al. (2004). Using a similar approach, Shen et al. (2017) set the CSL to be a function of Lode angle. However, these approaches introduce a non-unique CSL that depends on sample fabric and loading direction, which is contrary to one of the fundamental concepts of critical state soil mechanics where the CSL is unique for a particular soil. As discussed by Jefferies and Been (2016), the idea of a CSL that depends on loading direction is likely to be a result of the phase-transformation line, which has been shown to depend on loading direction and initial fabric, being wrongly identified as the CSL for tests performed on initially loose sands.

Therefore, within the model used here an anisotropic fabric scaling factor, f_A, which is a function of the anisotropic scalar, A, has been introduced to determine an anisotropic state parameter ψ_A (Equation 19). As a consequence, the size of the dilatancy and bounding surfaces, and therefore the stress-dilatancy and hardening modulus response, vary with loading direction by way of adjusting

the influence of the state parameter rather than modifying the CSL. According to Dafalias et al. (2004), this approach captures the general trends observed from laboratory test data; importantly, it also maintains a unique CSL. Interpreted triaxial extension and compression test data presented by Azeiteiro et al. (2017) appear to confirm this hypothesis that the phase transformation (i.e. dilatancy surface) and peak stress ratio (i.e. bounding surface) depend on the state parameter and the loading direction to a higher degree than β; however, it is acknowledged that further high-quality laboratory testing is needed to confirm this. The function (Equation 20) used in the current model is based on the function proposed by Dafalias et al. (2004), though it has improved versatility for calibration to laboratory data.

2.1.5 Elastoplastic stiffness matrix

For an infinitesimal strain increment, $\delta\boldsymbol{\varepsilon}$, during plastic loading the resulting increment of the stress, $\delta\boldsymbol{\sigma}$, is

$$\delta\boldsymbol{\sigma} = \mathbf{D}^{\mathrm{ep}}\delta\boldsymbol{\varepsilon} \tag{28}$$

where,

$$\mathbf{D}^{\mathrm{ep}} = \mathrm{E}_{\mathrm{fact}}\mathbf{D}^{\mathrm{e}} - \frac{\mathrm{E}_{\mathrm{fact}}\mathbf{D}^{\mathrm{e}}\left(\frac{\partial \mathrm{g}}{\partial \boldsymbol{\sigma}}\right)\left(\frac{\partial \mathrm{f}}{\partial \boldsymbol{\sigma}}\right)^{\mathrm{T}}\mathrm{E}_{\mathrm{fact}}\mathbf{D}^{\mathrm{e}}}{\left(\frac{\partial \mathrm{f}}{\partial \boldsymbol{\sigma}}\right)^{\mathrm{T}}\mathrm{E}_{\mathrm{fact}}\mathbf{D}^{\mathbf{e}}\left(\frac{\partial \mathrm{g}}{\partial \boldsymbol{\sigma}}\right) + \mathrm{H}} \tag{29}$$

The isotropic elastic stiffness matrix, $\mathbf{D}^{\mathrm{e}}$, is formulated using Equations 1 and 2. It should be noted that a hypoelastic formulation is used; however, a hyperelastic formulation, i.e. derived from a free energy potential, is preferred and should be included as a further improvement to the model. Therefore this elastic formulation should be used with caution, particularly for cyclic loading, since it results in an non-conservative elastic response which is not strictly thermodynamically acceptable.

The parameter $\mathrm{E}_{\mathrm{fact}}$ is introduced within the model to account for the degradation of the elastic stiffness that is known to occur during shearing (Loukidis and Salgado, 2009). An alternative approach, utilised by Loukidis and Salgado (2009) and Taborda et al. (2014), would be to include an explicit elastic stiffness degradation rule to account for this. However, the simplified approach adopted here is considered sufficient since the nonlinear elastic behaviour under very small strains

(i.e. within the yield surface) is not considered to be of particular significance for the current study, in which the overall response is driven principally by the elastoplastic response of the constitutive model. The $\mathbf{D}^{e}$ matrix used to formulate $\mathbf{D}^{ep}$ is not of great importance when simulating the drained response; however, it has a significant effect on the undrained response. This is due to the influence of the elastic bulk modulus on the stress-dilatancy response when the volumetric strain is constrained (e.g. for undrained or partially drained).

Within the formulation discussed above the occurrences of p' in the model are replaced by p'_t, where $p'_t = p' + p'_c$. This adds an apparent cohesion to the model; this was found to reduce the risk of convergence issues at low mean effective stresses. A value of 5 kPa was adopted for p'_c within this study for all analyses performed, which is consistent with the value adopted by Cerfontaine et al. (2015) for modelling a suction bucket in dense sand using a multi-surface model. The use of an apparent cohesion value primarily affects the drained strength at very low mean effective stresses. However, this is likely to have a small effect on the response of a suction bucket under tension loading which is governed by the skirt interface properties. For loading rates that result in an undrained or partially drained response the choice of p'_c also has a minimal effect since the response is dominated by significant dilation induced negative excess pore water pressures.

2.2 Parameter calibration

The following section outlines calibration of the model parameters to laboratory element test data for University of Western Australia (UWA) silica sand. The e_{max} and e_{min} are 0.84 and 0.50, respectively, and the particle size distribution is presented in Figure 3. This sand was used for model calibration as it is the soil used for the main suction bucket centrifuge model experiments that form the basis for verification of the model performance in FEA (Section 3.2). It is also considered broadly representative of a North Sea sand (see Figure 3). The laboratory element tests presented in this section were performed at the UWA and Fugro UK laboratories. The reconstituted test specimens were prepared to their required initial void ratio(s) using the water sedimentation and moist tamping sample preparation methods (details of the methods are given by Ishihara, 1993).

The laboratory testing performed was representative of a standard offshore site investigation testing programme and hence the model calibration approach described is considered feasible for application to a typical industry project dataset.

The CSL is defined by five parameters: $e_{cs,ref}$, λ_c, ξ define the CSL in $e - p'$ space and M_{cs}, β define the gradient in $p' - q$ space. The elastic behaviour is controlled by a further three parameters (G_{ref}, ν and n) and the elastic threshold (i.e. size of the yield surface) is defined by the parameter m. A group of seven parameters (n^b, n^d, h_0, A_0, μ, e_{max} and E_{fact}) influence the elastoplastic and stress-dilatancy response. In addition, the fabric orientation parameter a and the fabric scaling constants b and c play a role in modifying the response in non-triaxial compression conditions to match laboratory observations.

After interpreting parameters from the available laboratory tests, a calibration exercise is required to ensure that the single-element response in the FEA is comparable to observed behaviour from laboratory tests. The parameters are calibrated using a hierarchical approach. The calibration sequence and the laboratory tests that should ideally be employed for the calibration are specified in Table 2. A detailed description of the calibration process has been given by several authors who focused on single-element calibration of Manzari-Dafalias type models (e.g. Loukidis and Salgado, 2009; Taborda et al. 2014) and hence only a brief overview of the parameter calibration for UWA silica sand is given below.

2.2.1 UWA silica sand constitutive model calibration

The elastic parameters, G_{ref} and n, were calibrated by fitting Equation 1 to measured shear modulus data from bender element tests, G_0, as shown in Figure 4. Direct determination of the small-strain Poisson's ratio, ν, from laboratory data requires high resolution axial and radial local strain gauges; however, such data were not available. A value of ν = 0.15 was therefore assumed which is consistent with values reported by Loukidis and Salgado (2009) for silica sand. Due to the absence of available repeat loading resonant column tests or small-amplitude cyclic triaxial tests, the value of m (controlling the size of the elastic zone) was assumed as m = 0.06, which is consistent with

values reported by other authors for silica sands (e.g. Loukidis and Salgado, 2009; Taborda et al., 2014).

Since the model formulation is based on the state parameter, the CSL in $e - p'$ space is of considerable importance for the calibration of the other parameters (e.g. n^d, n^b, h_0, A_0) and therefore must be determined early in the calibration process (see Table 2). Figure 5 presents the calibrated CSL based on Equation 4 to represent the results from drained and undrained triaxial compression tests on UWA silica sand. Determining the CSL at low void ratios (i.e. dense state) is very difficult as it requires specialised high pressure triaxial equipment. Figure 6 presents a comparison of the calibrated CSL shape to other published curves, with the void ratio normalised by the critical state void ratio at 10 kPa. As can be seen from Figure 5, if considering only the available test data, the CSL could be represented well with a different curve (i.e. a straight line in $e - \ln p'$ space). However, based on other CSL experimental data (Figure 6) this would to lead to an overprediction of the critical state p' at low void ratios, which in turn would significantly overpredict the undrained strength. Therefore the CSL (Figure 5) was calibrated using both the available data and other CSL sand data trends presented in the literature (Figure 6).

The slope of the CSL in $p' - q$ space, under triaxial compression conditions (i.e. M_{cs}), was found to be 1.25. This value is consistent with values reported by Verdugo and Ishihara (1996) for Toyoura sand, which has a similar particle size distribution, and corresponds to a friction angle, φ'_c of 31.2°. Based on the available experimental data, it was not possible to identify the slope of the CSL for triaxial extension conditions (i.e. $M_{ecs} = \beta M_{cs}$) due to excessive sample necking and shear localisation at axial strains greater than about 5%. Therefore, M_{ecs} was assumed to be 0.90 based on values reported by Dafalias and Manzari (2004) and Azeiteiro et al. (2017). This corresponds to β = 0.72, which falls within the typical range of 0.67 – 0.75 for silica sand as reported by Loukidis and Salgado (2009).

The n^d and n^b values in Equations 9 and 11 were obtained by considering the state parameter (based on the derived CSL) at the phase transformation line and the peak stress ratio for each triaxial test. The stress-dilatancy constant, A_0, was then obtained from the measured dilatancy, D, versus $M_{cs} - M_d$ response (Figure 7). The dilatancy, D, is determined from the following expression:

$$D = \frac{d\varepsilon_v^p}{d\varepsilon_q^p} \approx \frac{\delta\varepsilon_v - \delta\varepsilon_v^e}{\delta\varepsilon_q - \delta\varepsilon_q^e} \approx \frac{\left(\varepsilon_{v,i+1} - \varepsilon_{v,i}\right) - \frac{p'_{i+1} - p'_i}{E_{fact}K}}{\left(\varepsilon_{q,i+1} - \varepsilon_{q,i}\right) - \frac{q_{i+1} - q_i}{3E_{fact}G}} \tag{30}$$

The parameters K and G, which were assumed to be constant for each step *i*, are the elastic bulk and shear modulus used to form the $\mathbf{D}^e$ matrix in the constitutive model. The changes in total volumetric strain, $\delta\varepsilon_v$, and deviatoric strain, $\delta\varepsilon_q$, across each increment (i to $i+1$), were obtained from triaxial test data in which $\varepsilon_v = \varepsilon_a + 2\varepsilon_r$ and $\varepsilon_q = 2/3(\varepsilon_a - \varepsilon_r)$, where the subscripts a and r denote the axial and radial directions, respectively (compression positive). It can be shown that $D = \sqrt{2/3}\,A_0(q/p' - M_d)$ for triaxial conditions (see Dafalias and Manzari, 2004). Hence, A_0 is determined using the measured triaxial data, by plotting D versus $\sqrt{2/3}(q/p' - M_d)$ (Figure 7), in which M_d is determined from Equation 9. From Equation 30, when $\delta\varepsilon_v = 0$ (i.e. undrained conditions) the magnitude of plastic volumetric strain is equal to the magnitude of elastic volumetric strain (i.e. $\delta\varepsilon_v^p = -\delta p'/E_{fact}K$) and hence the elastic bulk modulus has a significant effect on the stress-dilatancy response in this case. As shown by Loukidis and Salgado (2009), the use of bender element test data to calibrate the elastic stiffness properties, an approach in which elastic stiffness degradation is not accounted for, results in a significant discrepancy between the stress-dilatancy responses interpreted from drained and undrained tests. Therefore, as discussed above, the parameter E_{fact} was incorporated within the $\mathbf{D}^{ep}$ matrix to reduce the elastic stiffness during plastic loading. The value of E_{fact} was calibrated to ensure that the undrained and drained stress-dilatancy responses were broadly similar, as shown on Figure 7.

Finally, the anisotropy parameters (a, b, c) were derived using an iterative approach to best match the triaxial extension (up to the point at which excessive necking occurs) and direct simple shear data, thus accounting for testing under different loading directions in stress space.

The calibrated parameter set is presented in Table 3. Single-element simulations compared to laboratory data are presented in Figure 8 and Figure 9, from which it can be seen that a reasonably good agreement between the model and the measured data is obtained across a large range of initial conditions (i.e. initial e and p') and different test types (i.e. undrained/drained triaxial and undrained direct simple shear). For each of the undrained triaxial extension and direct simple shear tests an additional simulation was performed with anisotropy effects removed from the model. The data in Figure 9 indicate that when isotropy is assumed (i.e. when Equations 18 to 21 are not included in the model formulation) a significant overprediction of the mobilised stress response occurs in undrained triaxial extension and direct simple shear tests. This is because the difference in response is due only to the shape of the surfaces in the deviatoric plane (controlled by β), an effect that appears to be insufficient to capture the measured response from undrained laboratory element tests. Therefore, inherent anisotropy effects must be considered within the constitutive model to avoid overprediction for any boundary value problem in which a triaxial compression stress path is not expected to dominate the overall response.

2.2.2 UWA silica sand permeability-void ratio model

Since fully coupled flow-deformation FEA is to be conducted (Section 3) it is important to account for the dependency of permeability on void ratio. The permeability is assumed to depend on void ratio according to:

$$\log\left(\frac{k}{k_0}\right) = \frac{\Delta e}{c_k} \tag{31}$$

where k is the current (isotropic) permeability, k_0 is the initial permeability (i.e. at the initial e value) and c_k is a constant parameter. A value of $c_k = 0.48$ was found to represent well the permeability testing of UWA silica sand reported by Tran (2005), as shown in Figure 10. Back-calculation of k from in situ permeability tests performed in centrifuge model experiments reported by Senders (2008) also compares well with the data presented in Figure **10**.

3 Finite Element Analysis

3.1 Model set up

Axisymmetric fully coupled flow-deformation FEA of a suction bucket undergoing pull-out was performed for several different cases using the commercial finite element code Plaxis (Plaxis, 2017). The constitutive model specified in Section 2 has been implemented as a user-defined soil model in Plaxis, as a dynamic link library (DLL), programmed in Fortran. This DLL routine receives information on the current stress state ($\boldsymbol{\sigma}$) the current state variables and an overall strain increment ($\Delta\boldsymbol{\varepsilon}$). The model then delivers updated stresses and state variables corresponding to the end of the increment, employing an explicit sub-stepping approach with automated error control, based on the recommendations given by Sloan et al. (2001).

The soil domain for each analysis was discretised using approximately 7,000 15-noded triangular elements. The soil was modelled using the parameters presented in Table 3. A coefficient of earth pressure at rest, K_0, of 0.45 was assumed for all analyses. The suction bucket was modelled as a non-porous linear elastic material.

The sides of the soil domain were fixed radially, and the base of the model was fixed radially and vertically. An impermeable boundary was set at the axis of symmetry and the pore pressures at the other boundaries were fixed at values equal to the initial pore pressures (i.e. free draining). The foundation dimensions used in each test are given in Table 5. A model depth of 30 m and radius of 50m in the axisymmetric model was used, which was sufficient to avoid significant boundary effects and is consistent with other, similar, numerical studies (e.g. Thieken et al., 2014).

Zero-thickness Mohr-Coulomb interface elements with a tension cut off were used between the bucket skirt wall and the soil. The friction angle and normal stiffness of the interface elements were set to $\varphi' = 22^{\circ}$ and $E = 10^4$ kPa, respectively, based on aluminium-to-soil direct shear tests performed by Tran (2005) with UWA silica sand. To simulate the region directly beneath the bucket lid, a thin layer of soft 'water gap elements' was introduced (Figure 11) following the recommendations of Mana et al. (2014), Thieken et al. (2014) and Maitra et al. (2019). The water gap elements ensure that the lid and the soil can 'separate' during tension loading while also allowing for equal pore

pressure across the gap. The effective bulk modulus and Poisson's ratio of the water gap material were set to low values ($K = 10^{-4}$ kPa and $\nu = 0$ respectively) to ensure that negligible effective stresses develop across the gap, while the pore fluid was set to be almost incompressible (K_w=2GPa). The permeability of the water elements was set significantly higher than the soil elements (k = 100 m/s) to ensure that the pore pressures were uniform across the gap. The initial thickness of the water gap was set as 10 mm.

In reality, the absolute pore pressures, u, are limited by the cavitation pressure, which is given as $u_c = -100$kPa. The allowable negative excess pressure depends on the water depth, h_w, with the maximum allowable negative excess pore pressure generation given by $u_e = u_c - (z + h_w)\,\gamma_w$, where z is the depth below the seafloor. A cavitation cut off scheme was not considered for this study since the excess pore pressures in all of the numerical analysis and experimental results presented were within the cavitation limit. If the behaviour of the suction bucket at larger displacements was to be reviewed, a cavitation cut off scheme would have to be included; however, this is not the focus of the current study. For many practical design cases it is likely that the cavitation pressure will limit the design in tension; however, the force-displacement response up to this point is still considered to be of significant importance, and is the focus of the present analyses.

Finally, to improve the numerical performance of the model (i.e. to minimise the risk of convergence issues) a superficial top sand layer outside the bucket, and around the skirt tip, was included and modelled as linear elastic (Figure 8). Based on recommendations by Cerfontaine et al. (2015), the properties of the elastic superficial layer were defined by E = 10 MPa and $\nu = 0.2$. The use of the elastic regions follow recommendations by Cerfontaine et al. (2015) and Shen et al. (2017) to minimise the risk of stress concentrations causing numerical issues within similar advanced constitutive models. Sensitivity FEA of a suction bucket presented by Cerfontaine et al. (2015) showed that the adopted properties for the elastic layer were suitable. Figure 11 illustrates the portion of the FEA mesh around the suction bucket.

3.2 Centrifuge experiments compared to finite element analysis

3.2.1 Overview of tests and simulations

All of the centrifuge experiments used for comparison with FEA predictions were performed in the beam centrifuge at UWA at an acceleration of 100g. The centrifuge equipment is described in Randolph et al. (1991). Table 4 presents details of the centrifuge model tests that were used as the basis of the current study. The corresponding foundation dimensions (prototype scale) used in each test are given in Table 5. The suction bucket used in the centrifuge experiments was fabricated from aluminium (E = 70 GPa, ν = 0.3) as opposed to steel (the typical material of suction buckets used in the field).

As discussed above, the constitutive model was calibrated to laboratory element tests performed on UWA silica sand; this parameter set was used for all FEA simulations performed as part of the current study. The majority of the simulations are compared with results from centrifuge model tests conducted using UWA silica sand (i.e. UWA-1 to UWA-4), apart from the Baskarp-1 test which was performed using Baskarp sand. Baskarp sand is representative of a typical North Sea sand (Bienen et al., 2018a) and has a particle size distribution similar to that of UWA silica sand (see Figure 3). Therefore, it is considered reasonable that a single parameter set should be suitable for both sands.

For all of the centrifuge model test experiments the sand samples were prepared by dry pluviation followed by saturation from the base.

3.2.2 Scaling from centrifuge to prototype

It is possible to perform the FEA at model scale and apply an increased gravitational field (i.e. apply 100g in FEA) or alternatively the FEA can be performed at prototype scale (i.e. apply 1g in FEA). For this study we opted to perform the FEA at prototype scale as this allows the predicted responses to be compared easily to other published sources. To perform a FEA simulation of a centrifuge model test at protype scale it is important to consider carefully the appropriate scaling laws. During a centrifuge model test the model is subjected to an inertial acceleration field of N times Earth's

gravity, g; hence adoption of a scale factor $1:N$ (model:prototype) for linear dimensions (and displacements) results in scaling of stresses and strains as 1:1.

As discussed by Taylor (1992), when considering the dissipation of excess pore pressure (i.e. consolidation) in centrifuge experiments, the protype time, t_p, can be related to the model time, t_m, by:

$$t_p = t_m N^2 \frac{k_m}{k_p} \tag{32}$$

where k_m and k_p are the model and prototype permeabilities respectively. Assuming the same permeability at both scales, a scaling factor of $1:N^2$ is required to model the dissipation of excess pore pressure correctly. As a result, when considering the dissipation of excess pore pressures, time does not automatically scale with the linear dimensions. For the centrifuge model test experiments considered here, the viscosity of the pore fluid was increased to a minimum value of 100 cSt (see Table 6) resulting in the effective permeability reducing by a factor of at least 100. For the FEA simulations, the prototype permeabilities were set equal to 100 times the model permeabilities ($k_p = 100k_m$) and a time scale factor of 100 was used for all cases ($t_p = 100t_m$). As a result, the time scales in the same way as linear dimensions, and therefore the pull-out displacement rates used in for the centrifuge experiments are equal to those used in the FEA. Table 6 presents the protype permeabilities and initial void ratios used for the FEA modelling.

3.2.3 Verification results

A comparison of the FEA results with those from the centrifuge model tests is presented in Figure 12 to 15. The applied tension stress, V/A, where V is the vertical load and A is the area of the bucket lid, and the upward vertical displacement, U_y, are positive. Note that this sign convention for the global bucket response is contrary to the constitutive model formulation, in which compression is taken as positive. The drained centrifuge model tests (Figure 14) were performed with the top valve in the bucket lid open to ensure no excess pore pressure build up and the FEA was also performed fully drained. From inspection of Figure 12 to 15, reasonably good matches to the experimental

force-displacement responses are obtained from the FEA calculations for all cases considered. This is a promising result in which calibration of a constitutive model from soil element testing has been used, without back-calculation of parameters to fit the centrifuge model test results. The initial response from the FEA is generally stiffer than is observed in the experiments (Figure 12a and 13a); this is thought to be due to the excess pore pressure being mobilised at a significantly faster rate in the FEA than in the experiments (Figure 12b and 13b). This suggests that the dilation rate predicted by the constitutive model in the FEA is greater than that in the centrifuge experiments. The difference could be due to the use of water to saturate the laboratory test samples used to calibrate the model, whereas 100 cSt silicon oil was used as the pore fluid in the centrifuge experiments. This hypothesis is supported by unpublished data cited by Byrne and Houlsby (2004), who reported that the dilation rate reduced when Baskarp sand was saturated with 100 cSt silicon oil rather than water. Alternatively, the observed differences could be due to experimental issues in the centrifuge model tests that are not captured within the FEA, for example, full saturation of the pore space may not have been achieved (i.e. air bubbles present) or the bucket skirts may not have been fully penetrated. It is interesting to note that FEA performed by Thieken et al. (2014) also showed a faster rate of excess pore pressure mobilisation compared to the Luce Bay small-scale field tests reported by Houlsby et al. (2006); however, there is uncertainty in this case with respect to the in situ permeability and the measured excess pore pressures in the field tests. It should also be noted that the changes to the in situ soil state following suction bucket installation are not captured with the FEA model, where the foundation is 'wished in place'.

For the Baskarp-1 test a short cyclic loading history was applied in the centrifuge prior to the pull-out test (Bienen et al., 2018a; Bienen et al., 2018b), which was not applied in the FEA model. From a review of the cyclic testing outlined in Bienen et al. (2018b), the response is almost fully undrained (i.e. there is no significant dissipation of excess pore pressures) and very little change in stiffness is measured during the axial cyclic loading of the suction bucket. This is consistent with the FEA prediction which matches well with the centrifuge pull-out test (Figure 15) despite no initial cyclic history being applied within the model.

3.3 Sensitivity analyses

All of the sensitivity analyses described below were performed using the Bucket B dimensions (Table 5).

3.3.1 Silicon oil versus water pore fluid

As discussed above, there is some uncertainty with respect to the dilation rate and peak friction angle for the centrifuge tests when the sand is saturated with silicon oil. Therefore, the simulation of UWA-2 (0.1 mm/s pull-out rate) was repeated, employing a reduced value of A_0 (which controls the dilation rate). The UWA-2 test was repeated since it had the largest discrepancies in the initial stiffness and excess pore pressure responses between the FEA and the centrifuge results. The value of A_0 was reduced from 1.2 to 1.0, which is considered to represent a reasonably large reduction, accounting for the use of silicon oil, based on observations reported by Byrne and Houlsby (2004) for Baskarp sand. Figure 16 shows that use of the altered A_0 parameter has only a minimal effect on the predicted response of the suction bucket. Therefore, it can be concluded that the effect of the silicon oil pore fluid on the dilatant response of the soil is not the primary cause of the observed difference in the stiffness response between the FEA and the centrifuge model tests.

3.3.2 Pull-out rate

Figure 17 presents results for a range of different pull-out rates for an initial void ratio of 0.535. The observed trend of increasing capacity with increasing pull-out rate is consistent with other, similar, numerical studies (e.g. Thieken et al., 2014; Cerfontaine et al., 2015).

While the results shown in Figure 17 are of interest, from a practical perspective it is more useful to present them within a normalised design space. Figure 18 shows the normalised vertical load ($V/V_{drained}$) versus the normalised time factor ($T_{Uy}= c_v^* t/D^2$) for a range of pull-out displacements. Here, t is the loading time and c_v^* is the coefficient of consolidation determined using the elastic constrained modulus $\left(M_0 = \frac{2G_0(1-\nu)}{1-2\nu}\right)$ in this study (i.e. $c_v^* = k_0 M_0/\gamma_w$). The shaded zones of undrained, partially drained and drained response were determined approximately from reviewing the point at which each displacement contour line shows a distinct gradient change. Figure 19 shows

vertical displacement contours in the soil at an upward bucket displacement of 0.05 m (L/D=0.83%). At very slow pull-out rates (< 0.1 mm/s) practically no vertical displacement occurs in the soil since sufficient seepage occurs to expand the water elements beneath the bucket lid (i.e. a water filled gap between the bucket lid and the seafloor develops). Subsequently, as the pull-out rate is increased, the expansion of the water gap beneath the bucket decreases which causes more soil plug uplift to occur, confirming that the water elements beneath the bucket lid are performing as expected. It can also be seen from Figure 19 that as the pull-out rates increase (i.e. towards an undrained response) the volume of soil mobilised beneath skirt tip level also increases.

3.3.3 Anisotropy effect

The pull-out tests at rates of 50 mm/s and 0.5 mm/s were repeated with, and without, anisotropy activated to investigate the importance of considering inherent anisotropy effects within the constitutive model for this boundary value problem. The results are illustrated in Figure 20. The 50 mm/s pull-out rate is considered to represent a nearly undrained response and the 0.5 mm/s rate a partially drained response (see Figure 17). As discussed in the model calibration section (Section 2.2) an anisotropic fabric tensor must be included in the model formulation to reasonably capture the response of undrained direct simple shear and triaxial extension tests. From inspection of Figure 20 it can be seen that without inherent anisotropy effects, an overly optimistic (i.e. unconservative) prediction is made with respect to the mobilised tension capacity of the suction bucket. However, the effects of inherent anisotropy are shown to be more significant when considering the faster pull-out rate. At an upward bucket displacement of 0.03 m (L/D=0.5%) a 54% increase in the mobilised stress is predicted for the faster pull-out rate (50 mm/s) but only a 7.3% increase is predicted for the slower pull-out rate (0.5 mm/s). This is expected, since the faster pull-out rate is more kinematically constrained (i.e. the response is closer to undrained) and as a result the stress-dilatancy response of the constitutive model, which is affected by the inherent anisotropy, has a more significant effect. In addition, it can be seen from Figure 20 that the stiffness response of the bucket is more affected at larger upward displacement when incorporating inherent anisotropy within the constitutive model.

Figure 21 shows an example spatial distribution of the Lode angle, θ, in the soil at an upward bucket displacement of 0.05 m (L/D=0.83%). The initial value of θ throughout the soil is -30^o, since $K_0<1$, which corresponds to a triaxial compression condition. However, it can be seen from Figure 21 that during loading there is a significant variation from triaxial compression conditions, with a triaxial extension (i.e. $\theta = +30^o$) stress path dominating the response in the soil below the skirt tip level.

These observations highlight the complex stress paths that occur during a suction bucket pull-out test, showing that it is not possible to identify a dominant stress path to calibrate a constitutive model to (e.g. triaxial compression) that is applicable across a range of bucket displacements. Therefore, if an isotropic constitutive model formulation is used to compute the response of a suction bucket for axial tension loading, calibration using triaxial compression tests alone is likely to overpredict the mobilised capacity.

3.3.4 Soil profile

The 0.5 mm/s (i.e. partially drained) case was repeated for soil profiles with varying relative density (D_r). The soil profiles considered are specified in Table 7 and Figure 22. Figure 23 presents the predicted load displacement response for the different soil profiles considered. SP3 shows a similar load-displacement responses to SP2 despite there being a top layer of looser sand. In addition, SP4 has a similar load-displacement response to SP1 at higher displacement levels. However, a stiffer initial response is observed, indicating that the top layer of soil is important when considering the initial pull-out response of the foundation. At larger displacements, the overall response is dominated by the soil local to the base of the skirt, since the failure mechanism is increasingly focused below the skirt tip level (unless fully drained). The impact of the soil local to the skirt tip would become increasingly significant at higher pull-out rates (i.e. toward undrained conditions).

4 Conclusions

The suitability of a bounding surface plasticity model for sand, based on the Manzari-Dafalias model architecture, for predicting the response of a suction bucket under tension loading has been investigated. A detailed overview of the model calibration is presented using a set of laboratory

element test data that is considered representative of data typically available from an offshore wind farm site investigation. Comparisons of single-element model computations with the laboratory element test data, conducted on UWA silica sand, show that the model can capture the effects of soil density, stress level and path dependency. The calibrated model is used in FEA of a boundary value problem involving a suction bucket under tension loading, and the computed results are compared with previously published centrifuge model test results. It is demonstrated that careful selection of model features and calibration of the adopted constitutive model is essential for accurate estimation of the suction bucket load-displacement response considering different pull-out rates. The results also highlight the importance of considering inherent anisotropy within the constitutive model and demonstrate that calibration processes relying only on triaxial compression test data will likely overpredict the load mobilised during tension loading.

Despite there being a significant number of examples in the literature of single-element calibration of advanced bounding surface constitutive models, there are few examples of model calibration followed by use of the model in FEA of realistic foundation configurations, with comparison of the numerical results with physical test data. Therefore, it is a promising outcome that reasonably good agreement is obtained between the centrifuge model test results and the numerical simulations when the constitutive model has been calibrated in advance from laboratory element test data. This study gives added confidence and guidance on the use of bounding surface, Manzari-Dafalias type, models for foundation analysis. However, the work presented has focused on the monotonic response only and further work is required to address the important area of cyclic loading.

Acknowledgements

This work was supported by grant EP/L016303/1 for Cranfield University and the University of Oxford, Centre for Doctoral Training in Renewable Energy Marine Structures - REMS (http://www.rems-cdt.ac.uk/) from the UK Engineering and Physical Sciences Research Council (EPSRC). This work forms part of the activities of the Centre for Offshore Foundation Systems (COFS), which is currently supported as a Centre of Excellence by the Lloyd's Register Foundation. Lloyd's Register Foundation helps to protect life and property by supporting engineering-related education, public engagement and the application of research.

References

Andrianopoulos KI, Papadimitriou AG, Bouckovalas GD. 2005. Bounding surface models of sands: pitfalls of mapping rules for cyclic loading. In 11th international conference on computer methods and advances in geomechanics, Torino. Italy, p241-248.

Azeiteiro RJ, Coelho PA, Taborda DM, Grazina JC. 2017. Critical state–based interpretation of the monotonic behavior of Hostun Sand. Journal of Geotechnical and Geo-environmental Engineering, 143(5):p1-14.
Been K, Jefferies MG, Hachey J. 1991. The critical state of sands. Géotechnique, 41(3):p365–381.
Bienen B, Klinkvort RT, O'Loughlin CD, Zhu F, Byrne BW. 2018a. Suction caissons in dense sand, part I: installation, limiting capacity and drainage. Géotechnique, 68(11):p937-952.
Bienen B, Klinkvort RT, O'Loughlin CD, Zhu F, Byrne BW. 2018b. Suction caissons in dense sand, part II: vertical cyclic loading into tension. Géotechnique, 68(11):p953-967.
Boulanger RW, Ziotopoulou K. 2013. Formulation of a sand plasticity plane-strain model for earthquake engineering applications. Soil Dynamics and Earthquake Engineering, 53:p254-267.
Bye A, Erbrich C, Rognlien B, Tjelta TI. 1995. January. Geotechnical design of bucket foundations. In Offshore Technology Conference. Houston, Texas, Paper OTC7793.
Byrne BW. 2000. Investigation of suction caissons in dense sand. DPhil Thesis, University of Oxford, UK.
Cerfontaine B, Collin F, Charlier R. 2015. Numerical modelling of transient cyclic vertical loading of suction caissons in sand. Geotechnique, 65(12):p121 - 136
Dafalias YF, Manzari MT. 2004. Simple plasticity sand model accounting for fabric change effects. Journal of Engineering mechanics, 130(6): p622-634.
Dafalias YF, Papadimitriou AG, Li XS. 2004. Sand plasticity model accounting for inherent fabric anisotropy. Journal of Engineering Mechanics, 130(11):p1319-1333.
Feld, T., 2001. Suction Buckets: A new innovation foundation concept, applied to offshore wind turbines. PhD Thesis, Aalborg University, Aalborg, Denmark.
Golchin A, Lashkari A. 2014. A critical state sand model with elastic–plastic coupling. International Journal of Solids and Structures, 51:p2807-2825.
Hardin BO, Richart FE. 1963. Elastic wave velocities in granular soils. Journal of Soil Mechanics and Foundations Div, 89(1):p33-66.
Hardin BO. 1978. The nature of stress-strain behavior for soils. In Volume I of Earthquake Engineering and Soil Dynamics. ASCE Geotechnical Engineering Division Specialty Conference, Pasadena, California, p3-90.
Houlsby GT, Byrne BW. 2005. Design procedures for installation of suction caissons in clay and other materials. Proceedings of the Institution of Civil Engineers-Geotechnical Engineering, 158(2):p75-82.
Houlsby GT, Kelly RB, Byrne BW. 2005. The tensile capacity of suction caissons in sand under rapid loading. In International Symposium on Frontiers in Offshore Geomechanics, Perth, Australia. p405-410.
Houlsby GT, Kelly RB, Huxtable J, Byrne BW. 2006. Field trials of suction caissons in sand for offshore wind turbine foundations. Geotechnique, 56(1):p3-10.
Ishihara K. 1993. Liquefaction and flow failure during earthquakes. Geotechnique, 43(3):p351-451.
Iskander MG, Olson RE, Pavlicek RW. 1993. Behavior of suction piles in sand. Design and Performance of Deep Foundations: Piles and Piers in Soil and Soft Rock, p157-171.
Jefferies M, Been K. 2015. Soil liquefaction: a critical state approach 2nd edition. CRC press, New York.
Kakasoltani S, Zeinoddini M, Abdi MR, Arabzadeh H. 2011. An experimental investigation into the pull-out capacity of suction caissons in sand. In 30th International Conference on Ocean, Offshore and Arctic Engineering, Rotterdam, Netherlands. p21-27.
Kelly RB, Byrne BW, Houlsby GT, Martin CM. 2004, Tensile loading of model caisson foundations for structures on sand. In Fourteenth International Offshore and Polar Engineering Conference, Toulon, France. p638-641.
Lashkari A. 2010. A SANISAND model with anisotropic elasticity. Soil Dynamics and Earthquake Engineering, 30(12):p1462-1477.
Li XS, Dafalias YF. 2000. Dilatancy for cohesionless soils. Geotechnique, 50(4):p449-460.
Li XS, Wang Y. 1998. Linear representation of steady-state line for sand. Journal of geotechnical and geoenvironmental engineering, 124(12):p1215-1217.
Loukidis D, Salgado R. 2009. Modeling sand response using two-surface plasticity. Computers and Geotechnics, 36:p166-186.
Maitra S, White D, Chatterjee S, Choudhury D. 2019. Numerical modelling of seepage and tension beneath plate anchors. Computers and Geotechnics, 108:p131-142.
Mana DS, Gourvenec S, Randolph MF. 2014. Numerical modelling of seepage beneath skirted foundations subjected to vertical uplift. Computers and Geotechnics, 55:p150-157.
Manzari MT, Dafalias YF. 1997. A critical state two-surface plasticity model for sands. Geotechnique, 47(2):p255-272.
Offshore Wind Accelerator (OWA), 2019. A Suction Installed Caisson Foundations for Offshore Wind: Design Guidelines. Carbon Trust, February 2019, Issue 1.
Papadimitriou AG, Bouckovalas GD. 2002. Plasticity model for sand under small and large cyclic strains: a multiaxial formulation. Soil Dynamics and Earthquake Engineering, 22(3):p191-204.
Papadimitriou AG, Dafalias YF, Yoshimine M. 2005. Plasticity modeling of the effect of sample preparation method on sand response. Soils and foundations, 45(2):p109-123.
Petalas AL, Dafalias YF, Papadimitriou AG. 2019. SANISAND-FN: An evolving fabric-based sand model accounting for stress principal axes rotation. International Journal for Numerical and Analytical Methods in Geomechanics, 43(1):p97-123.
Randolph MF, Jewell RJ, Stone KJ, Brown TA. 1991. Establishing a new centrifuge facility. In International. Conference on Centrifuge Modelling, Boulder, Colorado, p3–9.
Senders M. 2008. Suction caissons in sand as tripod foundations for offshore wind turbines. PhD Thesis, University of Western Australia. Perth, Australia.
Shen K, Zhang Y, Klinkvort RT, Sturm H, Jostad HP, Sivasithamparam N, Guo Z. 2017. Numerical Simulation of Suction Bucket Under Vertical Tension Loading. In 8th International Conference on Offshore Site Investigation and Geotechnics, London, UK, p488-497

Sheng D, Sloan SW, Yu HS. 2000. Aspects of finite element implementation of critical state models. Computational mechanics, 26(2):185-196.

Shonberg A, Harte M, Aghakouchak A, Brown CSD, Andrade MP, Liingaard MA. 2017. Suction bucket jackets for offshore wind turbines: applications from in situ observations. In Proc. TC209 Workshop, 19th International Conference on Soil Mechanics and Geotechnical Engineering, Seol, South Korea, p65-77.

Sloan SW, Abbo AJ, Sheng D. 2001. Refined explicit integration of elastoplastic models with automatic error control. Engineering Computations, 18(1/2):p121-194.

Staplefeldt M, Bienen B, Grabe J. 2019. The influence of the drainage regime on the installation and the response to vertical cyclic loading of suction caissons in dense sand (under review)

Sturm H. 2017. Design Aspects of Suction Caissons for Offshore Wind Turbine Foundations. In Proc. TC209 Workshop, 19th International Conference on Soil Mechanics and Geotechnical Engineering, Seol, South Korea, p45-63.

Tjelta TI. 2015. The suction foundation technology. In International Symposium on Frontiers in Offshore Geomechanics, Perth, Australia, p85-93

Taborda DMG, Zdravković L, Kontoe S, Potts DM. 2014. Computational study on the modification of a bounding surface plasticity model for sands. Computers and Geotechnics, 59:p145-160.

Taiebat M, Dafalias YF. 2008. SANISAND: Simple anisotropic sand plasticity model. International Journal for Numerical and Analytical Methods in Geomechanics, 32(8):p.915-948.

Taylor RE. 1992. Geotechnical centrifuge technology, 1st edition. Black Academic and Professional, Glasgow.

Thieken K, Achmus M, Schröder C. 2014. On the behavior of suction buckets in sand under tensile loads. Computers and Geotechnics, 60:p88-100.

Tran MN. 2005. Installation of suction caissons in dense sand and the influence of silt and cemented layers. PhD Thesis, University of Sydney, Sydney, Australia.

Verdugo R, Ishihara K. 1996. The steady state of sandy soils. Soils and foundations, 36(2):p81-91.

Von Wolffersdorff PA. 1996. A hypoplastic relation for granular materials with a predefined limit state surface. Mechanics of Cohesive-frictional Materials: An International Journal on Experiments, Modelling and Computation of Materials and Structures, 1(3):p251-271.

Whyte S, Rattley M, Erbrich CE, Burd HJ, Martin CM. 2017. A Practical Constitutive Model for Offshore Foundation Problems Involving Dense Sands in Partially Drained to Undrained Conditions. In 8th International Conference on Offshore Site Investigation and Geotechnics, London, UK, p400-407.

TABLES

Table 1: Equations of constitutive model and references

Parameters	Description	Governing equations	Eqn. No	Reference
Elastic Behaviour				
G_{ref}, n	Elastic shear modulus	$G = G_{ref} p_{ref} \frac{(2.97-e)^2}{(1+e)} \left(\frac{p'}{p_{ref}}\right)^n$	(1)	Hardin (1978) Hardin and Richart (1963)
ν	Elastic bulk modulus	$K = G \frac{2(1+\nu)}{3(1-2\nu)}$	(2)	
Surfaces				
m	Yield surface	$f = [(\mathbf{r}-\boldsymbol{\alpha}):(\mathbf{r}-\boldsymbol{\alpha})]^{\frac{1}{2}} - \sqrt{2/3}\, m = 0$	(3)	Manzari and Dafalias (1997)
$e_{cs,ref}$, λ_c, ξ	Critical state line in e-p' space and the state parameter	$e_{cs} = e_{cs,ref} - \lambda_c \left(p'/p_{ref}\right)^{\xi}$	(4)	Li and Wang (1998)
		$\psi = (e - e_{cs})$	(5)	
β	Shape in deviatoric plane	$R(\theta,\beta) = \left(\frac{2\beta^4}{((1+\beta^4)-(1-\beta^4)\sin 3\theta)}\right)^{\frac{1}{4}}$	(6)	Sheng et al. (2000)
M_{cs}	Critical state surface	$M_{cs}^{\theta} = R(\theta,\beta) M_{cs}$	(7)	
n^d	Dilatancy surface	$M_d^{\theta} = R(\theta,\beta) M_d$	(8)	Li and Dafalias (2000)
		$M_d = M_{cs} \exp(n^d \psi_A)$	(9)	
n^b	Bounding surface	$M_b^{\theta} = R(\theta,\beta) M_b$	(10)	Li and Dafalias (2000)
		$M_b = M_{cs} \exp(\langle -n^b \psi_A \rangle)$	(11)	
Plastic Behaviour				
-	Gradient of the yield surface	$\frac{\partial f}{\partial \boldsymbol{\sigma}} = \mathbf{n} - \frac{1}{3}(\mathbf{n}:\mathbf{r})\mathbf{I}$	(12)	Manzari and Dafalias (1997)
A_0	Gradient of the plastic potential function	$\frac{\partial g}{\partial \boldsymbol{\sigma}} = \mathbf{n} + \frac{1}{3} A_0 d_d \mathbf{I}$	(13)	Manzari and Dafalias (1997)

h_0, μ	Hardening modulus	$H = \frac{2}{3} p' h\, d_b$ $h = \frac{b_o}{(\boldsymbol{\alpha} - \boldsymbol{\alpha_{in}}) : \mathbf{n}}$ $b_o = h_0 G_{ref} (1 - e_h) \left(\frac{p'}{p_{ref}}\right)^{\mu}$	(14) (15) (16)	Dafalias and Manzari (2004) Papadimitriou and Bouckovalas (2002)
-	Back-stress ratio tensor update	$\Delta\alpha = \Lambda \left(\frac{2}{3}\right) h \left(\boldsymbol{\alpha}_{\mathbf{b}}^{\boldsymbol{\theta}} - \boldsymbol{\alpha}\right)$	(17)	Dafalias and Manzari (2004)
Anisotropy				
a	Second-order fabric tensor	$A = R(\theta, \beta)\, \mathbf{F} : \mathbf{n}$ $F_{11} = 0.5(1 - a) \quad F_{22} = 0.5(1 - a) \quad F_{33} = a$ $F_{ij} = 0 \ \ (\text{when } i \neq j)$	(18)	Dafalias et al. (2004)
b, c	Anisotropic fabric scaling factor	$\psi_A = f_A\, \psi$ $f_A = \exp^{-\left(b(A - A_c)\right)^c}$ $A_c = \sqrt{\frac{3}{2}} \left(a - \frac{1}{3}\right)$	(19) (20) (21)	

Notes:

Compression positive, $\Lambda = \text{plastic multiplier} = \frac{\left(\frac{\partial f}{\partial \boldsymbol{\sigma}}\right)^{\mathrm{T}} \mathbf{D}^{\mathbf{e}}\, \Delta\boldsymbol{\varepsilon}}{\left(\frac{\partial f}{\partial \boldsymbol{\sigma}}\right)^{\mathrm{T}} \mathbf{D}^{\mathbf{e}} \left(\frac{\partial g}{\partial \boldsymbol{\sigma}}\right) + H}$

Table 2: Model calibration overview

Symbol	Description	Order of Calibration	Test Type for Calibration	Additional Information
G_{ref}	Elastic shear modulus constant	1	Bender element tests and Triaxial tests with radial and axial local strain gauges	
ν	Poisson's ratio			
n	Elastic modulus mean effective stress power exponent			
m	Yield surface size	1	Repeat loading resonant column test or cyclic triaxial compression tests	Data often not available and hence values from literature typically used
E_{fact}	Elastic stiffness degradation factor to form elasto-plastic matrix	1	Undrained and drained triaxial tests	Derived from review of stress dilatancy response between undrained and drained tests
$e_{cs,ref}$	Critical state void ratio at p' = 0	1	Triaxial compression tests	Preferable loose samples to avoid excessive shear banding prior to reaching critical state
λ_c	Critical state line constant			
ξ	Critical state line constant			
M_{cs}	Critical state stress ratio in compression			
n^b	Effect of ψ on the bounding surface	2	Triaxial compression tests with radial and axial local strain gauges	CSL and elastic parameters required prior to calibrating
n^d	Effect of ψ on the dilatancy surface			
A_0	Stress-dilatancy parameter			
h_0	Hardening modulus constant	3	Triaxial compression tests at range of mean effective stresses	Trial and error curve fitting parameter match to stress-strain test data
μ	Hardening modulus mean effective stress power exponent			
e_{max}	Maximum void ratio	-	Minimum density test	Typically, $e_{c,ref}$ can be set equal to e_{max}
β	Ratio of M_{cs} in triaxial extension and compression	4	Triaxial extension tests	Critical state in extension difficult to realise therefore mc/me based on Mohr Coulomb
a	Fabric orientation scalar		Triaxial extension in addition to direct simple shear tests or other plane-strain tests	Trial and error curve fitting parameter match to stress-strain test data for tests with different loading directions
b	fabric scaling constants			
c	fabric scaling constants			

Table 3: UWA silica sand calibrated parameters

Symbol	Value
G_{ref}	225
ν	0.15
n	0.5
m	0.06
E_{fact}	0.5
$e_{c,ref}$	0.835
λ_c	0.026
ξ	0.61
M_{cs}	1.25
n^b	1.7
n^d	1.5
A_0	1.2
h_0	2.5
μ	0.4
e_{max}	0.835
β	0.72
a	0.27
b	350
c	0.1
Notes: p_{ref} = 100kPa	

Table 4: Centrifuge model tests of suction bucket under tension loading references

Test Ref.	Soil	Foundation Reference	Reference
UWA-1	UWA silica sand	B	Test 6-3 in Senders (2008)
UWA-2	UWA silica sand	B	Test 6-2 in Senders (2008)
UWA-3 and UWA-4	UWA silica sand	A	Drained tests in Stapelfeldt et al. (2019)
Baskarp-1	Baskarp sand	A	Test 6-1 in Bienen et al. (2018a)

Table 5: Suction bucket prototype dimensions

Bucket Ref.	D (m)	L (m)	L/D (-)	W_t (mm)	Reference
Bucket A	8	4	0.5	50	Bienen et al. (2018a) and Stapelfeldt et al. (2019)
Bucket B	6	6	1	30	Senders (2008)
Notes: D = diameter, L = embedment length, W_t = wall thickness, all dimension as protype dimensions, E=70 GPa, ν=0.3					

Table 6: Centrifuge model tests initial state and permeability considered for FEA

Test Ref.	Soil	Fluid Type	Viscosity (cSt)	Void Ratio (-)	Prototype Permeability (m/s)
UWA-1	UWA silica sand	Silicon Oil	100	0.535	1.09E-04*
UWA-2	UWA silica sand	Silicon Oil	100	0.535	1.09E-04*
UWA-3	UWA silica sand	Water with cellulose ether	100	0.57	1.29E-04*
UWA-4	UWA silica sand	Water with cellulose ether	100	0.57	1.29E-04*
Baskarp	Baskarp sand	Water with cellulose ether	660	0.57	1.22E-05^

Notes: * = determined from laboratory tests performed by Tran (2005**)** ^ = Permeability reported by Bienen et al (2018a) as 8.04e-05 for fresh water at e = 0.57

Table 7: Soil profiles considered for layering sensitivity study

Soil Profile Ref	Depth BSF (m) Top	Depth BSF (m) Base	Description	e (-)
SP1	0.0	Base of model	Medium dense sand	0.67
SP2	0.0	Base of model	Very dense sand	0.535
SP3	0.0	L/2	Medium dense sand	0.67
	L/2	Base of model	Very dense sand	0.535
SP4	0.0	L/2	Very dense sand	0.535
	L/2	Base of model	Medium dense sand	0.67

Notes: BSF = below seafloor, L = embedment length of suction bucket, e = void ratio

FIGURES

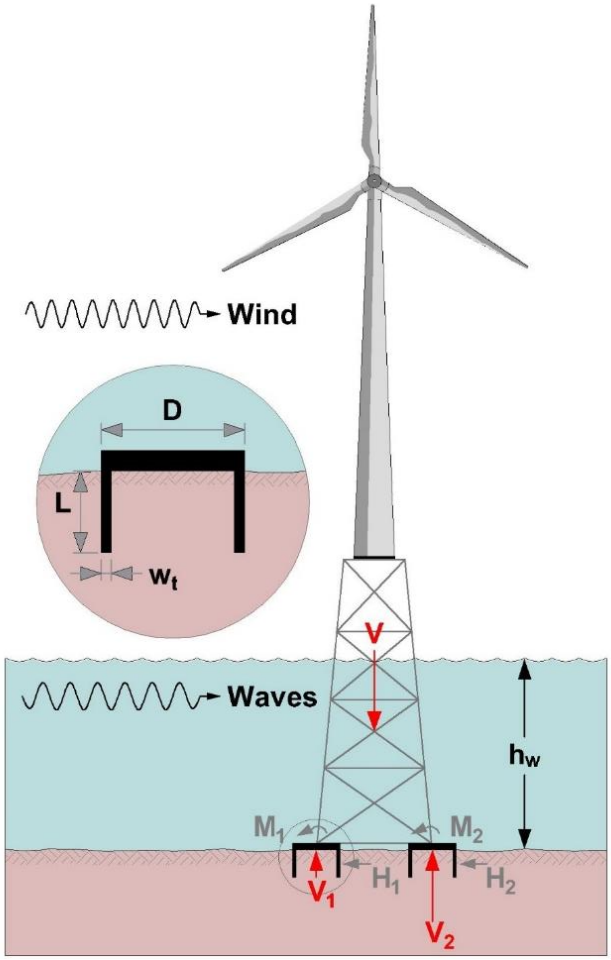

Figure 1: Illustration of the multi-bucket foundation system with foundation reactions

a)

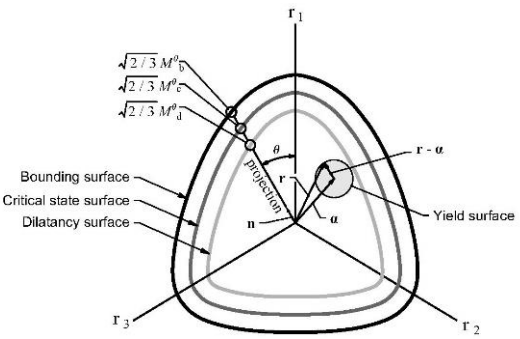

b)

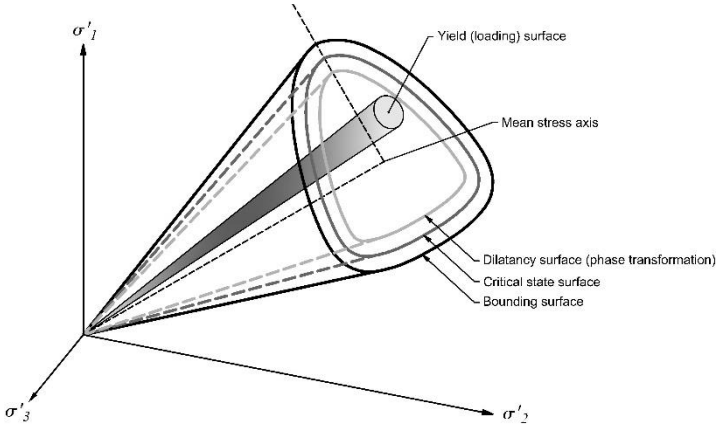

Figure 2: Illustration of the yield, bounding, dilatancy and critical state surfaces in a) the normalised deviatoric plane and b) principal stress space

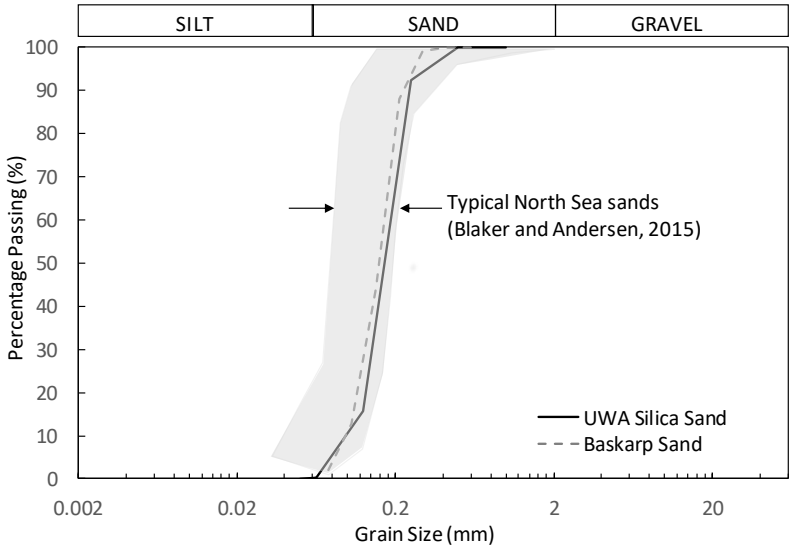

Figure 3: Gran size distribution of Baskarp and UWA silica sand with comparison to typical range for North Sea sands

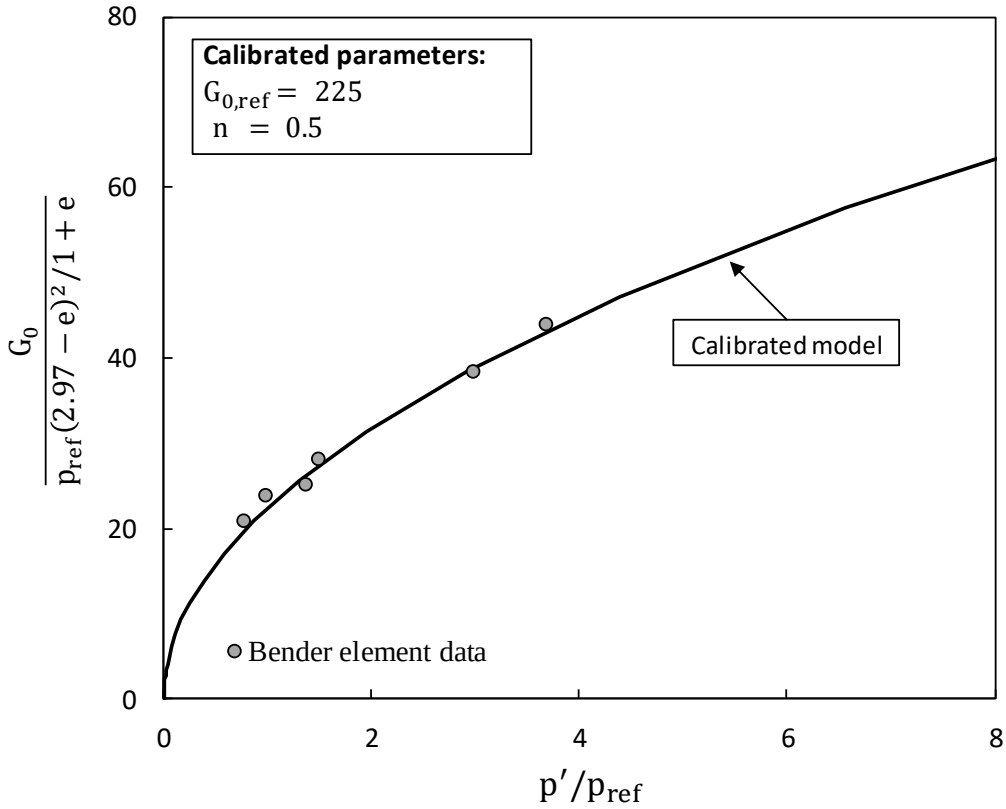

Figure 4: Measured G_0 data from bender element tests on UWA Silica Sand and calibrated hypoelastic model

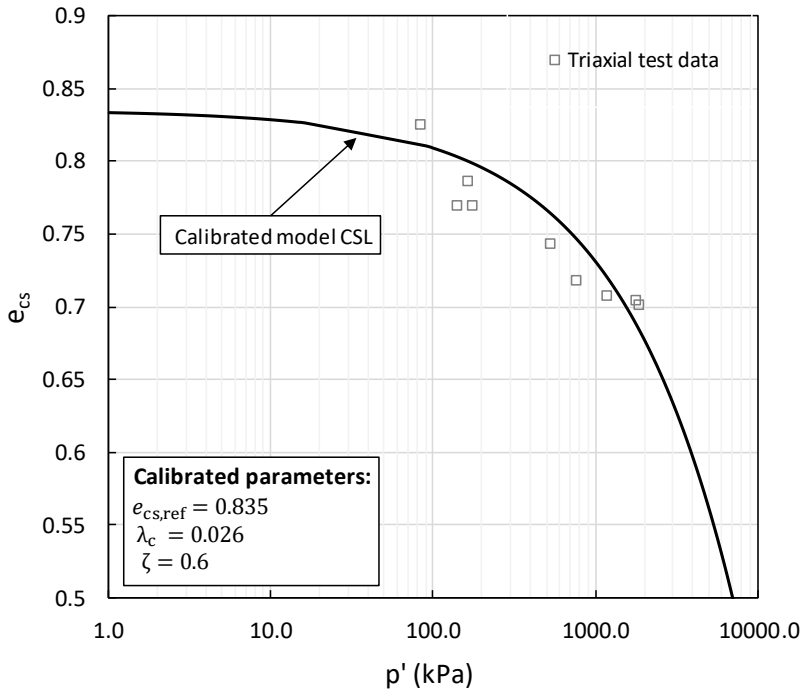

Figure 5: Measured void ratio and mean effective stress at critical state from triaxial compression tests on UWA silica sand and calibrated model CSL using a function initially proposed by Li and Wang (1998)

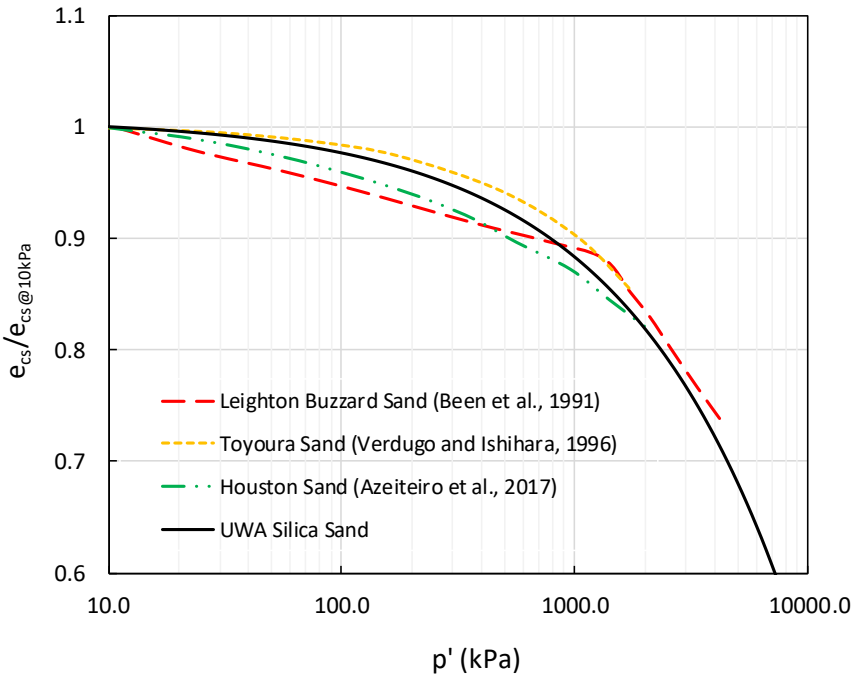

Figure 6: Comparison of calibrated CSL for UWA silica sand to other published curves, with the void ratio normalised by the critical state void ratio at 10 kPa for each CSL

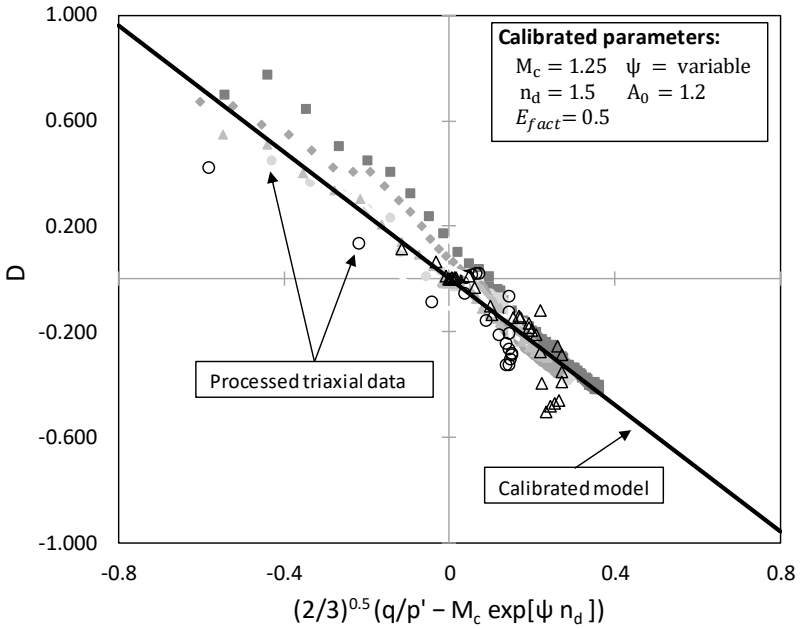

Figure 7: Modified stress dilatancy plot from UWA silica sand triaxial compression tests and calibration of A_0 parameter, open shapes represent undrained tests and filled shapes represent drained tests

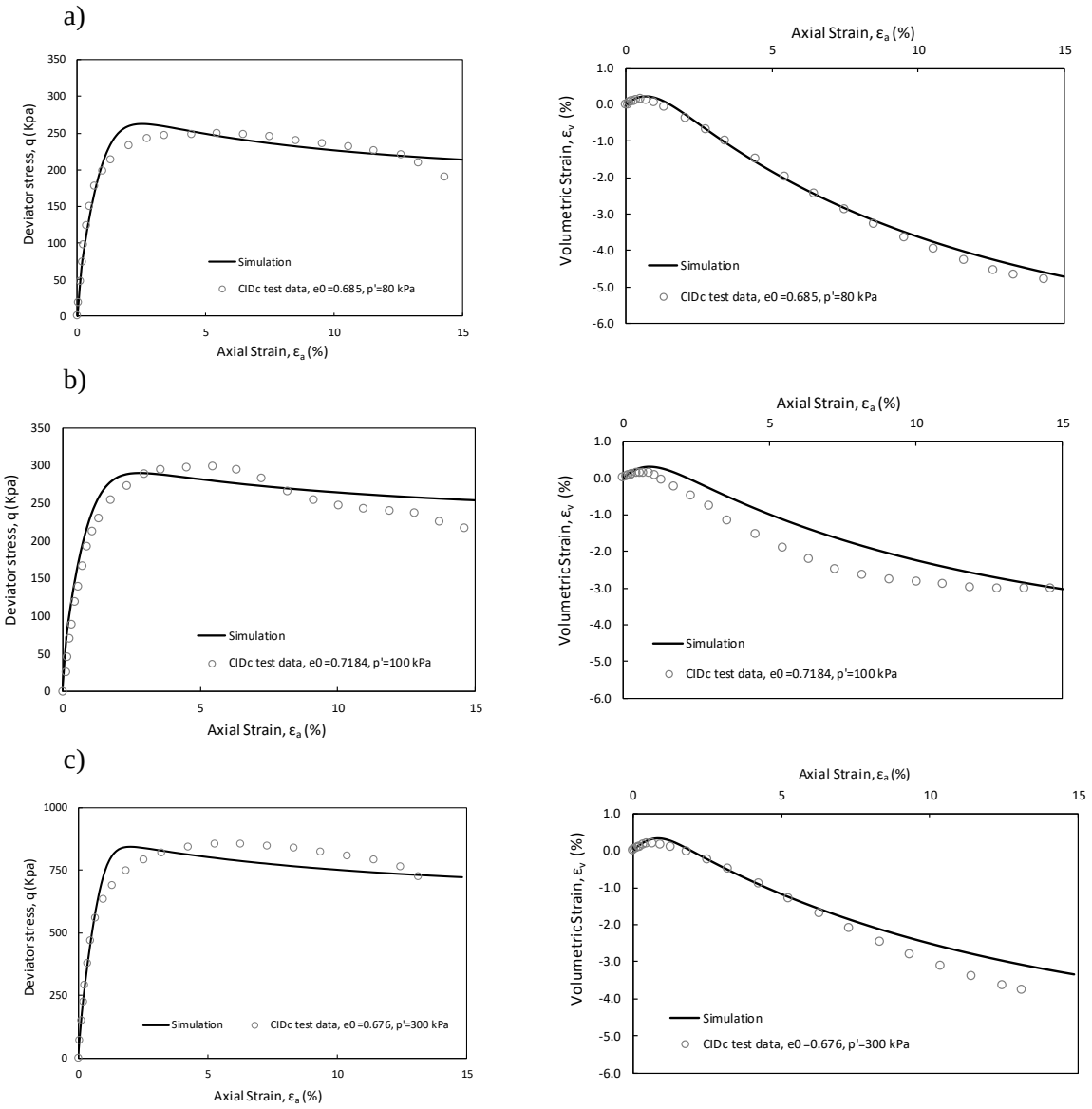

Figure 8: Isotropically consolidated drained triaxial compression test data compared to single element simulations for UWA silica sand

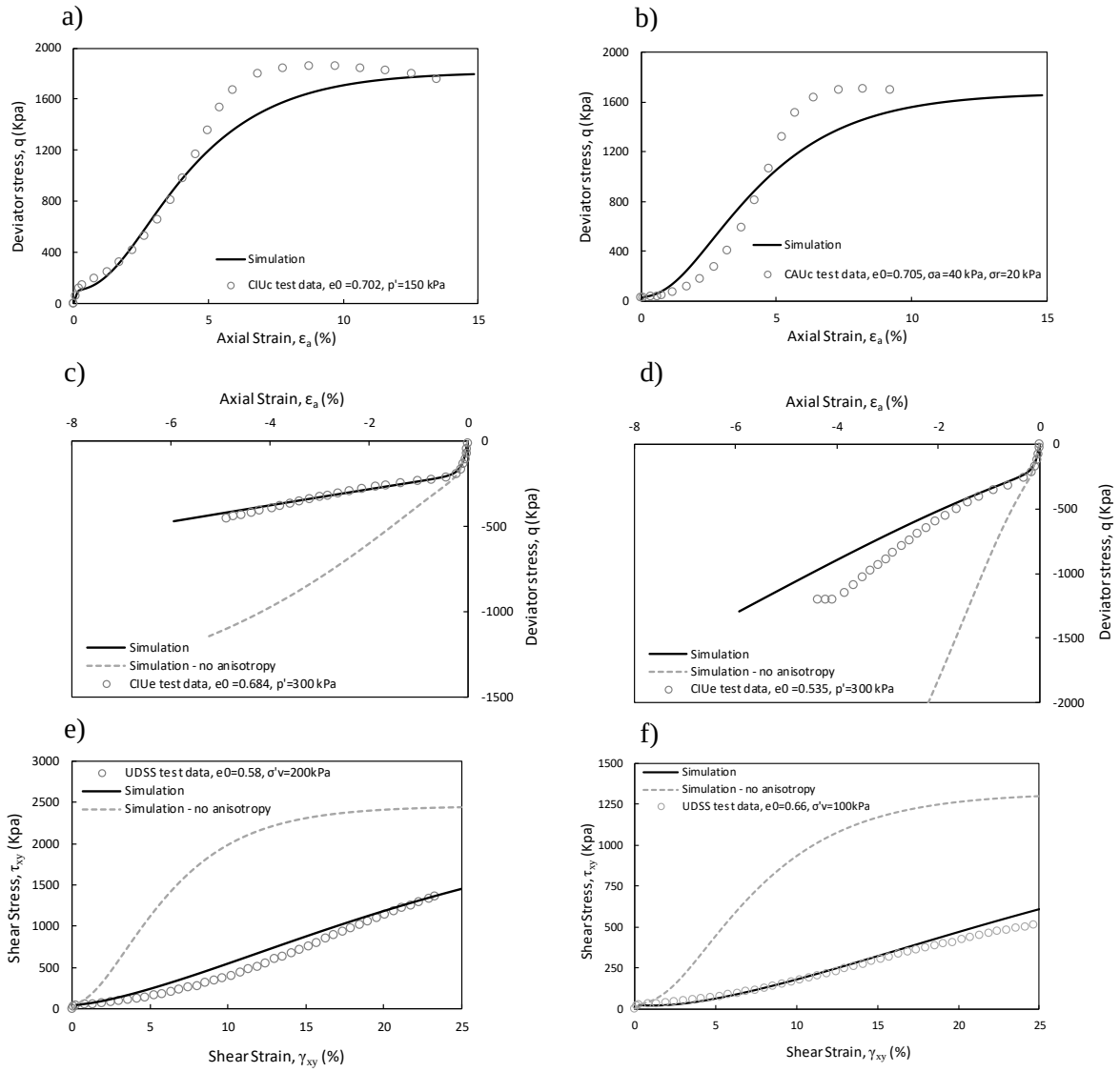

Figure 9: Stress-strain response compared to single element simulations for UWA silica sand considering undrained a,b) triaxial compression tests, c,d) triaxial extension tests and e,f) direct simple shear tests with initial K_0 of 0.5

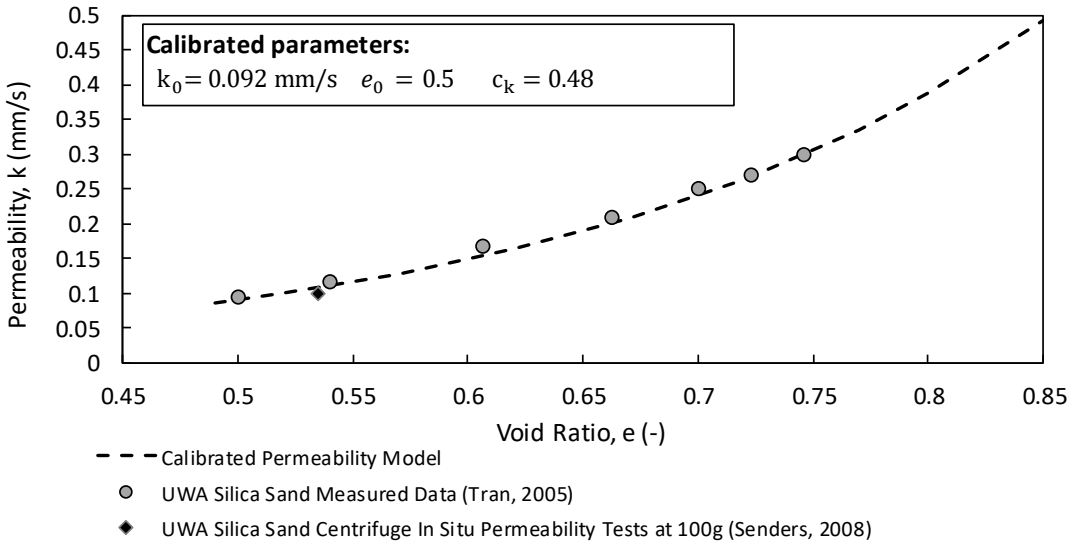

Figure 10: Permeability test data at different initial void ratios for UWA silica sand from Tran (2005) and calibrated permeability model

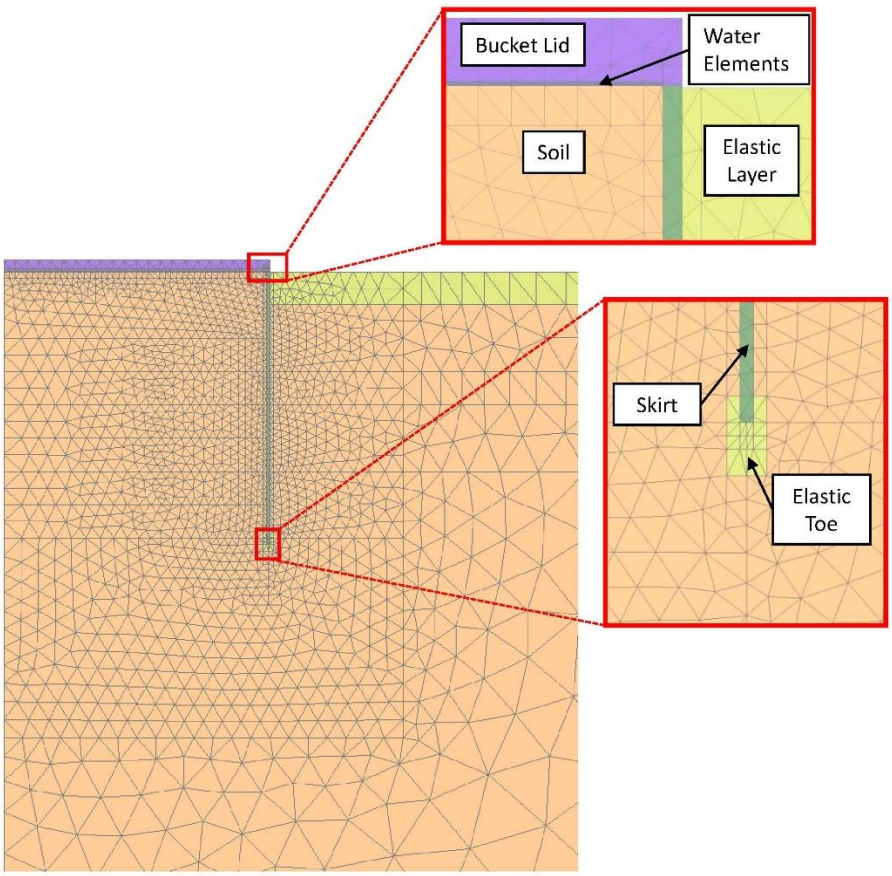

Figure 11: FEA model example zoomed in view of portion of mesh

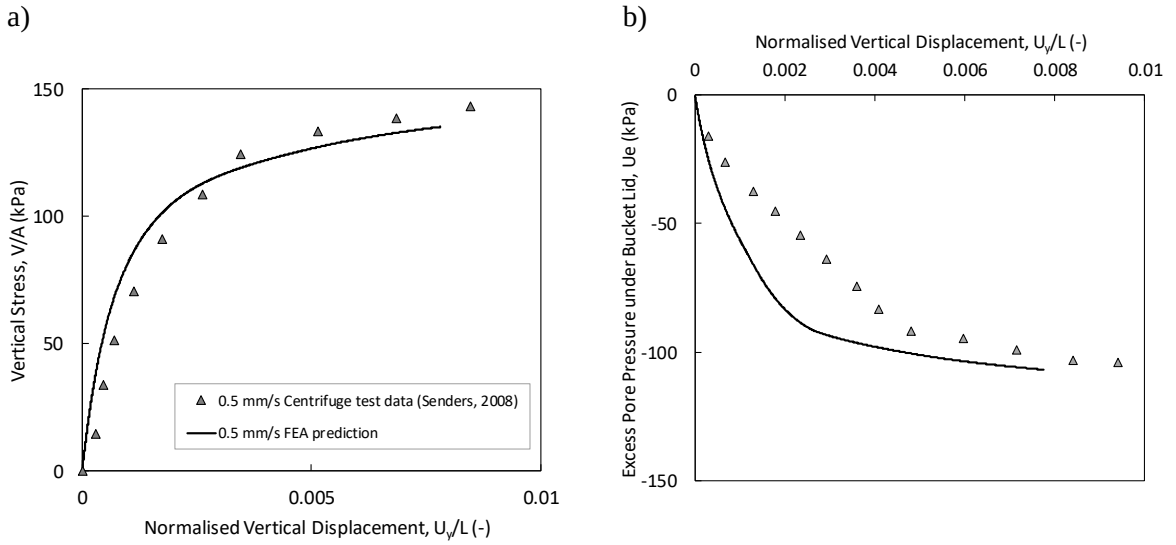

Figure 12: Comparison of FEA prediction compared to UWA-1 centrifuge test data published by Senders (2008) at initial void ratio of 0.535 and an applied pull-out rate of 0.5 mm/s

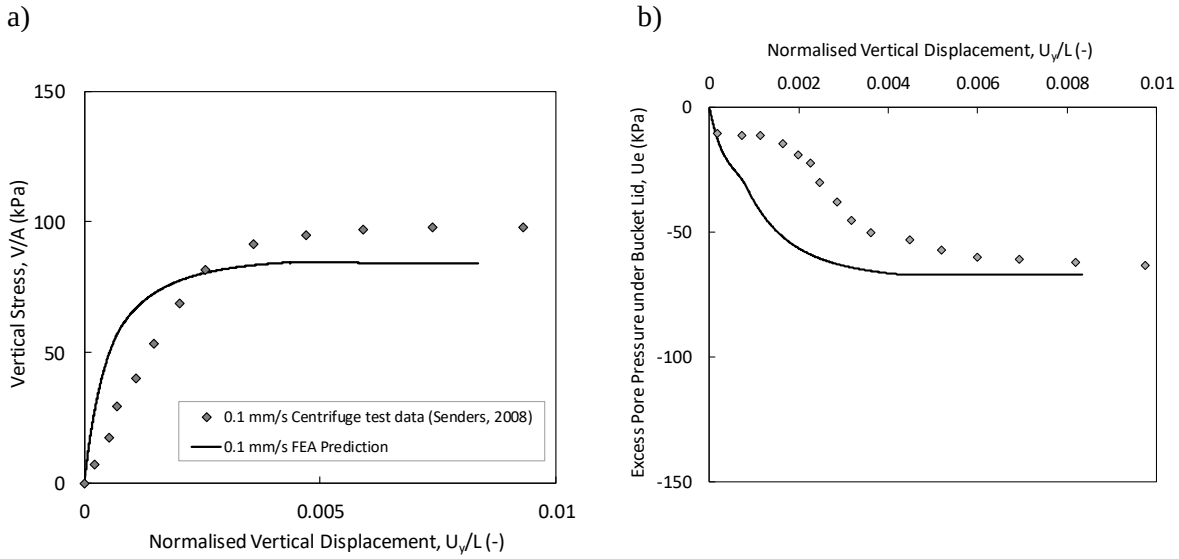

Figure 13: Comparison of FEA prediction compared to UWA-2 centrifuge test data published by Senders (2008) at initial void ratio of 0.535 and an applied pull-out rate of 0.1 mm/s

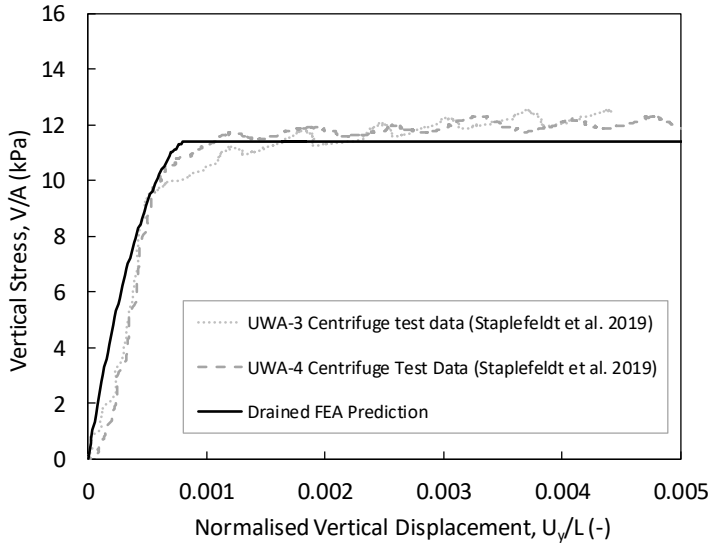

Figure 14: Comparison of FEA prediction compared to UWA-3 and UWA-4 centrifuge test data published by Staplefeldt et al. (2019) at initial void ratio of 0.57 for drained conditions

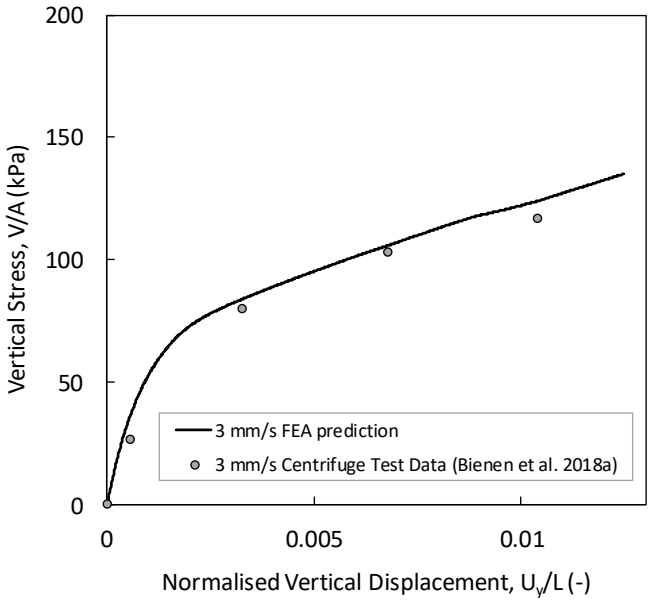

Figure 15: Comparison of FEA prediction compared to Baskarp-1 centrifuge test data published by Bienen et al. (2018a) at initial void ratio of 0.57 and an applied pull-out rate of 3 mm/s

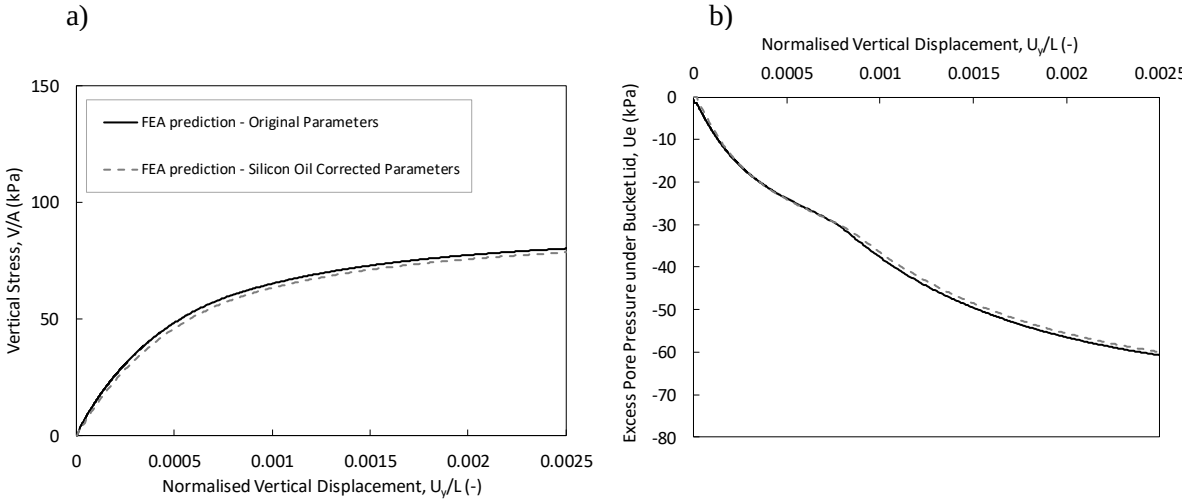

Figure 16: Comparison of FEA prediction using original parameters calibrated using water saturated samples compared to silicon oil corrected dilatnacy at initial void ratio of 0.535 and an applied pull-out rate of 0.1 mm/s and UWA-2 centrifuge test results

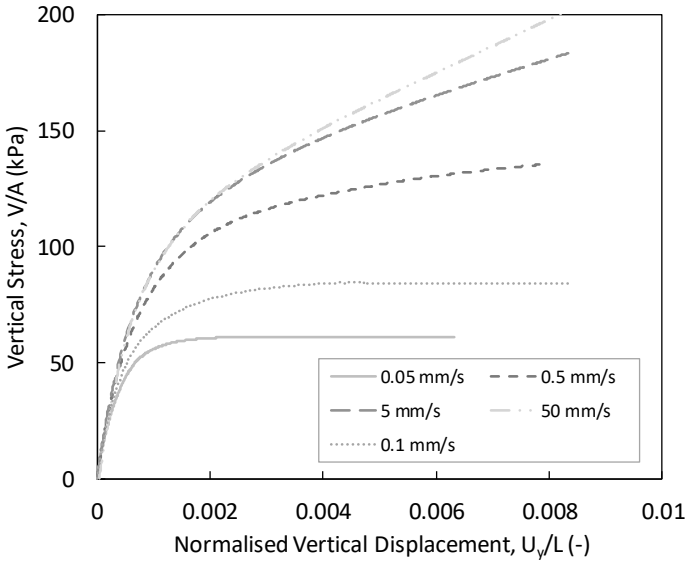

Figure 17: FEA prediction considering different pull-out rates for Senders (2008) model set up (Bucket B) at initial void ratio of 0.535

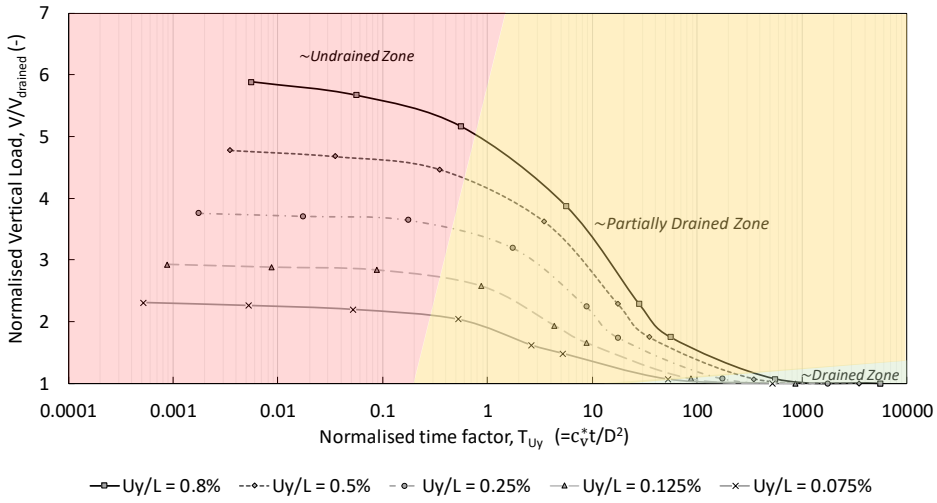

Figure 18: Normalised pull-out load versus normalised time factor interaction diagram

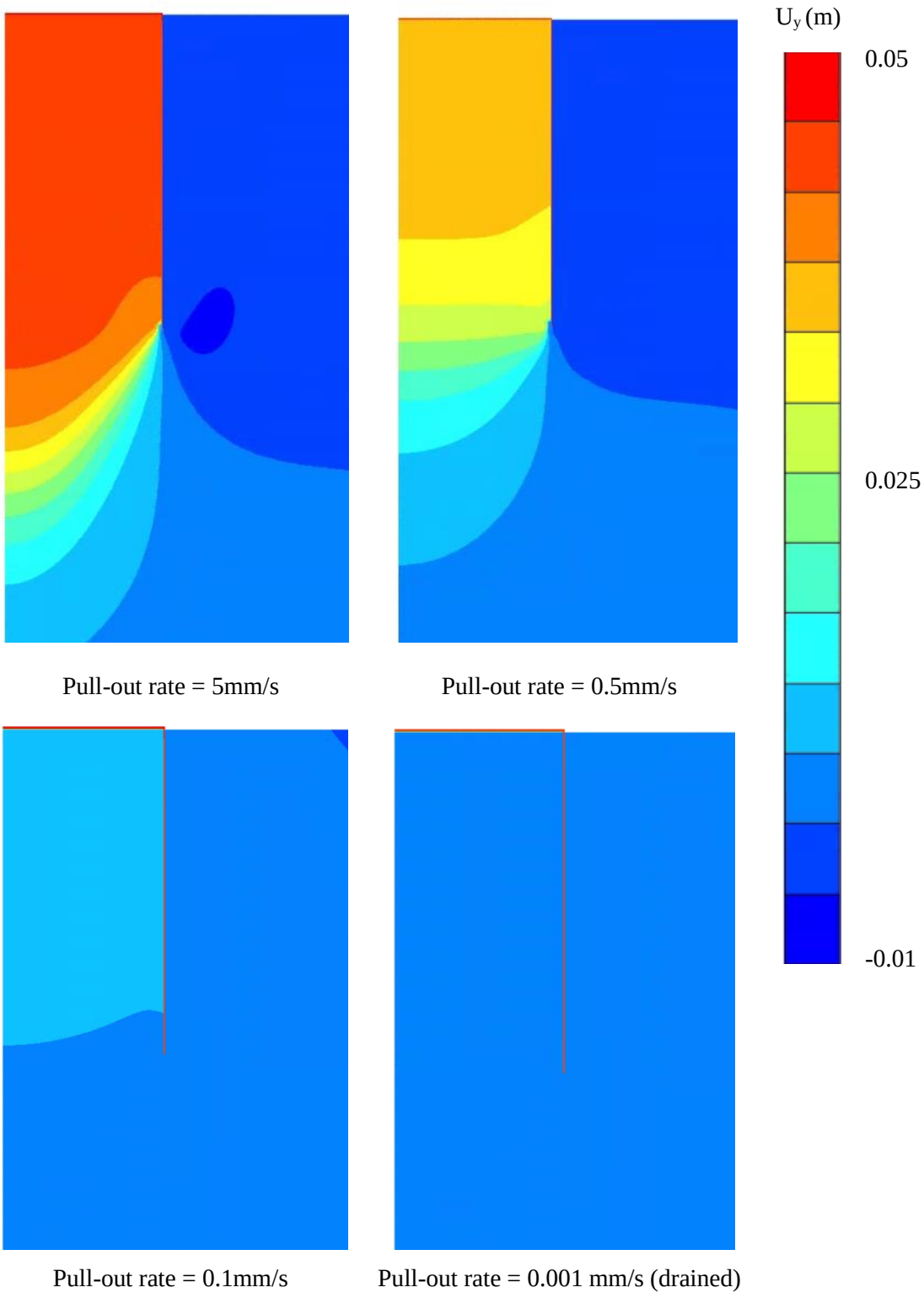

Figure 19: FEA vertical displacement contours at vertical displacement of 0.05m for Senders (2008) model set up (Bucket B) at initial void ratio of 0.535

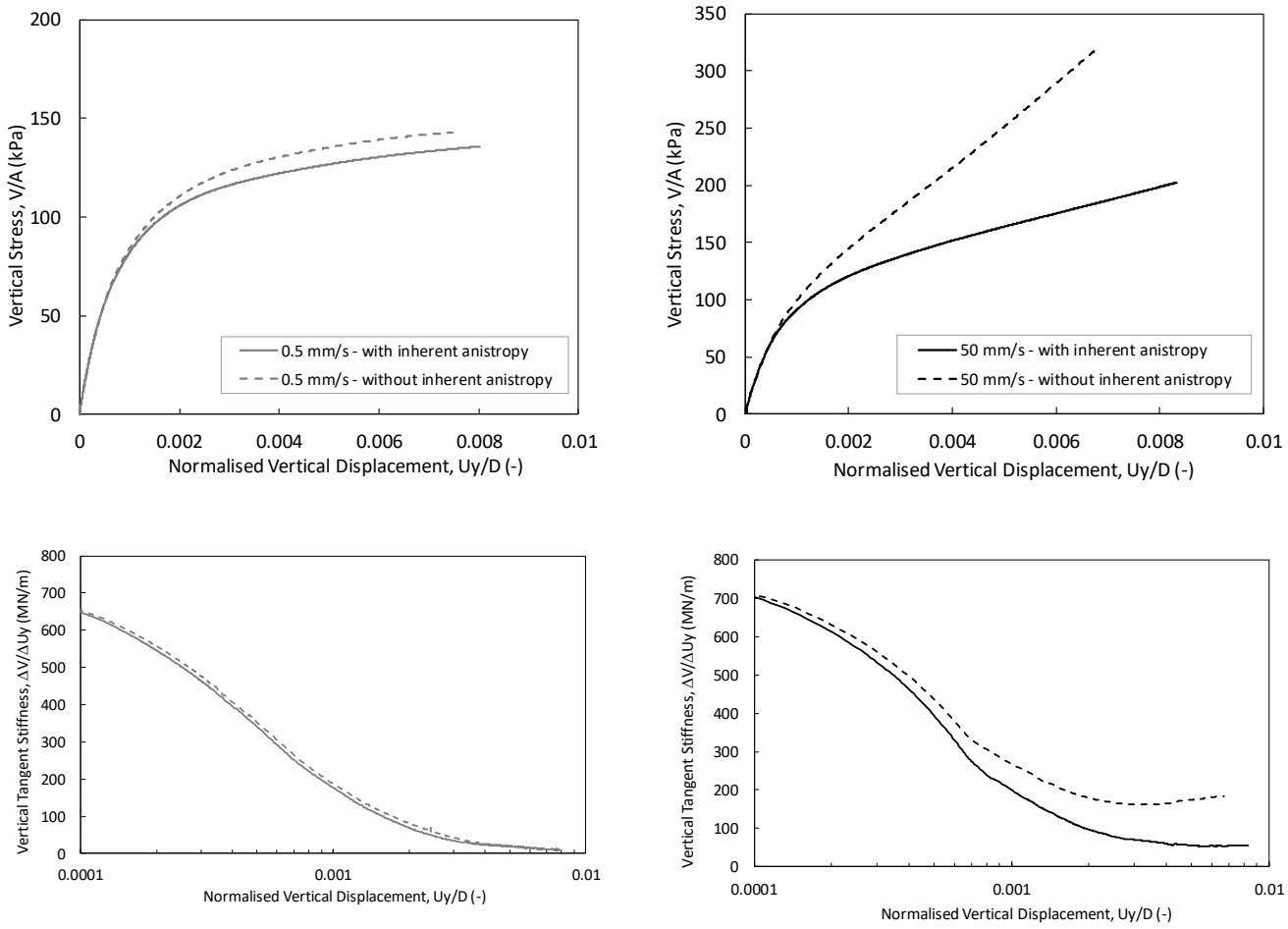

Figure 20: Predicted response with and without inherent anisotropy included in the constitutive model for Senders (2008) model set up (Bucket B) at initial void ratio of 0.535

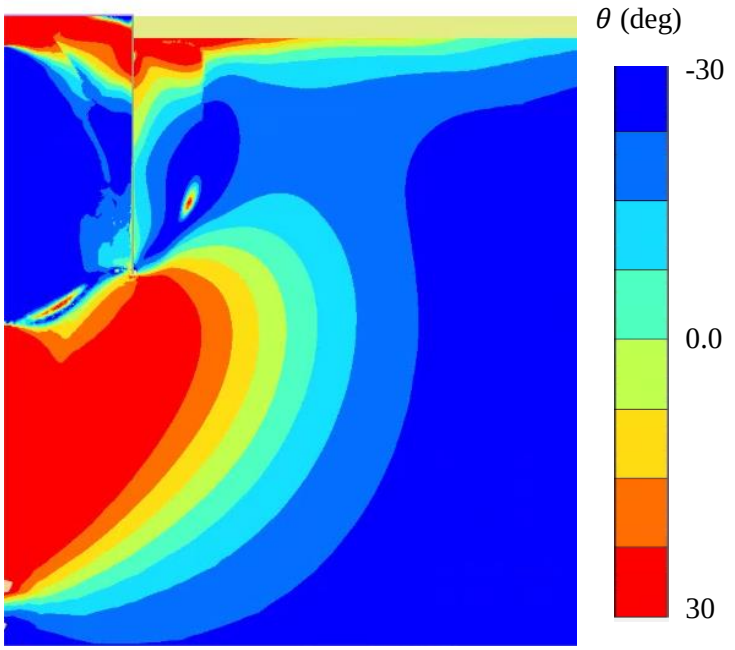

Figure 21: Contour plot of Lode angle parameter, θ, at a vertical displacement of 0.05m considering a pull-out rate of 50 mm/s using the Senders (2008) model set up (Bucket B) at initial void ratio of 0.535

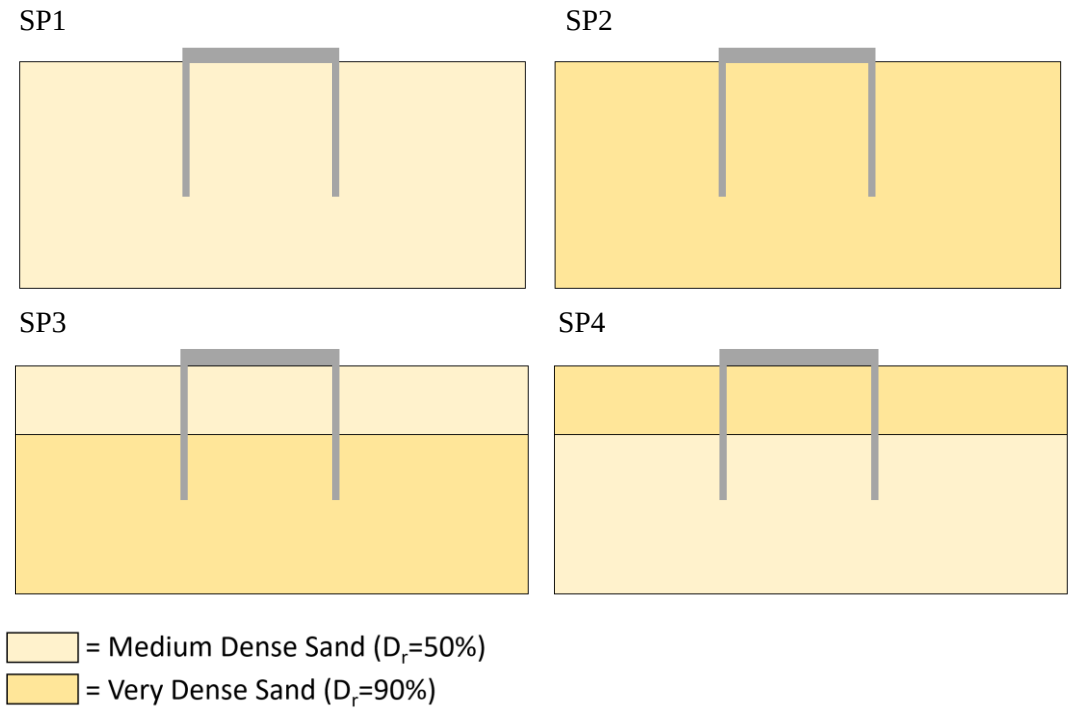

Figure 22:Illustration of layered profiles for FEA soil profile layering sensitivity study

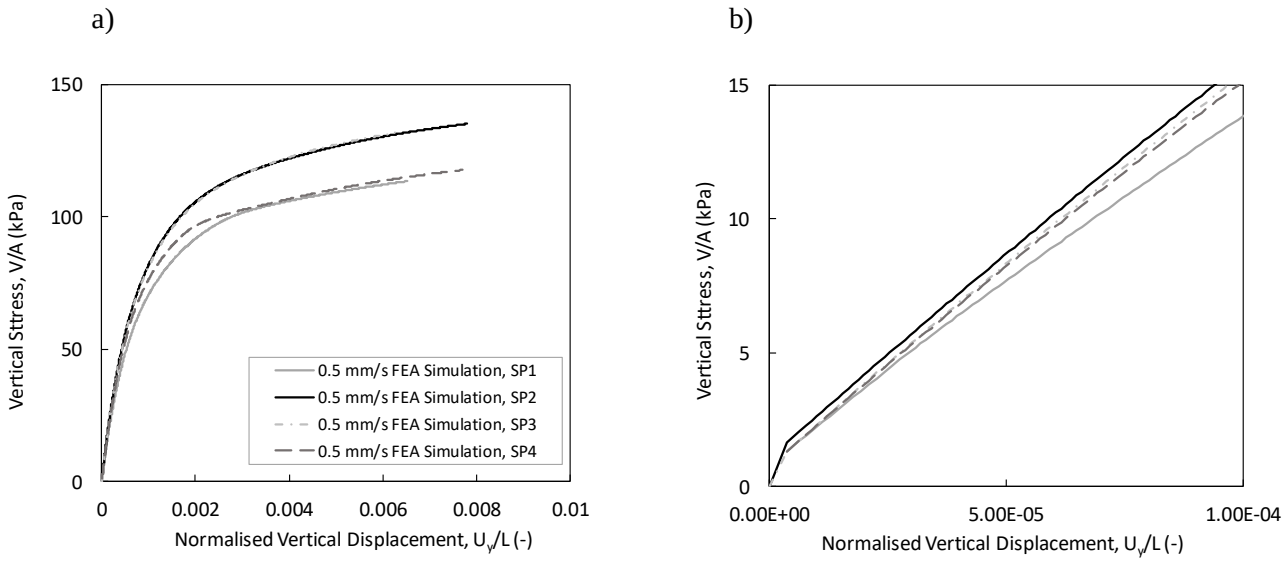

Figure 23: Predicted vertical load-displacement for soil profile layering sensitivity study with small displacement zoom view for Senders (2008) model set up (Bucket B) at initial void ratio of 0.535

6.3 Conclusions and Further Work

The suitability of a bounding surface plasticity model for sand, based on the Manzari-Dafalias model architecture, to predict the response of a suction bucket under tension loading has been investigated. The model formulation included several modifications to previous published versions of the model, most notably the inclusion of a fabric-dependent state parameter. Comparison of single element predictions to laboratory element tests, conducted on UWA silica sand, show that the model can capture the effects of soil density, stress level and stress path dependency. Use of the model in a boundary value problem of a suction bucket under tension loading is performed and compared with centrifuge test results. It is a promising result that a reasonably good agreement is obtained between the centrifuge results and the numerical model when the constitutive model is calibrated from laboratory element test data. This study gives added confidence and guidance on the use of bounding surface Manzari-Dafalias type models for foundation analysis.

The results highlight the importance of considering many different features of sand response within the constitutive model and demonstrate that calibration processes employing only triaxial compression test data will likely lead to an over-prediction of the load-displacement response for rapid tension loading. These results emphasise that although simpler constitutive models could be used for such analysis (e.g. SDS presented in Section 3) calibration of the parameters must be carefully considered for design analysis. It should be noted that analysis run times were slow (approximately ten times slower than equivalent analysis performed using the SDS model) and convergence issues were experienced. It is considered that use of this model for design FEA is possible and indeed beneficial given its predictive capability; however, it must be carefully considered based on the design schedule and the available laboratory data. It is proposed that the bounding surface model presented in this Section could be used for benchmark FEA of a particular foundation problem to help to provide guidance on suitable calibration considerations of parameters for simpler design models.

As discussed in Section 6.1, under certain cyclic loading conditions, drainage-induced upward ratcheting of the suction bucket can occur (Bienen et al., 2018). Therefore, as part of further work this case should be investigated numerically using the bounding surface model. It is anticipated that modifications to the model formulation may be required to capture the undrained cyclic response accurately (e.g. Boulanger and Ziotopoulou, 2013). However, since the upward ratcheting of the suction buckets under cyclic loading, observed from centrifuge tests, is primarily drainage-induced (Bienen et al., 2018) these modifications may not be essential. It is anticipated that the incorporation of inherent anisotropy within the model will be critical in order to predict the upward cyclic ratcheting phenomenon observed in centrifuge experiments.

Section 7

OFFSHORE WIND FARM MONOPILE FINITE ELEMENT ANALYSIS

Contents

7 OFFSHORE WIND FARM MONOPILE FINITE ELEMENT ANALYSIS

7.1 Introduction

This section provides an overview of the monopile foundation numerical analysis performed as part of the geotechnical design progression for an offshore wind farm (OWF) development in the North Sea. The work involved calibration of constitutive models and numerical analysis of monopile lateral load response.

Large diameter (D) monopiles with low embedment depths (L) below seafloor (BSF) are planned as the foundation concept to support wind turbine generators (WTG) as part of an OWF development in the Dutch sector, North Sea (exact site confidential). The aim of the work presented is to predict the lateral response of monopiles at a particular wind farm site using three-dimensional (3D) finite element analysis (FEA). In addition, the soil reaction curves around the piles are extracted for use in a one-dimensional (1D) finite element models, using the approach proposed by Byrne et al. (2017), to allow for rapid design optimisation at each individual wind turbine location.

Figure 7.1 presents the project design team outlining their roles and where appropriate reference is given in this section to the breakdown of work performed by the DEng candidate or other project team members.

7.1.1 Motivation for Work

When considering monopiles for an OWF, a large number of analyses are required to optimise the foundation size and 3D FEA cannot realistically be used for the design of each monopile due to the high computational cost. It is therefore preferred to perform the design iterations using 1D Winkler beam type models using soil reaction curves derived from 3D FEA (e.g. Erbrich et al., 2010; JeanJean et al., 2017; Byrne et al., 2017).

7.1.1.1 1D Modelling Background

Offshore pile design in non-carbonate sands and clays is typically carried out in accordance with the recommendations of API (2011) or DNV (2014), which adopt the p-y curve method to represent the relationship between the horizontal soil resistance and lateral displacement of the pile in a 1D model. The methodology has historically been widely adopted for design of piled foundations in the North Sea and elsewhere.

The limitations of the API *p-y* approach for predicting the response of large diameter monopiles have been well documented (e.g. Doherty and Gavin, 2011; JeanJean et al., 2017; Byrne et al., 2017; Taborda et al., 2019; Zdravkovic et al., 2019). Table 7.1 presents a summary of some of the identified shortcomings of the API *p-y* approach for monopile design.

The limitations of the API *p-y* formulation for the application of monopile design led to recent joint industry/academic research initiatives such as the PISA project (Byrne et al., 2017). Byrne et al. (2017) and Burd et al. (2017) extended the traditional *p-y* approach (which only includes distributed horizontal load (p) versus lateral displacement curves (u_x) along the pile embedment depth (z)) to include the following additional soil reaction curves:

i. distributed moment (m) versus pile rotation (θ) reaction curves;
ii. a base shear (T) versus pile toe lateral displacement (u_x) reaction curve;
iii. a base moment (M) versus pile toe rotation (θ) reaction curve.

A schematic of the soil reactions around a monopile for use in a 1D model as proposed by Byrne et al. (2017) and Burd et al. (2017) is given in Figure 7.2.

7.1.1.2 3D to 1D Models

Byrne et al. (2017) also highlighted the potential for 3D FEA to be used to determine site-specific soil reaction curves for implementation into a 1D pile model. While the driving force behind the recommendation for 3D FEA-based design of monopiles has been the limitations of the soil reaction model of the API method (i.e. *p-y* only) when applied to the monopile design space, the

3D FEA approach also provides a means to improve upon the simple soil parameter representations of the API method. Figure 7.3 presents the improved monopile design process, considering recommendations from Byrne et al. (2017), with the orange shaded boxes outlining the components of the process performed as part of this study.

7.1.2 Project Overview

This study firstly presents verification of the 3D FEA by predicting the response of a number of pile load tests in dense sand, with subsequent sensitivity analyses performed to assess the influence of different soil layering profiles and loading rates. The site characterisation and constitutive model calibration are then presented for the different geotechnical soil units at the OWF site. Finally, a brief overview of the 3D FE design analyses for a large number of monopile locations at the OWF site are presented.

The main project tasks performed as part of this study (Tasks 1 to 6) are presented in Figure 7.4 and described in Table 7.2. Sections 7.2 to 7.4 present an overview of the key results/findings from each project Task.

7.2 Finite Element Analysis Prediction of Pile Load Tests

The OWF sites for which foundation design analysis was performed (Tasks 5 and 6) consisted of a mixture of different soil types due to varying geological features across the site (e.g. localised paleo-channels, glacial compaction). As a result, the dominant mechanical behaviour of the soil types varied significantly across the OWF site (e.g. clean highly dilative dense sands; glauconitic and silty sands which were highly contractive; overconsolidated stiff clays and soft clays); however, most of the site, within the depth of interest for the design of monopiles, consists of dense to very dense fine to medium sand.

This section therefore presents Class-C (design) and Class-C1 (calibrated) predictions of the PISA Dunkirk test pile response to verify the constitutive model calibration approach and the 3D FEA in dense sand. Table 7.3 presents the prediction class definitions used in this study, based on Lambe (1973). The Class-C predictions were made prior to the detailed measured pile load test results

being supplied. This is to say, the pile load tests had been performed, but the results were unpublished (and unavailable to the project team) when the prediction analysis was performed. The Class-C prediction allowed conclusions to be drawn on the accuracy of the design calibration and modelling process. Considering these conclusions, from the analysis performed as part of Tasks 1 and 2, an assessment was made as to the suitability of the selected constitutive model and the calibration approach for subsequent predictions of monopile lateral load response for sensitivity analyses (i.e. Tasks 3 to 4) and wind farm foundation design analyses (i.e. Tasks 5 to 6).

7.2.1 Overview of Pile Load Tests and Site investigation

7.2.1.1 Pile Load Tests

The pile load tests were carried out at Zip des Huttes, west of Dunkirk. The Dunkirk pile test site offers a profile of dense sand which is considered to be broadly similar to that found in the southern North Sea (Chow, 1997).

An extensive series of monotonic laterally loaded pile tests were performed at the Dunkirk pile test site to investigate pile response in typical North Sea sand as part of the PISA project. The results of the pile load tests were not publicly available at the time of this prediction exercise and were only made available after the Class-C prediction by Ørsted A/S (PISA project partner). The results have since been published by McAdam et al. (2019).

Three of the Dunkirk test piles were selected for the calibration exercise. Table 7.4 presents the geometries of the selected test piles; see Figure 7.5 for the definitions of the various monopile dimensions specified in the table.

7.2.1 Constitutive Model Selection

A qualitative review of possible constitutive models for dense sand was first undertaken using a weighted decision matrix (Table 7.5). The following models were considered:

- Fugro Dilational Model (FDM) incorporating stress- and strain-dependent elasticity (Section 4);

- Hardening soil with small strain stiffness overlay (HSsmall) model (Benz, 2007; Plaxis, 2017)
- Linear elastic-perfectly-plastic Mohr-Coulomb (MC) model (Plaxis, 2017)
- Manzari-Dafalias type bounding surface model (Dafalias and Manzari, 2004).

None of these models incorporated inherent anisotropy. This may be an important consideration for the lateral loading of a monopile, since a range of stress paths are expected to contribute to the overall response; however, it was decided to adopt a design approach and calibrate the constitutive model to the expected dominant stress path while also ensuring a moderately conservative assumption.

Table 7.5 presents the weighted decision matrix results for the constitutive model selection. The FDM incorporating stress- and strain-dependent elasticity was selected to model dense sand. Details of the FDM formulation and implementation are given in Section 4.

It should be noted that post-peak softening cannot be simulated by the FDM. This is a simplification which eases the numerical complexity of the model but should be considered with caution, particularly for fully drained analysis. Significant post-peak softening is difficult to deal with in standard FEA and leads to increasingly mesh-dependent results and significant risk of convergence issues (Potts et al., 1990; Brinkgreve, 1994; Summersgill et al., 2017c). For practical design, it is therefore advisable to avoid models with post-peak softening unless absolutely necessary.

7.2.2 Calibration of Constitutive Models for Class-C Prediction

7.2.2.1 Site Investigation and Data Sources

A pile test location-specific site investigation was performed at the Dunkirk pile test site in 2014 as part of the PISA project. A subsequent laboratory investigation was carried out in 2015. Table 7.6 summarises the pile load test specific site investigation datasets considered for input to the calibration exercise. The data presented in Table 7.6 were unpublished when this study was performed; a selection of the data has since been published in Taborda et al. (2019).

A comprehensive historical dataset is also available for the Dunkirk test site. These data were collected as part of various programmes of pile load tests and associated site investigations performed at the site and from related academic research programmes. Table 7.7 summarises the references and relevant datasets for the Dunkirk site, as employed in the calibration exercise.

7.2.2.2 Soil Profile and Initial Conditions

Table 7.8 summarises the general soil layering interpreted for the Dunkirk test site based on review of the borehole logs. The soil conditions were generally consistent across the three selected test pile locations (L2, M4 and M7). The physical properties of Dunkirk sand are presented in Table 7.9. The Hydraulic Fill soil unit is understood to have the same geological origin as the Flandrian Marine Sand (Chow, 1997). Based on the available site investigation data, and consistent with historical data, the ground water level (GWL) at the site is expected to be at approximately 4 m below ground level (BGL). The pore water pressure profile is assumed hydrostatic below GWL. The presence of soil suction in the Hydraulic Fill is discussed by Chow (1997); however, no soil suctions were modelled above GWL in the numerical analyses reported herein.

A single relative density (D_r) profile was derived for the three selected test pile locations considering the measured cone penetration resistance (q_c) data and the correlations proposed by Jamiolkowski et al. (2001). Figure 7.6 presents the correlated D_r data along with the design profile adopted. Despite some variations at the base of the Hydraulic Fill unit (~3.8 m BGL) and within the Flandrian Sand unit, the average D_r profile was assumed to be constant at around 87 % (e_0 = 0.614) to the depth range of interest (~12 m BGL i.e. maximum test pile depth plus one diameter). The (simplified) design profiling approach was considered to be consistent with the objective of the calibration exercise; that being to determine the adequacy of the numerical modelling design process for subsequent prediction of monopile lateral load response at the wind farm site.

For calculation of initial effective stresses in the FEA model, different bulk unit weights were assigned above and below GWL (i.e. dry and saturated) but no distinction was made between soil

units (Table 7.10). A single value of K_0 (=0.5) was adopted for both soil units based on discussions presented in Kuwano (1999) and Aghakouchak (2015).

7.2.2.3 Calibration of the FDM

Calibration of the main constitutive model components for the FDM (i.e. stress- and strain-dependent stiffness model; critical state; stress-dilatancy response and yield strength) using laboratory data are described below.

Stress- and strain-dependent stiffness model

The isotropic elastic stiffness properties, at very small strains, were specified using G_0 and ν. The assumed dependency of G_0 on p' was described by Equation 4.1 in Section 4 (when $E_q = 0$). Table 7.11 lists the elastic stiffness parameters that control G_0 ($G_{ref}, n1, \nu, f_{e1}$), which were derived primarily using in situ seismic cone penetration test (SCPT) data. Figure 7.7 presents a comparison of the model G_0 profile with the available SCPT data. Since the cone penetration test (CPT) profiles are similar for the three selected test pile locations this elastic profile was considered suitable for all numerical analyses performed.

Triaxial stress-path data from Aghakouchak (2015) were used to calibrate the strain-dependent stiffness degradation model parameters (a, b, R_{Gmin}), since these were the only available data which included high resolution local strain measurements. Table 7.11 summarises the stiffness degradation model parameters selected.

Figure 7.8 presents the FDM calibrated strain-dependent tangent stiffness degradation model predictions compared to test data from Aghakouchak (2015). An empirical stiffness degradation curve for sand proposed by Oztoprak and Bolton (2013) was used to aid the calibration due to the lack of extensive laboratory data with high resolution local strain measurements. The mean empirical stiffness degradation curve proposed by Oztoprak and Bolton (2013), which was used to aid calibration, is based on a testing database of 454 tests.

Critical state

The CSL was determined by interpretation of stress-path triaxial data from Liu (2019), Aghakouchak (2015) and Kuwano (1999).

To help determine a representative CSL, the data were grouped in the broad ranges: loose to medium dense and dense to very dense. The reason for the general scatter in the data presented in Figure 7.9 was expected to be because the dense to very dense samples had potentially not reached a true critical state condition; although this assumption is consistent with general experience, it could not be verified as post-shear photographs were not available as part of the triaxial datasets. A Representative Estimate (RE) and High Estimate (HE) CSL were fit to the data, with the RE line adopted for the FDM Class-C prediction calibration. Although the RE CSL may lie slightly below the true CSL (defined as HE in this case), this was considered to be an appropriate design line.

Note, the variables p'_{cv} and e_{cv} are used in Figure 7.9 to reflect that the model calibrated 'CSL' may not be the true critical state of the material. Figure 7.9 presents the RE CSL used for the Class-C pile test predictions.

Stress-dilatancy response

The predicted stress-dilatancy response of the soil is controlled by the plastic potential function within the FDM (Paper 1, Equation 6). The p'_{cv} value which controls the level of dilation is state-dependent and is related to Figure 7.9. The dilatancy, D $\left(= d\varepsilon_v^p / d\varepsilon_q^p\right)$ from the model can be derived, considering a triaxial state of stress, by taking the partial derivatives of the plastic potential function with respect to the mean effective stress and deviatoric stress $\left(D = \frac{\partial g / \partial p'}{\partial g / \partial q}\right)$.

The D was determined from the laboratory data using the approach as discussed in Section 6 (Paper 3) for the modified Manzai-Dafalias type model, with E_{fact} used to define the elastic stiffness matrix reduction (Equation 4.3 in Section 4) when forming the elastoplastic stiffness matrix $\boldsymbol{D}_{ep}$. There was a lack of available undrained test data to determine E_{fact} hence a value of

0.5 was assumed based on values determined for UWA silica sand outlined in Section 6. The stress-dilatancy relationship is calibrated at the peak dilation state from each test.

The data presented in Liu (2019) were used to calibrate the plastic potential function. Figure 7.10 presents the Representative Estimate (RE) and Low Estimate (LE) stress-dilatancy response of the calibrated plastic potential function for the Flandrian Marine Sand at the Dunkirk site for a range of initial void ratios. The RE parameters were calibrated to triaxial compression test data (Figure 7.10a) and the LE parameters were calibrated to a selection of the available triaxial extension test data at the Dunkirk site (Figure 7.10b). Table 7.12 summarises the RE and LE plastic potential function parameters. It is important to note that below 100 kPa minimal test data was available to infer the stress-dilatancy behaviour and therefore the plastic potential in this zone should be treated with caution; however, empirical corrections presented by Chakraborty and Salgado (2010) were used to infer the most appropriate trendline in this zone.

The calibrated RE stress-dilatancy matched well with the relationships proposed by Chakraborty and Salgado (2010), which are also shown on Figure 7.10 for comparison. The RE stress-dilatancy parameters were used for the Class-C prediction.

Soil strength

The yield function (f) implemented within the FDM is a wedge-type pressure dependent surface, with f given by Equation 1 in Paper 1.

Post-peak softening may influence the ultimate lateral capacity of a fully drained pile in very dense sand, which could have implications on the Class-C prediction of the test pile response with the FDM model. However, since the test piles were only loaded to a lateral ground level displacement equal to about 10% of the pile diameter, the true ultimate geotechnical capacity is unlikely to have been mobilised in most cases and hence any post-peak softening effects are unlikely to have developed significantly (Ahmed and Hawlader, 2016), albeit this dependent on the softening rate. In addition, at higher peak design loads, associated with storm conditions, for large diameter monopiles significant

partial drainage (dilational) effects are expected to start to control the soil stress-strain response as opposed to post-peak softening.

Despite the forgoing, to investigate the influence of adopting a fixed yield surface for the test pile calibration exercise, different failure stress ratio values $M_c = q/p'$ in triaxial compression, were considered as part of a small parametric sensitivity study (presented in Section 7.2.4.2).

Figure 7.11 and Figure 7.12 present the maximum (peak), which represents the high estimate (HE), and the minimum (final), which represents the LE, values of M_c derived from the available triaxial compression test data. The design values for Dunkirk sand at different initial D_r values are presented in Figure 7.12 and the in situ values used for the Dunkirk pile load tests are listed in Table 7.13. The RE was selected for the Class-C prediction, allowing for a cautious estimate, in the absence of post-peak softening with the fixed yield surface implemented within the FDM, as discussed above and hence is lower than the HE from the data. The LE is essentially the critical state friction angle for the soil and hence is the lowest value that can be expected to be mobilised at very high confining stress and/or at very large shear strain.

Element test predictions

To confirm the suitability of the Class-C prediction model parameters, a variety of single element test predictions were run to compare with some available laboratory element test data.

Figure 7.13 presents a comparison of the predicted and measured drained stress-strain response based on the test data in Aghakouchak (2015). This dataset was the only available data to include high resolution strain measurements. For this comparison, the peak stress ratios were applied and hence it is expected (and indeed shown) that the predicted strength should match well with the measured peak strength. The pre-peak stress-strain response is also generally well matched, albeit tending to the over-stiff side just before the peak strength is mobilised.

7.2.3 Finite Element Analysis Model

7.2.3.1 Mesh Geometry

The 3D finite element (FE) mesh of both the soil and the pile was developed using 10-noded quadratic fully integrated tetrahedral elements. Table 7.14 summarises the general properties of each test pile FE model. Mesh generation was automated using a Python script (script written by Dr. Mikael Ramos Da Silva), ensuring repeatability and adequate scaling of the mesh for the different test pile sizes analysed.

Each FE model comprised half of the pile and soil, exploiting the symmetry. All vertical boundaries were normally fixed and the lower horizontal boundary was fully fixed. The finite element mesh extended 11 to 12 pile diameters horizontally outside the pile and 1.5 to 2 embedded pile lengths below the pile tip, which was considered to be sufficient to avoid any potential boundary effects. Figure 7.14 presents an example FE mesh.

The element distribution across the mesh was optimised to provide local refinement in the zones close to the pile shaft and tip, while limiting the total number of elements. The automated mesh generation process was setup to include 15-degree subdivisions in the circumferential direction around the pile and horizontal slices along the pile shaft. This approach allowed for a more repeatable mesh generation between models and to aid the extraction of soil reaction curve properties that are required during later tasks (see Figure 7.4).

7.2.3.2 Pile Model

The piles were modelled as solid linear elastic cylinders with outer zero-thickness interface elements linked to the adjacent soil to approximate the pile-steel-soil interaction. The interface elements were modelled with a friction angle of 28° and a stiffness of $50x10^3$ kPa.

Solid piles were adopted instead of plate element piles to overcome model convergence issues and improve computational speeds. The equivalent solid pile was defined as having the same total length and outer diameter as the open-ended pile. The equivalent Young's modulus required for

the solid pile was simply derived to ensure the bending stiffness of each test pile was equal to the bending stiffness of the solid pile.

Zhang and Anderesen (2019) outlined a method for soil reaction curve extraction, from 3D FEA of monopiles, and recommended the use of an equivalent idealised solid pile. Zhang and Anderesen (2019) noted that an external scooping failure mechanism forms at the base of a monopile, under lateral loading, and hence the use of a solid pile is not likely to effect the base shear response. However, it is important to note that FEA of different suction installed caisson geometries, performed by Dijk (2015), showed that for very low L/D values (L/D<1.0) it is possible that an internal scooping mechanism could develop at the pile base, and as such the use of a solid pile may not be suitable in all cases. The use of an equivalent idealised solid pile within the 3D FEA presented in this study is considered acceptable given the monopile L/D values simulated are all greater than two.

7.2.3.3 Load Model

The model piles were loaded at an elevation above ground level (h) of 10 m (Table 7.4). The FEA model was displacement controlled, meaning that an imposed displacement was applied at h and the resulting reaction loads were extracted from the analysis.

7.2.4 Class-C Prediction

7.2.4.1 Results

Following provision of the pile test predictions, the measured pile load test data for the L2, M4 and M7 piles were supplied (i.e. Class-C prediction). These pile load test data were subsequently compared to the Class-C predictions to allow the accuracy of the calibration and modelling process to be evaluated. These Class-C predictions (in which no pile load test data was available beforehand) are considered valuable to assess an FEA approach in which calibration has been performed as it would be for a design case. Such published blind prediction cases are rare in the literature.

Figure 7.15 to Figure 7.17 shows the Class-C predictions compared to the measured pile load test data. Overall the prediction was considered reasonable for a true 'blind' design prediction. For all piles, the Class-C predictions are observed to underestimate the initial measured pile stiffness. For the L2 and M4 piles the ultimate capacity predicted at 0.1*D* is underestimated (by less than 10 %), which is considered acceptable considering the design basis of the Class-C prediction. The predicted tangent stiffness at 0.1*D*, is comparable to the measured results for the L2 and M4 piles but is overestimated for M7.

Based on these findings, it was considered beneficial to investigate whether any reasonable variation of the constitutive model input parameters, within the measured range of the available calibration dataset, could result in an improved model prediction. Following this parameter review, updated Class-C1 predictions were made for each test pile.

7.2.4.2 Pile L2 Sensitivity Analysis

In addition to the Class-C RE prediction for the L2 pile, which is the largest of the test piles considered, an additional parametric variation, considering the LE soil strength model (i.e. friction angle) parameters was run (Table 7.13).

Comparison of predicted load-displacement data highlights the influence of the soil strength model (i.e. friction angle) on the lateral pile response. Only a moderate influence is observed at relatively large ground level lateral displacements, which is considered reasonable given the relatively small variation in equivalent friction angle between the two strength models adopted.

7.2.5 Class-C1 Prediction

Comparison of the Class-C pile test predictions and the measured pile load test data indicated that the initial soil stiffness response was the principal variable that was at variance with the measured response. However, it was expected that simply adjusting the soil stiffness parameters alone would most likely just stiffen the overall pile response, such that the response at 0.1*D* would then be too stiff and the capacity overestimated.

A holistic review was therefore conducted of the key parameters thought to control the overall shape of the load-displacement response and adjustments were proposed where sufficient laboratory data was available to support a reasonable modification. The selected modifications are described in the following sections.

7.2.5.1 Re-Calibrated Parameters (Class-C1)

Stress- and strain-dependent stiffness model

Based on the comparisons described in Section 7.2.4 it was apparent that the initial stiffness of each test pile was significantly underestimated using the stiffness parameters defined in Table 7.11. It was concluded that this was most likely due to an underestimation of G_0 in the constitutive model. Review of the adopted G_0 profile and in situ measurements shown on Figure 7.7 indicated that a reasonable increase in the adopted G_0 profile could be justified in the depth interval from 0 m to approximately 6 m BGL. Table 7.15 summarises the revised elastic stiffness parameters which control G_0 for the Class-C1 prediction analyses. Using these updated parameters, Figure 7.19 presents a comparison of the updated G_0 profile with the available SCPT data.

The strain-dependent stiffness degradation model parameters were also considered to be a potential contributing factor to the underestimate of the pile stiffness response. However, there was considered to be insufficient data available to justify any significant modification.

Stress-dilatancy response

From comparison of the Class-C prediction to the shortest test pile (M7) measured response, the pile tangent stiffness and capacity at large displacements were overestimated. It is considered that this behaviour was most likely related to an overestimation of the stress-dilatancy response at low mean effective stresses. Therefore, stress-dilatancy parameters for the FDM were adjusted following review of the laboratory data.

It is well established that the loading direction significantly affects the stress-dilatancy response of sand due to fabric effects (as discussed in Paper 3); with the most significant difference expected

between triaxial extension and compression load paths. For the RE Class-C predictions, the stress-dilatancy response was calibrated based solely on data from triaxial compression tests. This calibrated relationship matched well with that proposed by Chakraborty and Salgado (2010), which is also for triaxial compression conditions, as shown in Figure 7.10a. However, after further consideration, given the range of stress paths expected around the monopile during lateral loading, it was decided that it would be more appropriate to use an average stress-dilatancy relationship which fell between the triaxial compression and extension datasets (i.e. between the Class-C RE and LE calibrated stress-dilatancy trends). This was also anticipated to be approximately representative of a direct simple shear (DSS) response, which is typically considered to be broadly representative of the average stress path in the soil for laterally loaded monopiles (JeanJean et al., 2017), albeit this assumption cannot be confirmed in the absence of any DSS data. The updated Class-C1 stress-dilatancy parameters are summarised in Table 7.16. Figure 7.20 presents the stress-dilatancy response using the updated Class-C1 parameters in comparison to the measured results from triaxial compression and extension tests at two initial void ratios.

7.2.5.2 Finite Element Model

The finite element mesh, pile model and load model employed for the Class-C1 predictions were the same as used for the Class-C predictions, as described in Section 7.2.3. The only change incorporated was the use of updated (Class-C1) constitutive model parameters.

7.2.5.3 Results

The results of the Class-C1 predictions are presented in Figure 7.15 to Figure 7.17. For all test piles, the Class-C1 predictions give an improved representation of the initial measured pile stiffness, particularly for pile M7. However, as the displacement starts to increase, there remains a tendency for underprediction of stiffness for piles L2 and M4. Nevertheless, for these latter two piles the ultimate capacity predicted at 0.1D is now in close agreement with the measured results. However, for pile M7 the improved initial stiffness is achieved at the expense of an increased overestimate of the capacity at 0.1D (i.e. 16% over), with a steadily increasing overestimate of the secant stiffness for displacements greater than ~ 4 mm (i.e. ~ 0.5 % of D).

In considering these updated results it is worth noting that in practical design the limiting displacement for the piles will be much less than 0.1*D*, given the strict rotation tolerances that are imposed. Over this permitted operating range, which will typically constrain head displacements to less than about 0.01*D* for a full scale monopile, the updated Class-C1 predictions are universally better than the original Class-C predictions.

7.3 Soil Profile Sensitivity Study Analysis

7.3.1 Introduction

This section presents 3D FEA simulations of monopile lateral load response which were performed under Task 3 and Task 4 of the project scope of work (Figure 7.4).

The dense sand constitutive model and FEA approach, which were evaluated against measurements from onshore laterally loaded pile tests (Section 7.2), were used as a basis for the model sensitivity study reported in this section. In addition to the calibrated model for dense to very dense sand presented in Section 7.2, calibrated constitutive models are introduced for medium dense sand and clay layers as part of the soil layering sensitivity study. The model sensitivity cases considered were defined within two project tasks:

- Task 3: considering various soil profiles of varying sand relative density and layering;
- Task 4: considering the impact of loading rate on monopile response.

The synthetic soil profiles and model inputs considered for each sensitivity study are described in the following sections.

7.3.2 Soil Profiles and Pile Geometry

Eight different soil profiles were considered as part of the Task 3 and 4 sensitivity analysis, including three uniform soil profiles with varying relative density and five layered soil profiles. The profiles developed are based on typical North Sea soil profiles. Table 7.17 summarises the soil profile cases considered. Figure 7.21 presents a schematic illustration of the layered soil profiles. In addition, the SP1 profile was considered for the loading rate sensitivity analyses

performed under Task 4. Table 7.18 summarises the monopile geometry considered for Task 3 and Task 4.

7.3.3 Soil Models

Tasks 3 and 4 required geotechnical parameterisation of the soil profiles summarised in Table 7.17. Table 7.19 summarises the constitutive model calibrations as considered for each soil type.

The FDM calibration for dense to very dense sand, present at the Dunkirk test pile locations, is described in Section 7.2. In these sands, from a review of the laboratory test data, the response was observed to be dominated by shear-induced dilation. However, from review of the published test data for the Dunkirk sands (See Table 7.7) it was observed that at lower relative densities (i.e. $D_r \leq 50\%$) more significant contraction occurred up to reasonably large shear strains, after which lower maximum dilation rates occurred. As a result it was considered that the FDM should not be used to model the response, particularly when considering partial drainage conditions (Task 4). For this reason, the HSsmall model (Benz, 2007), termed HSsmall(E) in this study, was adopted to model the response of medium dense sand layers. In addition, all clay layers were modelled using a total stress implementation version of the HSsmall model (Plaxis, 2017), termed the HSsmall(T) model in this study. The HSsmall(T) is an isotropic hardening Tresca model and the HSsmall(E) is an isotropic hardening Mohr-Coulomb model.

The HSsmall model has the flexibility to include a Matsuoka-Nakai (MN) or a Mohr-Coulomb failure criterion. The Mohr-Coulomb failure criterion was utilised within the model for this study which simplifies to a Tresca surface when total stress strength parameters are used (i.e. HSsmall(T)). The HSsmall model is an isotropic double hardening plasticity model with a shear hardening yield surface (f_s) and a volumetric hardening cap yield surface (f_c). The stiffness parameters E_{50}^{ref} and E_{oed}^{ref} are used to control the hardening of f_s and f_c respectively according to a hyperbolic function. E_{ur}^{ref} is then used to control the unload-reload stiffness within the yield surface. The stiffness parameters used in the model formulation (E_{50}, E_{oed}, E_{ur}) are a power

function of the current stress level, the reference stiffness parameters (E_{50}^{ref}, E_{oed}^{ref}, E_{ur}^{ref}) and the exponent m.

Both models also include a modified form of the Hardin and Drnevich (1972) strain-dependent hyperbolic function to define the elastic stiffness matrix controlled by G_0^{ref} and $\gamma_{0.7}$. A detailed description of the model formulation is presented by Plaxis (2017) and Benz (2007).

All sand model calibrations considered the in situ and laboratory datasets available for the Dunkirk pile test site as summarised by Section 7.2.2.1.

7.3.3.1 Dense to Very Dense Sand Layers

All dense to very dense sand layers were modelled using the Class-C1 calibrated constitutive model (FDM) parameters discussed in Section 7.2.5.1.

7.3.3.2 Medium Dense Sand Layers

The HSsmall(E) model was used to simulate the response of medium dense sand at a relative density D_r of 50 %. A similar modelling approach is used for some of the sand soils for the wind farm foundation design tasks (i.e. Tasks 5 and 6 discussed in Section 7.4) in which extensive silty and glauconitic (highly contractive) sands are present at the site. The HSsmall(E) medium dense model parameters were calibrated based on the limited available drained triaxial test data presented by Liu (2019) and undrained triaxial test data presented by Kuwano (1999), both relating to the behaviour of the Dunkirk sand. Table 7.20 summarises the calibrated model parameters selected.

Figure 7.22 presents a comparison of predicted and measured drained response for triaxial compression test data presented by Liu (2019). The HSsmall(E) model was used since the medium Dunkirk sand was more contractive and significantly less dilative than the dense to very dense Dunkirk sand. It was found that the HSsmall(E) model provided a significantly better calibration, to the medium dense Dunkirk sand triaxial test data, than the FDM. However, it should be noted given it was a clean sand modest contraction was observed in comparison to the extensive silty

and glauconitic sands found at the wind farm site (Section 7.4). The element test predictions were made using a RE friction angle and hence it is expected (and indeed shown) that the predicted strength will tend to slightly underestimate the measured peak strength in drained tests; however, this is consistent with the design approach adopted in this study in which no post peak softening was modelled.

Figure 7.23 presents a comparison of the predicted and measured undrained response for triaxial test data presented by Kuwano (1999). The laboratory test data is limited to one triaxial compression test and one triaxial extension test, however the model simulations provide an acceptable representation of this data.

A limitation of the HSsmall(E) model is that a fixed dilation angle is assumed when the maximum yield surface size is reached (i.e. φ') and as such careful selection of the dilation angle is therefore required to ensure it is suitable for design analysis. As can be seen from Figure 7.23 a level of conservatism was tolerated in the triaxial compression representation, with respect to the dilation angle assumed, to ensure a tolerable prediction of the triaxial extension data.

7.3.3.3 Clay Layers

All clay soil layers were modelled with the HSsmall(T) model formulation (Plaxis, 2017). The model input parameters were correlated to s_u for generalisation of the model. An s_u of 150 kPa was used for all clay layers used as part of the soil profile sensitivity study.

The model parameters were obtained by calibrating the response to the normalised stress-strain backbone curve (i.e. τ/s_u versus γ). The calibrated model parameters adopted were the same as those used for modelling the response of the clay soils across the OWF development as part of Task 5 and 6. The model parameters are given in Table 7.21. Figure 7.24 presents the corresponding normalised stress-strain and stiffness-strain backbone curves.

7.3.4 Finite Element Analysis Model

7.3.4.1 Mesh Geometry and Pile Model

The 3D FE models were developed using a similar configuration to that discussed in Section 7.2.3.1 and 7.2.3.2. Table 7.18 presents the monopile geometry considered for all Task 3 and 4 sensitivity analyses performed. The FE mesh properties for the different soil profiles are presented in Table 7.22. Figure 7.25 presents an example finite element mesh for the Task 3 and 4 analyses. Pile-soil interface properties were modelled with:

- An interface friction angle of 28 degrees, where the interface was adjacent to sand layers. This value followed the recommendations of CUR (2001) allowing for driven pile installation and cyclic mobilisation of the pile interface stress and was considered appropriate for analyses under Task 3 and Task 4.
- An interface reduction factor of 0.6 was applied to the soil s_u for clay layers to derive the interface undrained shear strength $s_{u,int}$. This value was based on the lower bound post-installation equalised values recommended by Lehane and Jardine (1994) for piles jacked into overconsolidated clay at the Cowden pile test site.

7.3.4.2 Soil Model

The FEA adopted the soil profiles described in Section 7.3.2 and the parameters described in Section 7.3.3 of this report.

The default (base case) drainage state assumption specified for Task 3 was for fully drained conditions in sand soil units and undrained conditions in clay soil units. Task 4 considered fully coupled flow-deformation analyses of the medium dense sand profile (i.e. SP 1) where the drainage state of the sand soils varied during the analysis. In the latter case the same effective stress model as for fully drained analyses (i.e. HSsmall(E)) was employed to simulate the soil response. Fully coupled flow-deformation FEA was performed for SP1, considering different loading rates, as it was considered possible that the partially drained case could be less conservative than the drained case for the medium dense sand. The soil profiles considering dense to very dense sand are not considered for fully coupled flow-deformation FEA as the strong dilational behaviour of the material, which would manifest as significant negative excess pore

pressure development under undrained to partially drained conditions, would mean the drained case is certainly conservative and hence should be used for design.

For the coupled flow-deformation analyses a soil permeability (k) of 10^{-5} m/s was used for the medium dense sand. This permeability, which is considered representative of a typical North Sea sand, was based on a review of the measured permeability data from the sand units at the OWF considered in Task 5 and 6. This permeability was assumed to be fixed during analysis i.e. it was not set to change with void ratio.

7.3.4.3 Cavitation Cut-Off

The coupled flow-deformation FEA performed under Task 4 modelled the water depth (h_w) and pile dimensions specified in Table 7.18. In reality, the absolute pore pressures (u_w) are limited by the cavitation pressure of the pore fluid, which is assumed as $u_c \approx -100$kPa for water. The maximum allowable negative excess pore pressure (u_e) is then given by $u_e = u_c - (h_w + z)\,\gamma_w$, where γ_w is the unit weight of water which is assumed as 10 kN/m^3 within this study and h_w is the height of the water level above seafloor. The mobilised strength will therefore be lower than the theoretical undrained or partially drained strength predicted by the constitutive model implementation if the cavitation pressure is exceeded. Not considering the cavitation cut-off for negative excess pore water pressure generation in the model can be very unconservative for sands.

In fully coupled flow-deformation FEA the excess pore pressure u_e is calculated as a degree of freedom at the nodes rather than the Gaussian integration points. Hence u_w is calculated from the solution of the global system of equations and therefore it cannot be manipulated by the constitutive model subroutine at the integration points. Therefore, in fully coupled flow-deformation analysis no cavitation cut-off can be activated at constitutive level. This has proved to be a common issue for fully coupled flow-deformation FEA, and as a consequence a cavitation cut-off has not been incorporated in most previous studies when partially drained conditions are considered, and the cavitation pressure is likely to be exceeded in some regions of the model (e.g. Bye et al., 1995; Thieken et al., 2014).

For the coupled flow-deformation FEA performed under Task 4, a user-defined hydraulic model which imposes an artificially reduced stiffness of water as a function of the current level of suction pressure was used to simulate cavitation. This approach was implemented by making use of the user-defined hydraulic model, which is typically used to describe the behaviour of unsaturated soils. Using this model, the bulk modulus of water was relaxed within the global system of equations once the cavitation pressure was reached to ensure that the overall water suction pressure did not violate the cavitation limit. The bulk modulus of water used in the calculations (K_{fc}) to form the global stiffness matrix is therefore calculated by,

$$K_{fc} = K_f \mathrm{WS}_f \qquad 7.1$$

where K_f is the bulk modulus of water (≈ 2 GPa) and WS_f is the water stiffness factor, which varies from an initial value of 1 to ~0 as the cavitation pressure is reached. Figure 7.26 presents the WS_f versus suction pressure user-defined model used for the analysis to simulate cavitation cut-off.

Once the cavitation limit is induced, no further excess pore water pressure is developed and the response essentially becomes drained at the current effective stress state.

7.3.4.4 Load Model

For the Task 3 soil profile sensitivity analysis, the model piles were loaded under displacement control at an elevation (h) of 37.5m above seafloor as specified in Table 7.18. Displacement was applied uniformly around the perimeter of the monopile at this elevation.

The Task 4 FEA model was load controlled, meaning an imposed load was applied to a rigid body ring at the top of the pile. For the fully coupled flow-deformation analysis performed under Task 4, two loading rates were considered. These loading rates were defined as being broadly representative for wind loading and wave loading cases based on a review of example load time history data provided by Ørsted (Ørsted, personal communication, 31 October, 2017). An additional undrained analysis was performed to provide a reference (along with the fully drained

base case analyses performed under Task 3) for the variable load rate response. Table 7.23 summarises the loading rates applied in Task 4.

7.3.5 Results and Discussion

Reaction curves based on the recommendations of Byrne et al. (2017), as shown schematically in Figure 7.2, were extracted for all soil profiles modelled. An overview of the results is given below.

7.3.5.1 Extraction of soil reaction curves and equilibrium checks

For each loading stage the effective normal stresses, horizontal shear stresses and vertical shear stress are extracted at each integration point on the interface elements around the pile. The soil reaction curves proposed by Byrne et al. (2017) were then derived using a Python script developed by Fugro (reaction curve extraction script originally written by Dr. Mikael Ramos Da Silva).

Lateral load equilibrium checks were performed to ensure that the ratio between the applied horizontal load, *H*, and the sum of the horizontal reactions around the pile (i.e. from the extracted reaction curves) was within acceptable limits. The equilibrium error, E_{error}, was determined at each displacement increment for which the reaction curves were extracted by the following expression,

$$E_{error} = \frac{H}{(\sum_{i=1}^{n} R_i + R_{base})} \qquad 7.2$$

where R_i is the total lateral reaction force from each extraction slice (~1.5 m thick for this study) along the pile, the subscript i refers to the extraction slice number, n is the total number of slices along the pile and R_{base} is the extracted pile shear reaction force (i.e. T).

The lateral load equilibrium errors were less than 2% for all analyses performed under Task 3. An example of the extracted equilibrium error check for the SP2 analysis is presented in Figure 7.27.

7.3.5.2 Pivot Point

All FEA simulations performed indicated a pivot-point which developed at some elevation above the base of the monopile under lateral loading. Figure 7.28 presents a schematic illustration of the

pivot-point behaviour observed from the extracted distributed horizontal load reactions along the pile. Below the pivot point the deflection of the pile is negative, i.e. the displacement of the distributed horizontal load transfer curves reverses compared to the response noted above the pivot-point. In the depth vicinity of the pivot-point the distributed horizontal load transfer curves are distorted due to this behaviour.

The observations are as expected; however, they should be considered carefully when incorporating the distributed horizontal load transfer curve data, particularly from layered soil profiles, into a normalised framework for use in a 1D model, since the development of the pivot point (i.e. depth of occurrence) is specific to the monopile geometry and soil profile considered.

7.3.5.3 Soil profile variations

Figure 7.29 shows the global lateral load-displacement response and Figure 7.30 shows the global moment-rotation response for each of the soil profile sensitivity cases.

The differences shown in Figure 7.29 and Figure 7.30 between the three uniform soil profile cases, SP1, SP2 and SP3 are as expected, with the stiffness and capacity of the monopile increasing with increasing relative density of the uniform soil. Table 7.24 summaries the lateral pile head resistance (H) ranking of the layered soil profile cases (i.e. SP4 to SP8) at three seabed displacements. It is observed that SP4 yields the highest initial global pile stiffness and SP5 mobilises the largest ultimate capacity (i.e. at 0.1D). In these soil profiles very dense sand (D_r = 100 %) is present at the top (SP4) and base (SP5) respectively. The rankings (and related results) confirm an expectation that the response at small to intermediate pile displacements is governed by the upper soil layers. At larger displacement the contribution of the soil layers below the pivot-point of the pile and at the pile base has a significantly larger impact on the pile response.

Figure 7.31 presents a comparison of the distributed horizontal load transfer curves extracted from the Task 3 soil profile cases at three elevations along the pile:

- Figure 7.31a: Near seafloor, at a depth of 1.5 m to 3.0 m BSF;
- Figure 7.31b: Around pile mid-depth, at depths between 10.5 m and 12.0 m BSF;

- Figure 7.31c: Near the pile base, at a depth of 21.0 m to 22.5 m BSF.

From a more detailed review of the soil profile cases in which a 'weak' layer is overlain by a 'strong' layer some clear trends are observed with respect to the effect soil layering has on the extracted soil reaction curves. Figure 7.32 to Figure 7.34 shows the extracted distributed horizontal load-displacement and moment-rotation curves in the strong layer (i.e. dense sand or very dense sand) for uniform soil profile cases (i.e. SP2 and SP3) compared to layered cases in which weaker layers (i.e. medium dense sand and clay layers) are situated below the strong layer (i.e. SP4, SP6 and SP7). From inspection of Figure 7.32 to Figure 7.34 it is clear that the largest reduction (strength and stiffness) of the soil reaction curves occurs in close proximity to the layer change boundary, with gradually diminishing effects observed with distance from the layer change. It can be seen that the distributed horizontal load-displacement reaction curves are affected up to a maximum distance of approximately 0.5*D* from the layer change. A larger zone of influence is observed for the moment-rotation curves, with the reduction observed up to approximately 0.6*D* to 0.9*D* from the layer change. In addition, a larger relative reduction in the mobilised reaction for the moment-rotation curves compared to the distributed horizontal load-displacement curves is observed. It is also observed that there is very little reduction in the initial stiffness response of the soil reaction curves in all cases.

SP3 compared to SP4 (Figure 7.34) shows the most significant reduction in the moment-rotation response near the layer change with approximately a 90% reduction in the distributed moment at a rotation of -0.05 radians predicted for the layered case compared to the uniform profile. Figure 7.35 shows the displacement contours around the pile for SP3 (i.e. uniform dense sand profile) and SP4 (dense sand over medium dense sand) at a mudline displacement close to 0.1*D*. It can be seen from Figure 7.35 that a more significant rotational mechanism has developed for SP4 in comparison to SP1, caused by the weaker material in the lower half of the pile. This increased rotational mechanism developing in SP4 is expected to have a detrimental effect on the moment-rotation curves in the upper dense sand. Figure 7.36 presents the effective horizontal stress (σ'_{xx}) contours around the pile for SP3 and SP4 where it can be seen clearly that the lower weaker layer

is significantly affecting the upper strong layer near the layer transition. From Figure 7.36 it is can be seen that the lateral stresses become more concentrated in the upper layer when considering the layered case (i.e SP4 shown on Figure 7.36b) compared to the homogenous single layer case (i.e. SP3 shown on Figure 7.36a).

7.3.5.4 Load rate effect

Figure 7.37 presents a comparison of the global monopile response for each load rate sensitivity analysis performed for SP1, which comprises a uniform sand profile at D_r = 50%. Figure 7.37a shows the predicted global pile lateral load-displacement response and Figure 7.37b shows the global moment-rotation response at seafloor level.

Four variations of analysis are presented in Figure 7.37 as summarised in Table 7.23. It is observed from the comparison shown in Figure 7.37 that the undrained (SP1b), wave (SP1c) and wind (SP1d) case analyses show a very similar initial response. The undrained, wave and wind load cases remain continuously higher than the drained case across the full range of displacements analysed, due to the negative excess pore water pressures developed in these cases, which act to increase the effective stresses in the soil above those for the drained case.

Despite the variations in load rate between the analyses, no significant variation in the response between the undrained, wind and wave cases is observed until a seabed level displacement of approximately 0.05*D*. After this point the load-displacement response of the undrained and wave cases remain similar, however the wind case (at a lower load rate than the wave case) begins to reduce with respect to the undrained case. This reduction relates to dissipation of the negative excess pore water pressures at the slower rate of loading as the loading continues, and a small variation in the pile pivot-point depth.

Figure 7.38 presents a comparison of the excess pore pressure contours for the undrained, wave and wind loading cases at a pile head load of 20 MN. It is observed that similar contours of excess pore water pressure are developed in both the undrained and wave load rate cases and significantly lower excess pore pressures develop for the wind loading rate. The development of excess pore

water pressure is dominant in the shallow soils and around the pile base. In both the undrained and wave load cases the imposed cavitation limit is reached in a large number of soil elements at these locations, which may explain the similarity of the response observed at this load level. Were the cavitation limit not imposed in these analyses the monopile response would be expected to indicate a larger lateral resistance, although the magnitude of the difference cannot be quantified from the analyses performed. The impact of loading rate on the development of excess pore water pressure for the SP1 profile at the load indicated is clear from comparison of the wave and wind loading cases shown in Figure 7.38b and Figure 7.38c, respectively. Significantly lower negative excess pore water pressures are observed in the slower wind loading case and the cavitation limit is not reached at any point within the FE mesh.

Figure 7.39 shows a comparison of distributed horizontal load transfer curves for the fully drained (SP1a), undrained (SP1b) and wind (SP1d) cases. Note that the wave load case is not presented in Figure 7.39 since the curves are very similar to the undrained case. The comparison indicates, as expected, that the wind case curves typically fall between those of the fully drained and undrained cases at shallow depths. Around the middle pile section (Figure 7.39b) the wind case curves are higher than the undrained case owing to the differences in the excess pore pressure profiles illustrated in Figure 7.38. At the pile base the wind case curves are only slightly higher than the fully drained case; this appears to relate to significant dissipation of negative excess pore water pressure at the base of the pile and explains why a larger difference in the global pile response at larger displacements is observed between the wind and the wave cases, i.e. where the mobilisation of the base shear and moment resistance contributes more substantially to the global pile response.

Although differences are observed in the pile response due to loading rate at large lateral pile displacements (>0.05D), the lateral pile response for expected characteristic design loads and associated seafloor lateral displacements (< 0.025D) are very similar for all loading rates considered. As a result, fully drained conditions are considered sufficient for large diameter monopile design in sands.

7.4 Wind Farm Monopile Design Finite Element Analysis Study

7.4.1 Project Overview and Background

This section gives an overview of the monopile foundation numerical analysis performed as part of the geotechnical design progression for the offshore wind farm (exact site name confidential).

It is planned to install approximately 90 WTG structures across the site; each WTG will be founded on a monopile. The bathymetry across the site ranges between 14 m and 40 m water depth, with respect to lowest astronomical tide (LAT).

The work involved calibration of constitutive models across the site (Task 5) and 3D FEA of monopile lateral load response at the site to extract reaction curves to be used for 1D monopile design optimisation analysis (Task 6). The constitutive models used within the numerical analyses are the FDM and the HSsmall models.

It is important to note that scour, around the monopiles, was not considered in the 3D FEA since it was concerned with extraction of soil reaction curves only. However, it should be considered as part of detailed design, within the 1D structural design calculations using the extracted soil reaction curves, particularly for cases in which sand sediments are prominent near seafloor. It should be noted, that scour protection is typically employed and as such scour effects are not always taken into account.

7.4.2 Site Characterisation and Constitutive Model Calibration

For large offshore wind farms CPT data constitutes the main tool used to determine the soil conditions and soil parameters across the site, since it is not feasible to perform sampling boreholes at every WTG location. Typically, a limited number of sampling boreholes are performed across the site for laboratory testing and subsequently CPTs are performed at each planned WTG location. Therefore, it is important that all the constitutive model parameters can be correlated to CPT data for each geotechnical soil unit at the wind farm.

As part of this study, all parameters for the FDM and HSsmall model were calibrated from the available laboratory dataset for the site, with the parameters then correlated to CPT data so that

constitutive model design parameters could be determined across the OWF using WTG position-specific CPT data.

Constitutive model selection (i.e. HSsmall(E); HSsmall(T) or FDM) for profiling at each monopile design position was generally based on geotechnical soil unit designation. Stress-dilatancy observed from laboratory element test data and the CPT characteristics of the soil were also considered across particular soil units to guide the selection of the constitutive model to use for the location-specific FEA.

The FDM was utilised for sand soil units in which the response was primarily dilational (i.e. clean dense sands) and the HSsmall(E) model was utilised for glauconitic sands in which a highly contractive response was observed from the laboratory data. In addition, the HSsmall(T) model was used for the few occurrences of clay across the site. The general calibration approach considered correlation of the constitutive model parameters with profiling parameters which could be derived from CPT data. As a result, geotechnical soil unit specific correlations were developed to calibrate the constitutive models across the site in a reliable consistent way.

7.4.3 Finite Element Analysis for Monopile Design Locations

7.4.3.1 Design Location-Specific FEA Model Calibration

The constitutive model calibration approach for each soil unit were used to perform design FEA at a number of WTG locations across the site as part of the foundation design.

In total 11 different locations, with highly variable soil conditions, were selected for 3D FEA to be performed with location-specific reaction curves extracted for 1D FE design calculations i.e. following the monopile design approach outlined in Figure 7.3.

Table 7.25 summarises the constitutive model selection approach at each design position for the different soil units across the site. The identified geotechnical soil units were grouped for suitability to each constitutive model based on their dominant characteristic response (i.e. contractive sand, dilational sand or undrained clay). The sand Unit E occurrences were split into two groups: Unit E with high glauconitic content (Unit E1 which was highly contractive) and

clean dense sand (Unit E4 which was highly dilational). When developing location-specific design profiles for the FEA models it was important to determine if the Soil Unit E1 (i.e. using HSsmall(E) model) or E4 (using FDM) calibration should be adopted. Figure 7.40 presents a flow chart outlining the selection and constitutive model calibration approach for Unit E from CPT data. In addition, Figure 7.41 presents a typical soil profile where Soil Unit E1 and E4 are identified based on the CPT profile, with the measured laboratory data also presented..

An overview of the soil units at each design location are given in Table 7.26 and the monopile dimensions modelled are presented in Table 7.27. As discussed only an overview of the individual design FEA locations is presented in this section and hence the detailed parameterisation and FEA model set up of each monopile design location is not given. However, Figure 7.42 presents an example of the design profiling, from CPT data, for design locations C01 and L07..

7.4.3.2 Design Finite Element Analysis Results

The default (base case) drainage state assumption was fully drained in sand soil units as this was assumed to be conservative based on analysis performed in Section 7.3.5.4. However, undrained analysis was also run for a selection of design locations that were considered critical, and similar results to those presented in Section 7.3.5.4 were obtained. Therefore, it was confirmed that the drained assumption was conservative for all cases and hence should be adopted for design.

Full results and extracted reaction curves for each of 3D FEA models were developed for design of the OWF. The development of each 3D FEA model was consistent with that outlined in Section 7.3.4. Detailed description of the extracted reaction curves is not included within this summary section; however, the predicted load-displacement response at seafloor level for each design location is presented in Figure 7.43 for reference. It can be seen from Figure 7.43 that a highly variable lateral pile response is predicted for the different design locations across the site due to the complex heterogeneous ground model. The average run time of each 3D FEA model to a seafloor displacement of 0.1*D* was approximately 120 hours. Each 3D FEA mesh consisted of approximately 40,000 elements and was run using Intel Xeon 3.10 GHz processor (4 processors).

Given the relatively high run times of the 3D FEA and the highly variable soil profile across the site, clearly faster 1D model calculations must be used for design optimisation of each WTG monopile (approximately 90 planned WTG locations in total at the site).

The predicted 3D FEA extracted curves were used to perform 1D FE calculations following the approach outlined by Burd et al. (2017) and Byrne et al. (2017). A MATLAB implementation of OxPile, which was developed by Prof. Harvey Burd, was used to perform the 1D FE calculations. Details of the 1D FE modelling approach and formulation used in OxPile are outlined by Burd et al. (2017), Byrne et al. (2017) and Burd et al. (2019). The extracted reaction curves from the 3D FEA models were first normalised using the normalisation formulae for sand and clay reaction curves (see Table 7.28) proposed by Burd et al. (2017) and Byrne et al. (2017). The extracted reaction curves at the pivot point (see section 7.3.5.2) were removed and replaced with extrapolated curves from the normalised reaction curves. The 1D FE models used 2-noded elements with 4 Gaussian integration points. The 1D FE model mesh was set up with at least one full element in each soil layer with a maximum element length of 2 m below seafloor level.

Comparison of the monopile load-displacement and moment-rotation responses at seafloor level for the 3D and 1D FE models are presented in Figure 7.44 up to the characteristic design load for pile locations C01 and L07 (soil profile interpretation given in Figure 7.42). It can be seen that very good agreement is achieved between the 3D and 1D models for two of the layered soil profiles (C01 and L07). This is a very promising result and confirms a) that the PISA 1D modelling approach is a reasonable simplification of a 3D model and b) the validity of the extracted soil reaction curves from 3D FEA performed as part of this study.

7.5 Conclusions and Further Work

Extensive design numerical analysis of monopile foundations has been performed. The work involved calibration of constitutive models and 3D FEA of monopile lateral load response.

Class-C (design) and Class-C1 (calibrated) predictions of test piles at a dense sand site were performed to verify the constitutive model calibration approach and the 3D FEA. Comparison of

Class-C pile test predictions (i.e. results not known before prediction) and the measured pile load test data were considered reasonable. These Class-C predictions, in which no pile load test data were available beforehand, are considered extremely valuable to review the predictive performance of a real FEA design situation.

A holistic review was then conducted with respect to the key parameters thought to control the overall features of the pile response, and adjustments were proposed where sufficient laboratory data were available for a set of Class-C1 predictions to be made. This process helped to gain a better understanding of the most suitable parameter calibration process for key model features when modelling a monopile under lateral loading. The results of the Class-C1 predictions were universally better than the original Class-C predictions, particularly over the expected operational load range of wind turbines.

Soil profile sensitivity analysis in which eight different soil profiles were considered was also performed using the calibrated models. The soil profiles were considered representative of typical North Sea conditions. Valuable insight was gained on the effect of different soil layering profiles on the extracted soil reaction curves around the pile. It was shown that for cases in which weak and strong soil layers are adjacent to each other, the soil reaction curves can be affected up to a distance of one pile diameter from the layer boundary. Therefore, when considering such soil profiles in a 1D model a reduction factor may need to be applied to the soil reaction curves, if they were obtained from FEA of homogeneous soil profiles. The results presented in this section will help guide the expected reduction factors and zone of influence for different soil layering configurations. It was observed that the layering effects were not significant for the initial stiffness response of the soil reaction curves, and hence if only small displacements are to be considered within a 1D model no correction of the soil reaction curves is expected to be required.

Further FEA work is recommended, considering a systematic review of different layer thicknesses and soil types to develop a framework for the application of soil layering reduction factors within a 1D PISA model (i.e. 1D model based on recommendations of Byrne et al., 2017 and Burd et al.,

2017). It is considered that this future work is required to make practical use of the PISA design approach for typical North Sea layered soil profiles.

Finally, calibrations of various constitutive models for monopile FEA design were presented. The calibration approach outlined demonstrates the need to have a systematic parameterisation approach for constitutive models from CPT data for large OWFs.

Further work should be performed to develop efficient calibration approaches of different constitutive models across large areas with many highly variable soil types. There is a need to develop site-specific correlations for model parameters from CPT data where possible to make 3D FEA of monopiles feasible at large OWF sites.

It was noted that the run times of the 3D design FEA were generally considered to be slow (approximately 120 hours to simulate lateral seafloor displacements of 0.1D). When implementing a constitutive model there is typically a balance to be struck between model robustness and speed. The implemented user-defined soil model (FDM) was generally robust (i.e. few convergence issues) and provided results with low equilibrium errors. Further work should be done to improve the run times of the analysis when using user-defined models. This is considered particularly important if more advanced models (see Paper 3) are to be employed in such 3D FEA.

7.6 Tables

Table 7.1: Identified issues with *p-y* approach for monopiles

Issue	Comments
The *p-y* reaction curves alone within a 1D model are not suitable to capture the response of monopiles with low L/D ratios (Byrne et al., 2017)	General constraint of *p-y* approach
Initial stiffness response poorly predicated by API approach for both sand and clays (JeanJean, 2009; Byrne et al., 2017; Taborda et al., 2019)	Issue with formulation of *p-y* curves using API approach
API approach predicts lower than expected lateral bearing capacities in clay at low z/D ratios (i.e. within wedge mechanism) when compared to theoretical upper bound solutions (JeanJean et al., 2017)	Issue with formulation of *p-y* curves using API approach
Method of calibrating from laboratory and in situ data not clear and *p-y* curves are overly sensitivity to a small number of input parameters	Issue with formulation of *p-y* curves using API approach

Table 7.2: Overview of offshore wind farm monopile FEA tasks

Task No.	Overview of Tasks	Objective
1	Calibration of constitutive model and site characterisation for Dunkirk site	Verification of monopile modelling approach
2	Class-C/C1 FEA prediction of Dunkirk pile load tests	
3	Sensitivity study for varying relative density and layered soil profiles considering extracted soil reactions curves	Sensitivity analysis
4	Sensitivity study on load rates effects for medium dense soil profile considering extracted soil reactions curves	
5	Offshore wind farm site characterisation and calibration of constitutive models	Overview of offshore wind farm monopile design study
6	FEA of monopile positions at wind farm site and extraction of soil reaction curves	

Table 7.3: Classification of geotechnical prediction (Lambe, 1973)

Prediction Class	Time of Prediction	Results at Time of Prediction
A	Before event	-
B	During event	Not known
B1	During event	Known
C	After event	Not known
C1	After event	Known

Notes: Prediction Class-C and Class-C1 performed as part of this study

Table 7.4: Selected test pile geometries for prediction exercise

Test Pile	D [m]	L [m]	L/D [-]	h [m]	t [mm]	D/t [-]
L2	2.00	10.50	5.25	10.00	38	53
M4	0.76	4.00	5.25	10.00	14	54
M7	0.76	2.30	3.00	10.00	10	76

Notes: D= Pile diameter, L= Pile length, h= Pile stick-up (load application level), t= Pile wall thickness

Table 7.5: Constitutive model decision matrix for monopile design FEA

Criteria	Information	Weight	Constitutive Model			
			FDM~	HSsmall*	Manzari-Dafalias#	MC
Soil behaviour						
Stress-state dependent dilation	Could have significant effect for drained analysis since rotational and flow around mechanism is kinematically constrained. Very important for undrained to partially drained analysis.	0.20	3	0	3	0
Non-linear strain and stress dependent stiffness	Considered very important for FLS and SLS design.	0.25	3	3	3	0
Post-peak softening	Considered important at large displacements	0.15	0	0	3	0
Practical constraints						
Computational Speed	Expected speed of model in 3D boundary value problem based on experience.	0.10	3	4	1.5	4
Model Computational stability	Likelihood of convergence issues in 3D boundary value problem based on experience.	0.20	3.5	4	1.5	4
Ease of calibration	Ability to calibrate model to standard laboratory dataset.	0.10	3	4	2	4
Total Score			**2.65**	**2.35**	**2.45**	**1.6**

Notes: MC = Mohr-Coulomb; ~ = Model details given in Section 4; *= Model details given in Plaxis (2017); # = Model details given in Dafalias and Manzari (2004); FLS = Fatigue limit state; SLS = Serviceability limit state
0 = Very poor model performance; 4 = Very good model performance

Table 7.6: Summary of pile load test specific datasets for the Dunkirk pile test site

Reference	Dataset	Notes
Concept (2014)	Borehole logs (3 No.)	
In Situ (2014)	■ CPTs (38 No.) ■ SCPTs (2 No.) Pressuremeter tests (4 No.)	
Liu (2019)	Triaxial stress-path tests	Imperial College Thesis*

Notes: * = Thesis currently unpublished , data supplied by Ørsted A/S

Table 7.7: Summary of reference datasets for the Dunkirk pile test site

Reference	Dataset	Notes
Chow (1997)	■ Borehole logs ■ CPTs ■ SCPTs ■ Dilatometer tests ■ Laboratory classification tests ■ Mineralogy	Imperial College Thesis
Kuwano (1999)	■ Triaxial stress-path tests ■ Direct shear tests ■ Interface direct shear tests	Imperial College Thesis
Aghakouchak (2015)	■ Laboratory classification tests ■ Triaxial stress-path tests* ■ Oedometer tests	Imperial College Thesis

Notes: CPT= Cone penetration test, SCPT= Seismic cone penetration test, *= Tests included local strain measurement

Table 7.8: Soil profile at the Dunkirk pile test site

Soil Unit*	Sampled Depth [m]	Generalised Soil Description*
Hydraulic Fill	0 to 3.8†	Light greyish brown fine to medium SAND with occasional light brown and off-white coarse sand and fine to medium gravel sized shell fragments.
Flandrian Marine Sand	3.8† to 20.0^	Brown becoming grey fine to coarse SAND with frequent light brown, off-white and grey coarse sand and fine to coarse gravel sized shell fragments.

Notes: *= From Concept (2014), †= Interpretation from Concept (2014) and test pile location specific CPT data (In Situ, 2014), ^= Maximum depth of investigation (Concept, 2014)

Table 7.9: Physical properties of sand at Dunkrik test site

d_{50} [µm]	C_u [-]	PD [-]	e_{min} [-]	e_{max} [-]
268.8	1.56	2.65	0.57	0.91

Notes: C_u = coefficient of uniformity; PD = particle density; d_{50} = particle diameter corresponding to 50% finer on the cumulative particle-size distribution curve

Table 7.10: Initial in situ stress state parameters

Parameter	Symbol	Representative Estimate	Unit
Unsaturated bulk unit weight	γ_{dry}	17.1	kN/m^3
Saturated bulk unit weight	γ_{sat}	19.9	kN/m^3
Earth pressure coefficient	K_0	0.50	[-]

Table 7.11: Elastic stiffness model parameters

Parameter	Symbol	Representative Estimate	Unit
Empirical constant	G_{ref}	6668.8	[-]
Empirical exponent	$n1$	0.6	[-]
Poisson's ratio	ν	0.2	[-]
Void ratio dependency empirical constant	f_{e1}	2.17	[-]
Empirical shape parameter	a	9.5E^{-5}	[-]
Empirical shape parameter	b	1.1	[-]
G_{tan}/G_{max} at large strain	R_{Gmin}	0.03	[-]

Table 7.12: Dilational model parameters

Parameter	Symbol	Representative Estimate	Low Estimate	Unit
Empirical constant	A	170	380	[-]
Empirical constant	x	2.55	2.55	[-]
Empirical constant	y	1.1	1.1	[-]
Initial 'critical state' point	p'_{cv}	State dependent	State dependent	kPa

Table 7.13: Yield surface parameters

Parameter	Symbol	Representative Estimate	High Estimate	Low Estimate
Stress ratio q/p'	M_c *	1.50	1.69	1.31
Lode angle dependency	α	0.75	0.75	0.75

Notes: * = Relates to triaxial compression,

Table 7.14: General finite element mesh properties

Test Pile	W_x [m]	W_y [m]	W_z [m]	N_{el} [m]
L2	50	25	25	17208
M4	17.5	8.75	10	19297
M7	17.5	8.75	7	13785

Notes: W_x= Model width in the x direction (i.e. horizontal in the direction of loading)**;** W_y= Model width in the y direction (i.e. perpendicular and opposite to the direction of loading) **;** W_z= Model depth (z direction)**;** N_{el}= Number of elements

Table 7.15:Updated Class-C1 elastic stiffness model parameters

Parameter	Symbol	Calibrated Estimate	Unit
Empirical constant	G_{ref}	16672	[-]
Empirical exponent	$n1$	0.4	[-]
Poisson's Ratio	v	0.2	[-]

Table 7.16: Updated Class-C1 dilational model parameters

Parameter	Symbol	Calibrated Estimate	Unit
Empirical constant	A	240	[-]
Empirical constant	x	2.55	[-]
Empirical constant	y	1.1	[-]
Initial 'critical state' point	p'_{cv}	State dependent	kPa

Table 7.17: Summary of Task 3 and Task 4 soil profile cases

Soil Profile	Depth BSF [m]		Description	D_r [%]	s_u [kPa]
	Top	Base			
SP1	Uniform profile		Medium dense sand	50	--
SP2	Uniform profile		Dense sand	75	--
SP3	Uniform profile		Very dense sand	100	--
SP4	0.0	11.25	Very dense sand	100	--
	11.25	40.0	Medium dense sand	50	--
SP5	0.0	11.25	Dense sand	75	--
	11.25	40.0	Very dense sand	100	--
SP6	0.0	7.5	Very dense sand	100	--
	7.5	15.0	Strong Clay	--	150
	15.0	40.0	Dense sand	75	--
SP7	0.0	7.5	Dense sand	75	--
	7.5	15.0	Medium dense sand	50	--
	15.0	40.0	Strong clay	--	150
SP8	0.0	7.5	Dense sand	75	--
	7.5	15.0	Strong clay	--	150
	15.0	24.4	Medium dense sand	50	--
	24.4	40.0	Strong clay	--	150

Notes: BSF= Below seafloor**;** D_r= Relative density**;** s_u= Undrained shear strength

Table 7.18: Summary of monopile geometry and water depth used for Task 3 and 4 sensitivity analysis

Soil Profile	Water Depth [m]	D [m]	L [m BSF]	L/D [-]	h [m]	t [mm]
All*	30.0	7.5	22.5	3.0	37.5	68.0

Notes: BSF= Below seafloor**;** L= Monopile embedment depth**;** D= Monopile diameter**;** h= Monopile stick-up**;** t= Monopile wall thickness**;** *= Refers to all soil profiles

Table 7.19: Summary of constitutive models used for Task 3 and 4 sensitivity analysis

Soil Type	D_r [%]	Model
Dense and Very Dense Sand	75, 100	FDM
Medium Sand	50	HSsmall(E)
Clay	--	HSsmall(T)

Notes: FDM= Fugro Dilational Soil Model**;** HSsmall(E)= Hardening Soil Small Strain Stiffness Model - Effective stress input**;** HSsmall(T)= Hardening Soil Small Strain Stiffness Model - Total stress input

Table 7.20: HSsmall(E) parameters for sand (Dr=50%) at Dunkirk site used for Task 3 and 4 sensitivity analysis

Parameter	Symbol	Representative Estimate	Unit
Elastic model parameters:			
Reference shear modulus	G_0^{ref}	21000	kPa
Poisson's Ratio	ν	0.2	[-]
Empirical shape parameter	$\gamma_{0.7}$	0.006	[%]
Power exponent for stress-level dependency of stiffness:			
Empirical exponent	m	0.4	[-]
Parameters to control stiffness and isotropic hardening rules:			
Deviatoric plastic strain modulus	E_{50}^{ref}	7300	kPa
Primary compression modulus	E_{oed}^{ref}	7300	kPa
Unload-reload modulus	E_{ur}^{ref}	14600	kPa
Reference pressure	p^{ref}	1	kPa
Hyperbolic hardening function parameter	R_f	0.9	[-]
Yield surf ace and dilational parameters:			
Cohesion	c'	0.0	kPa
Friction angle	φ'	34.0	[°]
Dilation angle	ψ	4.0	[°]

Notes: p^{ref}=1kPa; details of model parameters given in Plaxis (2017); Dilatancy cut-off was included and was set to occur when e=0.91

Table 7.21: HSsmall(T) parameters for clay used for Task 3 and 4 sensitivity analysis

Parameter	Symbol	Representative Estimate	Unit
Elastic model parameters:			
Reference shear modulus	G_0	$500s_u$	kPa
Poisson's Ratio	ν	0.499	[-]
Empirical shape parameter	$\gamma_{0.7}$	0.012	[%]
Stiffness and hardening parameters:			
Deviatoric plastic strain modulus	E_{50}	$72s_u$	kPa
Unload-reload modulus	E_{ur}	$144s_u$	kPa
Failure strength:			
Undrained shear strength	s_u	Location specific	kPa

Notes: $Rf = 0.85$; p^{ref} and m not applicable for total stress variant of HSsmall model since stiffness values not stress dependent

Table 7.22: General finite element mesh properties

Soil Profile	W_x [m]	W_y [m]	W_z [m]	N_{el} [-]	N_{node} [-]
SP1	200	100	70	26804	40371
SP2	200	100	70	26804	40371
SP3	200	100	70	26804	40371
SP4	200	100	70	29588	44073
SP5	200	100	70	29588	44073
SP6	200	100	70	33421	49524
SP7	200	100	70	33421	49524
SP8	200	100	70	42587	62230

Notes: W_x= Model width in the x direction (i.e. horizontal in the direction of loading)**;** W_y= Model width in the y direction (i.e. perpendicular and opposite to the direction of loading) **;** W_z= Model depth (z direction)**;** N_{el}= Number of elements**;** N_{node}= Number of nodes

Table 7.23: Summary of loading rate analyses

Case	Loading Rate	Task
Fully Drained (a)	--	Task 3
Undrained (b)	--	Task 4
Wave (c)	4 MN/s	Task 4
Wind (d)	10 MN/min	Task 4

Notes:-- = Loading rate not applicable for fully-drained and undrained analyses

Table 7.24: Capacity ranking of Task 3 layered soil profiles

Soil Profile	Depth BSF [m]		D_r [%]	Capacity Ranking [-]		
	Top	Base		0.05 % D	1 % D	10 % D
SP4	0.0	11.25	100	1	2	2
	11.25	40.0	50			
SP5	0.0	11.25	75	4	4	1
	11.25	40.0	100			
SP6	0.0	7.5	100	2	1	3
	7.5	15.0	(Clay)			
	15.0	40.0	75			
SP7	0.0	7.5	75	5	5	5
	7.5	15.0	50			
	15.0	40.0	(Clay)			
SP8	0.0	7.5	75	3	3	4
	7.5	15.0	(Clay)			
	15.0	24.38	50			
	24.38	40.0	(Clay)			

Notes: BSF = Below seafloor**;** D = Pile diameter**;** D_r = Relative density

Table 7.25: Summary of constitutive model selection at wind farm site

Model	Formulation	Soil Units*	Soil Type	Response Type^	Profiling Parameter
FDM	Effective Stress	A, B, C2, E4	SAND	Dilation	D_r
HSsmall(E)	Effective Stress	E1, F2	SAND	Contraction	q_c/σ'_{v0}
HSsmall(T)	Total Stress	C1, D, E2, F1	CLAY	Hardening	s_u

Notes: FDM= Fugro Dilational Soil Model**;** HSsmall(E)= Hardening Soil Small Strain Stiffness Model - Effective stress input**;** HSsmall(T)= Hardening Soil Small Strain Stiffness Model - Total stress input; Details of soil unit calibrations given in Section 0; ^= Relates to dominant mechanism governing stress-strain response

Table 7.26: Overview monopile depth soil unit summary by design position

Position	Pile Tip Depth [m BSF]	Soil Units Within Pile Depth						Soil Unit* at Pile Tip	Depth CPT Data [m BSF]
		A	B	C	D	E	F		
C01	24.0	✓	✓	✓	✓	✓		E1	33.4
D05	24.5	✓	✓	✓				C1, C2	>40.0
E06	21.1	✓	✓	✓				C2	33.1
F04	25.4	✓	✓	✓	✓			D	30.5
G06	23.9	✓	✓		✓	✓		E1	35.0
H06	22.4	✓	✓			✓		E1	25.4
J08	23.2	✓	✓			✓	✓	F1	28.6
L07	24.0	✓	✓			✓		E1	32.8
X01^	27.0			✓				C2	--
X02^	24.0					✓		E4	--
X03^	22.0					✓		E4	--

Notes: All positions were profiled to 40 m BSF; ^ = Synthetic design position; BSF = Below seafloor

Table 7.27: Overview monopile depth soil unit summary by design position

Position	L [m]	L+h [m]	D^[m]	t^[m]	L/D
C01	24.0	69.014	8.7	0.077 0.084 0.068 0.094	2.76
D05	24.5	79.060	8.3	0.065 0.090	2.95
E06	21.1	63.314	8.7	0.068 0.094	2.43
F04	25.4	80.291	8.5	0.066 0.092	2.99
G06	23.9	69.000	8.7	0.065 0.090	2.76
H06	22.4	67.570	7.8	0.075 0.073 0.066 0.061 0.085	2.87
J08	23.2	58.314	8.3	0.065 0.090	2.80
L07	24.0	78.850	8.7	0.068 0.094	2.76
X01^	27.0	81.854	8.7	0.068 0.094	3.10
X02^	24.0	78.854	8.3	0.068 0.094	2.89
X03^	22.0	76.854	8.7	0.068 0.094	2.53

Notes: D = Pile diameter; T = Pile wall thickness; L = pile depth below seafloor; h = Applied load height above seafloor; ^ = Value(s) given for portion of pile below seafloor

Table 7.28: Normalisation of extracted soil reactions curves for use in 1D FE model

Normalised Component	Clay Normalisation	Sand Normalisation
Distributed shear load, $\bar{p}$	$\bar{p} = p/(s_u D)$	$\bar{p} = p/(\sigma'_{v0} D)$
Lateral displacement, $\bar{u}_x$	$\bar{u}_x = (u_x G_{max}/s_u)/D$	$\bar{u}_x = u_x G_0/(\sigma'_{v0} D)$
Distributed moment, $\bar{m}$	$\bar{m} = m/(s_u D^2)$	$\bar{m} = m/(pD)$
Pile rotation, $\bar{\theta}$	$\bar{\theta} = \theta(G_{max}/s_u)$	$\bar{\psi} = \psi\theta G_{max}/\sigma'_{v0}$
Base shear force, $\bar{T}$	$\bar{T} = T/(s_u D^2)$	$\bar{T} = T/(\sigma'_{v0} D^2)$
Base moment, $\bar{M}$	$\bar{M} = M/(s_u D^3)$	$\bar{M} = M/(\sigma'_{v0} D^3)$

Notes: Normalisation approach outlined by Burd et al. (2017) and (Byrne et al. 2017); s_u= Soil layer undrained shear stregnth; G_{max}= Soil layer maximum shear modulus; σ'_{v0} = Vertical effective stress

7.7 Figures

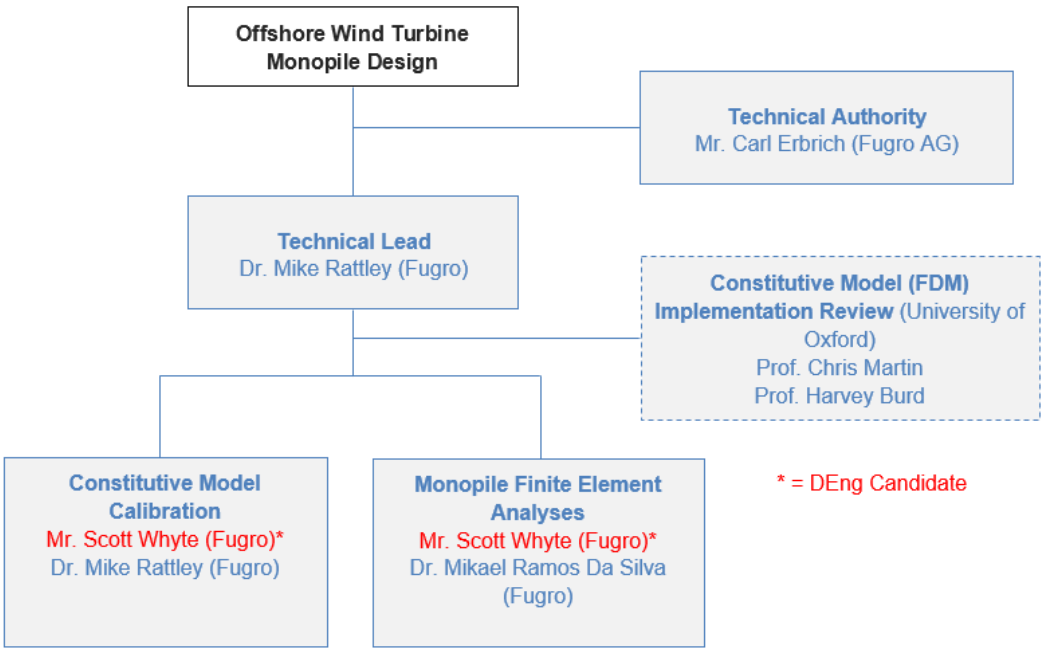

Figure 7.1: Offshore wind turbine monopile FEA design project team organigram

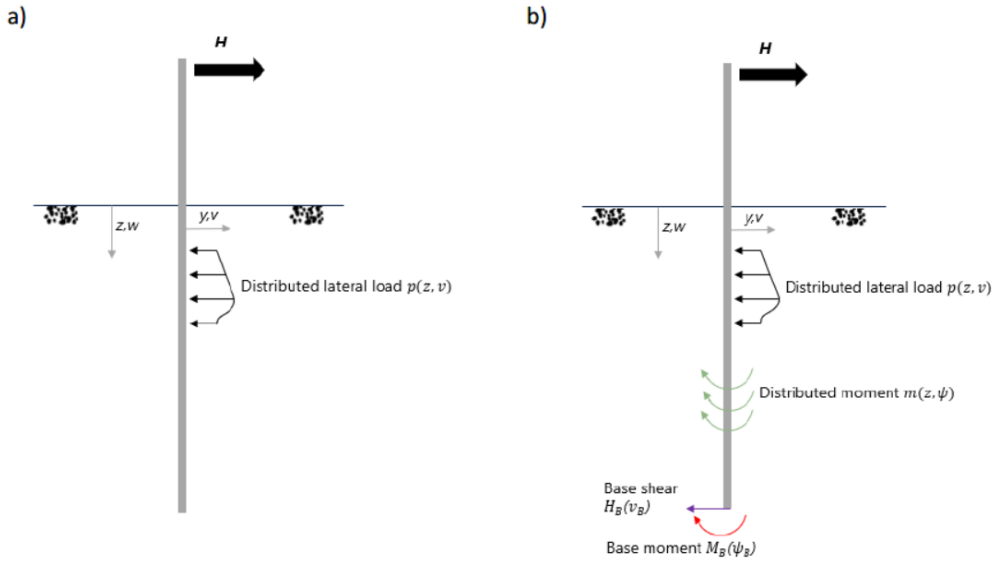

Figure 7.2: Schematic of a) *p-y* only model and b) PISA-type 1D model (based on Byrne et al. 2017)

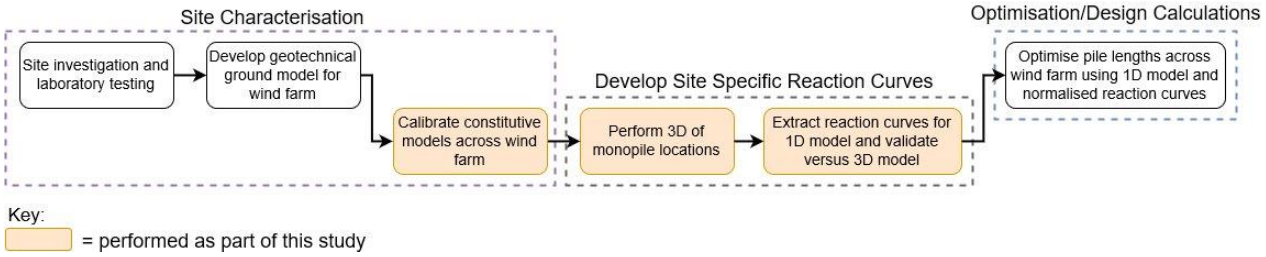

Figure 7.3: Monopile design process

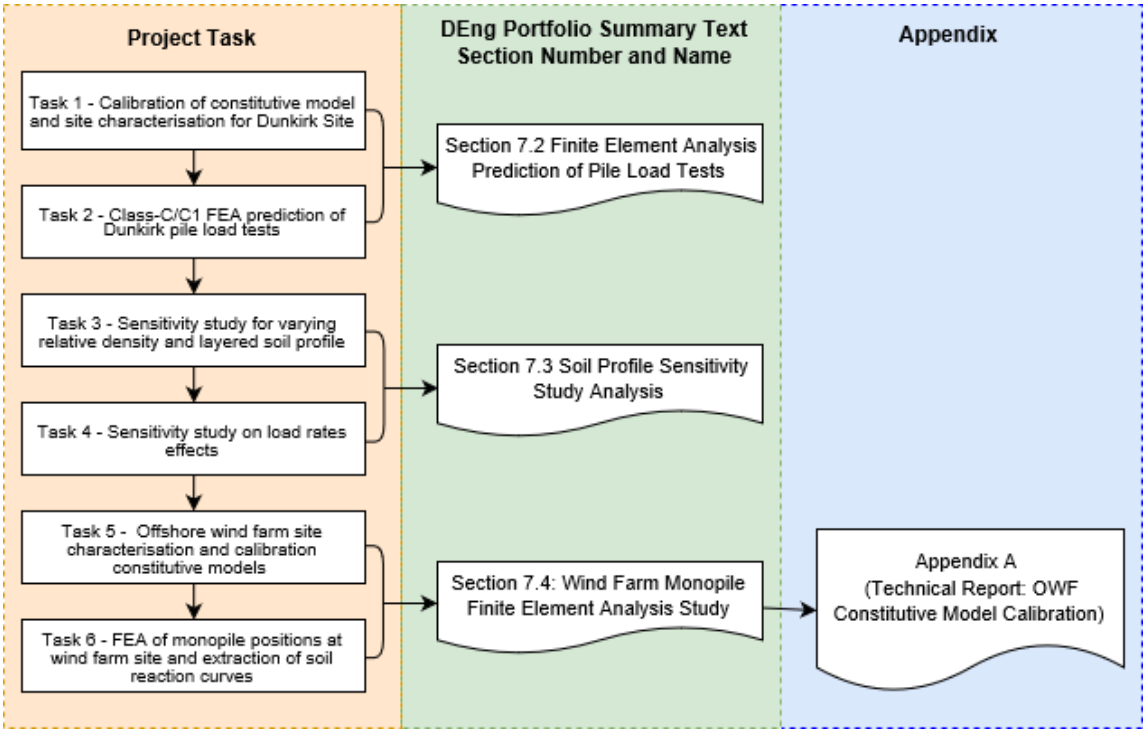

Figure 7.4: Scope of work for offshore wind farm monopile finite element analysis study with outline of main deliverables and reporting

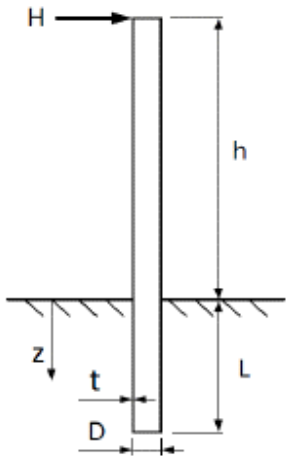

Figure 7.5:Definitions for test pile geometry

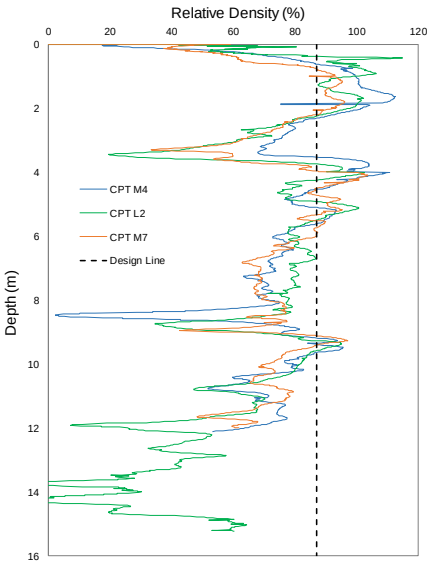

Figure 7.6: Dunkirk test pile location specific relative density profiles

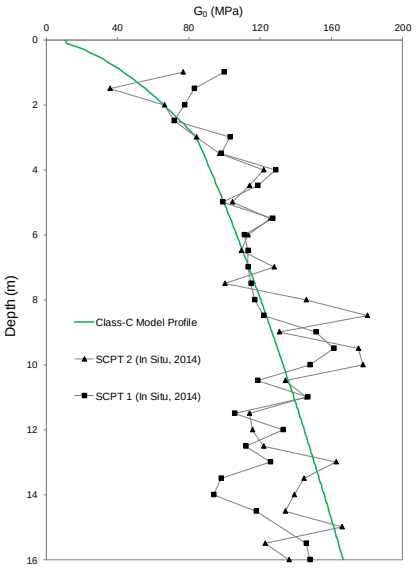

Figure 7.7: Dunkirk test pile site (Class-C) G_0 profile

a)

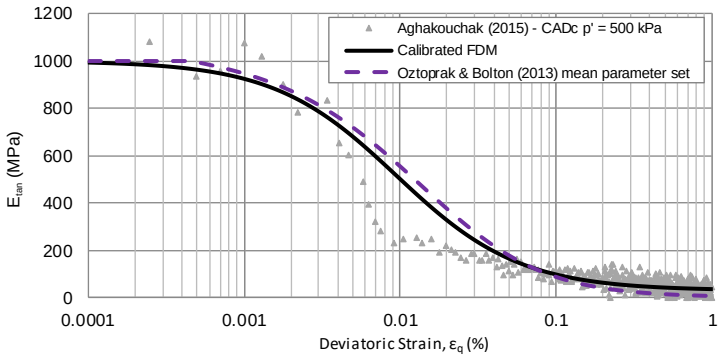

b)

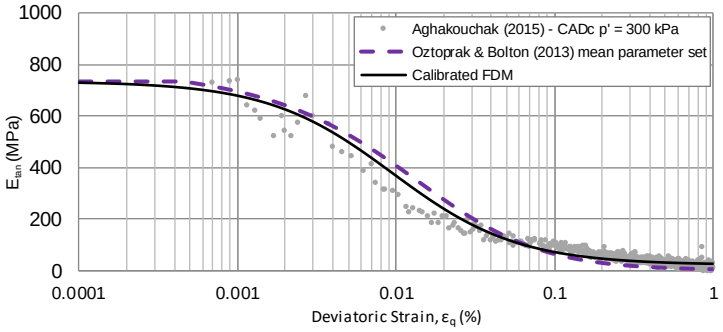

c)

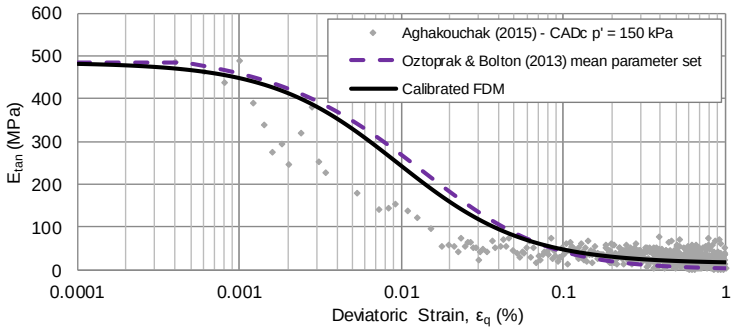

Figure 7.8: Tangent stiffness degradation model (Class-C) compared to Dunkirk sand and Oztorprak and Bolton (2013) mean trend

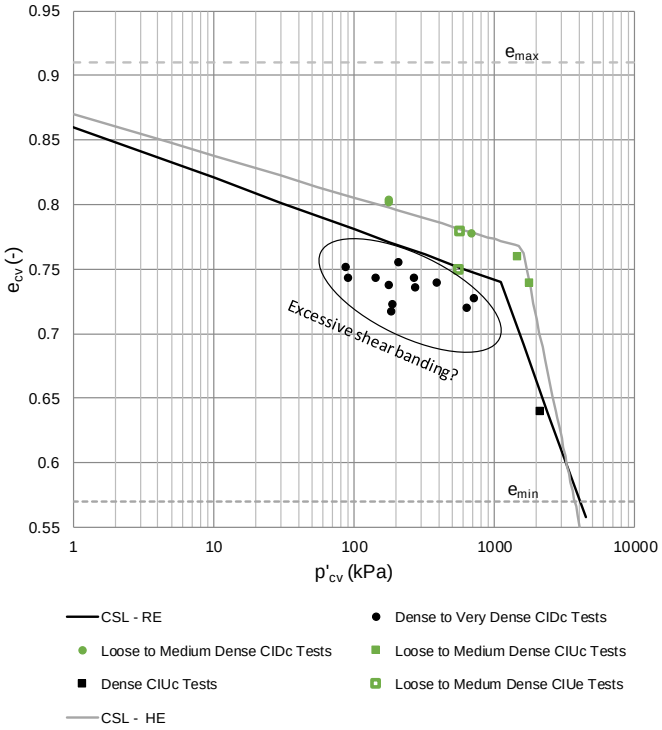

Figure 7.9: Representative estimate (Class-C) and high estimate critical state line

a)

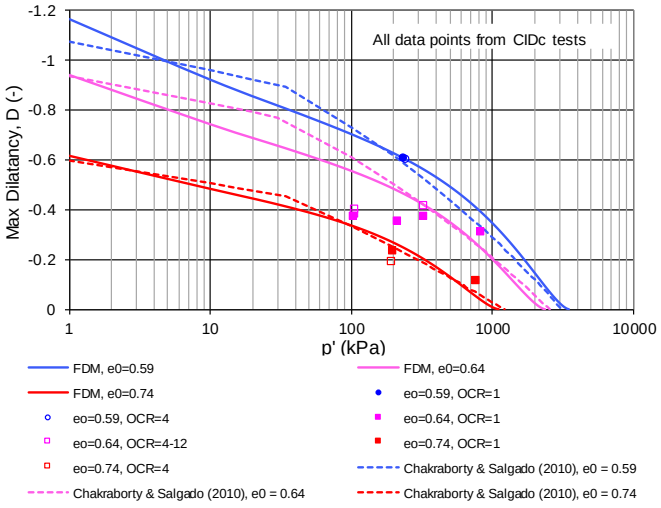

b)

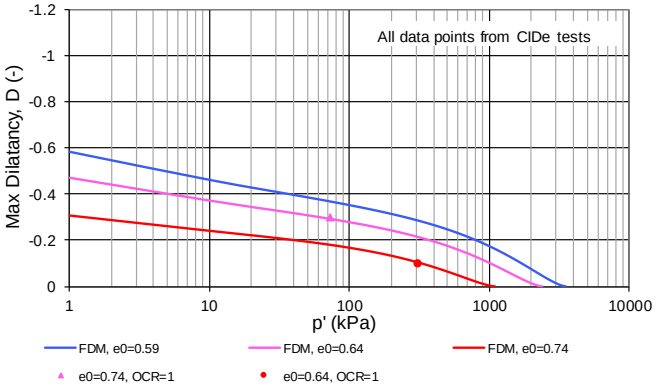

Figure 7.10: Stress-dilatancy a) representative estimate (Class-C) and b) low estimate design lines, low estimate calibrated to drained triaxial extension tests and representative estimate calibrated to triaxial compression tests in both cases *p'cv* values based on representative estimate critical state line

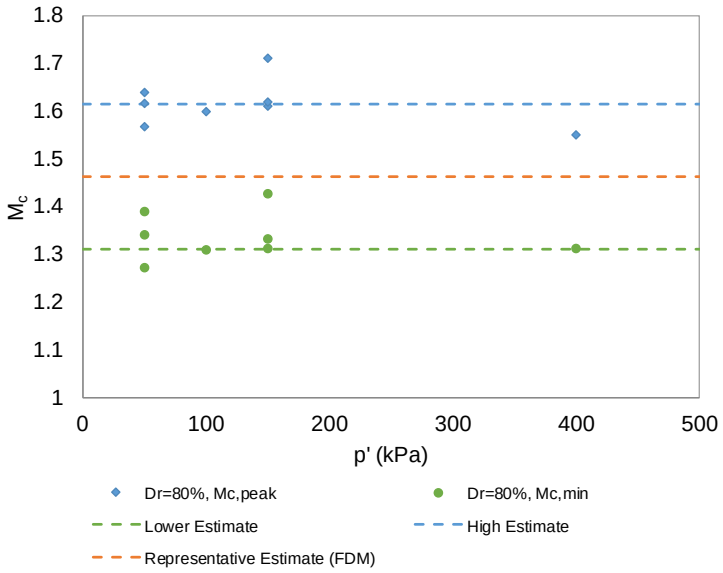

Figure 7.11: Model strength parameters in triaxial compression for Dr≈80% at range of p' values

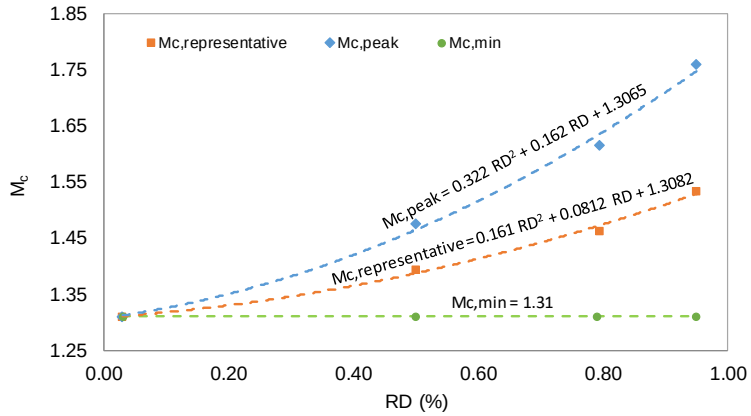

Figure 7.12: Average model yield surface size (M_c) from available triaxial compression tests performed at $50\ \text{kPa} < p' < 200\ \text{kPa}$ for range of relative density (RD) values, $M_{c,peak}$ refers to the peak stress ratio in triaxial compression, $M_{c,min}$ refers to the critical state failure stress ratio in triaxial compression and $M_{c,representative}$ refers to the failure stress ratio used for model calibration

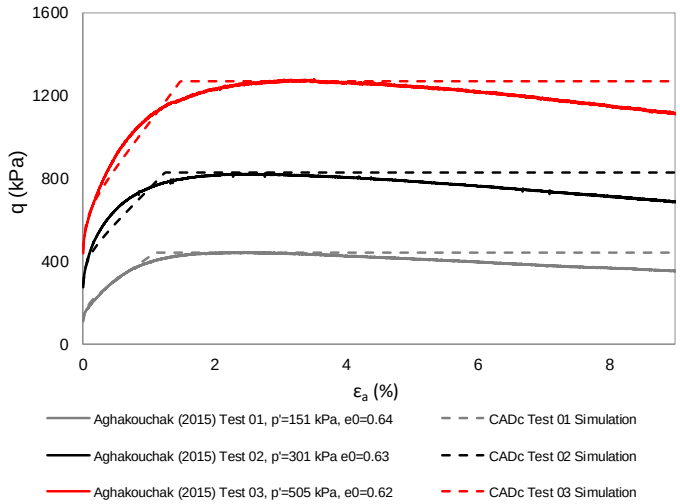

Figure 7.13: Drained triaxial test comparison stress-strain response using Class-C prediction parameter set

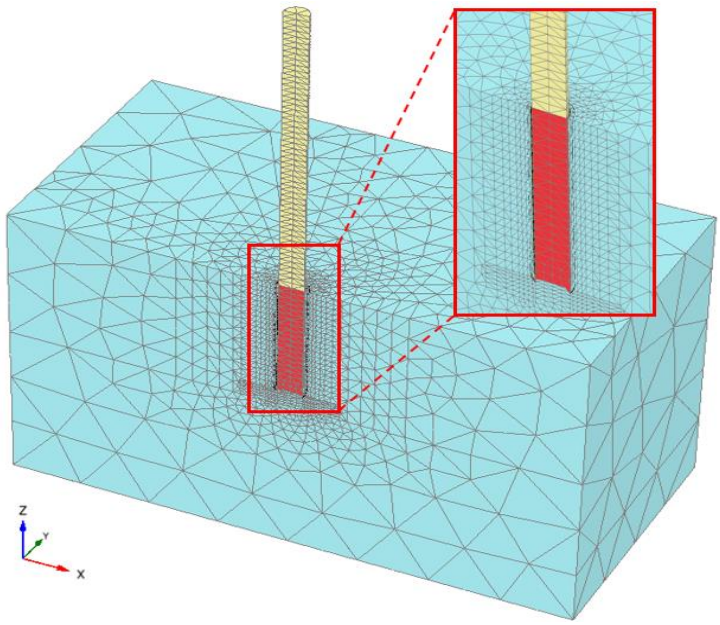

Figure 7.14: Finite element mesh for pile M4

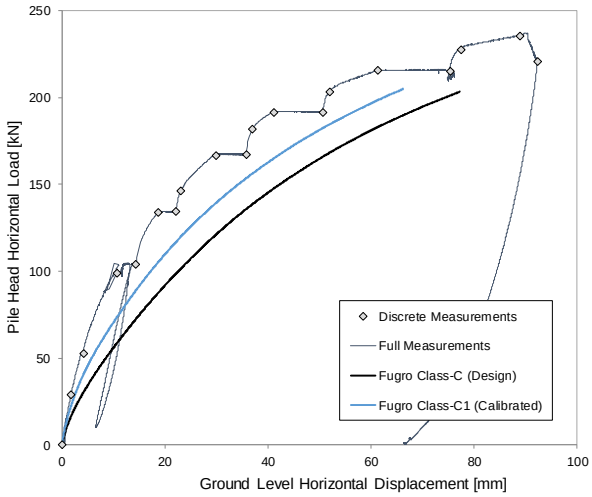

Figure 7.15: Comparison of measured pile test data and Class-C prediction (Pile M4)

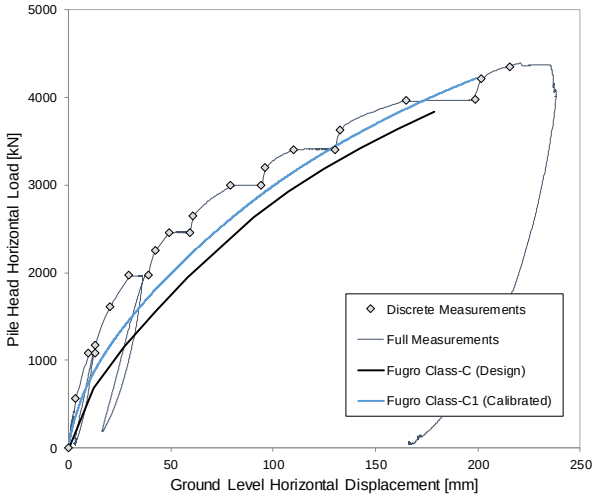

Figure 7.16: Comparison of measured pile test data and Class-C prediction (Pile L2)

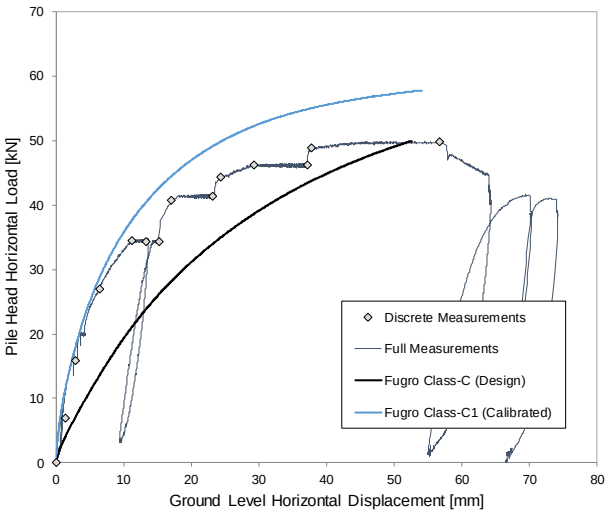

Figure 7.17: Comparison of measured pile test data and Class-C prediction (Pile M7)

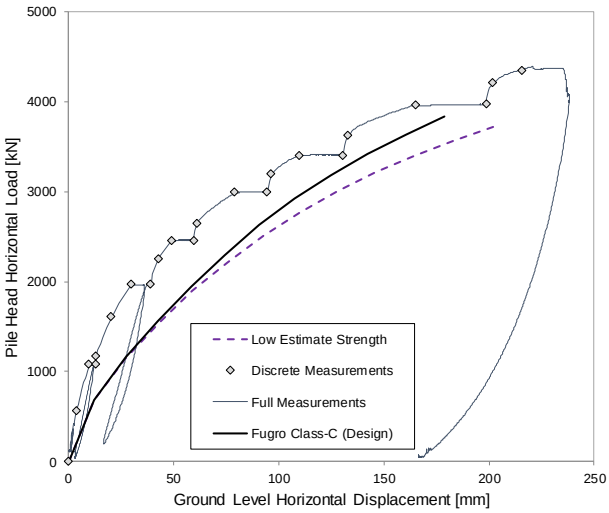

Figure 7.18: Sensitivity analysis results and Class-C prediction (Pile L2)

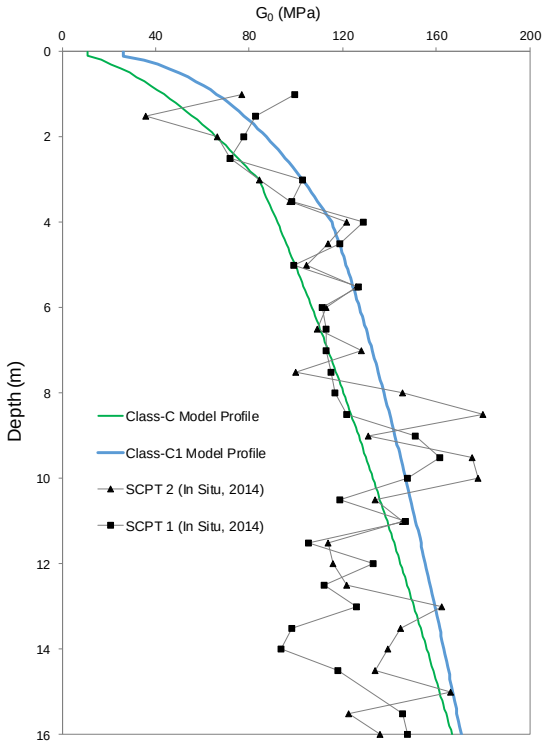

Figure 7.19: Updated (Class-C1) G_0 profile

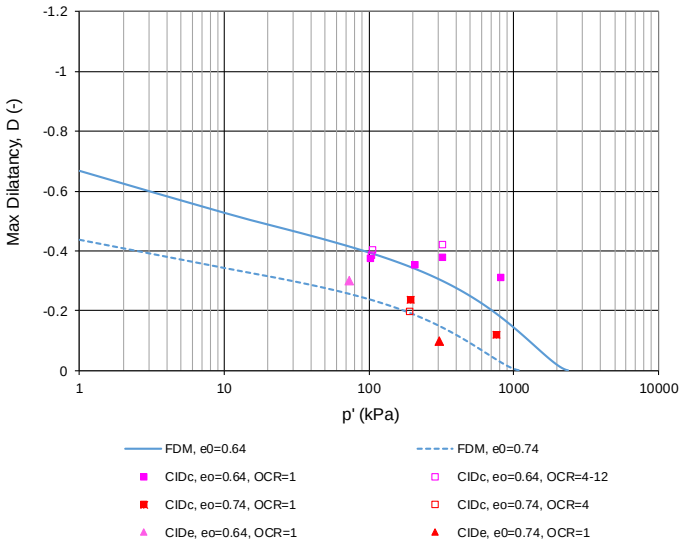

Figure 7.20: Updated (Class-C1) stress-dilatancy response

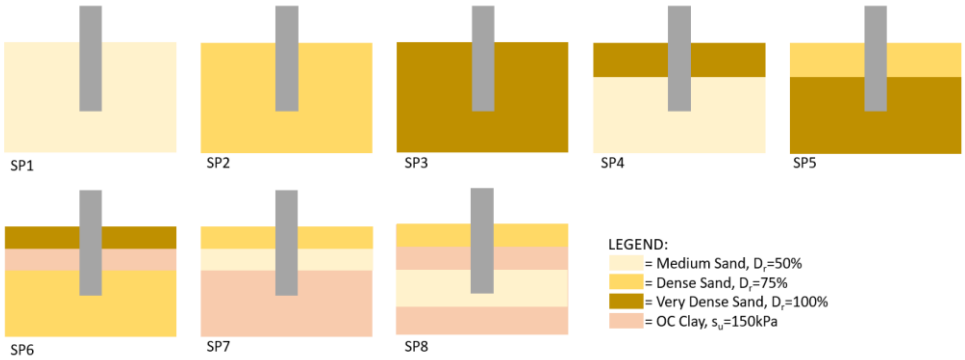

Figure 7.21: Schematic illustration of layered soil profiles for Tasks 3 and 4

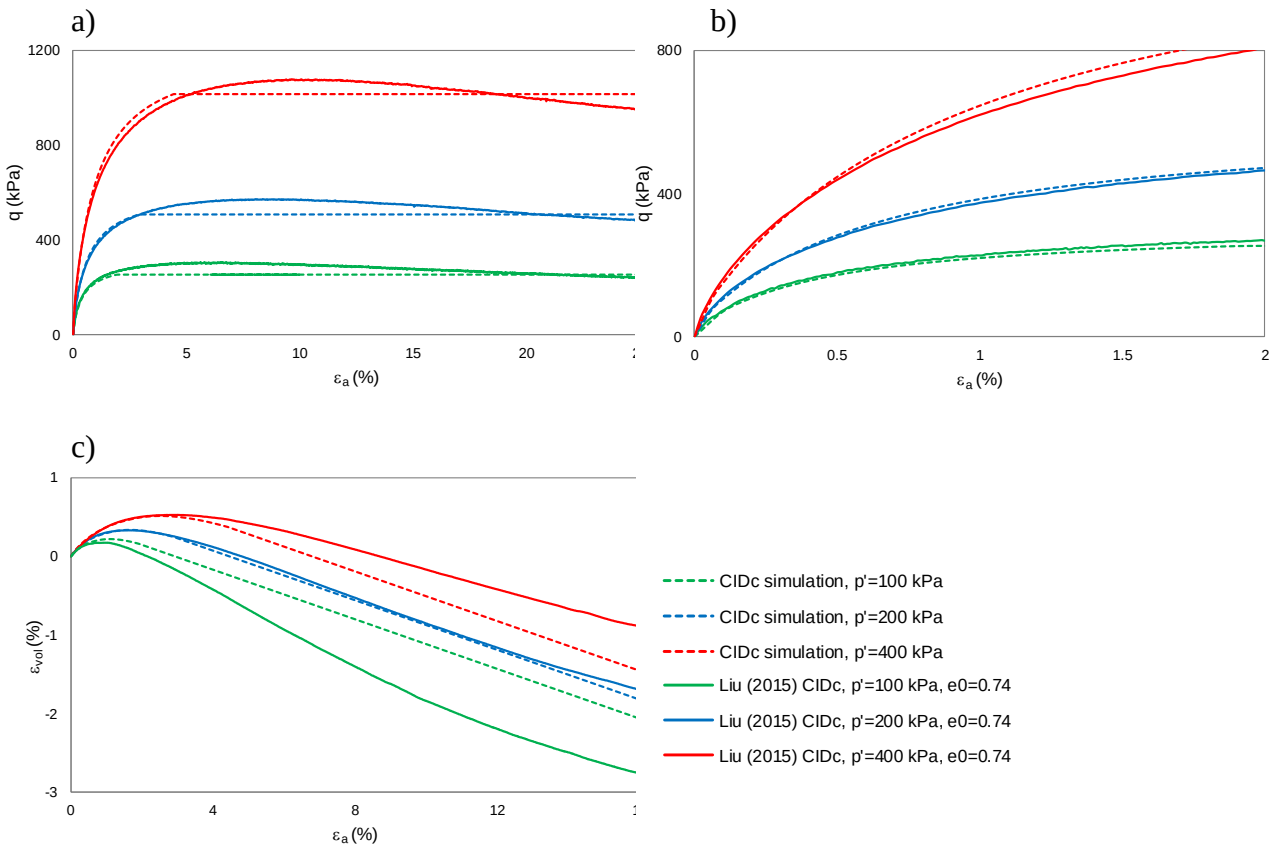

Figure 7.22: Calibrated medium dense sand model (HSsmall(E)) compared to drained triaxial compression (CIDc) a) deviatoric stress versus axial strain b) zoom view of deviatoric stress versus axial strain and c) volumetric strain versus axial strain laboratory data from Dunkirk site

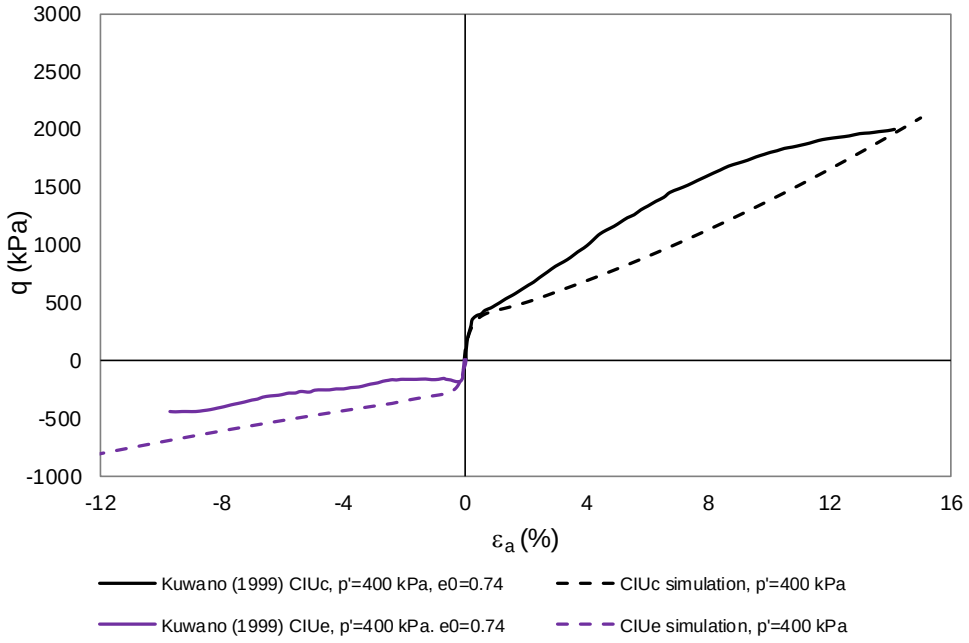

Figure 7.23: Calibrated medium dense sand model (HSsmall(E)) compared to undrained triaxial compression (CIUc) deviatoric stress versus axial strain laboratory data from Dunkirk site

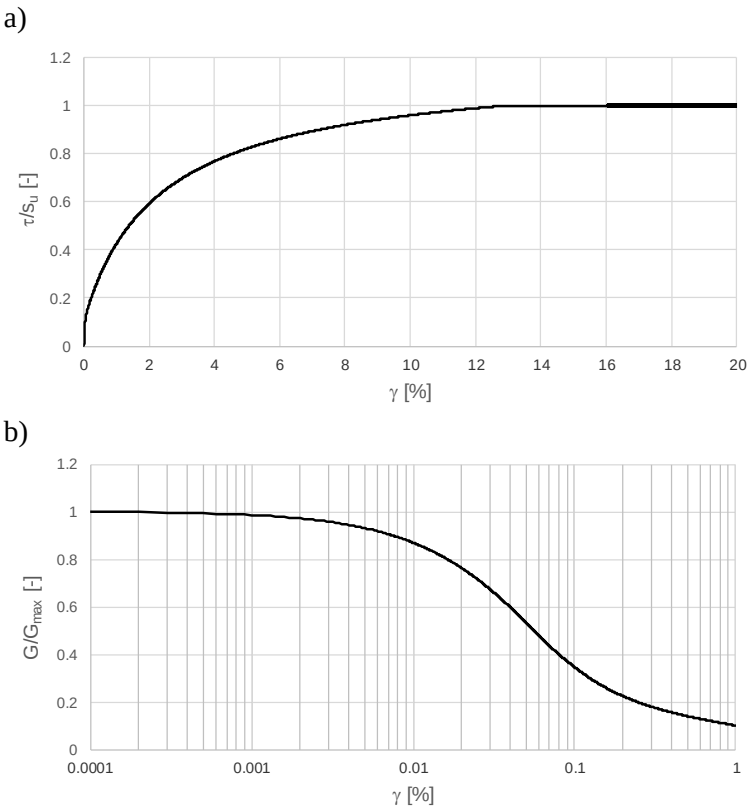

Figure 7.24: Calibrated clay model (Hardening Tresca HSsmall(T) model) normalised backbone a) shear stress versus shear strain and b) secant shear stiffness versus shear strain

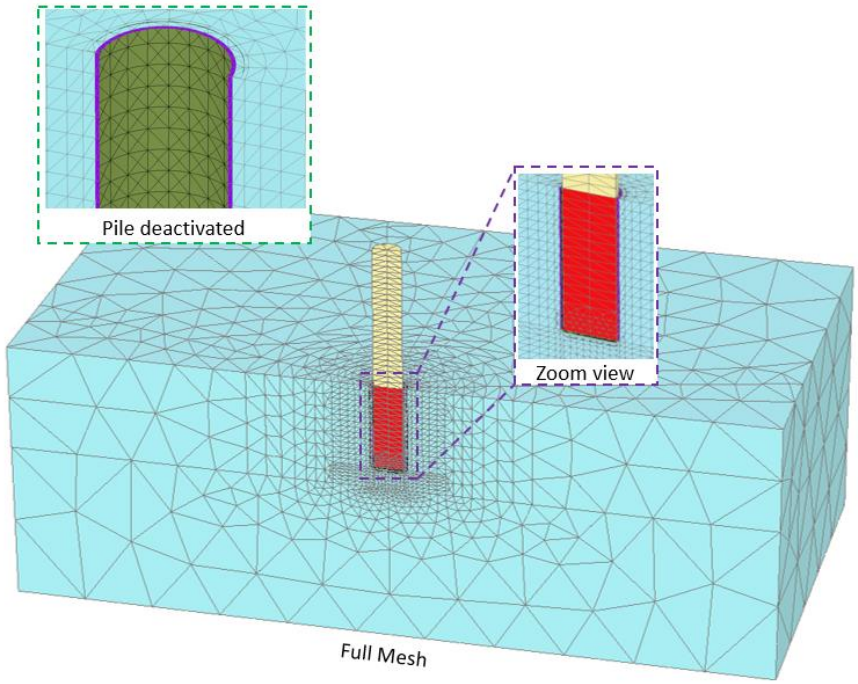

Figure 7.25: Example finite element mesh for pile Task 3 and 4 analysis

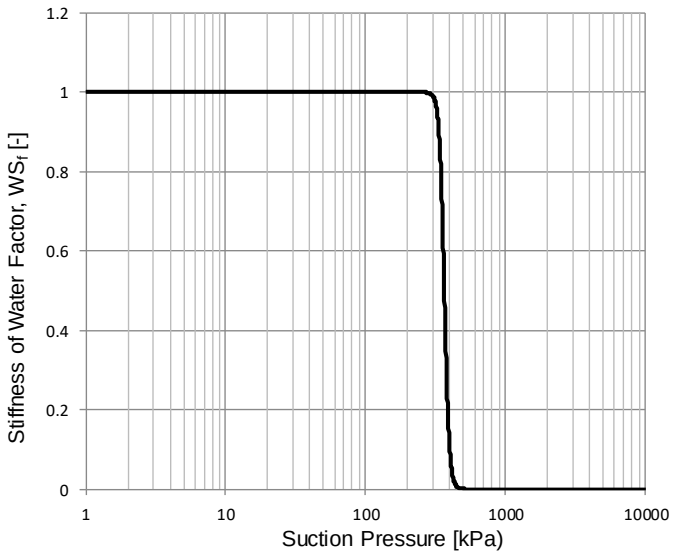

Figure 7.26: User-defined hydraulic model for cavitation cut-off (30 m Water Depth)

Phase	U_x at mudline	Error
1	0.0005	1.32%
2	0.0010	0.32%
3	0.0029	1.30%
4	0.0065	1.53%
5	0.0150	1.39%
6	0.0344	1.05%
7	0.0980	0.57%
8	0.2114	0.48%
9	0.3311	0.70%
10	0.3926	0.79%
11	0.4551	0.86%
12	0.5184	0.92%
13	0.5825	0.97%
14	0.6471	1.01%
15	0.7122	1.02%

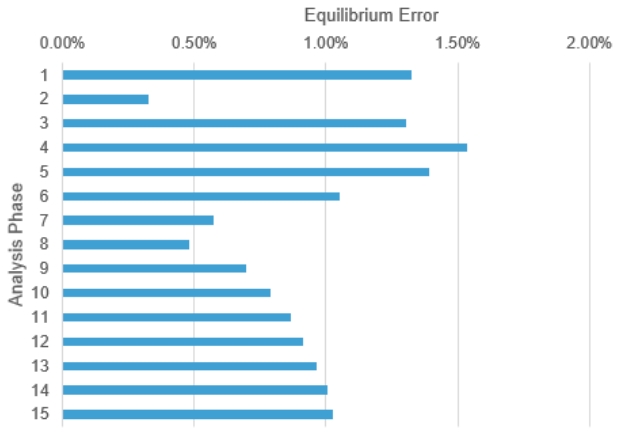

Figure 7.27: Equilibrium error check example for SP2 analysis

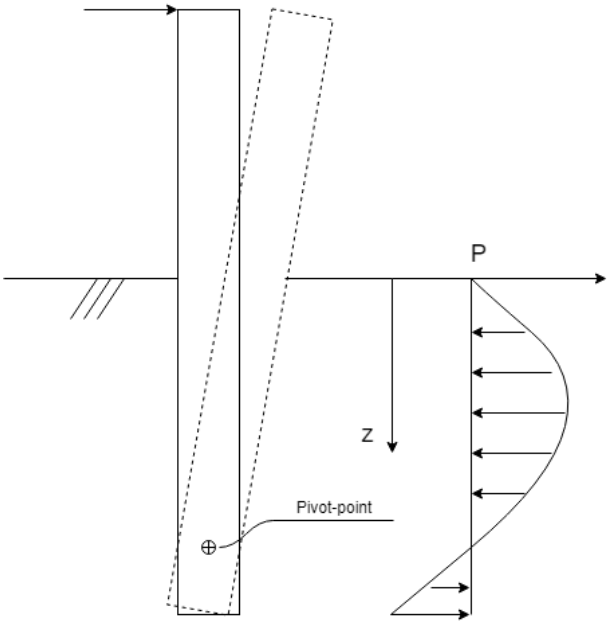

Figure 7.28:Development of pivot-point of monopile response

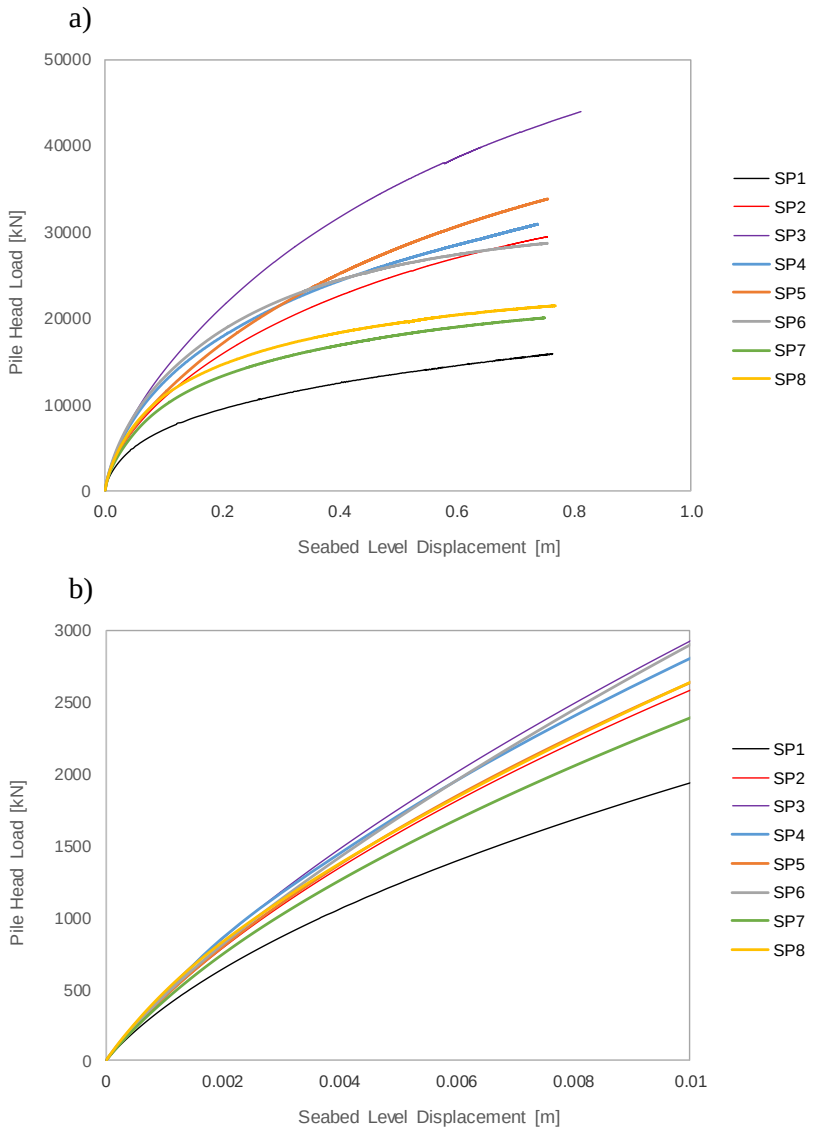

Figure 7.29: Pile lateral load-displacement response at seabed a) up to 0.1*D* seabed displacement and b) zoom at lower displacement level

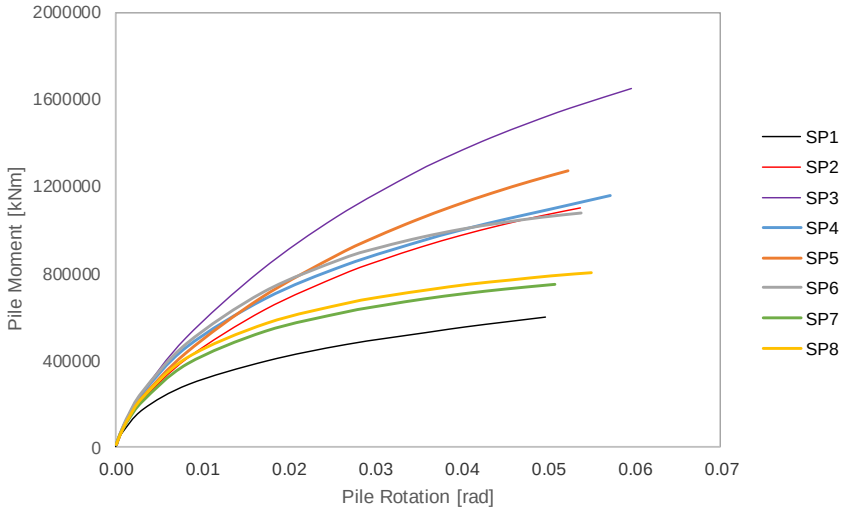

Figure 7.30: Pile lateral moment-rotation response at seabed up to 0.1*D* seabed lateral displacement and

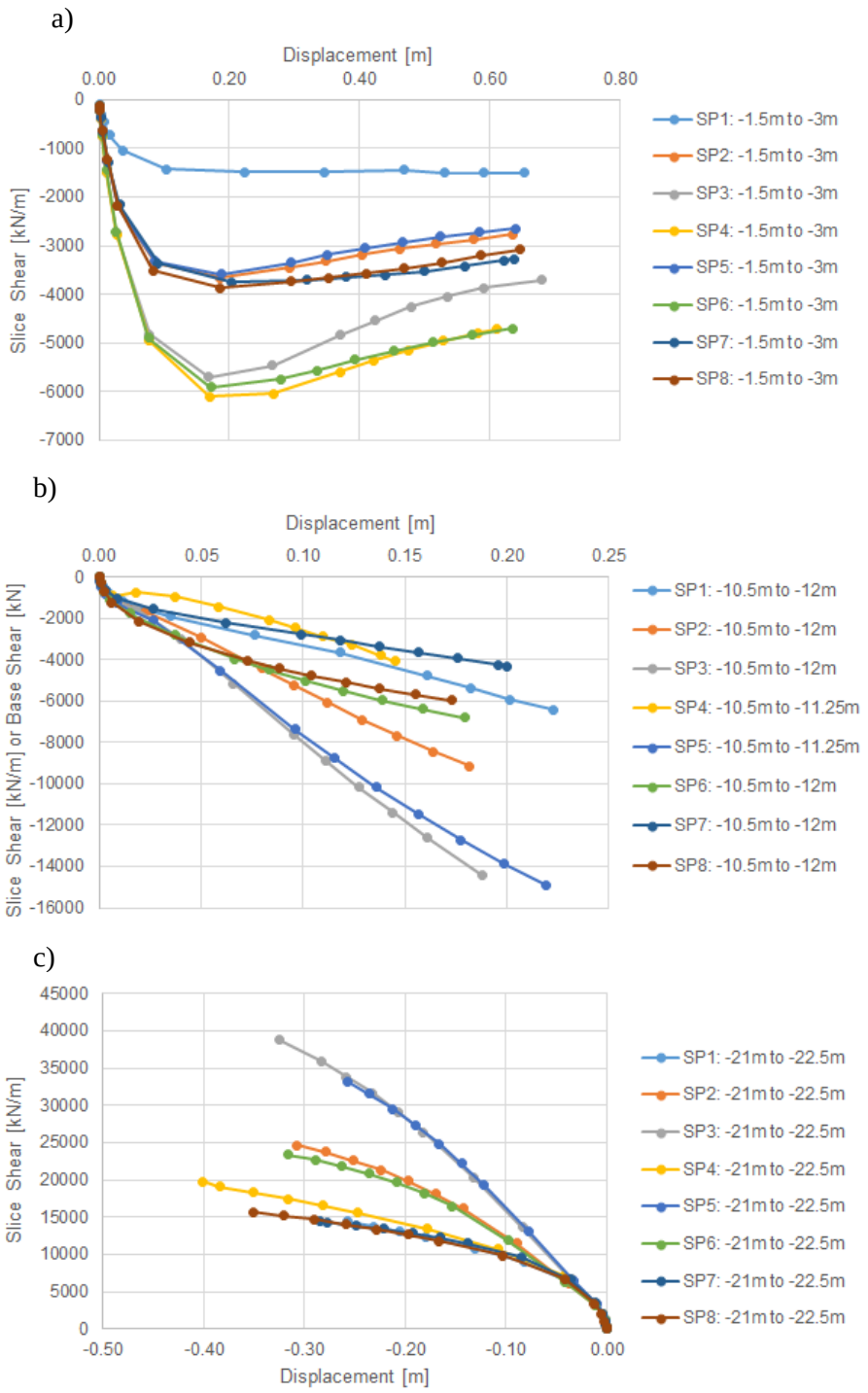

Figure 7.31: Distributed horizontal load transfer curves from sensitivity analyses a) near seabed, b) at mid embedment depth (z/l≈0.5) and c) near pile base

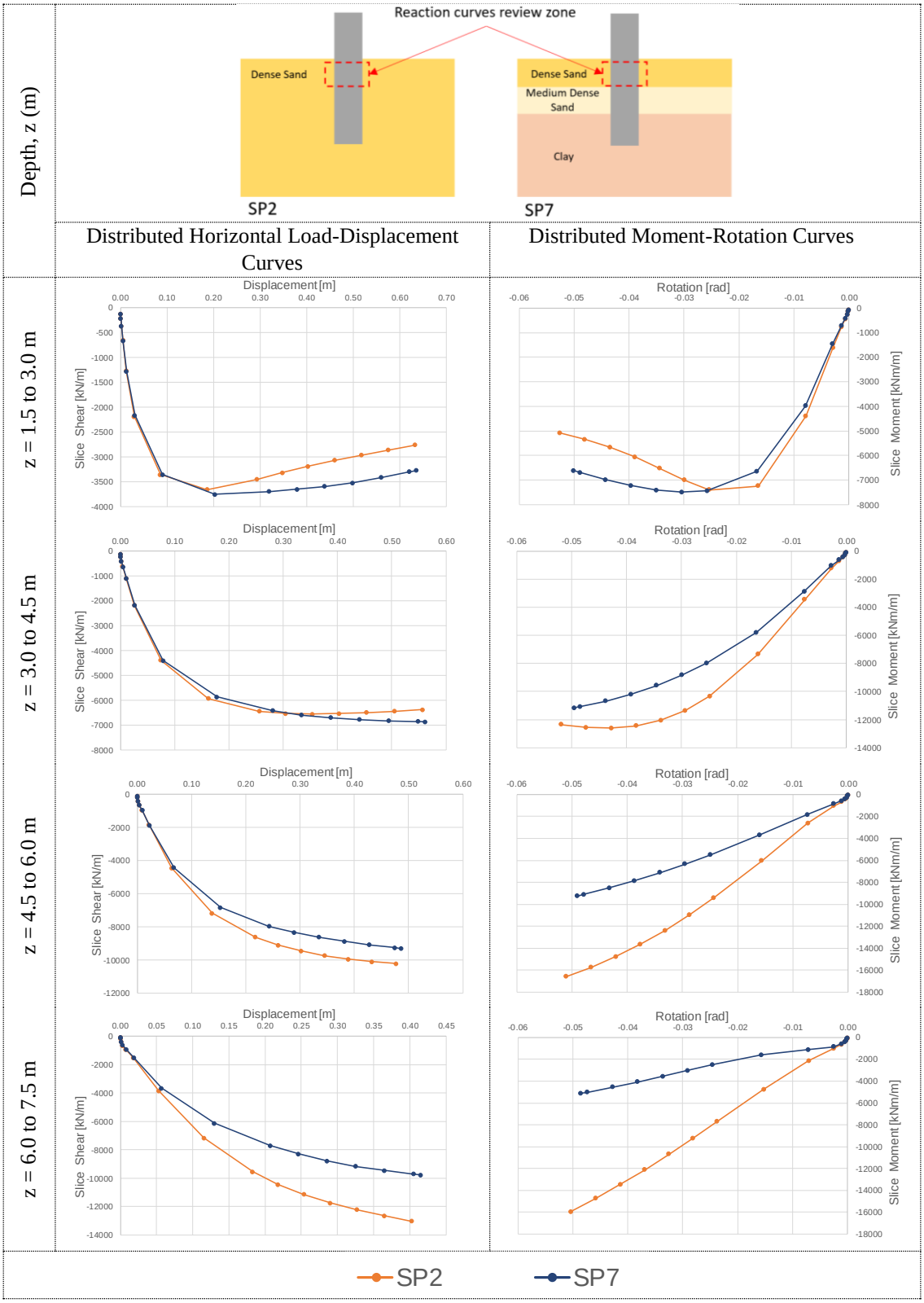

Figure 7.32: Review of reaction curves in dense sand layer between 1.5 m and 7.5 m for a uniform dense profile (SP2) and a layered profile with a dense layer from 0 to 7.5 m (SP7)

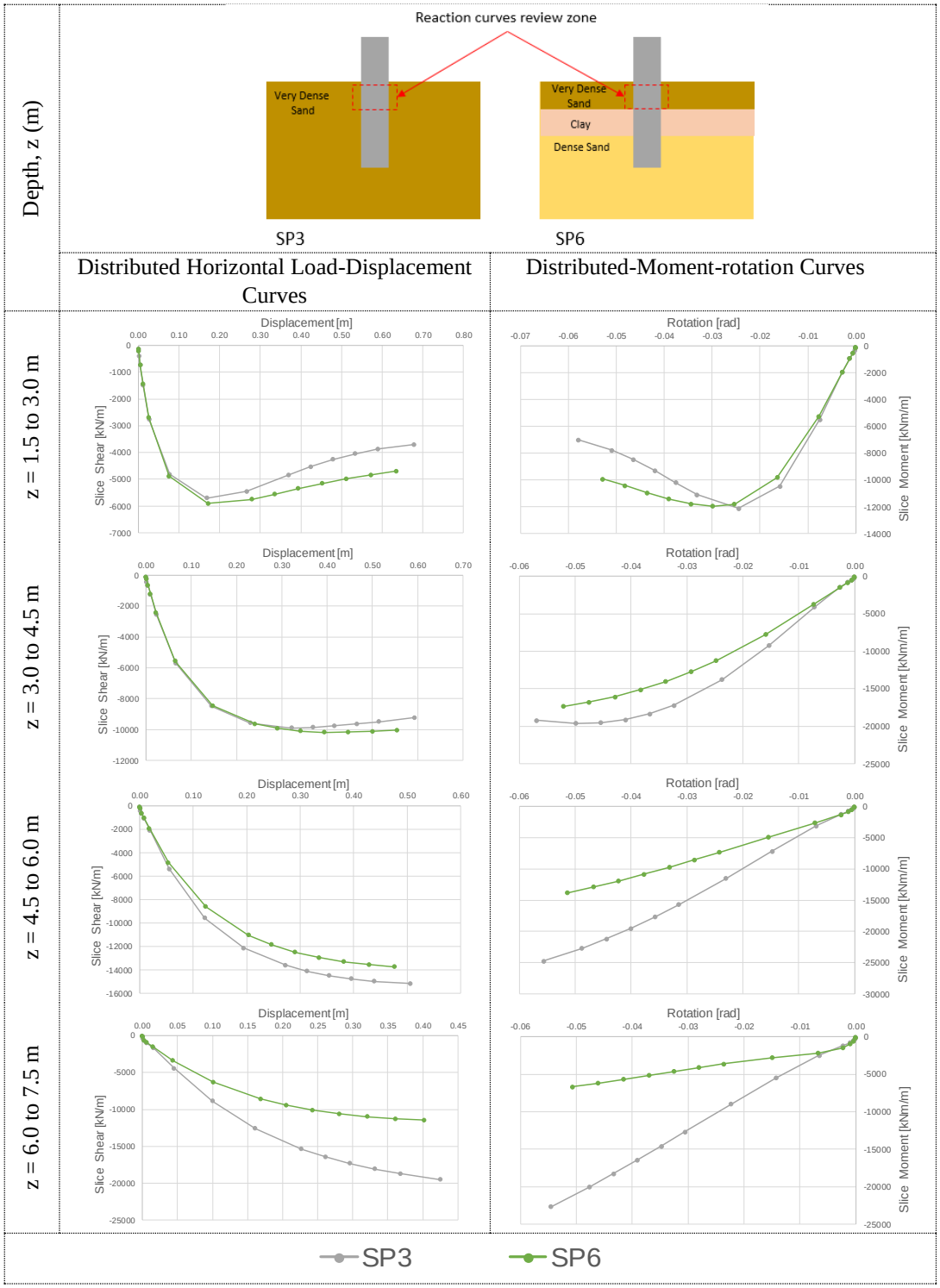

Figure 7.33: Review of reaction curves in dense sand layer between 1.5 m and 7.5 m for a uniform very dense profile (SP3) and a layered profile with a very dense layer from 0 to 7.5 m (SP6)

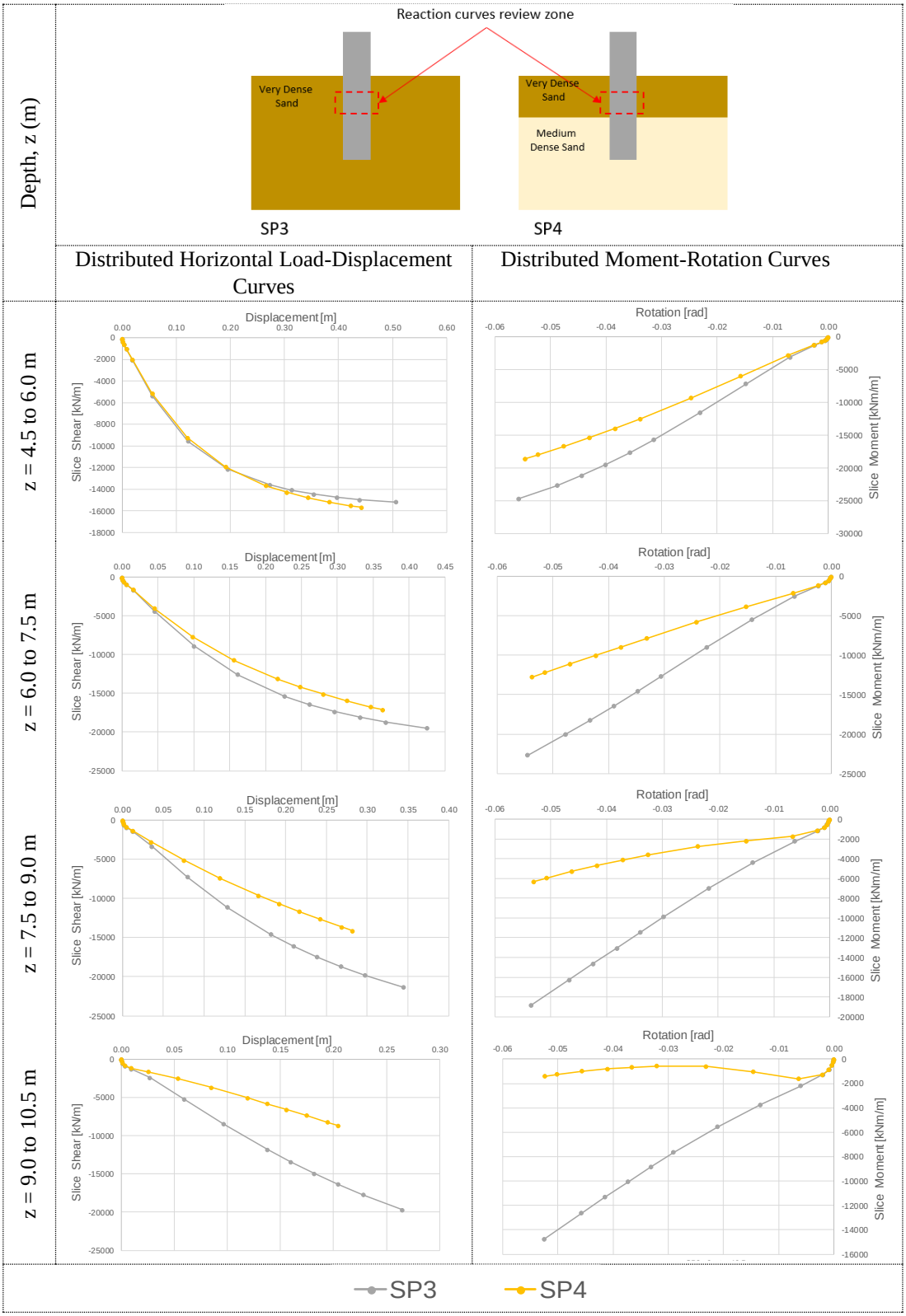

Figure 7.34: Review of reaction curves in dense sand layer between 4.5 m and 11.25 m for a uniform very dense profile (SP3) and a layered profile with a very dense layer from 0 to 11.25 m (SP4)

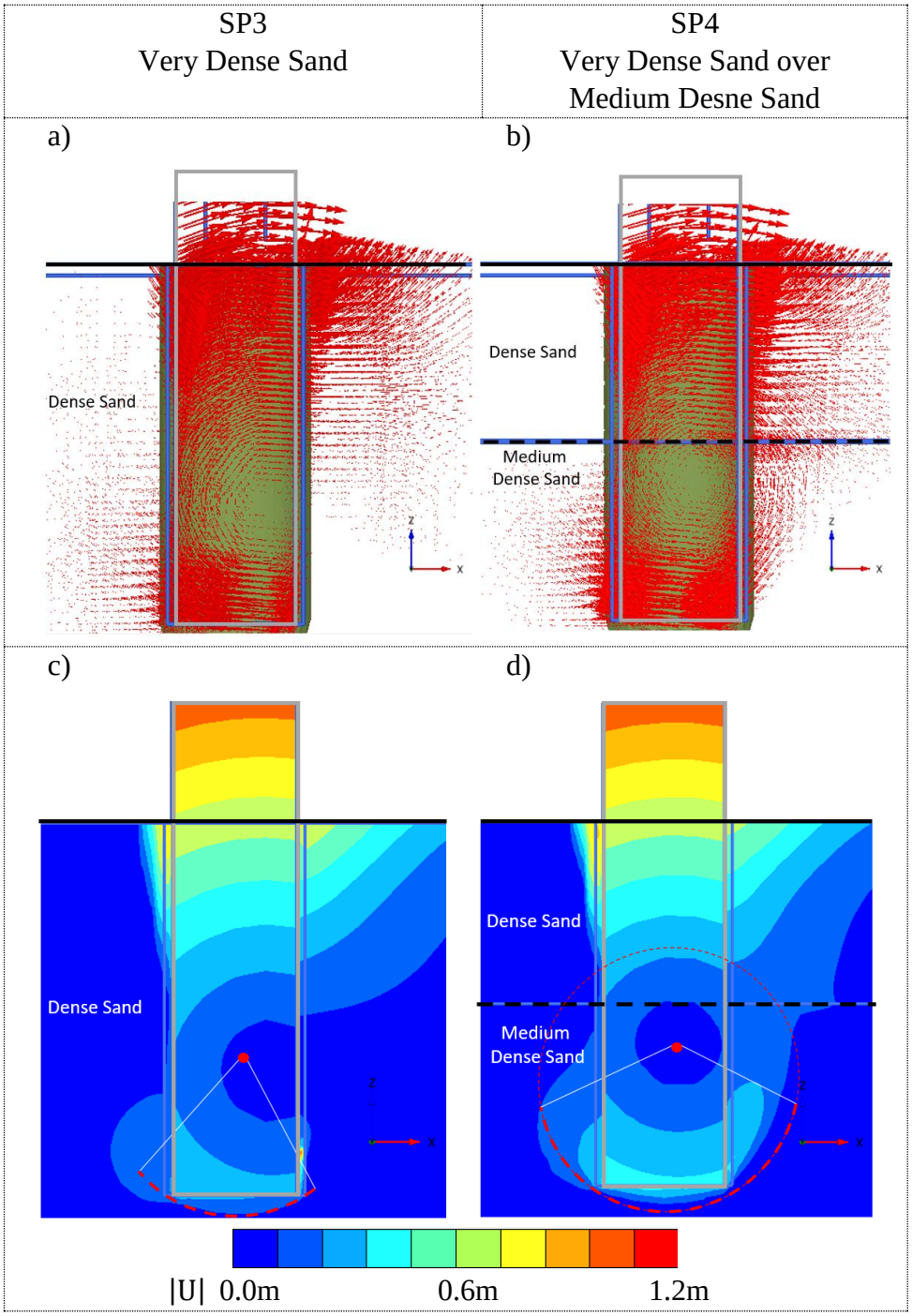

Figure 7.35: Total displacement vector arrows for a) SP3 and b) SP4 and the total displacement contour shadings around the pile for c) SP2 and d) SP4 analysis

a) SP3

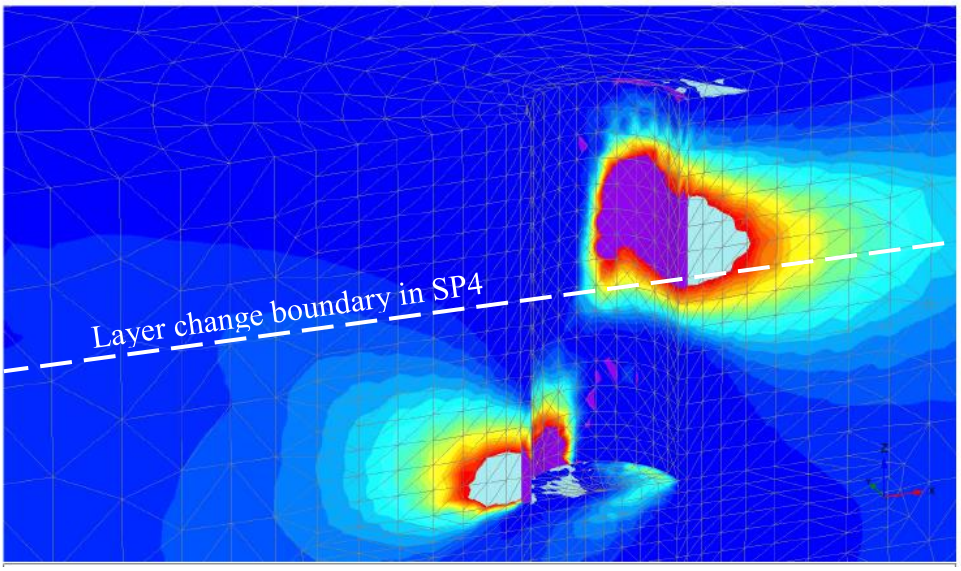

b) SP4

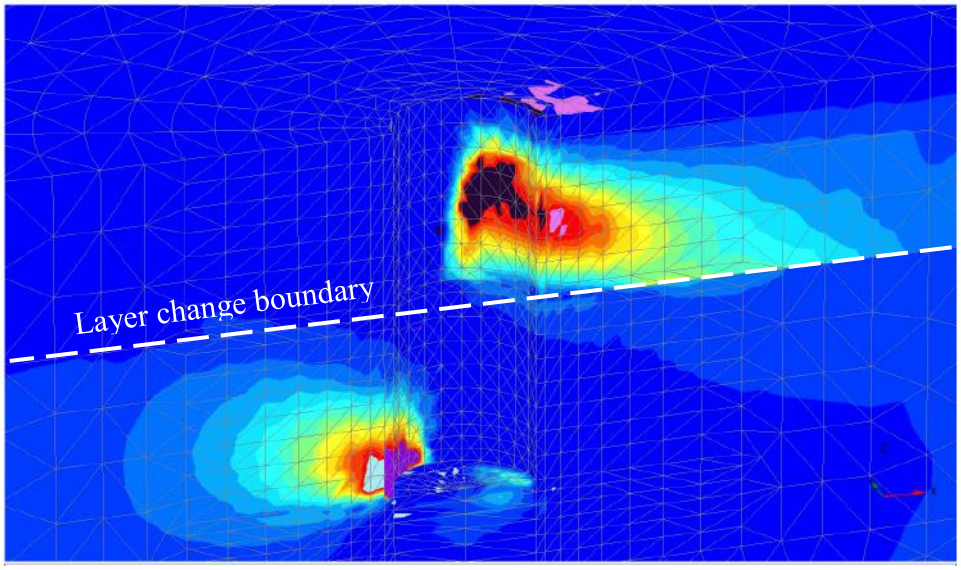

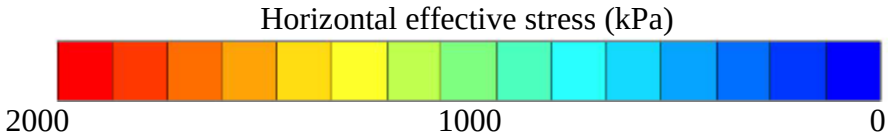

Figure 7.36: Horizontal effective stress contours at 0.1*D* seafloor lateral displacement for a) very dense sand profile – SP3 and b) very dense sand over medium dense sand profile – SP4, with SP4 layer change boundary shown on both a) and b)

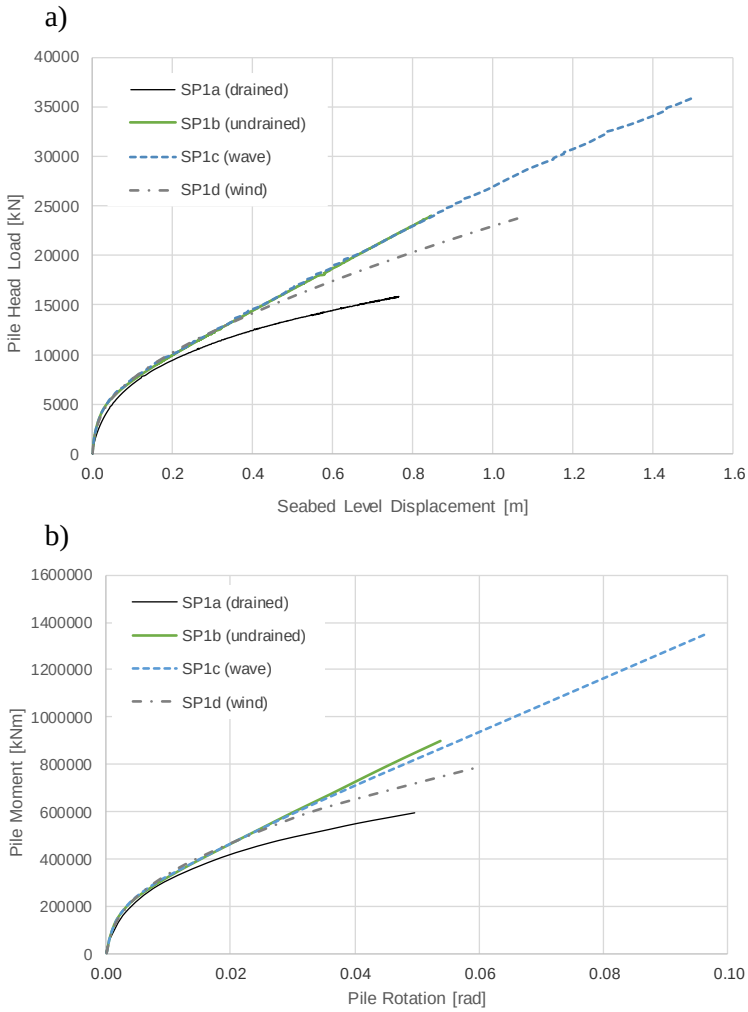

Figure 7.37: Global pile a) load-displacement and b) moment-rotation response at seabed for SP1 at different loading rates

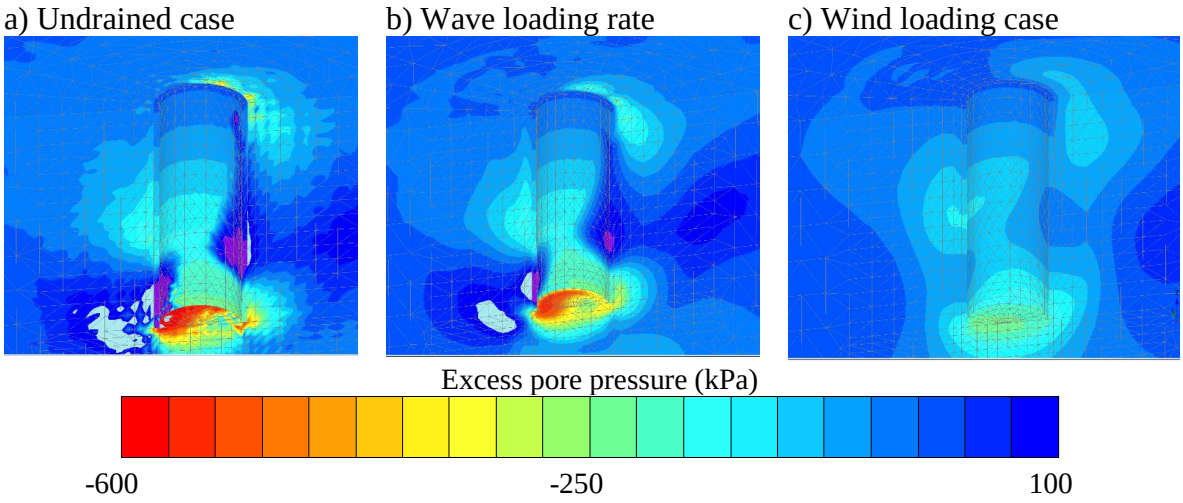

Figure 7.38: Excess pore pressure contours at 20 MN pile head load for a) SP1b undrained case, b) SP1c wave loading rate and c) SP1d wind loading rate

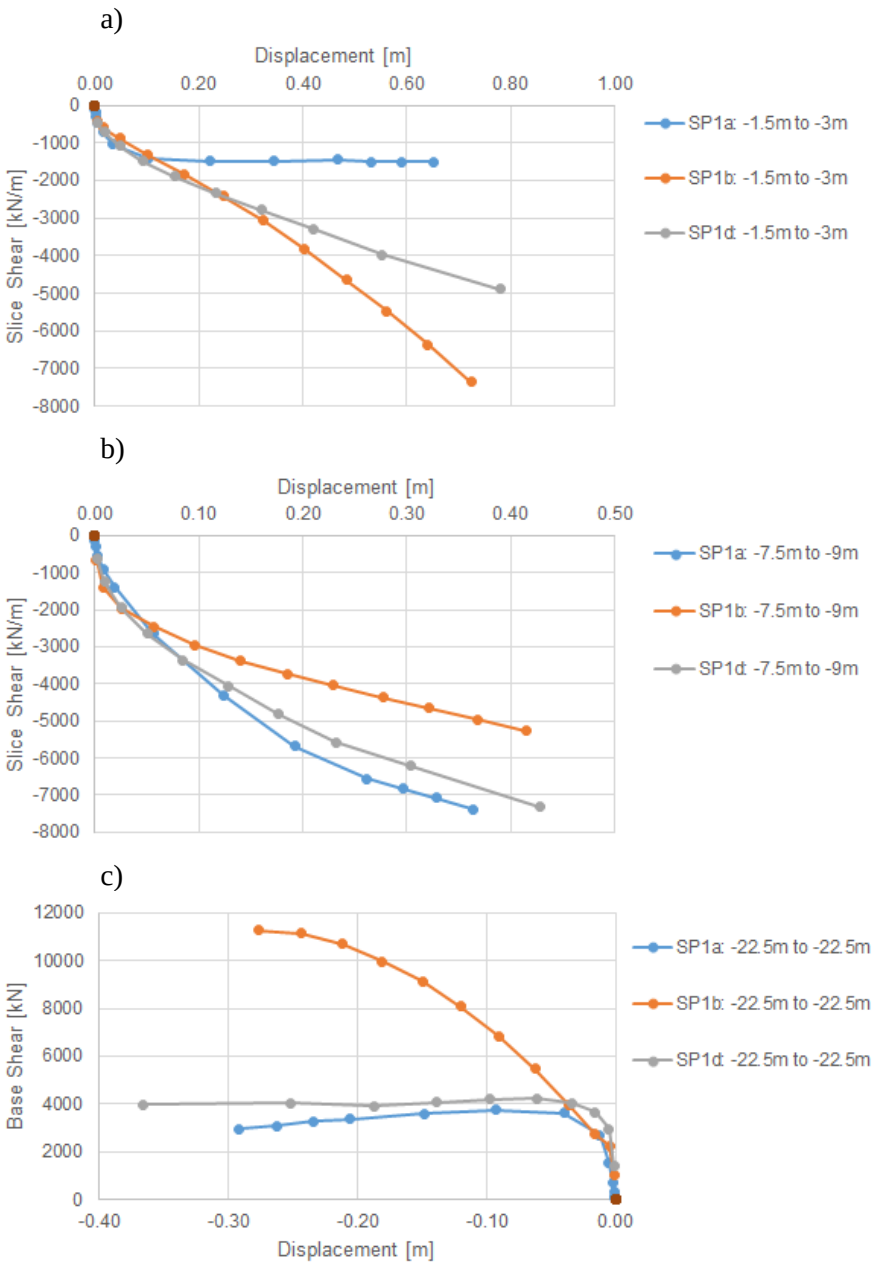

Figure 7.39: Comparison of distributed horizontal load transfer curves for SP1 drained (SPa), undrained (SPb) and wind loading rate (SPd) cases a) in shallow zone soil, b) above the pivot point and c) at pile base (i.e. base shear)

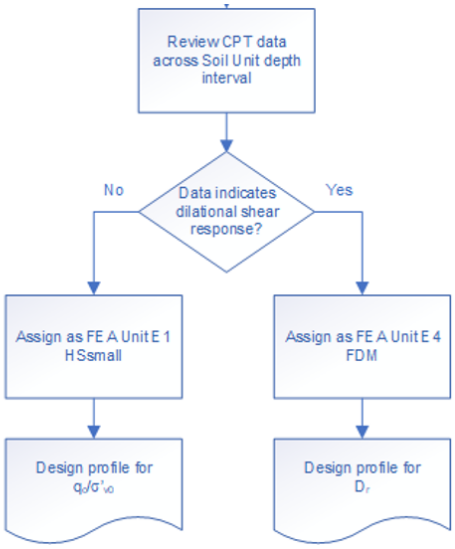

Figure 7.40: Unit E constitutive model assignment process

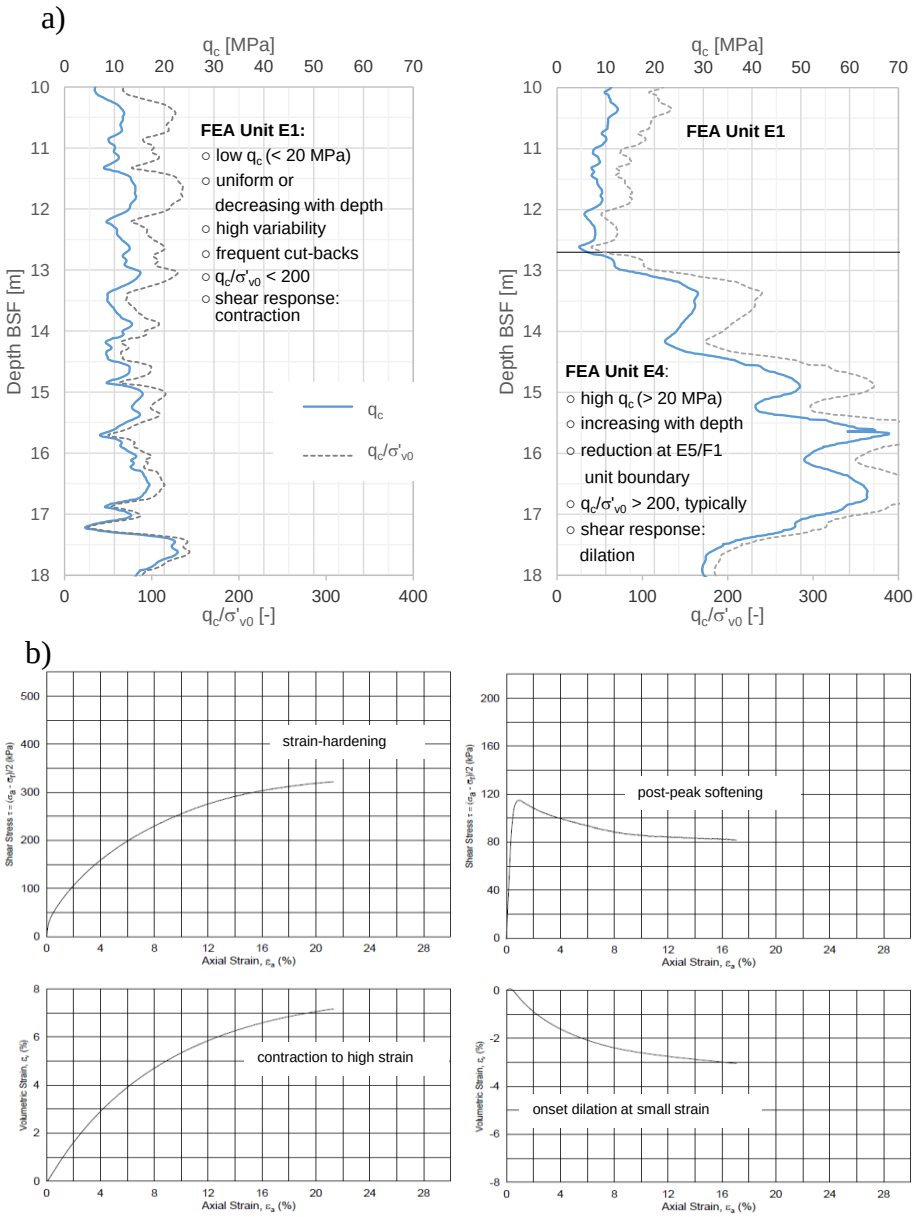

Figure 7.41: Unit E characterisation example with a) showing the distinction of CPT characteristics for assignment of FEA Unit E1 and E4 and b) showing distinction of (general) triaxial shear response for FEA Unit E1 (left) and Unite E4 (right)

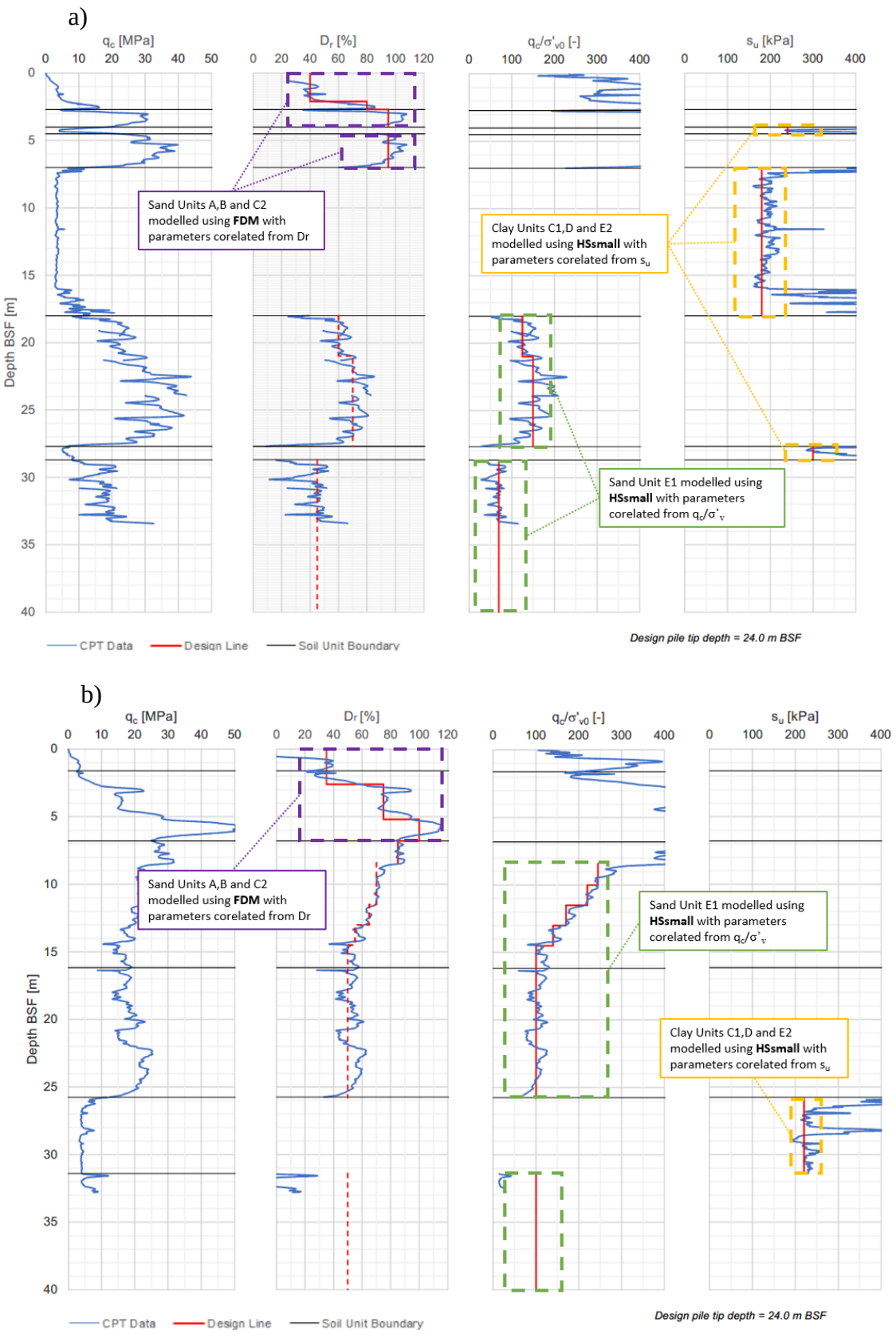

Figure 7.42: Cone penetration test data and derived design lines for the constitutive model calibration at locations a) C01 and b) L07

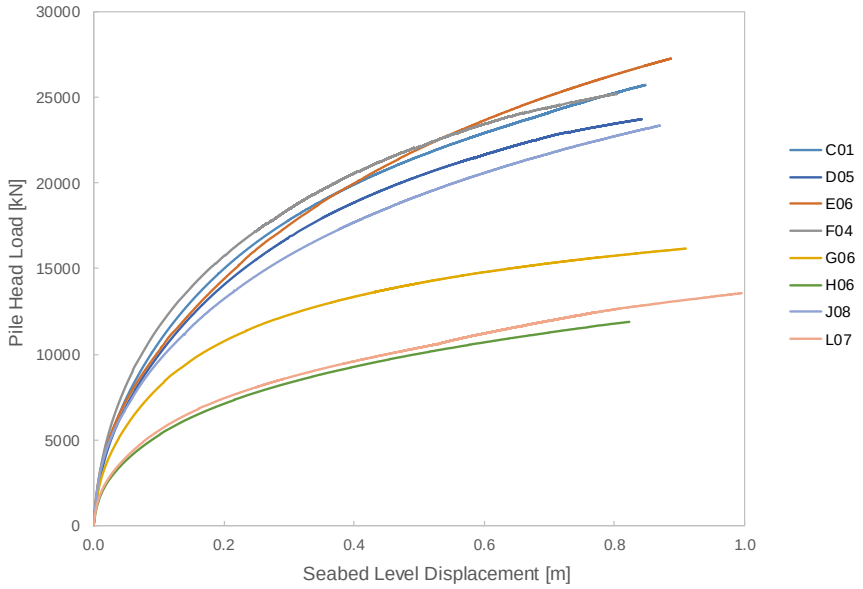

Figure 7.43: Task 6 FEA lateral load versus seabed displacement for all design profiles

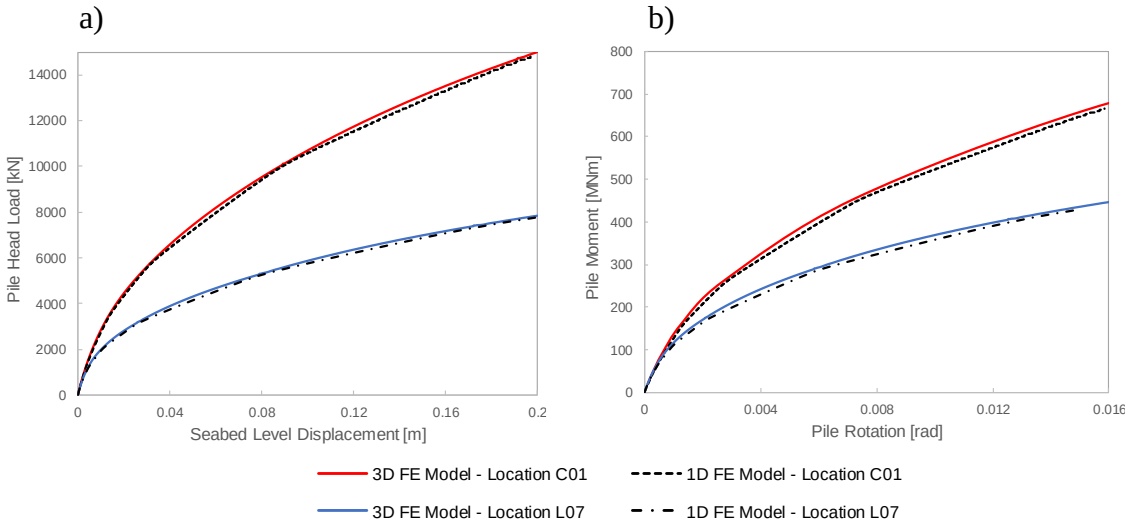

Figure 7.44: Comparison of 3D and 1D finite element model predations using extracted soil reaction curves for design locations C01 and L07

Section 8

SUMMARY, CONCLUSIONS AND RECOMMENDATIONS

Contents

8. SUMMARY, CONCLUSIONS AND RECOMMENDATIONS

This section provides overarching overall conclusions and recommendations to the project by comparing and contrasting each model and modelling technique presented, outlining the advantages and disadvantages where appropriate. Additional detailed conclusions are also presented for each component of this project within the individual portfolio sections.

8.1 Research Background and Objectives

With the increased use of FEA for the design of offshore wind turbine foundations, the availability of suitable constitutive models has become increasingly important to ensure accurate design analysis predictions are obtained. Many thousands of advanced elastoplastic constitutive models have been presented in the literature for soils. These models vary in complexity and specific formulations; however, broadly these can be characterised as either i) single surface, ii) multi-surface or iii) bounding surface elastoplastic models. Many models (particularly advanced models) are presented for single-element calculations only and are not demonstrated to work robustly in complex 2D or 3D boundary value problems.

The primary objective of this project was to develop constitutive models that have value in a foundation design context for offshore wind turbines. For such a model to be successful, it must be i) scientifically robust (to ensure the model predictions are reliable) and ii) capable of being implemented in an engineering design environment. Item ii) requires considerations of implementation, parameter calibration procedures and numerical robustness within an FEA foundation design context.

This project allowed for a unique review of models suitable for foundation design FEA. The full development process of each implemented constitutive model was considered, from single-element level to full 3D FEA. For each model developed within this study extensive calibration at single-element level to laboratory test data is presented (primarily from North Sea soil units) followed by the FEA of offshore foundations, and where possible with comparison to foundation load tests.

8.2 Motivation for Modelling Approaches and Developed Models

Each modelling technique and proposed specific models have their own advantages and disadvantages, which make them more applicable for different foundation design problems. For example different tailored bespoke models may be required depending on the specific loading conditions (e.g. monotonic, small number of load cycles); specific soil conditions (e.g. dense sand or overconsolidated clay) and different specific design conditions (e.g. fatigue limit state or serviceability limit state), as opposed to a single all-encompassing constitutive model (i.e. Philosopher model). The subsections below present an overall summary of the motivation for the development of each model in this study, each of which was developed for a specific offshore foundation design problem.

8.2.1 Single Surface Model for Sand

FEA is typically performed as part of the detailed design stage for offshore foundations; however, it can also be required at early design stages to review specific loading situations, which will likely be critical for the foundation design. Accepting that FEA is a necessary component of the full geotechnical design process (i.e. early stage concept to final stage detailed design stage), a hierarchical approach to the FEA complexity is required for design analysis. In this approach, a relatively simple constitutive model is considered at the start of design and additional complexity is added as the project develops.

For relatively large foundations, which are being used for offshore wind turbines, the drainage response is likely to vary from partially drained to undrained in sand. Therefore a review of the foundation response under partially drained conditions in sand often has to be performed at an early stage of the design process, as it can be critical to review the feasibility of a foundation option. It was identified that there was a lack of practical constitutive models, available as built-in soil models within commercially available FEA software, that are suitable for predicting the response of dense sands at low initial p' values when considering undrained to partially drained conditions. Although a number of advanced constitutive models have been proposed in the literature, which represent the

response of dense sand reasonably well, most are considered too complicated for use at the early stage of a design project. Therefore, a relatively simple single surface model was developed for foundation analysis in dense sand. The developed practical robust single surface sand model formulation and implementation is presented in Section 4 with extensive calibration of the model to laboratory tests data, at a number of different sites, followed by FEA of suction bucket (Section 4) and monopile foundations (Section 7).

8.2.2 Multi-Surface Model for Clay

A review of the cyclic loading response is critical for the design of offshore wind turbine foundations. Various advanced constitutive models have been proposed to capture the behaviour of clay for monotonic and cyclic loading in design FEA. The majority of these models are complex effective stress bounding surface constitutive models. However, use of these models for design FEA is typically not feasible due to their complex calibration procedures and the prevalence of numerical convergence issues and lengthy run times, particularly when considering cyclic loading.

In design situations involving short-term loading of a foundation embedded in low permeability soil (i.e. clay or sand with a high percentage of fines), total stress constitutive models are an attractive option for use in FEA, as an alternative to effective stress approaches. Total stress models provide a means of specifying undrained shear strength as a model input parameter. Additionally, they tend to be simpler to implement, faster to compute and more stable than advanced effective stress models.

Therefore, a total stress multi-surface model was developed to be used for monotonic and cyclic design FEA of offshore monopiles. A multi-surface model, named the Parallel Iwan Multi-Surface (PIMS) model, suitable for FEA of soil-structure interaction problems involving clay undergoing undrained monotonic and cyclic storm-type loading is developed in Section 5.

8.2.3 Bounding Surface Model for Sand

It is shown that the developed effective stress FDM/SDS single surface model(s) is suitable for foundation design FEA if carefully calibrated (Sections 4 and 7); however, it does not capture some

important features of sand response. For example, it cannot simulate a state dependent peak friction angle, post peak softening, a state dependent phase transformation line and induced/inherent anisotropy.

Although the PIMS model is shown to be suitable to capture the response of undrained clay under monotonic and cyclic loading (Section 5), it is not suitable for modelling the behaviour of sand under partially drained conditions. Therefore, it was considered necessary to develop a more sophisticated effective stress constitutive model for dense sand. One option was to alter the total stress PIMS model to develop an effective stress version of the PIMS model, for example by using multiple Mohr Coulomb failure surfaces to define the micro models. However, the most well-established and widely used constitutive models for sand are based on bounding surface plasticity and incorporate the state parameter concept. Examples of their use in the literature have shown very good agreement with laboratory element test data; however, despite this, there are very few examples of model calibration to laboratory test data followed by FEA of centrifuge or field foundation load test experiments. Therefore it was considered more appropriate to build upon the Manzari-Dafalias model architecture by improving its formulation and assessing its performance in the boundary value problem of a suction bucket foundation under tension loading. An added benefit of developing a modified Manzari-Dafalias type model, as presented in Section 6, is that the three main elastoplastic modelling techniques are used within this study (i.e. single surface, bounding surface, multi-surface) and hence allows for high level comparison between the different modelling techniques. The developed modified Manzari-Dafalias bounding surface model was used for predicting the response of a suction bucket under tension loading and compared to centrifuge model test data.

8.3 Elastoplastic Modelling Approaches for Design FEA

The range of different elastoplastic modelling approaches typically employed in the literature for modelling soils were considered within this study by developing single surface, bounding surface and multi-surface plasticity models. Each modelling technique and proposed specific models have

their own advantages and disadvantages, which make them more suitable for different foundation design problems.

It is shown in Sections 4 and 7 that the use of a perfectly plastic (i.e. no yield surface hardening/softening) single surface constitutive model is appropriate under certain design circumstances and given its simplicity and robust numerical performance it is often preferred for design FEA. However, it is also shown, when using a single surface model, it is important that the particular model formulation is carefully considered to incorporate the correct features necessary to predict the response of the foundation problem being modelled. For example, as shown in Section 4, if the response at small strains is important a strain-dependent elastic overlay rule must be included and if the soil is highly kinematically constrained then a suitable state- and stress-dependent plastic potential function must be included. Therefore the use of a single surface model requires a high level of engineering judgement at the model development stage to ensure the correct features are included within the model to capture the most salient features of the soil response for the foundation problem being considered. Although a single surface model may be suitable in certain design situations, if carefully tailored to the problem being modelled (Sections 4 and 7), it is important to note that it is only suitable for monotonic loading.

A common approach for overcoming many issues associated with single surface model formulations is to use a bounding surface model. Comparisons of single-element model simulations with laboratory element test data, using the developed bounding surface model presented in Section 6, show that the model can capture the effects of soil density, stress level and stress path dependency. However, the model has 19 input parameters and calibration is therefore time consuming as it requires a significant amount of curve fitting of relatively arbitrary parameters. It is also possible that different parameter sets could be used to achieve a similar response at single-element level. This is an intrinsic disadvantage of a bounding surface model, as they must include complex, somewhat arbitrary, mapping rules to control their behaviour. This issue is exacerbated further when cyclic loading is considered in which additional mapping rules must be included.

In contrast to the bounding surface models, a multi-surface model intrinsically captures a nonlinear stress-strain response, the effects of stress-history and a realistic unload-reload response, without the need for complex mapping rules. Therefore, an elasto-plastic model incorporating multiple yield surfaces is preferred. Multi-surface models are typically implemented using several nested kinematic hardening yield surfaces (i.e. series Mroz-Iwan model). Despite offering an elegant modelling approach for simulating a nonlinear hysteretic response, tensorial series Mroz-Iwan models can become complex and implementation can be difficult. It is shown in Section 5 that a multi-surface parallel Iwan multi-surface model formulation is preferred since it is relatively easy to calibrate and implement, particularly in contrast to a bounding surface model.

8.4 Model Implementation

All constitutive models presented within the project were programmed in Fortran as user defined soil models for use in both Plaxis and Abaqus commercial FEA software. The overall implementation approach is the same for both cases and only slight differences are required with respect to variable names and interaction with the main FEA software. All models, within this project, are implemented using an explicit Runga-Kutta-Dormand-Prince integration scheme with automatic error control to determine the updated stress state. Despite this the numerical robustness, overall implementation complexity and computational speeds of the models differ significantly.

It was demonstrated in Section 4 that the developed single surface model is relatively simple to implement. The developed single surface FDM and SDS models proved to be numerically robust with little convergence issues encountered and reasonable computational times in comparison to other simple models. When performing FEA within a foundation design environment, the numerical robustness of the model is important, since there are typically short design schedules and as a result the risk of numerical convergence issues or lengthy simulation times causing a delay to the overall project would generally be considered an unacceptable risk. Therefore the developed model is considered to be useful for design monotonic FEA if carefully calibrated.

In contrast, implementation of the bounding surface model is relatively complex with many rules required to determine the distance to different surfaces and whether loading or unloading is occurring. In addition significant convergence issues and slow run times were encountered when using the bounding surface model in the FEA of a boundary value problem, which may make its use for design FEA impracticable. In general overly complex models, and hence less elegant formulations, tend to suffer more from numerical issues when used in advanced 3D FEA.

Interestingly, implementation of the developed multi-surface PIMS model proved easier than both the single surface and bounding surface models. This is because a multi-surface parallel Iwan framework was utilised and as such the micro models, which are arranged in parallel with strain equivalence, are very simple and the stress point algorithm, at single-element level, is unlikely to suffer from numerical issues. Within this study it was found that a parallel Iwan multi-surface model formulation performed better within FEA calculations (i.e. numerical robustness) than the bounding surface model considered. However, it is noted that this comparison between the numerical performance of a bounding surface and a parallel Iwan multi-surface model within this study is rather qualitative given they were used for different foundation problems. Although the use of a high number of surfaces implies a high computational memory demand within a parallel Iwan multi-surface model, this is somewhat offset by the fact that the micro model constitutive calculations are extremely simple and hence fast to compute.

The basic parallel Iwan framework adopted for the PIMS model is a well-established constitutive modelling approach, although there are few documented applications of this framework in geotechnical engineering. Although previous researchers have explored the application of series forms of the Iwan framework to represent soil behaviour, this study demonstrated that the parallel form is a particularly attractive option for practical geotechnical calculations. A further major advantage of using a parallel Iwan approach, outlined within this study, is that each micro model is implemented in the same manner as any other simple single surface plasticity model.

8.5 Calibration and Prediction for Offshore Foundations

It is shown in Sections 4 to 7 that with careful parameter calibration to single-element tests it is possible to accurately predict the response from foundation load tests for each constitutive model developed within this study.

The developed single surface SDS and FDM single surface models were calibrated to several North Sea sands in Sections 4 and 7 to simulate the response of a suction bucket under tension loading (Section 4) and a laterally loaded monopile (Section 7). The analysis of three of the PISA test piles, at the sand site, provides an indication of the predictive capabilities of the proposed relatively simple single surface model and calibration approach. The model did not capture some features of the observed sand response at single-element level (e.g. post-peak softening); however, it was shown to match the pile load tests reasonably well. This demonstrates that certain model deficiencies can be overcome with careful parameter calibration and indeed highlights that, although constitutive model selection is important, careful calibration of the selected model design parameters is also fundamental in achieving a realistic foundation response prediction in FEA.

The developed PIMS model presented in Section 5 is shown to be capable of capturing (i) nonlinear stiffness response from very small to large strains for different stress paths, (ii) different undrained shear strengths for different stress paths, (iii) effects of recent stress history, (iv) hysteretic unload-reload response and (v) cyclic degradation of stiffness and strength of clay at single-element level. A detailed overview of a normalisation approach for clay is presented for parameter calibration in Section 5, which shows that the use of the model for large offshore wind farm design is feasible. It is also shown that this normalisation approach could be applied more generally to improve existing stiffness reduction functions proposed in the literature. Example 3D FEA presented demonstrates the practical application of the PIMS model. The analysis of three of the PISA test piles, at the clay site, demonstrated the predictive capabilities of the approach. A separate example of a monopile subjected to cyclic lateral loading demonstrates the robustness and feasibility of the model implementation, with the computed results consistent with expected forms of behaviour. The total

stress PIMS model was primarily developed to predict the performance of offshore foundations in clay soils during, and immediately after, short-term storm-type cyclic loading events, therefore the model is not suitable for consolidation analysis or long term cyclic loading.

In Section 6 an effective stress bounding surface model is used in FEA of a boundary value problem involving a suction bucket under tension loading, and the computed results are compared with previously published centrifuge model test results. It is promising that reasonable agreement is obtained between the centrifuge model test results and the numerical simulations when the constitutive model has been calibrated in advance using laboratory element test data. This gives added confidence and guidance on the use of bounding surface, Manzari-Dafalias type, models for foundation analysis. The importance of considering inherent anisotropy within the constitutive model calibration is clearly demonstrated by comparison to triaxial compression, extension and direct simple shear tests. It is shown that calibration using triaxial compression test data alone will result in very unconservative foundation design, particularly when considering undrained conditions.

Although a relatively good match was achieved with the modified Manzari-Dafalias model at single-element level when compared to a range of different laboratory element tests, the parameter calibration is cumbersome and potentially non-unique given the number of parameters required. As a result the developed bounding surface model can be rather ‘black box’ since it is not clear in what way changing parameters will affect the overall response. For the range of stress paths in FEA of a foundation, this makes it very difficult to be conservative in design and is in contrast to the PIMS model in which there is a clear meaning to the parameter calibration approach, since points on a normalised stiffness-strain backbone curve are directly matched.

8.6 Further Work and General Recommendations

8.6.1 FDM and SDS Models

As part of future work for the FDM and SDS single surface models an improvement to the plastic potential function used could be developed to ensure a dimensionless form is adopted. This could be achieved by including a normalisation reference pressure to the stress invariant terms in the plastic potential function. A further improvement to the model, that could be included as part of future work, would be to use a function to represent the critical state line as opposed to the piecewise curve that is currently used. Various other modifications could be incorporated within the model as part of future work. For example, strain-softening and inherent anisotropy of some form could be added. Although it would be relatively trivial to implement these features, the purpose of this model is not to capture all sand response features but instead to capture the most relevant features of dense sand response while also ensuring the model is sufficiently robust and efficient.

8.6.2 PIMS Model

For the total stress PIMS model, further model extensions are considered feasible as part of further work, and indeed important for certain design problems. For example, incorporating rate effects explicitly in the model, rather than employing the simple rate correction approach that is adopted in the current work would be a very useful improvement. It would also be possible to incorporate different forms of cyclic response from that presented in this section, for example separate micro models for the stiffness and strength degradation components of behaviour could be included or additional micro models could be added to incorporate cyclic hardening. It is considered that a major advantage of the model formulation is that making further modifications to the model is relatively trivial since only the formulation of the individual simple micro models, arranged in parallel, has to be adapted.

8.6.3 Modified Manzari-Dafalias Model

The work presented in this project, using the modified Manzari-Dafalias model, has focused on the monotonic response only and further work is required to address the important area of cyclic

loading, which is of significant importance for the design of offshore foundations. It is recommended that the memory surface concept should be added to the model, as outlined by Liu et al. (2019), to improve its capability for cyclic loading. Similar to the model presented in Section 6, any developed cyclic model extension should be calibrated at single-element level to cyclic laboratory test data and then also used to perform cyclic FEA of a boundary value problem (i.e. considering the full constitutive model development process). It is recommended, to extend the work presented in this study, the FEA should be performed to investigate the response of a suction bucket under cyclic loading, in which the centrifuge data by Bienen et al. (2018) can be used for comparison.

The model formulation presented in this study utilised a non-conservative elastic formulation, as do almost all other Manzari-Dafalias type models formulations presented in the literature, and therefore it is recommended that as part of future work a hyperelastic, thermodynamically acceptable elastic stiffness matrix should be incorporated. This is considered to be of particular importance if cyclic loading is to be investigated.

8.6.4 General Recommendations

A multi-surface modelling approach is found to be the preferred framework for constitutive model development, for foundation design FEA, given it has been shown that they are relatively simple to implement and calibrate.

A major advantage outlined within this study of using a parallel Iwan approach to implement a multi-surface model is that each micro model is implemented in the same manner as any other single surface plasticity model. As a result, it has been shown that any single surface constitutive model that has been implemented as a user-defined soil model can be extended to a multi-surface model by applying a relatively simple parallel Iwan ‘wrapper’ code. This is a significant advantage, as despite the benefits of multi-surface models, the complexity of implementation is often considered a barrier. Therefore, as part of future work it is recommended that the area of multi-surface

modelling should be explored in more detail, particularly the development of an effective stress parallel Iwan multi-surface model for sand e.g. by arranging a number of linear elastic Mohr Coulomb models in parallel. For such a developed model the deviatoric stress versus deviatoric strain backbone curve would then be calibrated in a similar manner to the total stress PIMS model by altering the weights and size of each micro yield surface; however, in addition the plastic potential function in each micro model could be calibrated to match the volumetric strain versus deviatoric strain response. A normalisation approach similar to that developed for the total stress PIMS model could then be developed for this effective stress version. Another option would be to extend a number of relatively advanced effective stress hardening single surface models (e.g. CASM by Yu et al. 1998) into multi-surface models using a parallel Iwan framework. These developed multi-surface models should then be compared to investigate their performance in capturing the response of sand at single-element level and foundation load tests in FEA.

REFERENCES

Abbo AJ, Lyamin AV, Sloan SW, Hambleton JP. 2011. A C2 continuous approximation to the Mohr-Coulomb yield surface. International Journal of Solids and Structures, 48(21):p3001-3010.

Aghakouchak A. 2015. Laboratory characterisation of cyclic behaviour of driven piles in sand. PhD Thesis, Imperial College, London, UK.

Ahmed SS, Hawlader B. 2016. Numerical analysis of large-diameter monopiles in dense sand supporting offshore wind turbines. International Journal of Geomechanics, 16(5):p1-14.

Al-Tabbaa A, Wood DM. 1989. An experimentally based 'bubble' model for clay. Numerical Models in Geomechanics. NUMOG III, Niagra Falls, Canada, p91-99.

American Petroleum Institute (API). 2010. RP 2A-WD – Recommended Practice for planning, Designing and Constructing Fixed Offshore Platforms, Washington: American Petroleum Institute.

Anastasopoulos I, Gelagoti F, Kourkoulis R, Gazetas G. 2011. Simplified Constitutive Model for Simulation of Cyclic Response of Shallow Foundations: Validation against Laboratory Tests. Journal of Geotechnical and Geoenvironmental Engineering, 137(12):p1154-1168.

Arany L, Bhattacharya S, Macdonald J, Hogan SJ. 2017. Design of monopiles for offshore wind turbines in 10 steps. Soil Dynamics and Earthquake Engineering, 92:p126-152.

Been K, Jefferies MG. 1985. A state parameter for sands. Géotechnique, 35(2):p99-112.

Benz T. 2007. Small-strain stiffness of soils and its numerical consequences. PhD Thesis, University of Stuttgart, Germany.

Bienen B, Klinkvort RT, O'Loughlin CD, Zhu F, Byrne BW. 2018. Suction caissons in dense sand, part II: vertical cyclic loading into tension. Géotechnique, 68(11):p953-967.

Bolton MD. 1986. Strength and dilatancy of sands. Géotechnique, 36(1):p65-78.

Bolton MD, Dasari GR, Britto AM. 1994. Putting small strain non-linearity into Modified Cam Clay model. In 8th International Conference on Computer Methods and Advances in Geomechanics, Morgantown, West Virginia, p537-542.

Borja RI, Lee SR. 1990. Cam-clay plasticity, part 1: implicit integration of elasto-plastic constitutive relations. Computer Methods in Applied Mechanics and Engineering, 78(1):p49-72.

Borja RI, Tamagnini C, Amorosi A. 1997. Coupling plasticity and energy-conserving elasticity models for clays. Journal of Geotechnical and Geoenvironmental Engineering, 123(10):p948-957.

Boulanger RW, Ziotopoulou K. 2013. Formulation of a sand plasticity plane-strain model for earthquake engineering applications. Soil Dynamics and Earthquake Engineering, 53:p254-267.

Brinkgreve RBJ. 1994. Geomaterial models and numerical analysis of softening. PhD Thesis, Delft University, Netherlands.

Britto AM, Gunn MJ. 1987. Critical state soil mechanics via finite elements. Ellis Horwood, New York.

Burd HJ, Byrne BW, McAdam RA, Houlsby GT, Martin CM, Beuckelaers WJAP, Zdravković L, Taborda DMG, Potts DM, Jardine RJ, Gavin K. 2017. Design aspects for monopile foundations. In Proc. TC209 Workshop, 19th International Conference on Soil Mechanics and Geotechnical Engineering, Seoul, South Korea, p35-44.

Burd HJ, Taborda DMG, Zdravković L, Abadie CN, Byrne BW, Houlsby GT, Gavin K, Igoe D, Jardine RJ, Martin CM, McAdam RA, Pedro AMG, Potts DM. 2019. PISA design model for monopiles for offshore wind turbines: application to a marine sand (under review)

Burland JB. 1989. Ninth Laurits Bjerrum Memorial Lecture: Small is beautiful—the stiffness of soils at small strains. Canadian Geotechnical Journal, 26(4):p499-516.

Bye A, Erbrich C, Rognlien B, Tjelta TI. 1995. Geotechnical design of bucket foundations. In Offshore Technology Conference, Houston, Texas, Paper OTC7793.

Byrne BW. 2011. Foundation Design for Offshore Wind Turbines. In British Geotechnical Association, Institution of Civil Engineers, Géotechnique Lecture 2011, London, UK.

Byrne BW, McAdam RA, Burd HJ, Houlsby GT, Martin CM, Beuckelaers WJAP, Zdravković L, Taborda DMG, Potts DM, Jardine RJ, Ushev E, Liu T, Abadias D, Gavin K, Igoe D, Doherty P, Skov Gretlund J, Pacheco Andrade M, Muir Wood A, Schroeder FC, Turner S. & Plummer MAL. 2017. PISA: new design methods for offshore wind turbine monopiles. In 8th International Conference on Offshore Site Investigation and Geotechnics, London, UK, p142-161.

Callisto L, Calabresi G. 1998. Mechanical behaviour of a natural soft clay. Géotechnique, 48(4):p495-513.

Centre of Civil Engineering Research and Codes (CUR). 2001. Bearing Capacity of Steel Pipe Piles. CUR Report.

Chiang DY, Beck JL. 1994. A new class of distributed-element models for cyclic plasticity-I theory and application. International Journal of Solids and Structures, 31(4):p469-484.

Chow F. 1997. Investigation into the behaviour of displacement piles for offshore foundations. PhD Thesis, Imperial College, London, UK.

Clayton CRI. 2011. Stiffness at small strain: research and practice. Géotechnique, 61(1):p5-37.

Collins IF, Kelly PA. 2002. A thermomechanical analysis of a family of soil models. Géotechnique, 52(7), p507-518.

Concept Site Investigations (Concept). 2014. PISA Dunkirk Site Investigation Borehole Logs. Concept Job No. 14/2634.

Corti R, Diambra A, Wood DM, Escribano DE, Nash DF. 2016. Memory surface hardening model for granular soils under repeated loading conditions. Journal of Engineering Mechanics, 142(12):04016102.
Dafalias YF, Popov EP. 1975. A model of nonlinearly hardening materials for complex loading. Acta Mechanica, 21(3):p173-192.
Dafalias YF, Manzari MT. 2004. Simple plasticity sand model accounting for fabric change effects. Journal of Engineering Mechanics, 130(6):p622-634.
Dafalias YF, Papadimitriou AG, Li XS. 2004. Sand plasticity model accounting for inherent fabric anisotropy. Journal of Engineering Mechanics, 130(11):p1319-1333.
Dafalias YF, Manzari MT, Papadimitriou AG. 2006. SANICLAY: Simple anisotropic clay plasticity model. International Journal for Numerical and Analytical Methods in Geomechanics, 30(12):p1231-1257.
Darendeli MB. 2001. Development of a new family of normalized modulus reduction and material damping curves. PhD Thesis. University of Texas, Austin.
Dassault Systèmes. 2014. Abaqus user manual, version 6.13. Simulia Corp, Providence, RI, USA.
Det Norske Veritas (DNV). 2014. DNV-OS-J101 – Design of Offshore Wind Turbine Structures. Oslo: Det Norske Veritas.
van Dijk BF. 2015. Caisson capacity in undrained soil: failure envelopes with internal scooping. In 3rd International Symposium on Frontiers in Offshore Geotechnics, Oslo, Norway, p337-342.
Ding Y, Huang W, Sheng D, Sloan SW. 2015. Numerical study on finite element implementation of hypoplastic models. Computers and Geotechnics, 68:p78-90.
Doherty PGF, Gavin K. 2011. Laterally loaded monopile design for offshore wind farms. Proceedings of the ICE-Energy, 165(1):p7-17.
Doherty JP, Wood DM. 2013. An extended Mohr-Coulomb (EMC) model for predicting the settlement of shallow foundations on sand. Géotechnique, 63(8): p661-673.
Doherty JP, Gourvenec S, Gaone FM. 2018. Insights from a shallow foundation load-settlement prediction exercise. Computers and Geotechnics, 93:p269-279.
Dunne FPE, Petrinic N. 2005. Introduction to computational plasticity. OUP, Oxford, UK.
Einav I, Puzrin AM. 2004. Pressure dependent elasticity and energy conservation in elastoplastic models for soils. Journal of Geotechnical and Geoenvironmental Engineering, 130(1):p81-92.
Einav I, Collins IF. 2008. A thermomechanical framework of plasticity based on probabilistic micromechanics. Journal of Mechanics of Materials and Structures, 3(5):p867-892.
Einav I. 2012. The unification of hypo-plastic and elasto-plastic theories. International Journal of Solids and Structures, 49(11-12):p1305-1315.
Elgamal A, Yang Z, Parra E, Ragheb A. 2003. Modelling of cyclic mobility in saturated cohesionless soils. International Journal of Plasticity, 19(6):p883-905.
Erbrich C. 1994. Modelling oF Novel Foundations for Offshore Structures, 9th UK Abaqus Users Conference.
Erbrich C, O'Neill MP, Clancy P, Randolph MF. 2010. Axial and lateral pile design in carbonate soils. In 2nd International Symposium on Frontiers in Offshore Geotechnics, Perth, Australia, p125-154.
Gajo A, Wood DM. 1999. A kinematic hardening constitutive model for sands: the multiaxial formulation. International Journal for Numerical and Analytical Methods in Geomechanics 23(9):p925-965.
Gasparre A. 2005. Advanced laboratory characterisation of London Clay. PhD Thesis, Imperial College, London, UK.
Gens A, Nova R. 1993. Conceptual Bases for a Constitutive Model for Bonded Soils and Weak Rocks. In Symposium on Hard Soils–Soft Rocks. Athens, Greeze, p485-494.
Golchin A, Lashkari A. 2014. A critical state sand model with elastic–plastic coupling. International Journal of Solids and Structures, 51(15-16):p2807-2825.
Grammatikopoulou A, Schroeder FC, Brosse AM, Andersen KW, Potts DM. 2017. On the use of constitutive models in numerical analyses of offshore structures. In 8th International Conference on Offshore Site Investigation and Geotechnics, London, UK, p423-430.
Grimstad G, Andresen L, Jostad H. 2012. NGI-ADP: Anisotropic shear strength model for clay. International Journal for Numerical and Analytical Methods in Geomechanics, 36:p483-497.
Grimstad G, Rønningen J, Nøst H. 2014. Use of IWAN models for modelling anisotropic and cyclic behavior of clays. In 8th European Conference on Numerical Methods in Geotechnical Engineering, Delft, Netherlands, (1):p49-55.
Hardin BO, Richart FE. 1963. Elastic wave velocities in granular soils. Journal of the Soil Mechanics and Foundations Division, ASCE, 89(SM1):p33-65.
Hardin BO, Black WL. 1969. Closure to vibration modulus of normally consolidated clays. Journal of the Soil Mechanics and Foundation Division, 95(SM7):p1531-1537.
Hardin BO, Drnevich VP. 1972. Shear modulus and damping in soils: design equations and curves. Journal of Soil Mechanics and Foundations Division, 98(SM7):p667-692.
Herle I, Kolymbas D. 2004. Hypoplasticity for soils with low friction angles. Computers and Geotechnics 31:p365-373.
Houlsby GT, Wroth CP. 1991. The variation of shear modulus of a clay with pressure and overconsolidation ratio. Soils and Foundations, 31(3):p138-143.
Houlsby GT. 1991. How the dilatancy of soils affects their behaviour. 10th European Conference on Soil Mechanics and Foundation Engineering, Florence, Italy, (4):p1189-1202.
Houlsby, GT. 1999 A model for the variable stiffness of undrained clay. Proc. Int. Symp. on Pre-Failure Deformation Characteristics of Soils, Turin, (1):p443-450.

Houlsby GT, Amorosi A, Rojas E. 2005. Elastic moduli of soils dependent on pressure: a hyperelastic formulation. Géotechnique, 55(5):p383-392.
Houlsby GT, Puzrin AM. 2006. Advanced Plasticity Theories. Principles of Hyperplasticity: An Approach to Plasticity Theory Based on Thermodynamic Principles, Springer, London, UK.
Houlsby GT, Abadie CN, Beuckelaers WJ, Byrne BW. 2017. A model for nonlinear hysteretic and ratcheting behaviour. International Journal of Solids and Structures, 120:p67-80.
Humrickhouse PW. Sharpe JP, Corradini ML. 2010. Comparison of hyperelastic models for granular materials. Physical Review E, 81(1).
In Situ Site Investigation (In Situ) (2014) Dunkirk static cone penetration testing factual report. In Situ Report No. 1140181R001RW. East Sussex: In Situ Site Investigation.
Ishihara K, Tatsuoka F, Yasuda S. 1975. Undrained deformation and liquefaction of sand under cyclic stresses. Soils and Foundations, 15(1):p29-44.
Iwan WD. 1966. A distributed-element model for hysteresis and its steady-state dynamic response. Journal of Applied Mechanics, 33(4):p893-900.
Iwan WD. 1967. On a class of models for the yielding behavior of continuous and composite systems. Journal of Applied Mechanics, 34(3):p612-617.
Jamiolkowski M, Ladd CC, Germaine JT, Lancellotta R. 1985. New developments in field and laboratory testing of soils. In 11th International Conference on Soil Mechanics and Foundations Engineering. San Francisco, (1):p57-153.
Jamiolkowski M, Lo Presti DCF, Manassero M. 2001. Evaluation of relative density and shear strength of sands from CPT and DMT, ASCE Geotechnical Special Publication, 119:p201-238.
Jardine RJ, Potts DM, Fourie AB, Burland JB. 1986. Studies of the influence of non-linear stress–strain characteristics in soil–structure interaction. Géotechnique, 36(3):p377-396.
Jardine RJ. 1992. Some observations on the kinematic nature of soil stiffness. Soils and foundations, 32(2):p111-124.
Jeanjean P, Zhang Y, Zakeri A, Andersen KH, Gilbert R, Senanayake AIMJ. 2017. A framework for monotonic py curves in clays. In 8th International Conference on Offshore Site Investigation and Geotechnics, London, UK, p108-141.
Jeanjean P. 2009. Re-assessment of py curves for soft clays from centrifuge testing and finite element modelling. In Offshore Technology Conference. Offshore Technology Conference, Houston, Texas.
Jefferies M. 1993. Nor-Sand: a simple critical state model for sand. Géotechnique, 43(1):p91-103.
Jefferies M, Been K. 2015. Soil liquefaction: a critical state approach 2nd edition. CRC press, New York.
Jiang Y, Liu M. 2007. A brief review of granular elasticity. The European Physical Journal E, 22(3):p255-260.
Kallehave D, Thilsted CL, Troya A. 2015. Observed variations of monopile foundation stiffness. In 3rd International Symposium on Frontiers in Offshore Geotechnics, Oslo, Norway, p717-722.
Karstunen, M, Krenn H, Wheeler S, Koskinen M, Zentar R. 2005. The effect of anisotropy and destructuration on the behaviour of murro test embankment. International Journal of Geomechanics (ASCE) 5(2):p87-97.
Khong C. 2004. Development and Numerical Evalulation of Unified Critical State Models. PhD Thesis, University of Nottingham, UK.
Kishida T. 2008. Seismic site effects for the Sacramento-San Joaquin delta. PhD Thesis, University of California, Davis, CA.
Kolymbas D. 2000. The misery of constitutive modelling. In Kolymbas D. (ed.) Constitutive modelling of granular materials. Springer, Berlin, Heidelberg, p11-23.
Koskinen M, Karstunen M, & Wheeler, S. 2002. Modelling destructuration and anisotropy of a natural soft clay. In 5th European Conf. Numerical Methods in Geotechnical Engineering. Paris, p11-20.
Kouretzis G, Jubert P, Krabbenhøft K. 2017. Interpretation of vane shear tests for geotechnical stability calculations. Canadian Geotechnical Journal, 54(12):p1775-1780.
Kuwano R. 1999. The stiffness and yielding anisotropy of sand. PhD Thesis, Imperial College. London, UK.
Lade PV, Duncan J. 1975. Elastoplastic stress-strain theory for cohesionless soil. ASCE Journal of Geotechncial Engineering Division, 101(10):p1037-1053.
Lade PV, Mustante H. 1978. Three-dimensional behaviour of remoulded clay. ASCE Journal of Geotechnical Engineering Division, 116(3):p394-415.
Lagioia R, Puzrin AM, Potts DM. 1996. A New Versatile Expression for Yield and Plastic Potential Surfaces. Computers and Geotechnics, 19(3):p171-191.
Lambe TW. 1973. Predictions in soil engineering. Géotechnique, 23(2):p151-202.
Lashkari A. 2010. A SANISAND model with anisotropic elasticity. Soil Dynamics and Earthquake Engineering, 30(12):p1462-1477
Lehane BM, Jardine RJ. 1994. Displacement-pile behaviour in a soft marine clay. Canadian Geotechnical Journal, 31(2):p181-191.
Liu MD and Carter JP. 2000. Modelling the destructuring of soils during virgin compression. Géotechnique, 50(4):p479-483.
Liu HY, Abell JA, Diambra A, Pisanò F. 2019. Modelling the cyclic ratcheting of sands through memory-enhanced bounding surface plasticity. Géotechnique 69:p783-800.
Liu T. 2019 (expected). Advanced laboratory testing of offshore wind turbine foundations under lateral loading. PhD Thesis, Imperial College, London, UK.

Loukidis D, Salgado R. 2009. Modeling sand response using two-surface plasticity. Computers and Geotechnics, 36:p166-186.
Mair RJ. 1979. Centrifugal modelling of tunnel construction in soft clay. PhD thesis. Cambridge University. UK.
Mair RJ. 1993. Unwin Memorial Lecture: Developments in geotechnical engineering research: applications to tunnels and deep excavations, Proceedings of Institute of Civil Engineers, Civil Engineering, p27-41.
Manzari MT, Dafalias YF. 1997. A critical state two-surface plasticity model for sands. Géotechnique, 47(2):p255-272.
Manzari MT, Nour MA. 1997. On implicit integration of bounding surface plasticity models. Computers and Structures, 63(3):p385-395.
Martin CM, and Burd HJ. 2018. Numerical Analysis for Offshore Geotechnics, lecture notes, University of Oxford, UK.
Mašín D, Herle I. 2005. Numerical analyses of a tunnel in London clay using different constitutive models. In 5th International Symposium TC28 Geotechnical Aspects of Underground Construction in Soft Ground, Amsterdam, Netherlands, p595-600.
Mašín D. 2012. Hypoplastic Cam-clay model. Géotechnique, 62(6):p549-553.
Mašín D. 2014. Clay hypoplasticity model including stiffness anisotropy. Géotechnique, 64(3):p232-238.
Masing G. 1926. Eigenspannumyen und verfeshungung beim messing. In. International Congress for Applied Mechanics.p332-335.
Matsuoka H, Nakai T. 1974. Stress-deformation and strength characteristics of soil under three different principal stresses. In Proceedings of the Japan Society of Civil Engineers, 232:p59-70.
McAdam RA, Byrne BW, Houlsby GT, Beuckelaers WJAP, Burd HJ, Gavin K, Igoe D, Jardine RJ, Martin CM, Muir Wood A, Potts DM, Gretlund S, Taborda DMG, Zdravković L. 2019. Monotonic lateral loaded pile testing in a dense marine sand at Dunkirk. Géotechnique (in press).
Measham PG, Taborda DMG, Zdravković L, Potts DM. 2014. Numerical simulation of a deep excavation in London Clay. In 8th European Conference on Numerical Methods in Geotechnical Engineering, Delft, Netherlands, p771-776.
Mita KA, Dasari GR, Lo KW. 2004. Performance of a Three-Dimensional Hvorslev–Modified Cam Clay Model for Overconsolidated Clay. International Journal of Geomechanics, 4(4):p296-309.
Mroz Z. 1967. On the description of anisotropic work hardening. Journal of the Mechanics and Physics of Solids, 15(3):p163-175.
Murphy G, Igoe D, Doherty P, Gavin K. 2018. 3D FEM approach for laterally loaded monopile design. Computers and Geotechnics, 100:p76-83.
Niemunis A, Wichtmann T. and Triantafyllidis T. 2005. A high-cycle accumulation model for sand. Computers and Geotechnics, 32(4):p245-263.
Offshore Wind Accelerator (OWA). 2019. A Suction Installed Caisson Foundations for Offshore Wind: Design Guidelines. Carbon Trust, February 2019, Issue 1. Carbon Trust, London, UK.
Oztoprak S, Bolton MD. 2013. Stiffness of sands through a laboratory test database. Géotechnique, 63(1):p54-70
Papadimitriou AG, Bouckovalas GD. 2002. Plasticity model for sand under small and large cyclic strains: a multiaxial formulation. Soil Dynamics and Earthquake Engineering, 22(3):p191-204.
Parry RHG, Nadarajah V. 1973. A volumetric yield locus for lightly overconsolidated. Géotechnique, 23:p450-453.
Petalas AL, Dafalias YF, Papadimitriou AG. 2019. SANISAND-FN: An evolving fabric-based sand model accounting for stress principal axes rotation. International Journal for Numerical and Analytical Methods in Geomechanics, 43(1):p97-123.
Plaxis. 2017. Material Models Manual. Plaxis B.V, Delft, Netherlands
Potts DM, Dounias GT, Vaughan PR. 1990. Finite element analysis of progressive failure of Carsington embankment. Géotechnique, 40(1):p79-101.
Potts DM, Ganendra D. 1994. An evaluation of substepping and implicit stress point algorithms. Computer methods in applied mechanics and engineering, 119:p341-354.
Potts DM, Zdravković L. 1999. Finite element analysis in geotechnical engineering: theory. Thomas Telford, London, UK.
Potts DM, Zdravković L. 2001. Finite element analysis in geotechnical engineering: theory. Thomas Telford, London, UK.
Prashant A, Penumadu D. 2004. Effect of Intermediate Principal Stress on Overconsolidated Kaolin Clay. Journal of Geotechnical and Geoenvironmental Engineering, 130(3):p284-292.
Prévost JH. 1977. Mathematical modelling of monotonic and cyclic undrained clay behaviour. International Journal for Numerical and Analytical Methods in Geomechanics, 1(2):p195-216.
Prévost JH. 1979. Undrained shear tests on clays. Journal of Geotechnical and Geoenvironmental Engineering, 105(1):p59-64.
Prévost JH. 1985. A simple plasticity theory for frictional cohesionless soils. International Journal Soil Dynamics Earthquake Engineering, 4(1):p9-17.
Roscoe KH, Schofield AN, Thurairajah A. 1964. An evaluation of test data for selecting a yield criterion for soils. ASTM International Special Technical Publication, Laboratory Shear Testing of Soils.p111-133.
Roscoe KH, Burland JB. 1968. On the generalised stress-strain behaviour of wet clay. In Engineering Plasticity. Cambridge, UK, p535-609.
Rouainia M, Wood DM. 2000. A kinematic hardening constitutive model for natural clays with loss of structure. Géotechnique, 50(2):p153-164.
Rouainia M, Wood DM. 2001. Implicit numerical integration for a kinematic hardening soil plasticity model. International Journal for Numerical and Analytical Methods in Geomechanics, 25(13):p1305-1325.

Rowe PW. 1962. The stress-dilatancy relation for static equilibrium of an assembly of particles in contact. Proceedings of the Royal Society of London. Series A. Mathematical and Physical Sciences, 269:p500-527.
Schanz, T, Vermeer PA, Bonnier PG. 1999. The hardening soil model: formulation and verification. In 1st International Plaxis Symposium: Beyond 2000 in Computational Geotechnics, Rotterdam, Netherlands, p281-296.
Schroeder FC, Merritt AS, Sørensen KW, Wood AM, Thilsted CL, Potts DM. 2015. Predicting monopile behaviour for the Gode Wind offshore wind farm. In 3rd International Symposium on Frontiers in Offshore Geotechnics, Oslo, Norway, p735-740.
Sekiguchi H, Ohta H. 1977. Induced Anisotropy and time dependancy in clays. In 9th ICSMFE. Tokyo, p163-175.
Shakeel M, Ng CW. 2018. Settlement and load transfer mechanism of a pile group adjacent to a deep excavation in soft clay. Computers and Geotechnics, 96:p55-72.
Sheil BB, McCabe BA. 2016. Biaxial loading of offshore monopiles: numerical modelling. International Journal of Geomechanics, 17(2):p1-16.
Sheng D, Sloan SW, Yu HS. 2000. Aspects of finite element implementation of critical state models. Computational Mechanics, 26(2):p185-196.
Shibuya S, Mitachi T. 1994. Small strain modulus of clay sedimentation in a state of normal consolidation. Soils and Foundations, 34(4):p67-77.
Shonberg A, Harte M, Aghakouchak A, Brown CSD, Andrade MP, Liingaard MA. 2017. Suction bucket jackets for offshore wind turbines: applications from in situ observations. In Proc. TC209 Workshop, 19th International Conference on Soil Mechanics and Geotechnical Engineering, Seoul, South Korea, p65-77.
Sivasithamparam N. 2012. Development and implementation of advanced soft soil models in finite elements. PhD Thesis, University of Strathclyde. Glasgow, UK.
Sivasithamparam N, Karstunen M, Bonnier P. 2015. Modelling creep behaviour of anisotropic soft soils. Computers and Geotechnics, 69:p46-57.
Skau KS, Grimstad G, Page AM, Eiksund GR, Jostad, HP. 2018. A macro-element for integrated time domain analyses representing bucket foundations for offshore wind turbines. Marine Structures, 59:p158-178.
Skempton AW, Northey RD. 1952. The sensitivity of clays. Géotechnique, 3(1):p30-53
Sloan SW. 1987. Substepping schemes for the numerical integration of elastoplastic stress–strain relations. International journal for Numerical Methods in Engineering, 24(5):p893-911.
Sloan SW, Abbo AJ, Sheng D. 2001. Refined explicit integration of elastoplastic models with automatic error control. Engineering Computations, 18(1/2):p121-194.
Smith IM, Griffiths DV, Margetts L. 2013. Programming the finite element method 5th edition. John Wiley & Sons, Chichester, UK.
Stallebrass SE, Taylor RN. 1997. The development and evaluation of a constitutive model for the prediction of ground movements in overconsolidated clay. Géotechnique, 47(2):p235-253.
Sturm H. 2017. Design Aspects of Suction Caissons for Offshore Wind Turbine Foundations. In Unearth the Future, Connect beyond. In 19th International Conference on Soil Mechanics and Geotechnical Engineering TC 209 workshop, Seoul, South Korea, p45-63.
Sultaniya AK, Rattley MJ, Gibbs P, Andrade MP, Liingaard MA, Lam S, Erbrich C. 2017. Engineering Behaviour of Mercia Mudstone for Offshore Pile Design. In 8th International Conference on Offshore Site Investigation and Geotechnics, London, UK, p658-665.
Summersgill F, Kontoe S, Potts D. 2017a. Stabilisation of excavated slopes in strain-softening materials with piles. Géotechnique, 68(7):p636-639.
Summersgill FC, Kontoe S, Potts DM. 2017b. On the use of nonlocal regularisation in slope stability problems. Computers and Geotechnics, 82:p187-200.
Summersgill FC, Kontoe, S. and Potts DM. 2017c. Critical assessment of nonlocal strain-softening methods in biaxial compression. International Journal of Geomechanics, 17(7):p1-14.
Suryasentana S, Byrne BW, Burd HJ, Shonberg A. 2017. A simplified model for the stiffness of suction caisson foundations under 6 DOF loading. In 8th International Conference on Offshore Site Investigation and Geotechnics, London, UK, p554-561.
Taborda DMG. 2011. Development of Constitutive Models for Application in Soil Dynamics. PhD Thesis, Imperial College, London, UK.
Taborda DMG, Zdravković L. 2012. Application of a Hill-Climbing technique to the formulation of a new cyclic nonlinear elastic constitutive model. Computers and Geotechnics, 43:p80-91.
Taborda DMG, Zdravković L, Kontoe S, Potts DM. 2014. Computational study on the modification of a bounding surface plasticity model for sands. Computers and Geotechnics, 59:p145-160.
Taborda DMG, Potts DM, Zdravković L. 2016. On the assessment of energy dissipated through hysteresis in finite element analysis. Computers and Geotechnics, 71:p180-194.
Taborda DMG, Zdravković L, Potts DM, Burd HJ, Byrne BW, Gavin K, Houlsby GT, Jardine RJ, Liu T, Martin CM, McAdam RA. 2019. Finite element modelling of laterally loaded piles in a dense marine sand at Dunkirk. Géotechnique (in press).
Taiebat M, Dafalias YF. 2008. SANISAND: Simple anisotropic sand plasticity model. International Journal for Numerical and Analytical Methods in Geomechanics, 32(8):p915-948.
Thieken K, Achmus M, Schroder C. 2014. On the behaviour of suction buckets in sand under tensile loads. Computers and Geotechnics, 60(1):p88-100.

Tjelta TI. 2015. The suction foundation technology. In 3rd International Symposium on Frontiers in Offshore Geotechnics, Oslo, Norway, p85-93.
Tsiampousi A, Zdravković L, Potts DM. 2013. A new Hvorslev surface for critical state type unsaturated and saturated constitutive models. Computers and Geotechnics, 48:p156-166.
Van Eekelen HAM. 1980. Isotropic yield surfaces in three dimensions for use in soil mechanics. International Journal for Numerical and Analytical Methods in Geomechanics, 4(1):p89-101.
Vardanega PJ, Bolton MD. 2013. Stiffness of clays and silts: normalizing shear modulus and shear strain. Journal of Geotechnical and Geoenvironmental Engineering, 139(9):p1575-1589.
Von Wolffersdorff PA. 1996. A hypoplastic relation for granular materials with a predefined limit state surface. Mechanics of Cohesive-frictional Materials: An International Journal on Experiments, Modelling and Computation of Materials and Structures, 1(3):p251-271.
Wang ZL, Dafalias YF, Shen CK. 1990. Bounding surface hypoplasticity model for sand. Journal of Engineering Mechanics, 116(5):p983-1001.
Wang ZL, Dafalias YF, Li XS, Makdisi FI. 2002. State pressure index for modeling sand behaviour. Journal Geotechnical and Geoenviromental Engineering, 128(6):p11-19.
Wheeler SJ, Näätänen A, Karstunen M, Lojander M. 2003. An anisotropic elastoplastic model for soft clays. Canadian Geotechnical Journal, 40(2):p403-418.
Whittle AJ, Kavvadas MJ. 1994. Formulation of MIT-E3 constitutive model for overconsolidated clays. Journal of Geotechnical Engineering, 120(1):173-198.
Whyte S, Rattley M, Erbrich CE, Burd HJ, Martin CM. 2017, A practical constitutive model for offshore foundation problems involving dense sands in partially drained to undrained conditions. In 8th International Conference on Offshore Site Investigation and Geotechnics, London, UK, p400-407.
Wichtmann T, Triantafyllidis T. 2009. Influence of the grain-size distribution curve of quartz sand on the small strain shear modulus Gmax. Journal of Geotechnical and Geoenvironmental Engineering, 135(10):p1404-1418.
Wind Europe. 2018. Offshore Wind in Europe, key trends and statistics 2017. Wind Europe.
Woo SI, Seo H, Kim J. 2017. Critical-state-based Mohr-Coulomb plasticity model for sands. Computers and Geotechnics, 92:p179-185.
Wood DM. 1990. Soil Behaviour and Critical State Soil Mechanics, Cambridge University Press. UK
Wood DM. 1991. Approaches to Modelling the Cyclic Stress-Strain Response of Soils. In O'Reilly M, Brown F. (ed.). Cyclic Loading of Soils: From Theory to Design. Glasgow: Blackie and Son, p19-69.
Wu W, Kolymbas D. 2000. Hypoplasticity then and now. In Kolymbas D. (ed.) Constitutive modelling of granular materials. Springer, Berlin, Heidelberg, p57-105.
Ye G, Ye B, Zhang F. 2014. Strength and Dilatancy of Overconsolidated Clays in Drained True Triaxial Tests. ASCE Journal of Geotechnical and Geoenviromental Engineering, 140(3):06013006
Yimsiri S. 2001. Pre-failure deformation characteristics of soils: Anisotropy and soil fabric. PhD Thesis, University of Cambridge, Cambridge, UK.
Yin ZY, Karstunen M.2011. Modelling strain-rate-dependency of natural soft clays combined with anisotropy and destructuration. Acta Mechanica Solida Sinica, 24(3):p216-230.
Yiu WN, Burd HJ, Martin CM. 2017. Finite-element modelling for the assessment of tunnel-induced damage to a masonry building. Géotechnique, 67(9):p780-794.
Yu HS, Khong C, Wang J. 2007. A unified plasticity model for cyclic behaviour of clay and sand. Mechanics research communications, 34(2):p97-114.
Zdravković L, Taborda DMG, Potts DM, Abadias D, Burd HJ, Byrne BW, Gavin K, Houlsby GT, Jardine RJ, Martin CM, McAdam RA, Ushev E. 2019. Finite element modelling of laterally loaded piles in a stiff glacial clay till at Cowden. Géotechnique (in press).
Zhang J, Andrus RD, Juang CH. 2005. Normalized shear modulus and material damping ratio relationships. Journal of Geotechnical and Geoenvironmental Engineering, 131(4):p453-464.
Zhao J, Sheng D, Rouainia M, Sloan SW. 2005. Explicit stress integration of complex soil models. International Journal for Numerical and Analytical Methods in Geomechanics, 29(12):p1209-1229.
Zhang Y, Andersen KH. 2019. Soil reaction curves for monopiles in clay. Marine Structures, 65:p94-113.
Zytynski M, Randolph MF, Nova R, Wroth CP. 1978. On modelling the unloading-reloading behaviour of soils. International Journal for Numerical and Analytical Methods in Geomechanics, 2(1):p87-93.